EXPERIMENTAL MONITORING OF GEOTECHNICAL RESPONSE OF RAILWAY TRACK SYSTEMS

by

ABDULLAH H. ALSABHAN

A dissertation submitted in partial fulfillment of

the requirements for the degree of

Doctor of Philosophy

(Civil and Environmental Engineering)

at the

UNIVERSITY OF WISCONSIN-MADISON

2016

Date of final oral examination: May 2, 2016
Month and year degree to be awarded: August 2016

The dissertation is approved by the following members of the Final Oral Committee:
Dante O. Fratta, Associate Professor, Civil and Environmental Engineering
Tuncer B. Edil, Professor Emeritus, Civil and Environmental Engineering
William J. Likos, Professor, Civil and Environmental Engineering
James M. Tinjum, Associate Professor, Engineering Professional Development
David J. Hart, Professor, Wisconsin Geological and Natural History Survey

Dedication

To my lovely wife Hajir and our son Hamad for their unconditional love and support.

Abstract

An important issue that compromises rail track operations and safety is ballast fouling. Ballast fouling may lead to track deformation, reduction of track load capacity and train speed, and ultimately train derailment. This problem is quite costly for the railway industry thus, assessing and controlling ballast fouling and then preventing train derailment while optimizing maintenance operation is very important for reducing the overall cost of freight and passenger transportation. This study presents a proposed holistic methodology that extends assessing fouling while monitoring rail track deformation. The techniques uses deformation monitoring instruments (e.g., fiber optic (FO) sensors and LVDTs) coupled with Electromagnetic (EM) surveying: Ground penetrating radar (GPR) and a time domain reflectometry (TDR). The methodology aims at gathering data to create an early warning system that would allow railway engineers to develop a symptomatic approach to ballast maintenance procedures. This proposed methodology was tested on a full scale track model (FSTM). This model comprises 2.45 m rail supported by five ties embedded in ballast layer that was fouled under controlled conditions. The testing program considered three common types of fouling: mineral fouling, clay fouling, and silica sand fouling. A comparison between rail settlement measurements measured by LVDTs and rail bending strain measurement measured by FO sensors showed that FO sensors do not provide an indication of track deterioration due to cyclic loading, moisture content, and fouling depth. In addition, results showed a high correlation between rate of plastic settlement and amount of fouling detected by EM survey. Experimental results also showed that EM survey results can be used to determine depth and type of fouling.

Acknowledgements

I would like to express my very great appreciation to my academic and research advisors, professors D. Fratta, T. Edil, and J. Tinjum for their valuable and constructive suggestions during the planning and development of this research work. I extend my appreciation to professors D. Hart and W. Likos for serving on my thesis committee. I would also like to extend my thanks to the technicians of the laboratory of the civil and environment engineering department, Xiaodong Wang, William Lang, and Jacob Zeuske for their help and support in the lab.

Financial support for this study was provided by the King Saud University (KSU-Saudi Arabia) and by Center for Freight Infrastructure Research and Education (C-FIRE). Their support is greatly appreciated. I'm also greatly thankful to all of my friends who helped me during the development of this research work, Ben Warner, Andrew Keene, Tolga Dolcek, Matt Houde, and Damien Hesse.

Most importantly I owe a particular gratitude to Professor Abdullah Almuhaideb, who steered me into the area of geotechnical engineering and facilitated my admission to the University of Wisconsin-Madison.

I wish to thank my parents Hamad Alsabhan and Haya almudaiheem for all the support they have provided me over the years. Without them, I may never have gotten where I am today. Also, I thanks my brothers, Matab for his valuable advices and Talal for financially supporting me during my hard times. Also, I thank my uncle Abdulaziz almudaiheem for always encouraging me to pursue my graduate studies.

A special thanks to my teacher Mohammed Mahawish Al Dhafeeri for setting a great role model for me. He is one of the few teacher that left a lasting impression on me.

At last but not the least, I want to thank my friends I had in the USA, Naief Alotaibi, Ali Alqarni, Mohammed Alobaid, Bandar Aloyayydi, Adel Alshehri, Abdullah Alamri, Yousef Almoaleem, Mohammed Alhizan, and Ahmed Aljohni.

List of Contents

Dedication i

Abstract ii

Acknowledgements iii

CHAPTER 1: Introduction 1

1.1 Motivation and Scope 1

1.2 Description of the Fouling Process in Rail Track Structures 3

1.3 Current Evaluation Practices 4

1.4 Research Objective 5

1.5 Thesis Organization 6

1.6 Research Products 7

References 9

CHAPTER 2: Determination of Depth of Fouling and Fouling Type in Railway Track Substructure with Time Domain Reflectometer 11

Abstract 11

2.1 Introduction 12

2.2 Electromagnetic Properties of Geomaterials 14

2.2.1 Relative Dielectric Permittivity (ε_r) 14

2.2.2 Electrical Conductivity (σ) 15

2.3 Time Domain Reflectometry and the Measurement of Electromagnetic Properties 17

2.3.1 Spatial Sensitivity of TDR Probes 19

2.4 Materials 19

2.5 Methodology 20

2.5.1 Equipment 20

2.5.2 Specimen Preparation 20

2.5.3 TDR Probes Design 22

2.6 Results and Discussions 23

2.6.1 Observations during Ballast Specimen Preparation 23

2.6.2 Clean Ballast EM Properties Characterization 24

2.6.3 Fouled Ballast EM Properties Characterization 24

2.7 Field Implementation of Proposed Methodology 27

2.7.1 Methodology 27

2.7.2 Results and Discussion 28

2.8 Summary and Conclusions 29

Acknowledgments 31

References 32

Figures 35

CHAPTER 3: Assessment of Ballast Fouling with Ground-Penetrating Radar (GPR) ... 50

Abstract 50

3.1 Introduction 51

3.2 Theory and Background of GPR 52

3.3 Survey Design 53

3.3.1 Central Frequency 54

3.3.2 Station Spacing 55

3.3.3 Time Window 55

3.3.4 Selecting Antenna Orientation 55

3.4 Data Processing 56

3.4.1 Data Editing 56

3.4.2 Time Zero Correction and Dewowing 57

3.4.3 Filtering 57

3.4.4 Time Gain 58

3.5 Methodology - Case Study: Evaluation of Railway Track Substructure Using Ground Penetrating Radar Coupled with Time Domain Reflectometry 58

3.6 Results and Discussion 59

3.6.1 Ballast Section 59

3.6.2 Culvert Section 61

3.7 Summary and Conclusions 62

Acknowledgements 62

References 63

Figures 64

CHAPTER 4: Full Scale Track Model (FSTM) 77

Abstract 77

4.1 Introduction and General Description 78

4.2 Assessment of Boundary Conditions on the FSTM Results 81

4.3 Materials 83

4.4 Specimen Preparation 83

4.5 FSTM Instrumentation 86

4.6 Load Transfer Mechanisms 88

4.7 Testing Program 88

4.8 Results and Discussion 92

4.8.1 Measured Track Deformation 92

4.8.2 Measured EM Properties 95

4.8.3 Relationship between EM Measurements and Ballast Physical Parameters . 97

4.8.4 Ground Truthing 99

4.9 Summary and Conclusions 100

Acknowledgements 102

References 103

Figures 105

CHAPTER 5: Limitations of Using Fiber Optic Sensors to Assess the Effect Ballast Fouling on the Response of Railway Structures 128

Abstract 128

5.1 Introduction 129

5.2 Fiber Optic Sensors - Working Concepts 130

5.3 Classification of FO Sensors 133

5.3.1 Local FO Sensor Measurements 133

5.3.2 Quasi-Distributed Sensors - Fiber Bragg Grating 135

5.3.3 Distributed FO Sensors 136

5.4 FO sensors in Railway Rapid Mentoring 139

5.5 Railway Deformation Response 141

5.5.1 Effect Single Railway Cart and Adjoining Railway Cart Loading 142

5.5.2 Effect of Railway joints 143

5.6 Experimental Setup 144

5.7 Results and Discussion 145

5.8 Alternative Railway Tracks Instrumenting Techniques 146

5.8.1 Geophones 146

5.8.2 Microelectromechanical System (MEMS) accelerometers 147

5.8.3 Geodetic survey 148

5.9 Conclusions 148

References 150

Figures 153

CHAPTER 6: Summary and Conclusion 167

6.1 Major Findings 167

APPENDIX A: FSTM GPR Radargram Images 170

FSTM with Silica Sand Fouling 170

FSTM with Mineral Fouling 178

FSTM with Kaolinite Clay Fouling 182

APPENDIX B: TDR TRACES 190

APPENDIX C: FO Sensors Input Data 192

List of Tables

Table 1.1 Categories of Fouling based on FI, and PVC (modified after Indraratna 2012)5

Table 2. 1 Index Properties of Ballast and Fouling Materials 20

Table 2.2 Comparison of Relative Dielectric Permittivity of Different TDR Probes Configurations and Theoretical Value of Relative Dielectric Permittivity of Deionized water 23

Table 4. 1 Materials Properties 81

Table 4. 2 Index properties of ballast and fouling materials 83

Table 4.3 FSTM completed testing matrix 89

Table 4.4 Silica sand fouling testing parameters 90

Table 4.5 Kaolinite clay fouling testing parameters 91

Table 4.6 Mineral fouling testing parameters 91

Table 4.7 Clean ballast testing parameters 92

Table 4.8 Index properties of fouled ballast after $N= 8 \cdot 10^5$ 99

Table 5. 1 Advantages of Fiber Optics Sensors 132

Table 5. 2 FO Sensors Categories (Li et al. 2004; Glisic and Inaudi, 2007; Chang 2010) 133

List of Figures

Figure 1.1 Proposed EM-wave monitoring techniques: (a) TDR monitoring station and (b) GPR reflection survey 10

Figure 2.1 Typical components of railway track substructure and superstructure 35

Figure 2.2 TDR probe and typical waveform 36

Figure 2.3 Particle size distributions of ballast (AREMA # 25, AREMA # 24, AREMA # 4A, AREMA # 5), silica sand, and coal 37

Figure 2.4 Wooden box model: filled with silica sand with three different water levels (0, 0.1, and 0.2 m) measured from the bottom of the model..... 38

Figure 2.5 Preparation of fouled ballast due to spillage: (a) Placing clean ballast in 0.1 m lift, (b) pouring silica sand on the compacted ballast, (c) placing clean ballast on the compacted silica sand, (d) specimen consists of 0.1 m fouled ballast and 0.22 m clean ballast, (e) specimen consists of 0.2 m fouled ballast and 0.12 m clean ballast, (f) specimen consists of 0.32 m fouled ballast. 39

Figure 2. 6 Preparation of fouled ballast due to clay intrusion: (a) Placing clay in 0.1 m lift, (b) placing ballast on top of the compacted clay in lifts to form a specimen consists of 0.1 m fouled ballast and 0.22 m clean ballast, (c) placing ballast on top of the 0.2 m compacted clay in lifts to form a specimen consists of 0.2 m fouled ballast and 0.12 m clean ballast, (d) 0.32 m compacted clay specimen, (e) aerial view of clay intrusion into the clean ballast layer with 30% clay water content, (f) aerial view of clay intrusion into the clean ballast layer with 40% clay water content. 40

Figure 2.7 TDR waveform for deionized water, green lines are for coated TDR probe and black lines are for uncoated TDR probes. D is the diameter of the probes and S is their separations..... 41

Figure 2. 8 Change in relative dielectric permittivity and electrical conductivity of various types of ballast 42

Figure 2. 9 Measured relative dielectric permittivity as a function of volumetric water content. 43

Figure 2. 10 Measured TDR waveforms for a kaolinite fouled ballast with different volumetric water content for: (a) 0.22 m clean ballast and 0.1 m fouled ballast, and (b) 0.12 m clean ballast and 0.2 fouled ballast. 44

Figure 2. 11 Measured relative dielectric permittivity as a function of volumetric water content and embedded length of probe in fouled layer for: (a) silica sand fouled ballast, (b) coal fouled ballast, and (c) kaolinite fouled ballast. 45

Figure 2.12 Electrical conductivity measurements and reported electrical conductivity values in the literature. 46

Figure 2. 13 TDR waveform with multiple reflections at the horizontal position 63 m.... 47

Figure 2.14 GPR profile with DCP overlay. 48

Figure 2.15 Interpretation of the GPR profile with DCP profile. 49

Figure 3.1 GPR Separation Parameters (Annan 1992) 64

Figure 3.2 GPR Footprint (Jol 2008) 65

Figure 3.3 Common GPR Antenna Orientation (Annan and Cosway 1992)..... 66

Figure 3.4 Geographic location of the testing site: Dayton, IL (Source: Google Earth) . 67

Figure 3.5 Ballast Site Overview 68

Figure 3.6 Ballast Site Overview 69

Figure 3.7 TDR waveform with multiple reflections at the horizontal position 58 m in the Ballast Section 70

Figure 3.8 GPR profile with DCP overlay at the Ballast Section. 71

Figure 3.9 Interpretation of the GPR profile with DCP profile at the Ballast Section. 72

Figure 3.10 Culvert Site. Note Ballast Washout and Culvert. 73

Figure 3.11 TDR waveform with multiple reflections at the horizontal position 59 m in the culvert section 74

Figure 3.12 GPR profile with DCP overlay at the Culvert Section. 75

Figure 3.13 Interpretation of GPR profile with DCP profile at the Culvert Section. 76

Figure 4. 1 Full Scale Track Model (FSTM), (a) Plane view; (b) Side view 105

Figure 4. 2 Side View of Modeled FSTM Dimensions with 3 ties, 5 ties, 6 ties, and 7 ties. Tie spacing =0.495 m 106

Figure 4.3 Effect of Number of Ties on Deformational Behavior of Ballast..... 107

Figure 4. 4 Vertical Rail Deformations 107

Figure 4. 5 Particle size distributions of ballast (AREMA # 25), silica sand, and mineral fouling..... 108

Figure 4. 6 FO sensors identification labels 109

Figure 4.7 FO sensors locations on the rail 109

Figure 4. 8 Vertical Rail Deformations Measured with LVDTs..... 110

Figure 4. 9 LVDT raw deformation measurements. (a) Silica sand fouling, (b) Kaolinite clay fouling, (c) Mineral Fouling, (d) Clean ballast. 111

Figure 4.10 Combined analysis of: (a) Normalized rate of plastic deformation, and (b) Relationship between normalized rate of plastic deformation and loading cycles. 112
Figure 4.11 Combined analysis of normalized jumps of plastic deformation. 113
Figure 4.12 Comparison of normalized jumps of plastic deformation due to: (a) Change in moisture content (M.C), (b) Change in depth of fouling (d). 114
Figure 4.13 Defined Zone for Deformational Behavior of Fouled Ballast in ICP and FIP in the Soil Water Characteristics Curves of Fouling Materials (Note: C=clay fraction) (Ebrahimi 2011). 115
Figure 4.14 FO sensors strain deformation measurements 116
Figure 4.15 Bended rail in FSTM; black line represents the deformed shape immediately after applying load, and red line represents deformed shape after $N= 2 \cdot 10^5$. 117
Figure 4.16 An example taking out of experiment S-2-End of (a) TDR waveform reflection and (b) GPR radargram reflection. 118
Figure 4.17 Measured relative dielectric permittivity as a function of loading repetitions, volumetric water content, and depth of fouling for: (a) TDR (combined ballast layer), (b) GPR (top ballast layer), and (c) GPR (bottom ballast layer). 119
Figure 4.18 FSTM electrical conductivity measurements 120
Figure 4.19 Relationship between the combined permittivity of the system and the porosity. The dashed lines are for linear regression, taking for the individual material. Solid line is for linear regression, taking for all the materials. 121
Figure 4.20 Relationship between the relative dielectric permittivity of the combined system and the volumetric water content. The dashed lines are for linear regression,

taking for the individual material. Solid line is for linear regression, taking for all the materials..... 122

Figure 4.21 Relationship between the relative dielectric permittivity of the combined system and fouling depth. The dashed lines are for linear regression, taking for the individual material. Solid line is for linear regression, taking for all the materials. 123

Figure 4.22 Relationship between combined permittivity and (a) fouling index (FI), (b) non-clay fouling index (NFI), and (c) clay fouling index (CFI). 124

Figure 4.23 Relationship between electrical conductivity and (a) fouling index (FI), (b) non-clay fouling index (NFI), and (c) clay fouling index (CFI). 125

Figure 4.24 Vertical profile of FSTM test: (a) Silica sand fouling, (b) Kaolinite clay fouling, (c) Mineral Fouling, (d) Clean ballast..... 126

Figure 4.25 Particle size distributions of ballast (AREMA # 25), silica sand fouled ballast, kaolinite clay fouled ballast, and mineral fouled ballast. 127

Figure 5.1 FO sensors components (Signore et al. 1997) array. 153

Figure 5.2 Schematic of the Michelson interferometric sensors mechanism (Li et al. 2004) 154

Figure 5.3 Schematic of the Fabry–Perot sensors mechanism (Glisic and Inaudi 2007) 155

Figure 5.4 Periodic refraction index changes on FBG (Chang 2010) 156

Figure 5.5 (a) FBG fabrication using phase mask; (b) FBG sensor array for distributed sensing (Fernandez et al. 1996)..... 157

Figure 5.6 Spectral behavior of broadband light through a fiber with Bragg gratings (Fernandez et al. 1996) 158

Figure 5.7 Schematic shows simulated Brillouin scattering (SBS) Optical scattering components (Glisic and Inaudi, 2007) 159

Figure 5.8 Schematic shows simulated Brillouin scattering (SBS) in single mode optical fiber (Chang 2010) 160

Figure 5.9 (a) Rail deflection for 4- axles single cart loading, and (b) Rail Deformation for 4- axles adjoining carts loading 161

Figure 5.10 (a) Rail bending strain for 4- axles single cart loading, and (b) Rail bending strain for 4- axles adjoining carts 162

Figure 5.11 Rail deflection for single axle loading near railway joint 163

Figure 5.12 Rail bending strain for single axle loading near railway joint 164

Figure 5.13 (a) LVDT measurements, and (b) calculated track modulus 165

Figure 5.14 FO sensors strain deformation measurements 166

Figure A.1 S-1-Start 170

Figure A. 2 S-1-End 171

Figure A. 3 S-2-Start 172

Figure A. 4 S-2-End 173

Figure A. 5 S-3-Start 174

Figure A. 6 S-3-End 175

Figure A. 7 S-4-Start 176

Figure A. 8 S-4-End 177

Figure A. 9 K-1-Start 178

Figure A. 10 M-2-End 179

Figure A. 11 M-3-Start 180

Figure A. 12 M-4-End 181
Figure A. 13 K-1-Start 182
Figure A. 14 K-1-End 183
Figure A. 15 K-2-Start 184
Figure A. 16 K-2-End 185
Figure A. 17 K'-1-Start 186
Figure A. 18 K'-1-End 187
Figure A. 19 K'-2-End 188
Figure A. 20 K'-2-End 189
Figure B. 1 TDR waveform for FSTM fouled with Silica sand. 190
Figure B. 2 TDR waveform for FSTM fouled with kaolinite clay. 190
Figure B. 3 TDR waveform for FSTM fouled with minerals. 191
Figure B. 4 TDR waveform for FSTM with clean ballast. 191

CHAPTER 1: Introduction

1.1 Motivation and Scope

The need for a reliable, continuous, and remote monitoring routine for maintaining railway infrastructure has become a crucial factor in controlling the safety and the overall cost of the railway operations. Controlling the surface deformation of tracks is the main goal of rail maintenance. Track deformation is caused by a reduction in the bearing capacity and stiffness of ballast and subgrade layers and increase in rail loads and volume. Large track deformations reduce the load capacity of the rail line, forces a reduction in velocity and increases the potential for derailments. Therefore, the proper performance of the ballast in the rail structure is a crucial component in the transportation of freight and passengers by train.

Ballast layers serve several functions in the rail structure, including: distributing the rail loading over a much larger area so that the subgrade soil can support it, providing rapid water drainage, preventing vegetation growth between tracks, and reducing the level of vibration created by the passing-by trains (Ahlf 2011). However, ballast layers experience deterioration of its functions in proportion to the volume and weight of traffic, external contamination (car spelling, wind-blown material), ballast mineralogy, and absence of ballast maintenance (Walter and Selig 1994; Indraratna et al. 2011; Ahlf 2011; Ebrahimi 2011). Additionally, these mechanisms of deterioration may increase the generation of fine-grained particles leading to the reduction of load capacity, to an increase in compressibility, and to a larger retention of moisture. All these situations reduce the shear strength of the ballast during dynamic loading. The combination of these

deterioration mechanisms is known as ‘fouling.’ This process compromises the structural integrity of the railway structure leading to large track deformations and ultimately to train derailment (Walter and Selig 1994; Indraratna et al. 2011).

It is reported that North American railroads spent more than $8.9 billion per year on maintenance operations (AAR 2013). Although the cost and effectiveness of track maintenance are associated with the frequency of track inspection (i.e., selective drilling and digging at intervals along the track), it is mainly based on the judgment and experience of rail professionals. There is no quantitative, mechanistic assessment of deterioration yet. Thus, there is a high risk of functional or mechanical failure between two inspection events or that the inspection fails to properly evaluate the mechanistic mechanisms of the fouling process. For these reasons, a reliable, systematic, continuous, and sustainable inspection methodology needs to be developed, and demand for new technologies is increasing in the railway industry.

Deformation monitoring instruments (DMI - including fiber optic and displacement sensors) along with electromagnetic (EM) wave-based surveying techniques are proposed in this study to monitor and manage the ballast fouling deterioration and deformation process. Fiber optic arrays have the potential to create continuous sensing arrays and provide a warning system for inspection and maintenance activities during the rail track service life. However, DMI can only monitor the symptoms but not the causes for ballast fouling. To better evaluate the causes, it is proposed the deployment of (EM) wave-based surveying. Figure 1.1 presents the two proposed EM based techniques: time domain reflectometer (TDR) and ground penetrating radar (GPR). These two techniques are aimed at creating the image of the electromagnetic-wave properties of the material

within track cross-sections at critical spots identified by DMI. Coupling of these technologies provides information for strategic and sustainable maintenance activities and increases the safety of our national freight rail transportation network. The long term goal of the methodology is to evaluate the rate of track deterioration so the risk of derailment along the track length is decreased by developing a comprehensive warning system.

1.2 Description of the Fouling Process in Rail Track Structures

Railway substructure consists of two basic layers. The ballast layer which consists of a compacted stratum of 2 to 5 cm diameter, clean, open-voided, and free drainage particle structure. The subballast layer consists of an engineered compacted stratum of 1 to 3 cm particles in a less open structure. The subballast is, in most cases, the old ballast layer employed in earlier structures using smaller particles plus downwardly-migrated fine particles. The ballast and subballast layers distribute the vertical loads from the ties to the subgrade, providing lateral and longitudinal resistance to the tie movement by absorbing much of the impact and dynamic energy imparted by the passing of trains.

Ballast fouling is a progressive deterioration of the function of the ballast layer by increasing presence of fine particles and rising the moisture (Walter and Selig 1994; Indraratna et al. 2011). Fouling decreases the open voids in the ballast and causes moisture retention and loss of effective drainage thus increases in dynamic pore water pressure generation. This situations leads to a reduction in shear strength and stiffness increasing the need for maintenance operations. The fine particles created by the fouling

process are generated from different sources, i.e., ballast particle degradation, spillage on the track surface, and subballast and subgrade infiltration to the ballast layer (Selig and Waters 1994). Ebrahimi (2011) reported that the mechanical response of the fouled ballast does depend on the origin and properties of the fine material.

1.3 Current Evaluation Practices

Several parameters are used for evaluating the degree of ballast fouling in assessing the physical condition of the railway structure. Fouling index (FI) and percentage void contamination (PVC) are the most two common parameters employed for assessing the fouling condition of ballast (Indraratna, 2011). Fouling index is defined by Selig and Walters (1994) based on the gradations obtained for representative samples of ballast) as the sum of percentage of ballast passing sieve No. 4 (P4) and sieve No. 200 (P200):

$$\mathrm{FI} = \mathrm{P4} + \mathrm{P200} \tag{1.1}$$

The portion of ballast particles passing No. 200 is included twice to emphasize the importance of the finer fraction on the ballast response to loading.

Percentage void contamination emphasizes the effect of void change in ballast. It is defined as the ratio of bulk volume of fouling material to the initial volume of clean ballast voids (Feldman and Nissen 2002):

$$PVC = 100 \cdot \frac{V_1}{V_2} \tag{1.2}$$

where V_1 is the void volume between re-compacted ballast particles and V_2 is the total volume of re-compacted fouling material (particles passing 9.5 mm sieve).

Indraratna (2011) suggested that fouling index parameter FI provides a quick assessment of ballast condition while the determination of percentage void contamination is too time consuming and does not properly reflect the influence of gradation of fouling particles. Indraratna (2012) summarized categories of fouling based on the fouling index, and percentage void contamination in Table 1.1.

Table 1.1 Categories of Fouling based on FI, and PVC (modified after Indraratna 2012)

Category	**FI (%)**	**PVC (%)**
Clean	<1	0 to 20
Moderately clean	1 to < 10	N.A
Moderately fouled	10 to < 20	20 to 29
Fouled	20 to <40	>30
Highly fouled	≥ 40	N.A

1.4 Research Objective

This study is aimed at assessing the viability of using DMI coupled with EM surveying as a continuous monitoring system for railway track inspection. The proposed technique is aimed at improving track safety by developing a systematic early warning system for track inspection and maintenance. It extends the use of DMI to determine track deformation with electromagnetic waves techniques, including ground penetrating radar (GPR) and time domain reflectometry (TDR), to assess ballast fouling. The systematic

use of this combination of techniques can be then deployed as an early warning monitoring system. The hypothesis are (1) ballast fouling EM properties (i.e., real relative permittivity and electrical conductivity) can be characterized in the laboratory to predict type, amount, and depth of fouling in the field, (2) TDR can be used for calibrating the GPR data, particularly in fouled ballast with high moisture content environments, and (3) EM properties can be used to characterize ballast physical properties.

1.5 Thesis Organization

This thesis is divided into six chapters. Chapter 1 presents an introduction and the motivation of the study. Chapter 2 describes the use of time domain reflectometer (TDR) and ground penetrating radar in the determination of physical parameters in the railway subsurface. In this chapter, a combined methodology that uses TDR and ground penetrating radar (GPR) data is proposed to assess fouled ballast in high moisture content environments. Chapter 3 presents the development of the technique to conduct and analyze GPR survey as applied to railway monitoring. Results of 200 MHz GPR data on a case study are presented. These data have been successfully able to identify critical spots in troublesome railway sections. Chapters 4 describes the state of the art on ballast fouling and fouling type and their effect on the performance of railway systems using a full scale track model (FSTM). Fiber optic (FO) sensors and LVDTs along with electromagnetic (EM) wave-based surveying techniques are deployed to monitor and manage the ballast fouling process on the FSTM. Chapter 5 describes an elaborate literature review of FO sensors and its application for the monitoring of railway infrastructure. Also, it provides a technical note on in-situ instrumentation of railway track

that is based on what we learned of this study and provides alternatives techniques to monitor the track. Chapter 6 gives a brief summary and conclusions of this study.

1.6 Research Products

Journals

Alsabhan, A., Fratta, D., Tinjum, J., Edil, T., and Warren, B., 2016, Depth of Fouling and Fouling Type in Railway Track Substructure with Time Domain Reflectometry, Geotechnical Testing Journal (In preparation for publication).

Alsabhan, A., and Fratta, D., 2016, Testing Tools for Warning System and Inspection for Maintenance of Freight Railways, Journal of Transportation Engineering (In preparation for publication).

Alsabhan, A., and Fratta, D., 2016, Technical Note Limitations of Using Fiber Optic Sensors to Assess the Effect of Ballast Fouling on the Response of Railway Structure,, Journal of Transportation Engineering (In preparation for publication).

Conferences and Symposiums

Alsabhan, A., 2014, Testing Tools for Warning System and Inspection for Maintenance of Freight Railways, In Mid-Continent Transportation Research Symposium, Madison, Wisconsin.

Alsabhan, A., Fratta, D., and Tinjum, J., 2015, Evaluation of Railway Track Substructure using Ground Penetrating Radar Coupled with Time Domain Reflectometry. In From Fundamentals to Applications in Geotechnics: Proceedings of the 15th Pan-American

Conference on Soil Mechanics and Geotechnical Engineering, Buenos Aires, Argentina, IOS Press.

References

Ahlf, R. E., 2011. “Maintaining, re-habitation, and upgrading conventional railroad track-ballast”, unpublished short course, University of Wisconsin-Madison.

Chrismer, S., and Davis, D., 2000. “Cost comparisons of remedial methods to correct track substructure instability”. Transportation Research Records, National Research Council, Washington, D.C., vol. 1713, pp. 10-15.

Ebrahimi, A., 2011. “Deformational behavior of fouled railway ballast.” PhD thesis, Department of Civil and Environmental Engineering, University of Wisconsin, Madison.

Feldman, F., and Nissen, D., 2002. “Alternative testing method for the measurement of ballast fouling: percentage void contamination,” In Proceedings of the Conference on Railway Engineering, Wollongong, Australia, 10–13 November, Railway Technical Society of Australia, Canberra, Australia, pp. 101–109.

Indraratna, B., Salim, W., and Rujikiatkamjorn, C., 2011. Advanced Rail Geotechnology-Ballasted Track, Book, CRC Press, Taylor & Francis Group, London, UK.

Selig, E. T. and Walters, J. M., 1994. Track Geotechnology and Substructure Management, Book, Thomas Telford, New York, NY.

Stewart, H. E. and Selig, E. T., 1982. “Predicted and Measured Resilient Response of Track,” Journal of the Geotechnical Engineering Division, ASCE, vol. 108(GT11), pp. 1423–1442.

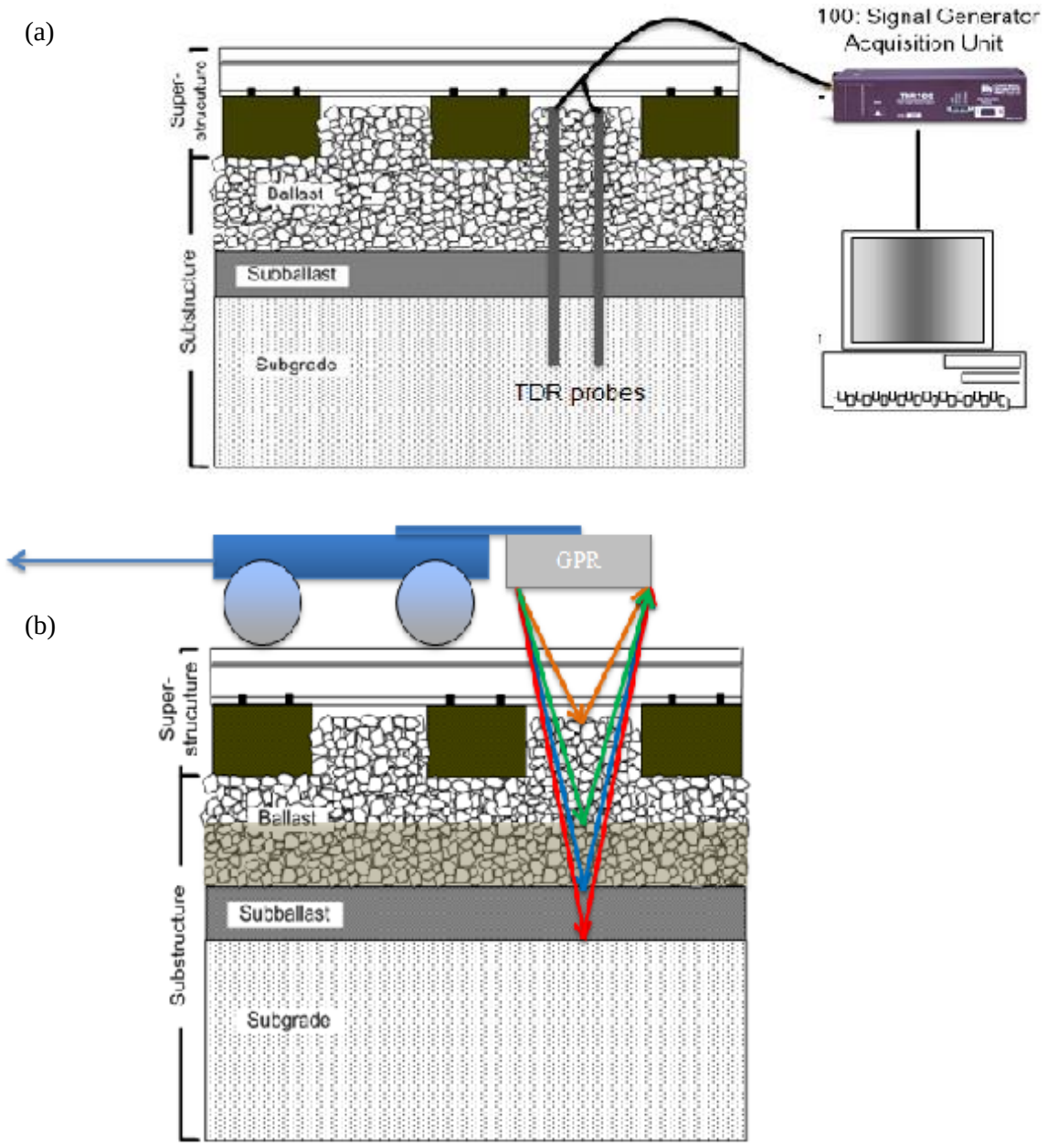

Figure 1.1 Proposed EM-wave monitoring techniques: (a) TDR monitoring station and (b) GPR reflection survey

This chapter is a reformatted version of the manuscript:

Alsabhan et al., 2016, “Determination of Depth of Fouling and Fouling Type in Railway Track Substructure with Time Domain Reflectometer,” to be submitted to the Geotechnical Testing Journal

CHAPTER 2: Determination of Depth of Fouling and Fouling Type in Railway Track Substructure with Time Domain Reflectometer

Abstract

Ballast fouling is one of the most challenging deterioration mechanisms of railway substructures. Fouling leads to a reduction in bearing capacity of the railway substructure, a decrease in the drainage capacity, and an increase in track deformations. As a consequence of these detrimental effects, rail tracks lose load capacity, ride comfort deteriorates, and trains may derail. This problem is quite costly for the railway industry thus, preventing the risk of train derailment while optimizing maintenance operations is very important for reducing the overall cost of freight and passenger transportation. This study presents the development of a procedure for the identification of depth and type of fouling using Time Domain Reflectometry (TDR). TDR waveforms were tested in the laboratory and yielded relative dielectric permittivity and electrical conductivity of ballast. TDR measurements characterize the effect of ballast gradation, mineralogy, and water content on the electromagnetic (EM) response. Experimental results also show how TDR results can be used to determine depth and type of fouling. Strong relationships between depth of fouling, volumetric water content and relative dielectric permittivity are developed. These results were then expanded to the interpretation of Ground Penetrating

Radar (GPR) inspection and to quantify the level of fouling in larger scale maintenance operations. The proposed technique has the potential of reducing some of the limitations observed in the sole application of GPR for the inspection of fouled ballast.

Keywords: Ballast, railroad, TDR, fouling, dielectric permittivity, electrical conductivity

2.1 Introduction

Railway substructure consists of three mainly structural components: ballast layer, subballast layer, and subgrade (Figure 2.1). The ballast layer consists of relatively large, angular, clean, open-voided particles that yield a free draining structure. The subballast layer consists of smaller particles that may include native soils, clean ballast and deteriorated ballast. In older railway substructures, the subballast layer is typically the ballast employed in earlier times plus downwardly-migrated fine particles. The subgrade is the natural soil, which may have been lightly compacted. The primary functions of the ballast are to distribute the vertical loads from the rail track and ties to the subgrade while providing lateral and longitudinal resistance to the displacement of the ties, facilitating drainage of rain water, and preventing the invasion of vegetation into the rail tracks (Ahlf 2011). The quality of all these functions deteriorates as the ballast experiences deterioration of its serviceable function in proportion to the volume of traffic, axle loading, external contamination (e.g., car spillage, wind-blown material, etc.), small particle migration, ballast mineralogy, and absence of ballast maintenance (Ahlf 2011). The increase in the amount of fine particles along with the associated moisture trapping creates a process known as ‘fouling’. This process may compromise the structural integrity of the ballast leading to large track deformation, reduction on track capacity, and

ultimately train derailment (Ebrahimi et al. 2011). Because of these effects yield potentially serious consequences to the performance of railways, costly preventive and corrective maintenance activities, such as undercutting, tamping, and shoulder cleaning must be performed by railway operators especially on tracks serving heavy axle load unit trains (Selig and Walters 1994). It is reported that North American railroads spent more than $8.9 billion per year on maintenance operations (AAR 2013). Currently, common inspection techniques use track geometry measurements and selective drilling and digging to assess the quality of the ballast and to monitor the effects of fouling on the tracks. These methods are time consuming, costly, and when conducted, they interfere with rail operations (Selig and Walters 1994).

Increasing demand for safety and sustainability in freight rail transportation results in the need for adopting new and cost effective inspection and monitoring technologies. Applying electromagnetic (EM)-based surveys as a method to assess the condition of railway infrastructure allows the continuous, rapid and non-destructive evaluation of the level of ballast fouling without interfering with rail operations. Ground penetrating radar (GPR) has been used by several investigators to monitor the rail substructures (Narayanan et al. 1999; Clark et al. 2001; Al-Qadi et al. 2008). For example, Narayanan et al. (1999) employed multiple GPR antennas to estimate the depth of subsurface layers and to identify anomalies under the ballast (e.g., water pockets). However, this technique has limitations, where in occasion, no layer reflections were detected due to gradational change of ballast properties and high electrical conductivity in wet fouled ballast (Al-Qadi et al. 2008). Therefore, if a proper assessment of the quality and performance of ballast is desired, new techniques are needed to better calibrate the GPR results and expand its

application to most types of substructure conditions. Furthermore, quantitative information would be required to provide engineers with parameters to estimate service life of railway structures and model the mechanical behavior of ballast systems.

In this paper, we propose a combined methodology that uses TDR and GPR (Ledieu 1986; Roth et al. 1990; Herkelrath 1991; Siddiqui and Drnevich 2000; Fratta et al. 2005) for calibrating the GPR data, particularly in fouled ballast with high moisture content. The local collection of data using TDR will complement the results from GPR for the rapid profiling of the rail substructure. The combination of both local measurements (i.e., TDR) and global measurements (i.e., GPR) is expected to provide not only geometric but also internal material parameters that will generate quantitative data to better maintain the infrastructure.

2.2 Electromagnetic Properties of Geomaterials

2.2.1 Relative Dielectric Permittivity (ε_r)

Dielectric permittivity ε is the ability of a material to polarize in response to the presence of an electrical field. In most geomaterials, the magnitude of the dielectric permittivity is caused mainly by the polarization of water molecules in the pore space and the effect of orientation polarization in clays (Baker et al. 2007). In many applications, the value of permittivity of a material is expressed as a function of the dielectric permittivity of free space: $\varepsilon=\varepsilon_r \cdot \varepsilon_o$ where ε_r is the relative dielectric permittivity and $\varepsilon_o = 8.85 \cdot 10^{-12}$ F/m is the dielectric permittivity of the free space. Both ε and ε_r may be complex magnitudes. The relative dielectric permittivity varies between 1 for air, 3 to 8 for most geological minerals, and 80 for water (Knight and Endres 2005). The low relative dielectric

permittivity of geological materials compared to that of water makes relative dielectric permittivity of moist soils and rocks highly dependent on the volumetric water content of soils (Siddiqui and Drnevich 2000).

As most geomaterials are assumed to be non-ferromagnetic, the magnetic permeability μ is equal to the magnetic permeability of free space ($\mu_o = 4\pi \cdot 10^{-7}$ H/m), and the imaginary component of the dielectric permittivity is insignificant. Therefore, the electromagnetic wave velocity V of a non-ferromagnetic material can be written as:

$$V = \frac{c_o}{\sqrt{\frac{1}{2} \cdot \left[\varepsilon_r + \sqrt{\varepsilon_r^{\,2} + \left(\frac{\sigma}{\omega \cdot \varepsilon_o} \right)^2} \right]}} \qquad (2.1)$$

where $c_o = (\varepsilon_o \mu_o)^{-1/2}$ is the EM wave velocity in free space, ε_r is the real component of the relative dielectric permittivity, σ is the electrical conductivity, and ω is the angular frequency. Furthermore, if the electrical conductivity of the material is insignificant with respect to the relative dielectric permittivity, Equation 2.1 simplifies to:

$$V = \frac{c_o}{\sqrt{\varepsilon_r}} \qquad (2.2)$$

Thus, relative dielectric permittivity ε_r of the material can be determined if the electromagnetic wave velocity is known.

2.2.2 Electrical Conductivity (σ)

The electrical conductivity is a measure of the mobility of electrical charges in a medium. In most dry soils, the electrical conductivity is low. However, electrical conductivity substantially increases in the soil-water mixtures. Santamarina and Klein (2003) associated the increase of electrical conductivity in soils to ionic conduction, hydrated ion mobility in the pore fluid, and surface conduction in materials with high specific surface areas. Furthermore, the hydration of excess cations and anions dissolved in the pore fluid, leads to the formation of electrolytes. The electrical conductivity of electrolyte is proportional to the ionic concentration (Annan 2005):

$$\sigma_{el} = 0.15 \cdot TDS \tag{2.3}$$

where the electrical conductivity of the electrolyte σ_{el} is expressed in mS/m if the total dissolved salts TDS is presented in mg/L.

In soils with low specific surface, electrolytes contribute the most to the electrical conductivity. The electrical conductivity in soils is also a function of porosity, degree of saturation, and the meandrous path (i.e., tortuosity) the hydrated ions need to travel (Santamarina and Klein 2003). Archie (1942) developed an empirical relationship to model the electrical conductivity of a wet low specific surface soil.

$$\sigma_{soil} = a \cdot \sigma_{el} \cdot S^{C} \cdot n^{m} \tag{2.4}$$

where a, c, and m are fitting coefficients (m= 1 to 2.4; c= 4 to 5), S is the degree of saturation, and n is the porosity.

However, in soils with high specific surface, surface conduction largely influences the electrical conductivity. This is because water interacts with the excess charges in the diffuse double layer around the particles greatly improving the electrical conductivity. In fine grained soils (where particle conductivity σ_p is large), the electrical conductivity can

be related to porosity n, electrolyte conductivity σ_{el}, surface conduction Θ, density ρ_g, and specific surface area S_g (Santamarina and Klein 2003):

$$\sigma_{soil} = n \cdot \sigma_{el} + (1-n) \cdot \sigma_p = n \cdot \sigma_{el} + (1-n) \cdot \Theta \cdot \rho_g \cdot S_g \quad (2.5)$$

2.3 Time Domain Reflectometry and the Measurement of Electromagnetic Properties

TDR is a nondestructive technique that allows the gathering of information from the subsurface of railway track to assess ballast condition. TDR is based on sending an electromagnetic pulse along the length of metal probes while monitoring reflections caused by changes in the properties of materials between the probes. By analyzing the travel time and reflection amplitudes information such as relative dielectric permittivity, electrical conductivity or depth of material layering (Jones et al. 2002; Bosscher and Benson 1999; Fratta and Schneider 2009) can be obtained. If the length L of the probes and travel time t of an electromagnetic wave is measured then the relative dielectric permittivity is:

$$\varepsilon_r = \left(\frac{c_o \cdot t}{2 \cdot L} \right)^2 = \left(\frac{L_a}{L} \right)^2 \quad (2.6)$$

where L_a is the apparent length of the probe measured from the difference in the apparent distances corresponding to the inflection points in the TDR waveform (Figure 2.2).

Many researchers (Topp et al. 1980; Roth et al. 1990; Wensink et al. 1993; Benson and Bosscher 1999) were successful in predicting volumetric water content by relating it to the measured relative dielectric permittivity. Topp et al. (1980) proposed an empirically

determined relationship between relative dielectric permittivity and volumetric water content θ_v of soils with different textures:

$$\varepsilon_r = 3.03 + 9.3\theta_v + 146.0\theta_v^2 - 76.7\theta_v^3 \quad (2.7)$$

Jones et al. (2002) reported that this equation fails to describe the ε_r-θ_v relationship adequately for volumetric water contents exceeding 0.5 and for soils with high organic matter or clay content.

The relative dielectric permittivity is also obtained by developing a mixing model relating the relative dielectric properties and the volume fraction of its constituents based on assumptions about the geometrical arrangement of the constituents (Roth et al. 1990):

$$\varepsilon_r = [(1-n)\cdot\varepsilon_{mineral}^{\beta} + n\cdot \mathrm{S}\cdot\varepsilon_w^{\beta} + n\cdot(1-\mathrm{S})\cdot\varepsilon_a^{\beta}]^{1/\beta} \quad (2.8)$$

where $\varepsilon_{mineral}$, ε_w, and ε_a are the relative dielectric permittivity of the solid mineral, pore water, and pore air phases; and β is an empirical parameter that represents the geometry orientation of the particles in the medium in relation to the direction of the wave guide (e.g., β=1 for an electric field parallel to soil layering, β=-1 for an electric field perpendicular to soil layering, and β=0.5 for an isotropic two-phase mixed medium – Roth et al. 1990).

TDR data also provide electrical resistivity information. Electrical conductivity σ is determined as a function of the reflection amplitude of the reflected pulses. Giese and Tiemann (1975) proposed a model to determine electrical conductivity as:

$$\sigma = \frac{\varepsilon_o c}{L}\frac{Z_p}{Z_c}\left(\frac{2V_T}{V_R}-1\right) = \frac{K}{Z_c}\left(\frac{2V_T}{V_R}-1\right) \quad (2.9)$$

where V_T is the incident pulse voltage at the beginning of the probe, V_R is the return pulse voltage, Z_p is the characteristic impedance of the probe, Z_c is the characteristics of the

cable tester Z_c, and K (1/m) is an experimentally determined geometric probe constant (Dalton et al. 1984; O'Connor and Dowding 1999).

2.3.1 Spatial Sensitivity of TDR Probes

Knight (1992) recommended using probes with a diameter to separation ratio greater than 0.1, due to the high sensitivity of the TDR probe to the area surrounding it. Petersen et al. (1995) investigated dependency of the spatial sensitivity of TDR probes design and reported that the spatial sensitivity of TDR techniques is highly dependent on the separation of probes. With respect to coating, Ferré and Rudolph (1996) reported that coated TDR probes do not measure the actual average dielectric permittivity of the material between the coat as the measurements are greatly influenced by the coating's properties.

2.4 Materials

Four types of standard ballast gradations AREMA #4, #5, #24, and #25 were obtained and tested to determine the EM properties of ballast. The gradations are specified by AREMA (2010). The particle size distributions of the ballast (ASTM D6913) are shown in Figure 2.3. AREMA #25 was used in all the fouled ballast tests. Three common fouling materials were considered in this study coal, silica sand, and kaolinite. Grain size distributions of the studied materials are shown in Figure 2.3, and physical properties are shown in Table 2.1.

Table 2. 1 Index Properties of Ballast and Fouling Materials

Sample	D_{50} (mm)	C_u	C_c	G_s	LL (%)	PL (%)	n_B	Sand Content (%)	Fines Content (%)	USCS Symbol
AREMA #25	48	1.4	0.6	2.6	NA	NA	0.4	0	0	-
AREMA #24	40	1.6	0.86	2.6	NA	NA	0.4	0	0	-
AREMA #4A	30	1.5	0.86	2.6	NA	NA	0.36	0	0	-
AREMA #5	17	1.2	0.53	2.6	NA	NA	0.35	0	0	-
Silica Sand	0.28	1.6	0.98	2.66	NP	NP	-	100	0.33	SP
Coal	1	113	4.5	1.3	31	NP	-	100	20	SM
Kaolinite	-	-	-	2.63	49	35	-	0	100	CL

Note. NP = not plastic, NA = not applicable, D_{50} = median particle size, C_u = coefficient of uniformity, C_c = coefficient of curvature, G_s = specific gravity, LL = liquid limit, PL = plastic limit, n_B = porosity of ballast. Particle size analysis conducted following ASTM D 422, G_s by ASTM D 854, USCS classification by ASTM D 2487, and Atterberg limits by ASTM D 4318.

2.5 Methodology

2.5.1 Equipment

TDR testing was conducted to assess the EM properties (i.e., real relative permittivity and electrical conductivity) of clean and fouled ballast under fouling scenarios with different water content environments. A Campbell Scientific TDR100 system (Campbell Scientific Inc. 2007) was used in this study. The cable has Z_0=50 Ω impedance. The PCTDR-V 2.08 software was used to control and save the collected TDR signals. The signals includes 2048 points and were captured using 4 events to improve signal to noise ratio. The testing was performed in a 0.31 m long, 0.27 m wide, and 0.32 m high wooden box with two transparent walls made of Plexiglass to permit the visualizing the ballast material and the rearrangement of particles during the fouling process (Figure 2.4).

2.5.2 Specimen Preparation

Clean Ballast. During field operations, ballast undergoes a process of densification that is controlled by the magnitude and the frequency of the traffic load. For this reason, ballast samples were prepared in the wooden box with a dynamic vibration in an attempt to reproduce field conditions. The clean ballast specimen preparation followed the following steps:

The wooden box was secured to a shaking table.

1- Ballast was placed in 0.1 m lifts.
2- For each lift a 100 N steel plate was placed on top of the ballast and the box was vibrated for 5 min. until no more particle settlement was noticeable.

Fouled Ballast due to Spillage. Fouled ballast specimens were prepared in the wooden box to simulate spillage contamination (e.g., spillage of coal dust and silica sand from cars) by spreading the fouling material over the surface according to the following steps (Figure 2.5):

1- 0.1 m lifts of clean ballast were prepared using the Clean Ballast procedure.
2- For each lift, fouling material (e.g., coal dust or silica sand) was spread over the compacted lift of clean ballast under vibration until all the voids were filled.
3- If required, water was evenly added from the top to the fouled ballast layer.
4- The remaining lifts of clean ballast were placed on the top of the fouled ballast (i.e., Clean Ballast procedure).

Clay Intrusion from the Subgrade Layer. Fouled ballast samples were prepared in a wooden box and simulate the real field conditions of clay intrusion from the subgrade layer (Figure 2.6) according to the following steps:

1- Kaolinite clay sample was mixed with water to obtain homogeneous water distribution and placed in the bottom of the testing box.
2- Standard proctor hammer, 25 blows on 0.05 m lifts, was used to compact the clay.
3- Clean ballast was placed on the top of the fouled ballast in 0.05 m lifts.
4- Standard proctor hammer, 25 blows on 0.05 m lifts was used to compact the ballast for allow for the intrusion of clay into the ballast.

2.5.3 TDR Probes Design

The spatial sensitivity of the TDR probes was assessed to optimize the design and obtain accurate measurements. Three different probe separations (i.e., 0.05 m, 0.1 m, and 0.2 m) for 0.01-m diameter and 0.30-m long coated and uncoated probes were used to find the optimum TDR probes design for this study.

The calibration of dielectric permittivity resolution was performed by using different TDR probes configurations with a solution of known real relative dielectric permittivity: deionized-water ε_r=80. Figure 2.7 shows the response of different TDR probes configurations in deionized water. For the uncoated TDR probes with different D/S ratios, the percentage of error between the measured relative dielectric permittivity of deionized water and the theoretical value of dielectric permittivity of deionized water ranged between 0.49 % and 0.55 %, when the D/S ratio decreases to 0.05 the percentage of error increases to 20.79 %. However, for coated TDR probes with D/S ratios equal to 0.2, 0.1 and 0.05, the percentage of error was 18.97 %, 17.14 %, and 21.71 %, respectively. Table 2.2 summarizes the results. Uncoated probes with D/S ratio of 0.2 were selected for the rest of the study.

Table 2.2 Comparison of Relative Dielectric Permittivity of Different TDR Probes Configurations and Theoretical Value of Relative Dielectric Permittivity of Deionized water

Coated?	D/S	In Deionized Water			In Air		
		Apparent Length L_a (m)	Dielectric Permittivity ε_r	Percentage of Error (%)	Apparent Length L_a (m)	Dielectric Permittivity ε_r	Percentage of Error (%)
No	0.20	2.87	80.49	0.49	0.319	0.9938	0.62
	0.10	2.86	79.66	0.55	0.322	1.0125	1.25
	0.05	2.55	63.45	20.79	0.305	0.9084	9.15
Yes	0.20	2.58	64.90	18.97	0.295	0.8499	15
	0.10	2.61	66.37	17.14	0.28	0.7656	23.43
	0.05	2.53	62.71	21.71	0.275	0.7385	26.14

2.6 Results and Discussions

2.6.1 Observations during Ballast Specimen Preparation

During the simulation of fouled ballast due to spillage (Figure 2.5), fouling occurred due to the migration of sand particles from top to bottom (as in the case of rail tracks that transport fracking sand). The ballast void space becomes filled with sand particles and the vibration forces the ballast particles to lose their contact and the space between the contacts is filled with sand as shown in Figure 2.5 (b) and 2.5 (c). In these figures, ballast particles' contact with the Plexiglass wall decreases until they disappear. In addition, during the simulation of the fouling process due to clay intrusion, the contamination of ballast particle-to-particle contact is not noticed until the clay reaches water contents of 30% as in the process documented in Figure 2.6. When the water content increases in the clay, an intrusion of clay into the ballast layer was observed. That is the shear strength of the clay is reduced with the increase in water content and the supporting layer fails allowing the ballast particles to slide into the clay layers. The process in the field will be

controlled by the ratio of the undrained shear strength to the induced stresses caused by the passing train.

2.6.2 Clean Ballast EM Properties Characterization

TDR measurements were taken to characterize the effect of ballast gradation and to assess the effect of mineralogy on the EM properties of clean ballast. Figure 2.8 shows the variation of EM properties of four types of standard ballast (i.e., AREMA #4, #5, #24, and #25). For ballast gradation comparison, the relative dielectric permittivity ranged between 4.3 and 4.93 for the AREMA #4 and #5 ballasts, whereas the relative dielectric permittivity showed a constant value of 3.05 for the AREMA #24 and #25 ballasts. The difference in relative dielectric permittivity is caused by the difference in porosity for the different specimens (see Table 2.1). For dry, coarse gradation ballast, the increase in porosity yields higher the EM velocity (given the same mineral composition of the solid particles). However, ballast mineralogy did not exhibit any significant effect on the measured EM properties, even though AREMA #4, #5 and #24 were primarily composed of dolomite while AREMA #25 was composed of granite. That is, the results were mainly controlled by the changes in porosity.

2.6.3 Fouled Ballast EM Properties Characterization

Determination of Volumetric Water Content. The effect of volumetric water content on the real relative permittivity for ballast fouled with kaolinite clay, silica sand, and coal is presented in Figure 2.9. Increasing volumetric water content, increases the relative dielectric permittivity and electrical conductivity of the fouled ballast. The relationship is similar to those previously reported in literature (e.g., Topp et al. 1980; Roth et al. 1990; Wensink et al. 1993; Benson and Bosscher, 1999). The changes in the fouled ballast

dielectric permittivity can be explained by the large value of relative dielectric permittivity of water (ε_w=80) with respect to the permittivity of the solid mineral ($\varepsilon_r = 3 - 8$) and air (ε_a=1). The high correlation of the measured dielectric permittivity with Topp's model suggests the ability of TDR in measuring the volumetric water content in railroad ballast substructures.

Determination of Depth of Fouled Ballast. TDR waveform traces for kaolinite fouled ballast with volumetric water contents ranging between 0.06 and 0.56 are shown in Figure 2.10. Multiple reflections occur in samples with high volumetric content (high impedance contrast at the fouling layer interface), whereas samples with low volumetric water content (low impedance contrast) yield lower amplitude reflections. Multiple waveform reflections in specimens with high volumetric water content are due to substantial differences in the relative dielectric permittivity between the two layers that the EM wave propagates through (i.e., clean ballast and fouled ballast layer). The first waveform reflection showed a constant relative dielectric permittivity ε_r of 3.3, which is consistent with the relative dielectric permittivity of clean ballast. Fouled ballast relative dielectric permittivity ε_r ranged between 26.26 and 36 for specimens with volumetric water contents ranging between 0.4 and 0.56. These results are consistent with the relationship between volumetric water content and relative dielectric permittivity. That is, the clean ballast layer does not retain moisture. Thus, a relationship between relative dielectric permittivity of clean ballast ε_{rb} and the apparent length of the first reflected waveform L_{ab} is established to calculate the depth of clean ballast L_b and fouled ballast L_f as:

$$L_b = \frac{L_{ab}}{\sqrt{\varepsilon_{rb}}} \tag{2.10}$$

$$L_f = L - L_b \tag{2.11}$$

$$\varepsilon_{rf} = \left(\frac{L_{af}}{L} \right)^2 \tag{2.12}$$

where L is the total length of TDR probe, ε_{rf} is the relative dielectric permittivity of fouled ballast, and L_{af} is the apparent length of the second reflected waveform that corresponds to the fouled ballast. Table 2.3 presents the processed TDR waveform shown in Figure 2.10 for ballast fouled with kaolinite clay.

Table 2.3 Results of processed TDR waveform in Figure 2.10 for apparent length of the first reflected waveform L_{ab}, relative dielectric permittivity of clean ballast ε_{rb}, apparent length of the second reflected waveform L_{af}, and relative dielectric permittivity of fouled ballast ε_{rf}.

(a) Results for 0.22 m Clean Ballast and 0.1 m Fouled Ballast					
θ_r	Multiple Reflections?	L_{ab} (m)	ε_{rb}	L_{af} (m)	ε_{rf}
0.06	No	N/A	N/A	0.619	4.27
0.25	No	N/A	N/A	1.06	12.5
0.4	Yes	0.4	3.3	0.41	26.26
0.56	Yes	0.4	3.3	0.48	36
(b) Results for 0.12 m Clean Ballast and 0.2 m Fouled Ballast.					
θ_r	Multiple Reflections?	L_{ab} (m)	ε_{rb}	L_{af} (m)	ε_{rf}
0.06	No	N/A	N/A	0.66	4.84
0.25	No	N/A	N/A	1.076	12.86
0.4	Yes	0.22	3.36	0.56	21.7
0.56	Yes	0.22	3.36	0.75	39

Equations 2.10 to 2.12 are applicable for specimens with high volumetric water content. They cannot be applied to specimens with low to moderate volumetric water content because the low contrast in relative dielectric permittivity between layers do not yield a clear reflection signal. The variation of relative dielectric permittivity with volumetric

water content at different depths is shown in Figure 2.11. An increase of the relative dielectric permittivity is observed with the increase of fouling depth at different volumetric water contents. The increase in fouling layer thickness decreases the porosity in the ballast layer and as a result the relative dielectric permittivity increases.

Determination of Fouling Type in the Ballast Layer. Electrical conductivity was used with the intention of differentiating various types of ballast fouling. For example, Figure 2.12 shows the measured electrical conductivities of fouled ballast and the reported electrical conductivity in the literature for typical geological materials found in the railroad ballast substructure (Palacky, 1987; Sharma, 1997; Annan, 2005). The conductivity of ballast fouled with kaolinite ranges between 0.005 S/m to 0.04 S/m depending on the volumetric water content. Whereas the electrical conductivity of ballast fouled with silica sand ranges between 0.00091 S/m to 0.001 S/m for all the tested volumetric water contents. The electrical conductivity of the ballast fouled with kaolinite is an order of magnitude greater than the electrical conductivity of ballast fouled with silica sand. This observation is important, as it shows that use of electrical conductivity can help in identifying different types of fouling materials. The type of fouling material then controls the overall performance of fouled layers as described in Ebrahimi (2011) and Hesse et al. (2014).

2.7 Field Implementation of Proposed Methodology

2.7.1 Methodology

Field data were collected in April 2015 on two bridge approaches on a mainline rail track section in Dayton, IL. This track services the local fracking sand industry by

transporting high tonnages of sand to larger rail hubs. Both bridge approaches show characteristic signs of deterioration and settlement. The two bridge approaches were surveyed using a pulseEKKO PRO GPR system with 200-MHz antennae. Raw GPR data were processed using MATGPR processing software (Tzanis and Kafetsis 2004). The data processing technique included time-zero correction, mean spatial filter, median spatial filter, and gain control function to improve the quality of the presentation and help in the interpretation.

Along with GPR data collection, TDR testing was conducted to calibrate the GPR results and to assess the EM properties of the mainline track section. The Campbell Scientific TDR100 system with an impedance coaxial cable Zo = 50 Ω was used in this field study. 1.4-m-long TDR probes, with separation of 0.1 m and diameter of 0.012 m, were driven into the ballast layer to collect the data.

A Dynamic Cone Penetrometer (DCP) survey was also conducted at the same locations as the TDR measurements to ground truth the geophysical data. The DCP system penetrated to depths of up to 7 m. The depth of penetration per blow (mm/blow) provides a measure of the inverse of shear strength of the soil. Thus using DCP profiles, the depth of the different subsurface layers is estimated (Chen et al. 2001; Herrick and Jones 2002).

2.7.2 Results and Discussion

A typical TDR waveform for the Railway section is shown in Figure 2.13. The multiple reflections correspond to substantial differences in the relative dielectric permittivity between the underlying layers that the EM wave propagates through and

clean ballast and fouled ballast layers. The first waveform reflection showed a relative dielectric permittivity (ε_{rb}) of 3, which is consistent with relative dielectric permittivity of laboratory ballast layers, whereas the relative dielectric permittivity (ε_{rf}) of the fouled ballast was 8. Thus, by incorporating this information to calibrate the GPR data the velocity of the combined clean/fouled ballast layer was calculated to be 0.15 m/ns.

Processed GPR data of the two bridge approaches in Figure 2.14 indicates four layer interfaces corresponding to a ballast layer, subballast layer, weak subgrade layer, and stronger subgrade layer. GPR data shows a local dipping in the subgrade layer close to the bridge abutments, likely resulting in poor track performance.

Figure 2.15 shows the DCP test profile. The DCP profile exhibits a strong (i.e., low penetration index) ballast layer followed by a weak layer at approximately 1 m depth. Below 1-m depth, the soil profile exhibits a decrease in the resistance to DCP penetration indicating a weak subgrade layer. Then at a depth of 1.9 m an increase in resistance to penetration with depth is noticed in the soil profile which may indicate a stronger subgrade layer. The DCP results correlate well with the GPR layer thickness and sampling conducted at this location. However, it is important to note that the successful interpretation of the GPR data was only possible with the calibration obtained from the TDR results.

2.8 Summary and Conclusions

Time Domain Reflectometry (TDR) testing was conducted to assess the electromagnetic (EM) properties (i.e., real relative permittivity and electrical conductivity) of clean and fouled ballast under different water content conditions, to evaluate the

validity of using TDR for calibrating the GPR data, particularly in fouled ballast with high moisture content environments. The spatial sensitivity of TDR probes was assessed to optimize the design of TDR probes in order to obtain accurate dielectric permittivity measurements and estimation of the depth of contrasting layers along the length of the TDR probes. TDR measurements were taken to characterize the effect of ballast gradation and mineralogy on the EM properties of clean ballast.

TDR results shows that the relative dielectric permittivity ranges from 3 to 5, whereas the electrical conductivity is very low and mainly constant for different clean ballast types. TDR was successful in determining the depth of fouled ballast for specimens that have high volumetric water content. In particular, multiple reflections occur in specimens with high impedance contrast layers. Thus, a relationship between relative dielectric permittivity of clean ballast (ε_{rb}) and the apparent length of the first reflected waveform (L_{ab}) is established to calculate the depth of clean ballast and therefore estimate the depth to the fouled layer. An increase of the relative dielectric permittivity is observed with the increase of fouling depth at different volumetric water contents. The increase in fouling layer thickness decreases the porosity in the ballast layer and as a result the relative dielectric permittivity increases. Electrical conductivity was used successfully differentiate between various types of ballast fouling.

A field implementation of the technique was conducted on two bridge approaches on a mainline track section that transport sand and fouling with it. TDR and GPR testing was conducted to assess the electromagnetic (EM) properties (i.e., real relative permittivity and electrical conductivity) of railway substructure. TDR results were then used to calibrate the GPR data, particularly in fouled ballast with high moisture content.

TDR successfully distinguished multiple layers in the railway substructure and gave an estimation of the wave velocity of the substructure. Dynamic cone penetrometer (DCP) testing validated the use of TDR to calibrate GPR data and to allow the imaging of the extent of ballast fouling that has contributed to ongoing deformation along two sections of the rail track.

Acknowledgments

Financial support for this study was provided by the Center for Freight Infrastructure Research and Education (C-FIRE) and the King Saud University (KSU – Saudi Arabia). Their support is greatly appreciated. Xiaodong Wang, William Lang, Tolga Dolcek, and Liangquan Wang (David) helped in the development of this work. URETEK ICR provided the dynamic cone data.

References

Ahlf, R. E., 2011. “Maintaining, rehabilitation, and upgrading conventional railroad track-ballast,” Unpublished short course, University of Wisconsin-Madison.

Al-Qadi, I., Xie, W., and Roberts, R., 2008. “Scattering analysis of ground-penetrating radar data to qualify railroad ballast contamination,” NDT&E International, Elsevier, vol. 41, pp.441- 447.

Annan, A. P., 2005. “An introduction to rock physics principles for near-surface geophysics, in near surface geophysics,” Tulsa: Society of Exploration Geophysicists, pp. 357- 438.

Archie, G. E., 1941. “The electrical resistivity log as an aid in determining some reservoir characteristics,” Petroleum Transactions, A.I.M.E., vol. 146, pp. 54-62.

AREMA, 2010, “AREMA manual for railway engineering - ballast gradations,”

Association of American Railroads (AAR), 2012. “Total annual spending 2011 data,” Available from: https://www.aar.org/Fact%20Sheets/Safety/2013-AAR_spending-graphic-fact-sheet.pdf#search=Total%20annual%20spending

ASTM D2487-11, 2011. “Standard Practice for Classification of Soils for Engineering Purposes (Unified Soil Classification System),” ASTM International, West Conshohocken, PA, www.astm.org.

ASTM D422–63, 2007. “Test method for particle-size analysis of soils. ASTM International,” West Conshohocken, PA, www.astm.org.

ASTM D4318-10, 2010. “Standard Test Methods for Liquid Limit, Plastic Limit, and Plasticity Index of Soils,” ASTM International, West Conshohocken, PA, www.astm.org.

ASTM D6913, 2009. “Standard test methods for particle-size distribution (gradation) of soils using sieve analysis,” ASTM International, West Conshohocken, PA, www.astm.org.

ASTM D854-14, 2000. “Standard test methods for specific gravity of soil solids by water pycnometer.” ASTM International, West Conshohocken, PA, www.astm.org.

Baker, G. S., Jordan, T. E., and Pardy, J., 2007. “AN introduction to ground penetrating radar (GPR),” Geological Society of America Special Papers, vol. 432, pp. 1-18.

Benson, C. H., and Bosscher, P. J., 1999. “Time-domain reflectometry (TDR) in geotechnics: a review,” Nondestructive and Automated Testing for Soil and Rock Properties, ASTM STP, vol. 1350, pp. 113-136

Chen, D. H., Wang, J. N., and Bilyeu J., 2001. “Application of dynamic cone penetrometer in evaluation of base and subgrade layers,” Transportation Research Record: Journal of the Transportation Research Board, Vol. 1764, pp. 1-10.

Clark, M. R., Gillespie, R., Kemp, T., McCann, D. M., and Forde, M. C., 2001. “Electromagnetic properties of railway ballast,” NDT & E International, Vol. 34, pp. 305-311.

Dalton, F. N., Herkelrath W. N., Rawlins, D. S., and Rhoades, J. D., 1984. “Time domain reflectometry: simultaneous measurement of soil water content and electrical conductivity with a single probe,” Science, vol. 224, pp.989–990.

Ebrahimi, A., 2011. “Deformational behavior of fouled railway ballast,” PhD thesis, Department of Civil and Environmental Engineering, University of Wisconsin-Madison.

Ferré, P. A., Rudolph, D. L., and Kachanoski, R. G., 1996. “Spatial averaging of water content by time domain reflectometry: implications for twin rod probes with and without dielectric coatings,” Water Resources Research, Vol. 32, pp. 271-279.

Fratta, D., Alshibli, K. A., Tanner, W. M., and Roussel, L., 2005. “Combined TDR and P-wave velocity measurements for the determination of in situ soil density-experimental study,” Geotechnical Testing Journal, Vol. 28, pp. 553.

Giese, K., and Tiemann, R., 1975. “Determination of the complex permittivity from thin-sample time domain reflectometry, improved analysis of the step response waveform,” Advances in Molecular Relaxation Processes, Vol. 7, pp.45-59.

Herkelrath, W. N., Hamburg, S. P., and Murphy, F., 1991. “Automatic, real - time monitoring of soil moisture in a remote field area with time domain reflectometry,” Water Resources Research, Vol. 27, 857-864.

Herrick, J. E., and Jones, T. L., 2002. “A Dynamic Cone Penetrometer for Measuring Soil Penetration Resistance,” Soil Science Society of America Journal, Vol. 66, pp. 1320-1324.

Hesse, D. E., Tinjum, J. M., and Warren, B. J., 2014. “Impact of increasing freight loads on rail substructure from fracking sand transport,” Transportation Geotechnics, vol. 4, pp. 241-256.

Jones, S. B., Wraith, J. M., and Or, D., 2002. “Time domain reflectometry measurement principles and applications”, Hydrological Process, vol. 16, pp.141-153

Knight, J. H., 1992. “Sensitivity of time domain reflectometry measurements to lateral variation in soil water content,” Water Resources Research, Vol. 28, pp. 2345-2352.

Knight, R. J., 2005. “An introduction to rock physics principles for near-surface geophysics, in near surface geophysics”, Tulsa: Society of Exploration Geophysicists, pp. 31-70.

Ledieu, J., De Ridder, P., De Clerck, P. and Dautrebande, S., 1986. “A method of measuring soil measuring soil moisture by time-domain reflectometry,” Journal of Hydrology, vol. 88, pp. 319-328.

Narayanan, R. M., Kumke, C. J., and Li, D., 1999. “Railroad track monitoring using ground penetrating radar: simulation study and field measurements,” In SPIE's International Symposium on Optical Science, Engineering and Instrumentation, pp. 243-251.

O'Connor, K. M. and Dowding, C. H., 1999. “Geomeasurements by pulsing TDR cables and probes,” CRC Press.

Palacky, G. J., 1988. “Resistivity characteristics of geologic targets,” electromagnetic methods in applied geophysics,” vol. 1, pp. 53-129.

Petersen, L. W., Thomsen, A., Moldrup, P., Jacobsen, O. H., and Rolston, D. E., 1995, “High-Resolution Time Domain Reflectometry: Sensitivity Dependency on Probe-Design,” Soil Science, Vol. 159, pp. 149-hyhen.

Roth, K., Schulin, R., Flühler, H., and Attinger, W., 1990. “Calibration of time domain reflectometry for water content measurement using a composite dielectric approach,” Water Resources Research, vol. 26, pp. 2267-2273.

Santamarina, J. C., Rinaldi, V. A., Fratta, D., Klein, K., Wang, Y. H., Cho, G. C., and Cascante, G., 2005. “A survey of elastic and electromagnetic properties of near-surface soils,” Near-Surface Geophysics, vol. 1, pp. 71-87.

Schneider, J. M., and Fratta, D., 2009. “Time-domain reflectometry — parametric study for the evaluation of physical properties in soils,” Canadian Geotechnical Journal, vol. 46, pp. 753-767.

Selig, E. T. and Waters, J. M., 1994. Track Geotechnology and Substructure Management, Book, Thomas Telford, New York, NY.

Sharma, P. V., 1997. Environmental and engineering geophysics, Book, Cambridge University Press.

Siddiqui, S. I., Drnevich, V. P., and Deschamps, R. J., 2000. “Time domain reflectometry development for use in geotechnical engineering,” ASTM Geotechnical Testing Journal, Vol. 23, pp. 9-20.

Topp, G., Davis, J., and Annan, A., 1980. “Electromagnetic determination of soil water content: measurements in coaxial transmission lines,” Water Resources Research, vol. 16, pp.574-582

Tzanis, A. and Kafetsis, G., 2004. “A freeware package for the analysis and interpretation of common-offset Ground Probing Radar data, based on general purpose computing engines,” Bulletin Geol. Soc. Greece, XXXVI., vol. 3, pp. 1347-1354.

Wensink, W. A., 1993. “Dielectric properties of wet soils in the frequency range 1-3000 MHz,” Geophysical Prospecting, vol. 41, pp. 671-696.

Figures

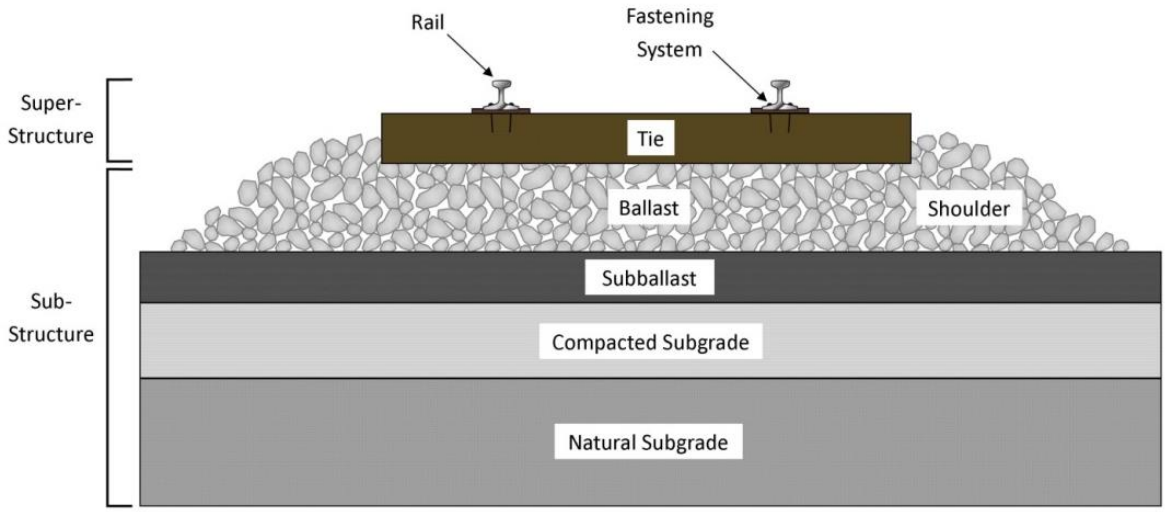

Figure 2.1 Typical components of railway track substructure and superstructure

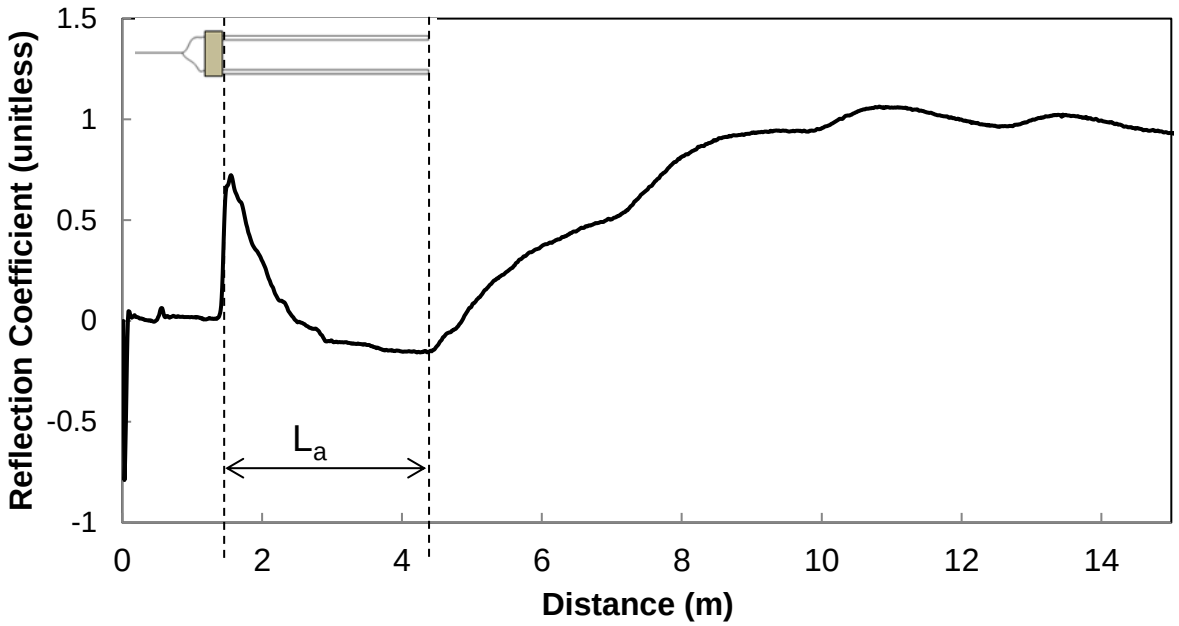

Figure 2.2 TDR probe and typical waveform

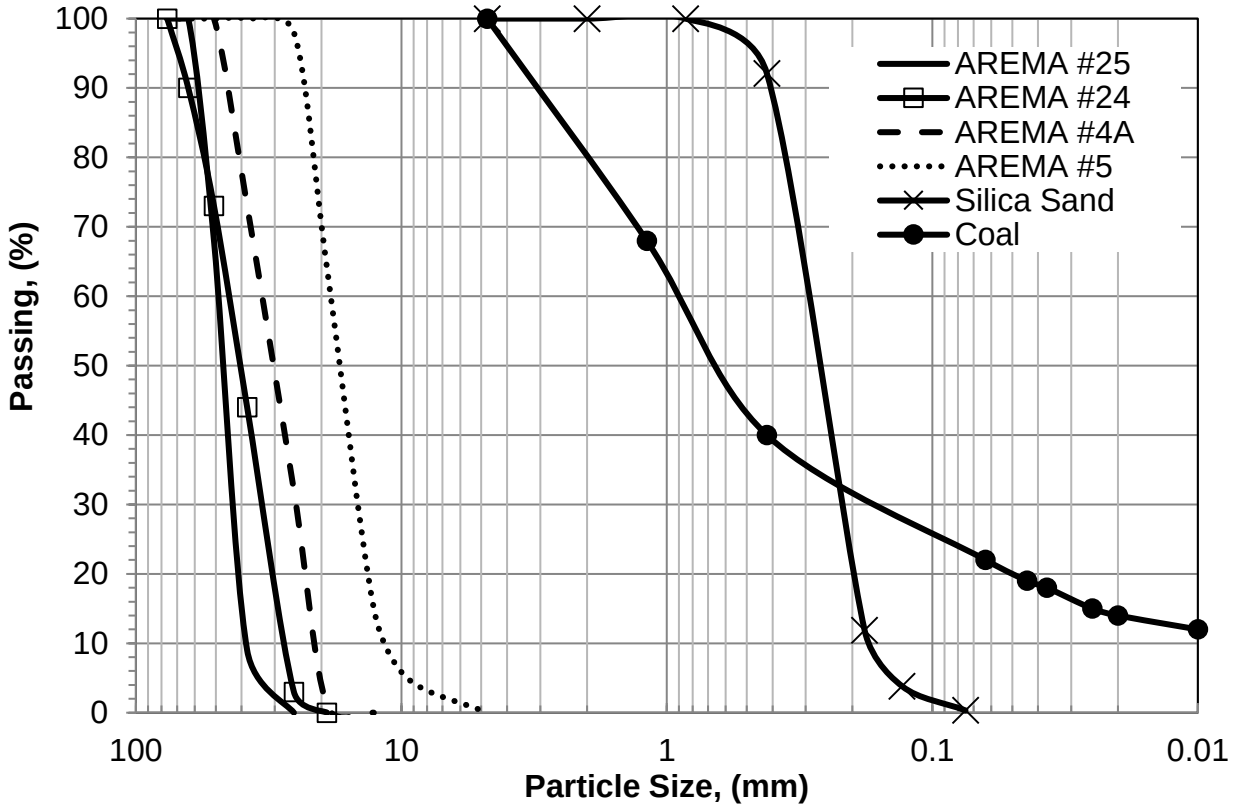

Figure 2.3 Particle size distributions of ballast (AREMA # 25, AREMA # 24, AREMA # 4A, AREMA # 5), silica sand, and coal

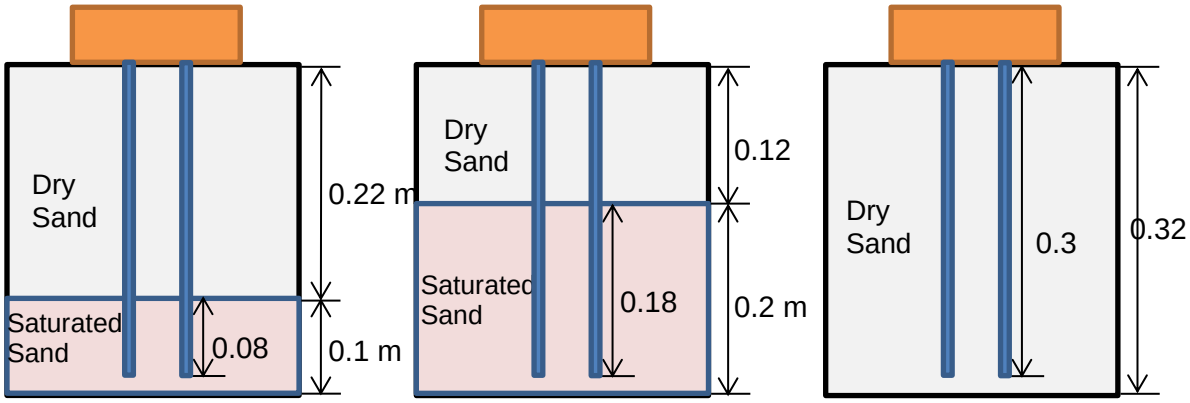

Figure 2.4 Wooden box model: filled with silica sand with three different water levels (0, 0.1, and 0.2 m) measured from the bottom of the model.

(a) (b)

(c) (d)

(e) (f)

Figure 2.5 Preparation of fouled ballast due to spillage: (a) Placing clean ballast in 0.1 m lift, (b) pouring silica sand on the compacted ballast, (c) placing clean ballast on the compacted silica sand, (d) specimen consists of 0.1 m fouled ballast and 0.22 m clean ballast, (e) specimen consists of 0.2 m fouled ballast and 0.12 m clean ballast, (f) specimen consists of 0.32 m fouled ballast.

(a)

(b)

(c)

(d)

(e)

(f)

Figure 2. 6 Preparation of fouled ballast due to clay intrusion: (a) Placing clay in 0.1 m lift, (b) placing ballast on top of the compacted clay in lifts to form a specimen consists of 0.1 m fouled ballast and 0.22 m clean ballast, (c) placing ballast on top of the 0.2 m compacted clay in lifts to form a specimen consists of 0.2 m fouled ballast and 0.12 m clean ballast, (d) 0.32 m compacted clay specimen, (e) aerial view of clay intrusion into the clean ballast layer with 30% clay water content, (f) aerial view of clay intrusion into the clean ballast layer with 40% clay water content.

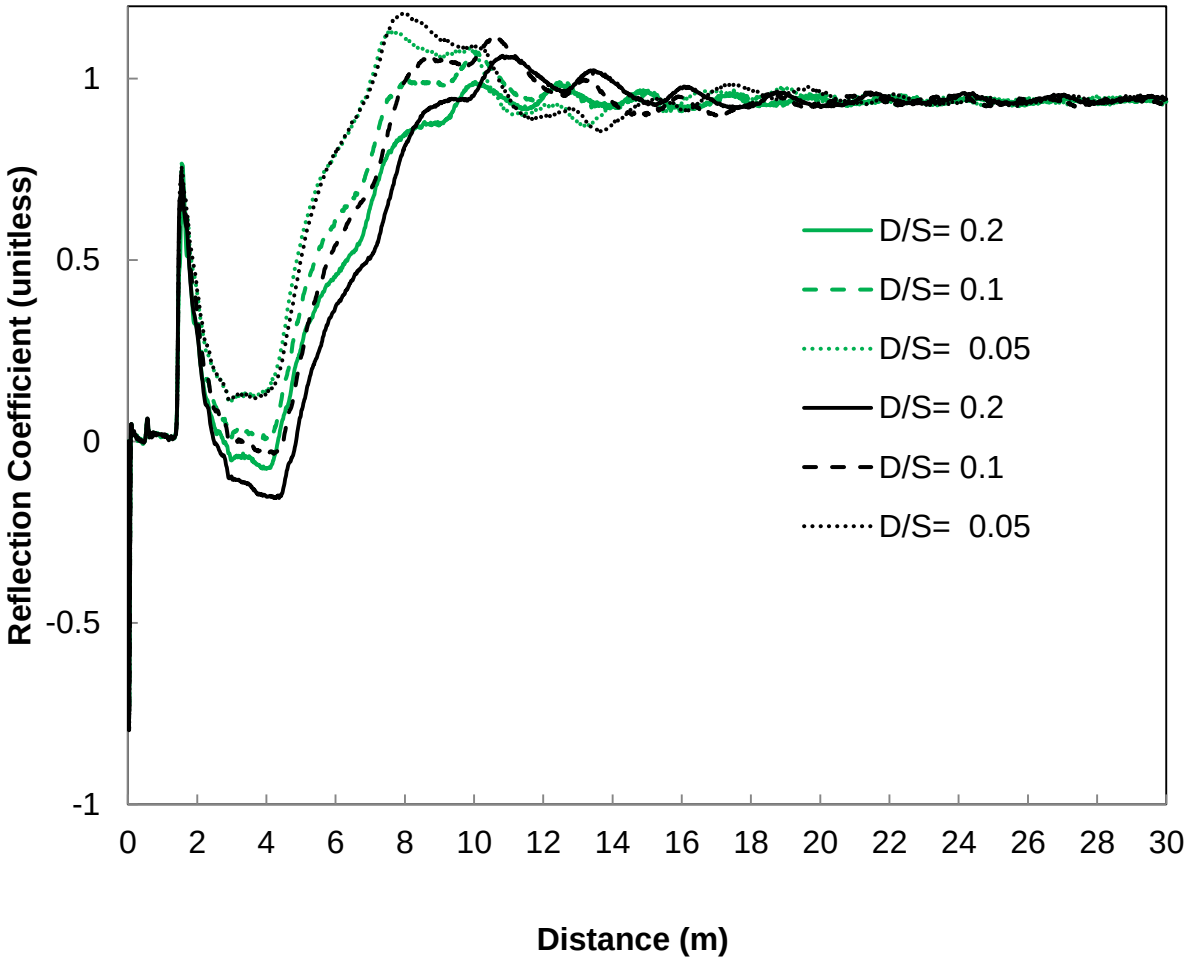

Figure 2.7 TDR waveform for deionized water, green lines are for coated TDR probe and black lines are for uncoated TDR probes. D is the diameter of the probes and S is their separations.

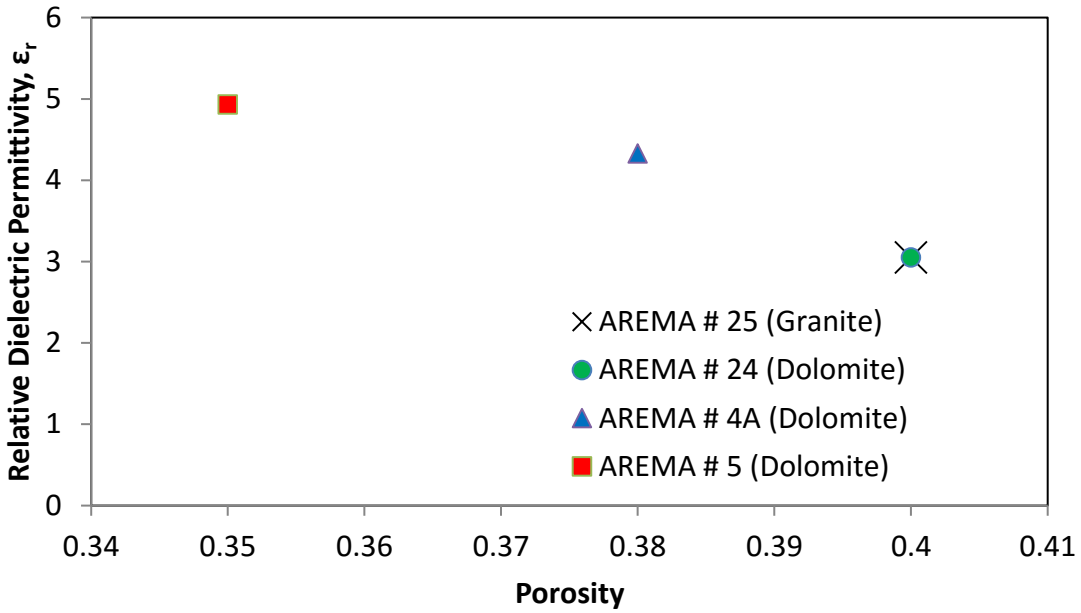

Figure 2. 8 Change in relative dielectric permittivity and electrical conductivity of various types of ballast

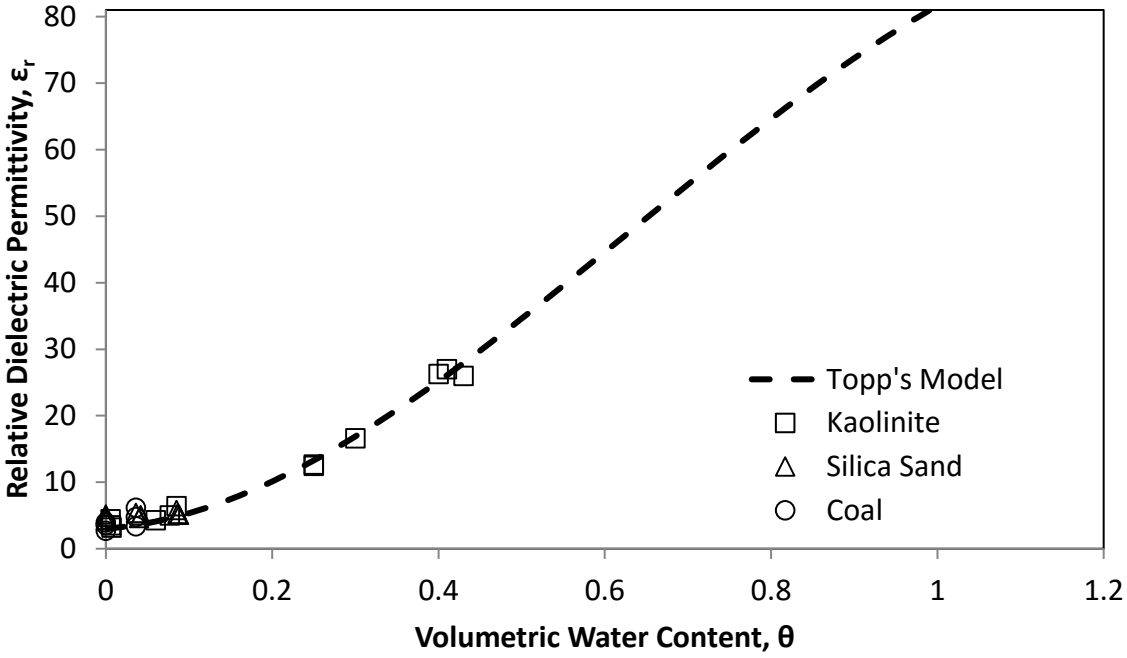

Figure 2. 9 Measured relative dielectric permittivity as a function of volumetric water content.

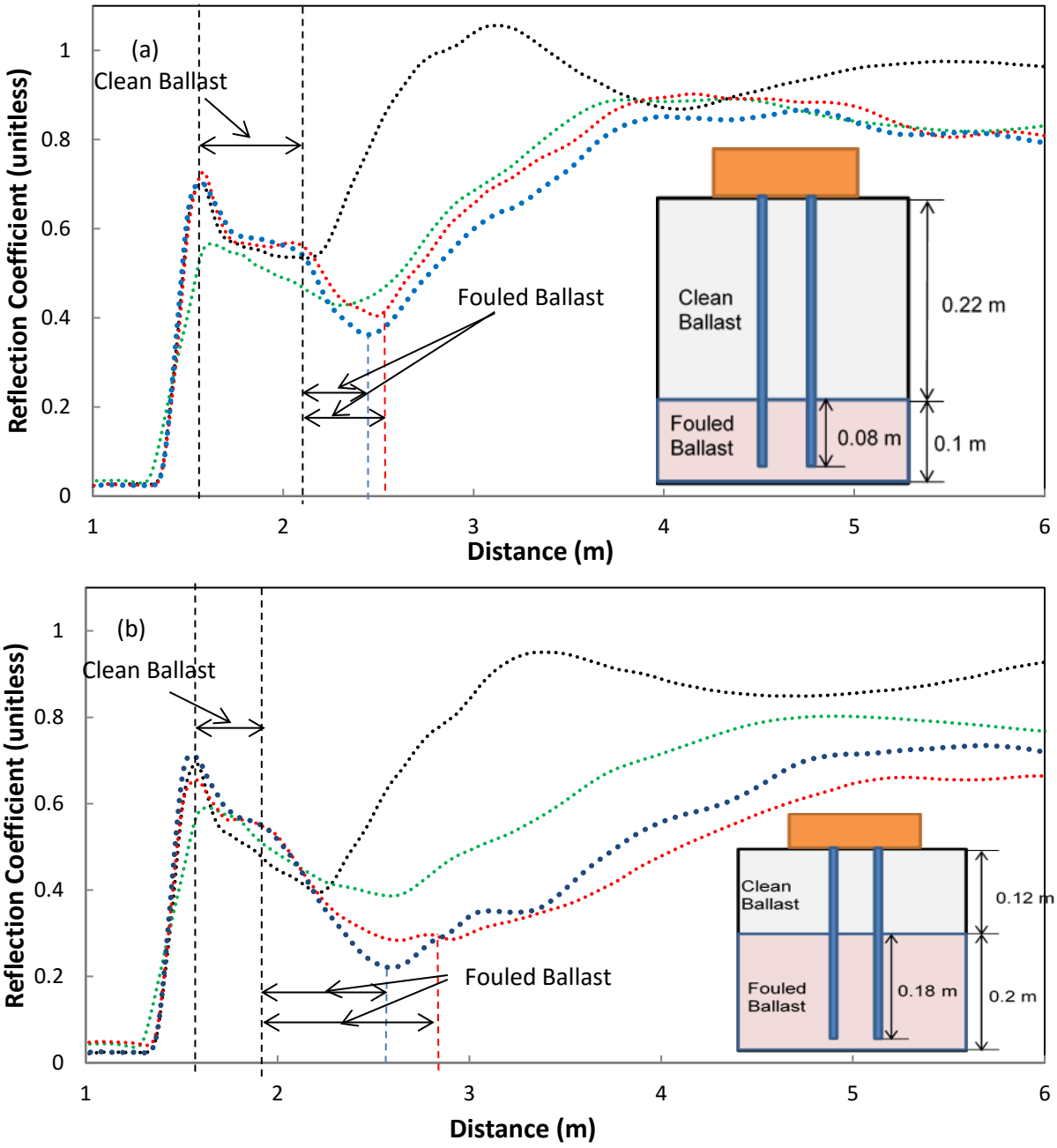

Figure Key			
Plot	Volumetric Water Content, θ_r	Plot	Volumetric Water Content, θ_r
.....	0.06	.....	0.4
.....	0.25	.....	0.56

Figure 2. 10 Measured TDR waveforms for a kaolinite fouled ballast with different volumetric water content for: (a) 0.22 m clean ballast and 0.1 m fouled ballast, and (b) 0.12 m clean ballast and 0.2 fouled ballast.

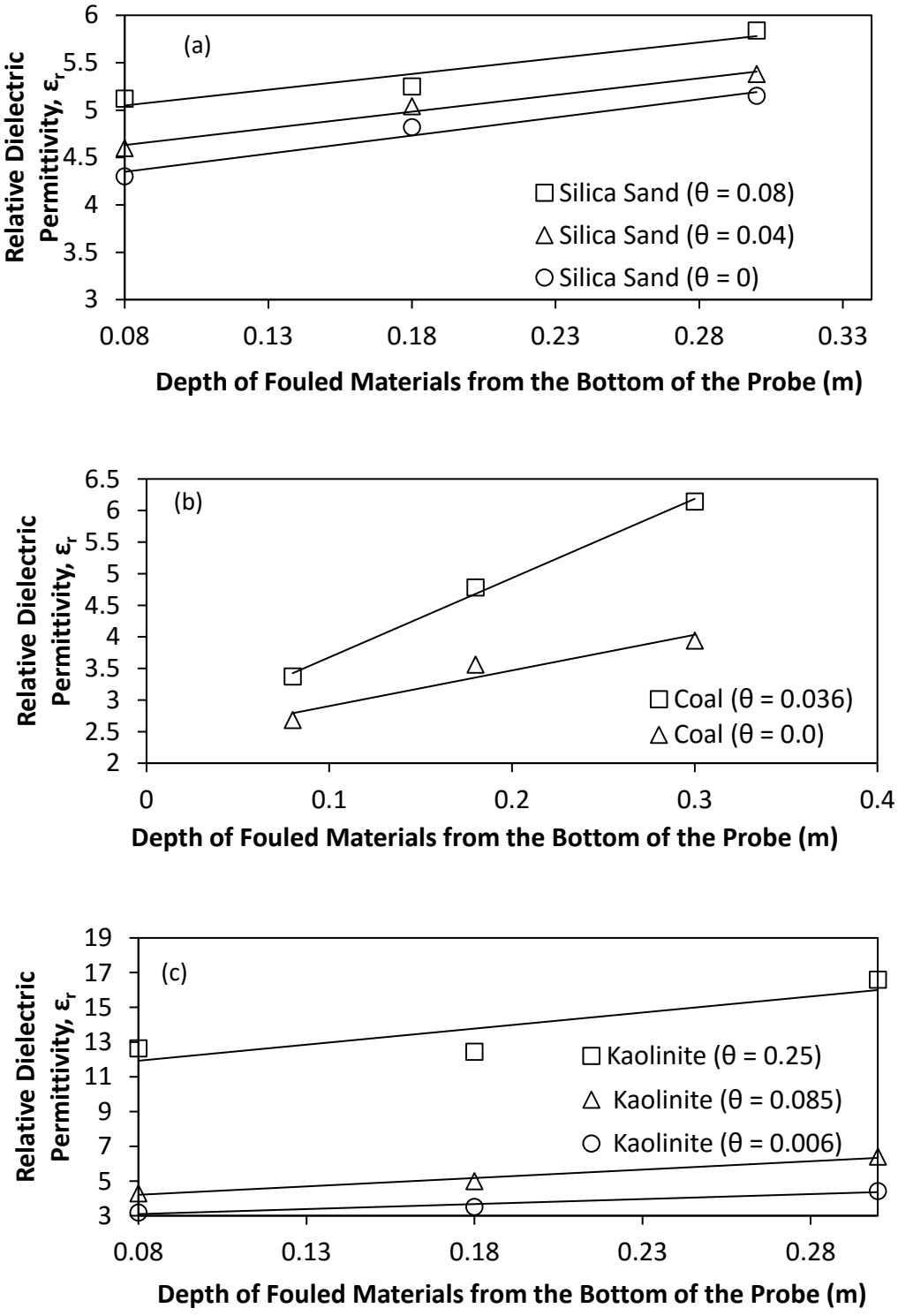

Figure 2. 11 Measured relative dielectric permittivity as a function of volumetric water content and embedded length of probe in fouled layer for: (a) silica sand fouled ballast, (b) coal fouled ballast, and (c) kaolinite fouled ballast.

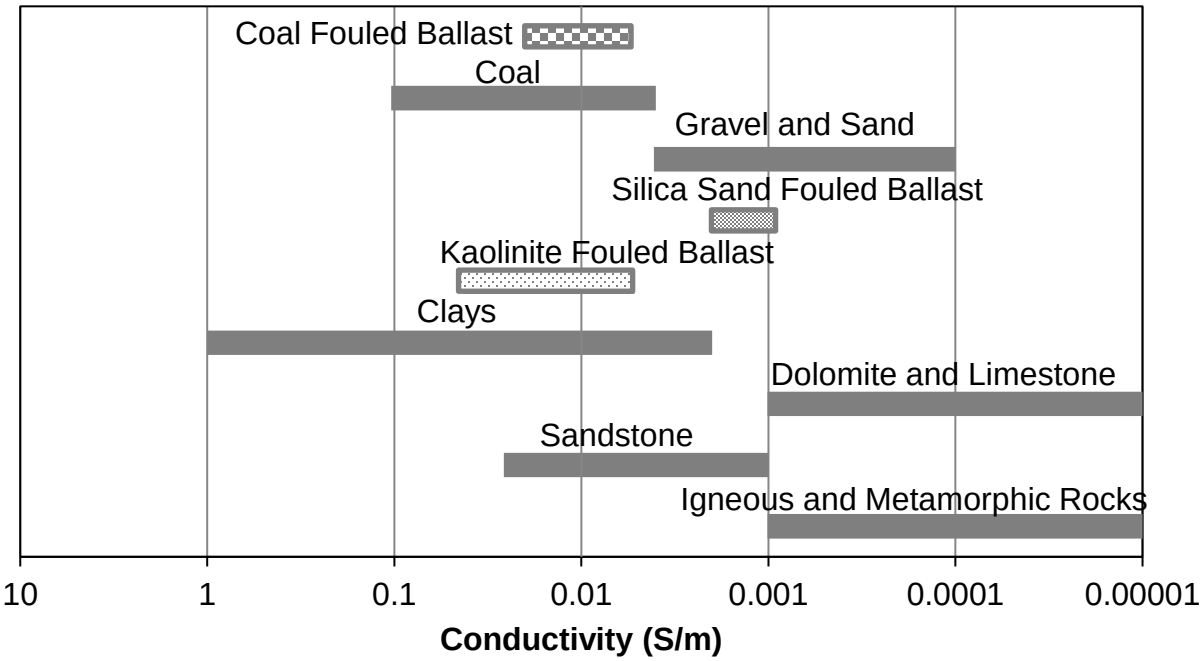

Figure 2.12 Electrical conductivity measurements and reported electrical conductivity values in the literature.

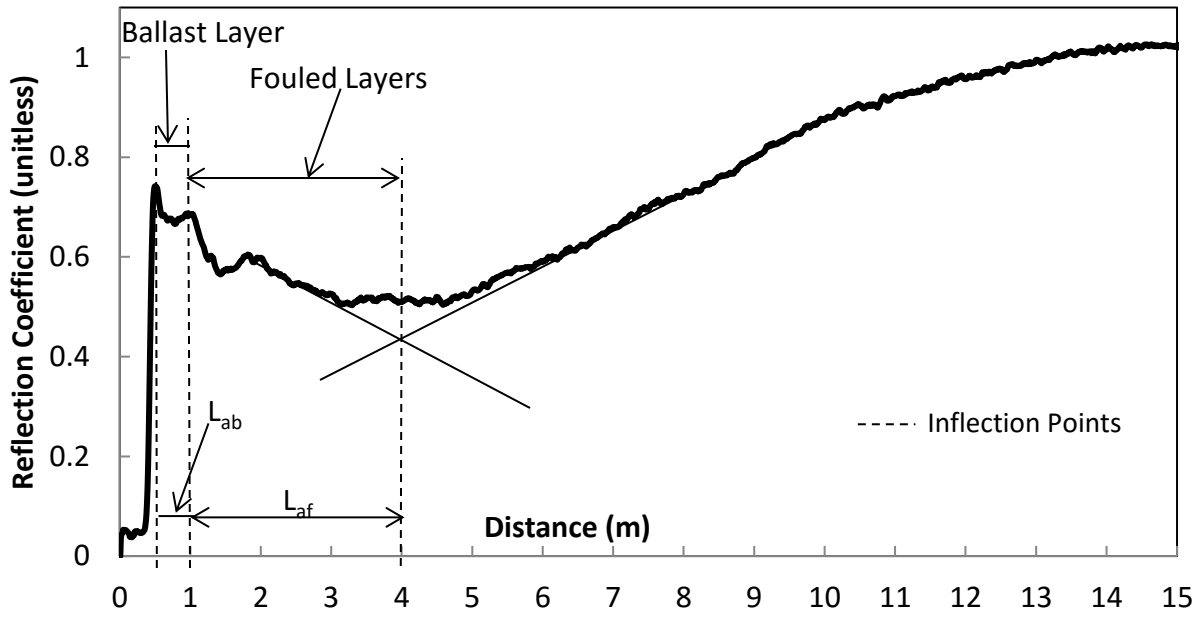

Figure 2. 13 TDR waveform with multiple reflections at the horizontal position 63 m.

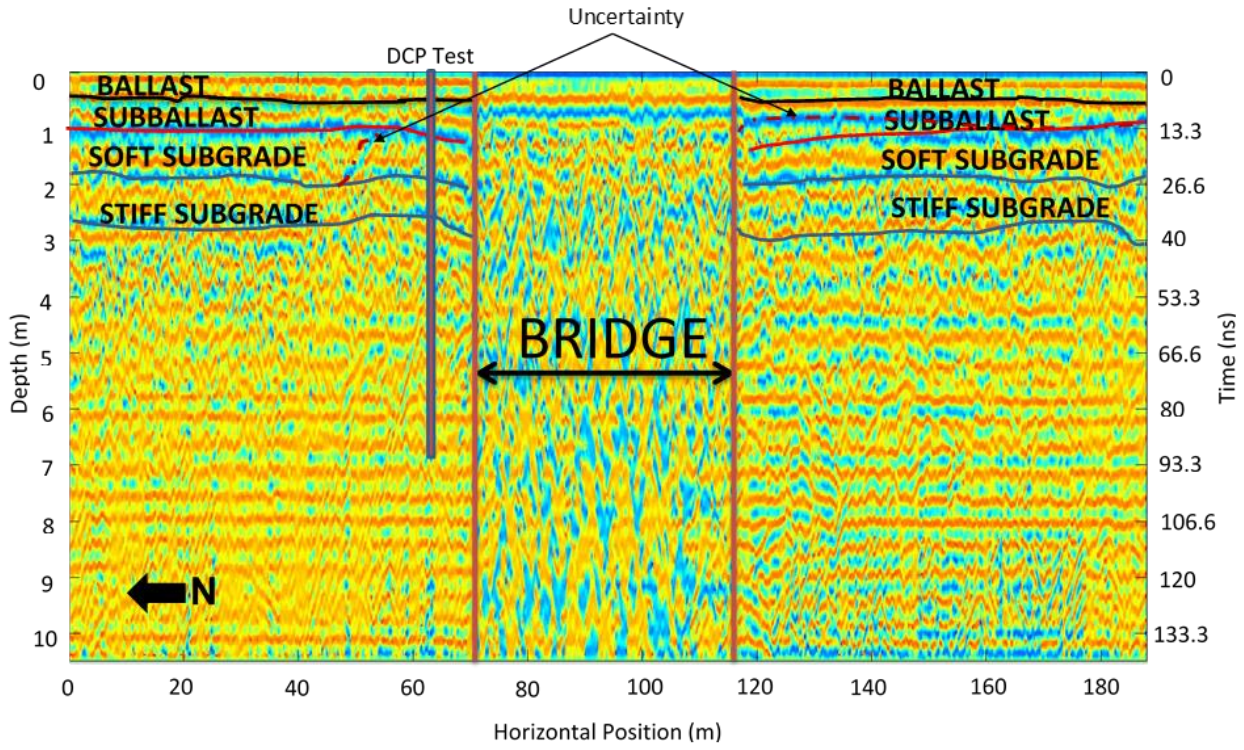

Figure 2.14 GPR profile with DCP overlay.

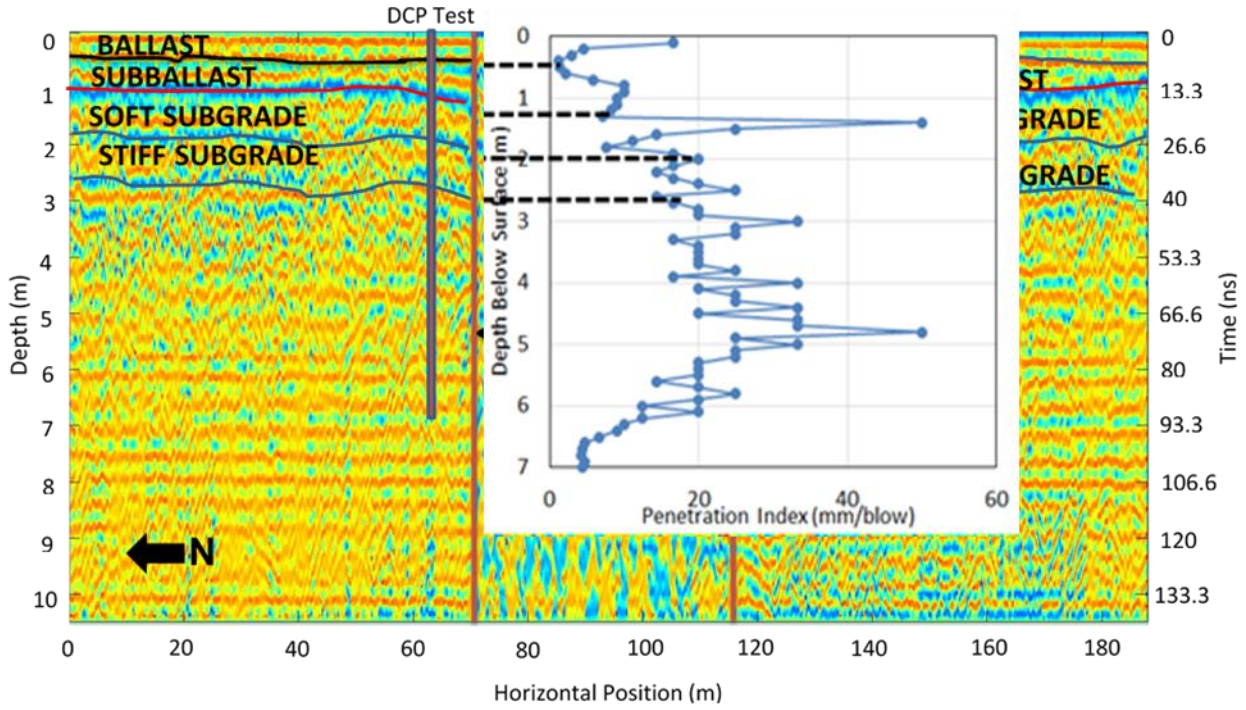

Figure 2.15 Interpretation of the GPR profile with DCP profile.

This chapter is a reformatted version of the manuscript:

Alsabhan et al., 2015, “Evaluation of Railway Track Substructure Using Ground Penetrating Radar Coupled with Time Domain Reflectometry,” In From Fundamentals to Applications in Geotechnics: Proceedings of the 15th Pan-American Conference on Soil Mechanics and Geotechnical Engineering, 15–18 November 2015, Buenos Aires, Argentina (p. 298). IOS Press.

CHAPTER 3: Assessment of Ballast Fouling with Ground-Penetrating Radar (GPR)

Abstract

Ballast fouling in railway substructure leads to a reduction in bearing capacity, a decrease in the drainage capacity, and an increase in track deformation. As a consequence of these detrimental effects, riding comfort, speed, and capacity are reduced and, if the problem is not addressed, track misalignment may lead to derailment. This problem is costly; thus, optimizing the maintenance operation is required to reduce the overall cost of freight and passenger transportation. This study presents a methodology to identify depth of fouling and fouling type in railway track substructure using Ground Penetrating Radar (GPR) coupled with Time Domain Reflectometry (TDR). This investigation was conducted on a mainline track section that has been underperforming with continuing maintenance operations. TDR measurements were conducted to determine the relative dielectric permittivity to thus calibrate and interpret the results obtained by 200-MHz-GPR profiles. Ballast specimens were obtained and tested in addition to Dynamic Cone Penetration (DCP) testing in the field to validate the geophysical results. Results show that TDR applications can be beneficial to the interpretation of GPR profiles and to quantify the level of fouling in larger scale maintenance operations.

Keywords. Ballast, railroad, TDR, GPR, fouling, relative dielectric permittivity

3.1 Introduction

Ground penetrating radar (GPR) is intended to provide images of the railway substructure, to evaluate its condition, and detect ballast fouling at critical sections of the track. Several publications have studied different aspects of GPR in railway maintenance applications. Clark et al. (2001) investigated the dielectric properties of railway ballast using GPR surveys. The study was conducted on two types of ballast materials: clean and fouled. They used 500 and 900 MHz GPR antennas. Better results were obtained using 500 MHz antennas, the data collected with the 900 MHz antenna yielded small depth of penetration of the subsurface due to large scattering on the ballast particles. For the 500 MHz surveys, the clean ballast relative dielectric permittivity (ε_r) was 3 while for the dry fouled ballast relative dielectric permittivity (ε_r) was equal to 4.3 as the overall porosity of the fouled material decreases. The relative dielectric permittivity (ε_r) of the material also increased when the water content in the fouled ballast increased.

Leng and Al-Qadi (2009) assessed the dielectric properties of two types of ballasts (e.g., granite and limestone) under various conditions of fouling and moisture using 2 GHz air-coupled GPR antennae. The study concluded that the granite ballast has smaller relative dielectric permittivity compared to the limestone ballast at the same fouling level and porosity. They also reported that the relative dielectric permittivity (ε_r) at a dry clay fouling level of 0 to 50% varied from 3.25 to 3.77 for the granite ballast and from 3.96 to 4.84 for the limestone ballast.

Narayanat et al. (1999) performed GPR survey on track substructure using three ground-coupled GPR antennae at 100, 400, and 900 MHz. The data collected with the 900 MHz antennae showed a strong surface reflection with very little information about the subsurface. Thus, due to the difficulty in maintaining the proper distance of the 900 MHz antenna within one-eighth of its wavelength (4 cm) above the ground so that the proper coupling of the antenna to the ground is achieved, it was determined that these data was unreliable for this application. The results of the 400 MHz antennae were better when estimating the depth of the subsurface layers while the 100 MHz antennae was better in identifying anomalies, such as water pockets, at deeper depths, compared to the 400 MHz system.

3.2 Theory and Background of GPR

A GPR system consists of a signal generator, a transmitting antenna, a receiving antenna, and a recording device. Short EM waves are emitted into the subsurface using the transmitter. The receiver collects the energy that bounces off the contrasting boundaries. The travel time and amplitude of the reflected signal is encoded into the captured reflected signal. GPR reflections are controlled by the electromagnetic properties of the shallow subsurface that are presented in Section 2.2. The thickness and condition of the subsurface are based on the propagation velocity and amplitude of the EM wave which are function of the relative dielectric permittivity (ε_r), the relative magnetic permeability (μ_r), and electrical conductivity (σ). If the materials in the near surface are assume to be non-ferromagnetic, the EM wave speed is expressed as:

$$v = \frac{c}{\sqrt{\varepsilon_r}} \quad (3.1)$$

Or as a function of the frequency and wavelength as:

$$\mathrm{v} = \lambda \times f \quad (3.2)$$

where, c is the speed of light, λ is the wavelength, v is the velocity, and f is the frequency.

GPR yields high-resolutions image of the subsurface. The vertical resolution is about a quarter of the wavelength (Burger et al. 2006). That is high frequencies yield fine resolutions. However, they attenuate more rapidly than longer-period waves and thus may yield smaller penetration depths. In the other hand, low frequency waves yield coarser resolutions at deeper depths of penetration. One problem with GPR is that EM waves attenuate faster in high conductivity environments.

3.3 Survey Design

There are different modes of GPR data acquisition mode each mode is dictated by a specific goal. The most common GPR data acquisition modes for railway investigations are: (1) common midpoint (CMP) mode, and (2) common offset (CO) mode. The CMP mode is used to estimate velocity of the substructure layers. The CMP mode principle is based on placing the antennas side by side and varying the separation between them relative to a fixed point in a reflector.

Common offset mode is used to map a subject or an interface in the substructure. CO mode is based on placing the antennas at a fixed separation and moving them along the line of the survey.

Annan (2005) defined several parameters that are important when designing a GPR survey. These parameters are frequency, station spacing, recording time window, the antenna spacing, and the antenna orientation. The following discussion describes importance of each parameter.

3.3.1 Central Frequency

The antenna frequency has an important role in determining the depth and resolution of the radar system. As mentioned in the previous section, low frequencies penetrate deeper depths, whereas high frequencies have higher resolution, but they tend to attenuate more rapidly. In addition, during high radar frequencies clutter become an issue due to responses from smaller scale features that mask the desired signals at deeper depths. Annan and Cosway (1994) preferred to trade off resolution for penetration because there will be no sense of choosing a high resolution radar frequency if it cannot detect a target. Annan (2005) proposed that selected the operating frequency f_c of the GPR system should take into consideration the desired spatial resolution and clutter limitation in which

$$f_c^R < f_c < f_c^C \tag{3.3}$$

where, f_c^R corresponds to the required frequency to achieve the desired resolution, and f_c^C corresponds to the clutter frequency constrain. Annan defined f_c^R and f_c^C limits as $f_c^R >$

$\frac{c}{4\Delta z\sqrt{\varepsilon_r}}$ and$f_c^C < \frac{c}{10\ \Delta L\sqrt{\varepsilon_r}}$, respectively, where, Δz is the spatial separation to be resolved, ε_r is the relative dielectric permittivity, and ΔL is the clutter dimension.

3.3.2 Station Spacing

Station spacing refers to the separation between two GPR discrete measurements (Figure 3.1). Adequately choosing the GPR station spacing is crucial in preventing spatial aliasing, where independent reflections become indistinguishable. Furthermore, at high station intervals dipping reflectors or diffraction events will not be properly captured. Annan (2005) reported that station interval (Δx) should be less than the Nyquist sampling interval to avoid spatial aliasing.

$$\Delta x \leq \frac{c}{4f_c\sqrt{\varepsilon_r}} \tag{3.4}$$

3.3.3 Time Window

Estimating a proper recording time window in GPR survey is a function of the desired depth of exploration. Annan defined the required recording time window as:

$$W = 1.3\frac{2D_{max}}{V_{min}} \tag{3.5}$$

where, D_{max} is the maximum depth, and V_{min} is the minimum velocity.

3.3.4 Selecting Antenna Orientation

Most common GPR antennas are dipolar with a preferred electrical field polarization in the direction along the long axis of the antennas (Annan 2005). Baker et al. (2007) described the effect of changing the antennas orientation on Fresnel's zone. Figure 3.2 illustrate the concept of Fresnel's zone in GPR surveys. The Fresnel's zone identifies the horizontal resolution limits at a certain depth.

Figure 3.3 shows the most common GPR antennas orientation. Due to the fact that GPR footprint appears as an ellipse of radar illumination, it is most effectively to use a broadside-perpendicular (PR-BD) configuration (see Figure 3.3) to obtain GPR footprint that is elongated in the line direction and narrowest perpendicular to the line direction.

3.4 Data Processing

In most cases, raw data collected needs to be processed to either improve the signal to noise ratio or to allow capturing the physical properties of the substructure. The goal of GPR data processing is to present the subsurface conditions accurately in radargrams. Raw data might undergo several processing steps that vary from basic processing steps (e.g., dewowing, and time gaining) to sophisticated steps (e.g., migration or background subtraction) to accomplish this goal. However, “overprocessing” the data may distort the final interpretation or may introduce artificial textures in the interpreted radargram. As rule of thumb, the best processing steps starts with a good acquisition quality. No good processing technique can enhance data that are poorly collected. Other steps included in the GPR data processing are: (1) data editing, (2) time zero correction, (3) dewow, (4) filtering, (5) and time gaining. Each one of these steps is described in the following section.

3.4.1 Data Editing

Good quality data depends on maintaining an effective data collection from the start. However, errors occur in the field such as incorrect header information, data file merging, and bad traces. Data editing enables the correction of these errors by modifying

header files and removing bad traces by a simple interpolation between properly collected neighboring traces.

3.4.2 Time Zero Correction and Dewowing

Time zero is referred to the GPR first signal arrival. This first arrival corresponds to the either the air or ground wave. Time zero might vary along the survey due to system timing, cable lengths, and antenna positioning (Olhoeft 2000). Therefore, it needs to be corrected in the radargram to a common first signal arrival. Dewowing is the removal of very low frequency and the initial DC signal components from the data (Jol 2008).

3.4.3 Filtering

Filters are used to improve the signal-to-noise ratio by removing clutters and noise from the data. Annan (2005) classifies filters into temporal and spatial filters. Temporal filters manipulate the data across the time axis to remove frequency components that are not on interests in the survey. Spatial filters manipulate the data across the position axis. This type of filters is used to emphasis or suppresses specific features (e.g., geological bedding, and dipping reflectors) in the GPR radargram (Jol 2008). Most often these two types of filters are combined. There are several types of filter operations such as: (1) mean filter, (2) median filter, (3) high pass filter, (4) low pass filter, and (5) band pass filter.

3.4.4 Time Gain

Time gain is used to compensate for signal attenuation to improve the interpretation of deeper structures in a radargram. In most cases, gains use a non-linear versus depth multiplication factors; i.e., amplitudes increase with deeper depths so reflections from shallower depths appear to have similar magnitudes than reflected signals from deeper formations. Knowing that time gaining is nonlinear requires the user to understand that filtering operations are not equivalent before and after the application of gains (Annan and Cosway 1992).

3.5 Methodology - Case Study: Evaluation of Railway Track Substructure Using Ground Penetrating Radar Coupled with Time Domain Reflectometry

Field data were collected in the Fall of 2014 on a mainline track section in Dayton, Illinois (Figure 3.4). This track services the local fracking sand industry by transporting high tonnages of sand to larger rail hubs. Over the 2.4-km rail stretch, two problem areas were investigated. These rail sections have systematic settlement and deformation problems, which limits train speed to 16 km/hr.

GPR data were collected using a pulseEKKO PRO system with 200-MHz antennae for the two sections of the track. Raw GPR data was processed using MATGPR processing software. The data processing technique included time-zero correction, mean spatial filter, median spatial filter, and gain control function to improve the quality of the presentation and help in the interpretation.

Along with GPR data collection, TDR testing was conducted to calibrate the GPR data and to assess the EM properties of the mainline track section. A Campbell TDR100 system (Campbell Scientific Inc. 2007) was used in this study with an impedance coaxial cable (Z_o) = 50 Ω. PCTDR-V 2.08 software was used to control the TDR100 signal. The record length was 2048 points along with 4-signal stacking. Stacking was used to improve the signal-to-noise ratio on the reflection waveforms. 0.9-m-long TDR probes, with separation of 0.05 m and diameter of 0.012 m, were driven into the ballast layer.

Dynamic Cone Penetrometer (DCP) was conducted at the same locations as the TDR measurements to ground truth the geophysical data. The DCP system penetrated to depths of up to 10 m during this field program. DCP tests provide an indirect measure of the shear strength in the underlying soil strata without the need for excavation. A weight of known mass is dropped a distance, the force that is created drives a cylindrical cone into the underlying soil strata. The depth of penetration per blow (mm/blow) provides a measure of the inverse of shear strength of the soil. Thus, using these information DCP profiles can be used estimate the depth of the different subsurface layers (Herrick and Jones, 2002).

3.6 Results and Discussion

3.6.1 Ballast Section

The first investigated section—known as the Ballast Section—had the simplest geometry (i.e., an embankment composed by subgrade, subballast, ballast, ties and railways) with no additional structures present (Figure 3.5 & 3.6). The investigated site

was a 76-m-long section with standard rail gauge of 1.435 m, and 1.8-m shoulders. The water table was at the base of the ballast layer. The ballast was of poor quality and multiple ballast types and fines were present. A typical TDR waveform for the ballast section is shown in Figure 3.7. The multiple reflections correspond to substantial differences in the relative dielectric permittivity between the underlying layers that the EM wave propagates through, clean ballast and fouled ballast layers. The first waveform reflection showed a relative dielectric permittivity (ε_{rb}) of 4, which is consistent with relative dielectric permittivity of clean ballast, whereas the relative dielectric permittivity (ε_{rf}) of the fouled ballast was 11.1. Thus, by incorporating these values into Equation 3.1, the velocity of the subsurface layer was calculated as 0.089 m/ns. Hence, GPR data calibrated with this layer velocity.

Processed GPR data of the Ballast Section in Figure 3.8 indicates three layer interfaces corresponding to a ballast layer, subballast layer, subgrade layer, and bedrock. GPR data shows a local dip in the track substructure coincides approximately with the settlement zone that spans from the horizontal position of 50 m to 85 m. The dip shown in the GPR data indicates the potential for accumulating moisture in the soft soil that might be responsible for the local settlement of the rail track in this section. Figure 3.9 shows the DCP test profile. The DCP profile exhibits a strong (i.e., low penetration index) ballast layer followed by a weak layer of approximately 1 m. Below 2-m depth, the soil profile exhibits increased resistance to penetration with depth. The DCP results correlate well with the GPR layer thickness and sampling conducted at this location.

3.6.2 Culvert Section

The second rail section—the Culvert Section—was constructed on a large embankment. The embankment has experienced vertical and horizontal displacements for many years. Multiple retaining structures have been constructed to prevent translation of material, but they have been unsuccessful in stopping deformation (Figure 3.10). Flowing water is present on the west side of the track, and a culvert is present beneath the track to aid drainage. TDR measurement was conducted on the same location as the DCP. Following the same procedure in the Ballast Section, the TDR waveform was used to estimate a velocity of the subsurface layer in the Culvert Section of 0.062 m/ns (Figure 3.11).

The processed GPR data of the Culvert Section are shown in Figure 3.12. GPR data indicates the presence of two layer interfaces that correspond to ballast, subballast, and subgrade layers. A deep ballast pocket is observed in the GPR data that starts at horizontal station of 45 m, ending at station 63 m; this is where the ballast washout occurs on the surface. A possible cause for ballast washout in this zone might be attributed to repeated ballast filling to compensate for track settlement. Furthermore, water trapped in this deep ballast pocket shown in the radargram appears to have weakened the subgrade by increasing the pore water pressure, thus causing more deformation in the subgrade layer.

DCP test results at this location (Figure 3.13) show the top 0.5 m of ballast is relatively loose or disturbed. A stronger layer is present from 0.5 m to 3 m. Below 3 m, the soil strength significantly decreases, shown by a high penetration index. GPR results

complement the DCP profile. Bedrock and refusal depth are verified between the methods.

3.7 Summary and Conclusions

Time Domain Reflectometry (TDR) and Ground Penetrating Radar (GPR) testing was conducted to assess the electromagnetic (EM) properties (i.e., real relative permittivity and electrical conductivity) of railway substructure. TDR results were then used to calibrate the GPR data, particularly in fouled ballast with high moisture content. In particular, multiple reflections take place in the TDR waveform, which correspond to substantial differences in the relative dielectric permittivity between the underlying layers. TDR successfully distinguished multiple layers in the railway substructure and gave an estimation of the wave velocity of the substructure. Dynamic cone penetrometer (DCP) testing validated the use of TDR to calibrate GPR data and to allow the imaging of the extent of ballast fouling that has contributed to ongoing deformation along two sections of rail track in Dayton, IL.

Acknowledgements

Financial and material support for this study was provided by the C-FIRE, Uretek USA, and OmniTRAX. B. Warren and J. Su participated in different aspects of the testing. Prof. T.B. Edil provided insights on the results.

References

Al-Qadi, I., Xie, W., Roberts, R., 2008. “Scattering analysis of ground-penetrating radar data to qualify railroad ballast contamination,” NDT and E Int., Elsevier, Vol. 41, pp.441–447

Annan, A. P., and Cosway, S. W., 1992. “Ground penetrating radar survey design,” In Proceedings of the 4th Annual Symposium on Applications of Geophysics to Engineering and Environmental Problems (SAGEEP), pp. 329-351.

Baker, G. S., Jordan, T. E., and Pardy, J., 2007. “An introduction to ground penetrating radar (GPR),” Geological Society of America Special Papers, Vol. 432, pp. 1-18.

Burger, H. R., Sheehan, A. F. and Jones, C. H., 2006. Introduction to applied geophysics, Book, New York : W.W. Norton and Company.

Clark, M. R., Gillespie, R., Kemp, T., McCann, D. M., and Forde, M. C., 2001. “Electromagnetic properties of railway ballast,” NDT and E International, Vol. 34, pp. 305-311.

Davis, J. L., and Annan, A. P., 1989. “Ground-Penetrating Radar for High-Resolution Mapping of Soil and Rock Stratigraphy1,” Geophysical Prospecting, vol. 37(5), pp. 531-551.

Herrick, J. E., and Jones, T. L., 2002. “A dynamic cone penetrometer for measuring soil penetration resistance,” Soil Science Society of America Journal, Vol. 66, pp. 1320-1324.

Jol, H. M., 2008. Ground penetrating radar theory and applications, Book, Published by Elsevier Science, Netherlands.

LENG, Z., Al-Qadi, I., 2009. “Dielectric constant measurement of railroad ballast and application of STFT for GPR data analysis,” NDTCE, Non-Destructive Testing in Civil Engineering, Nantes, France.

Narayanan, R. M., Kumke, C. J., Li D., 1999. “Railroad track monitoring using ground penetrating radar: simulation study and field measurements,” In: SPIE conference on subsurface sensors and applications, pp. 3752.

Olhoeft, G. R., 2000. “Maximizing the information return from ground penetrating radar,” Journal of Applied Geophysics, Vol. 43(2), pp.175-187.

Figures

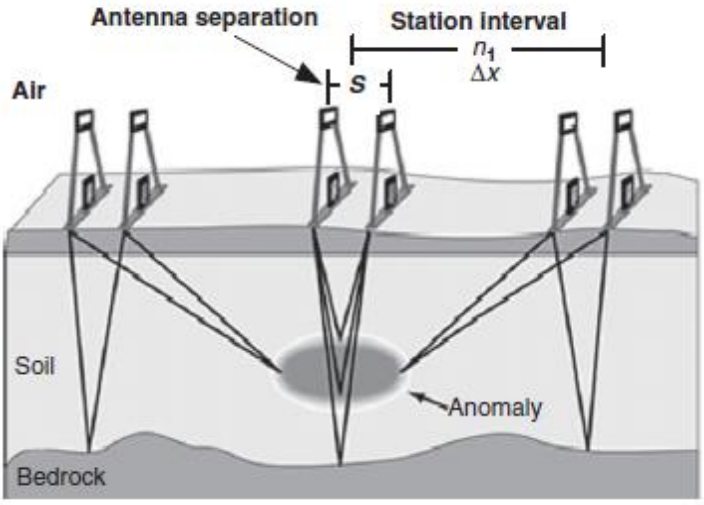

Figure 3.1 GPR Separation Parameters (Annan 1992)

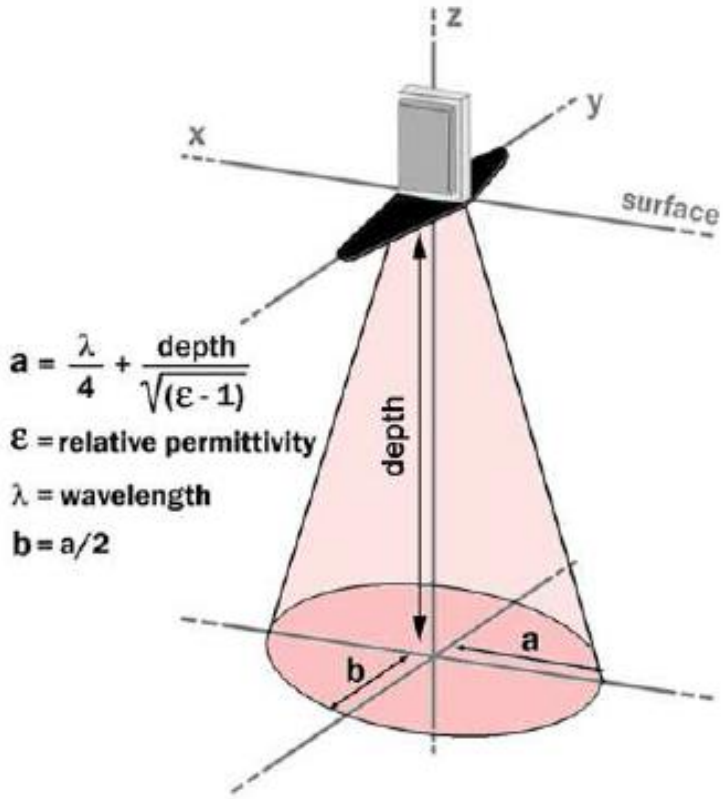

Figure 3.2 GPR Footprint (Jol 2008)

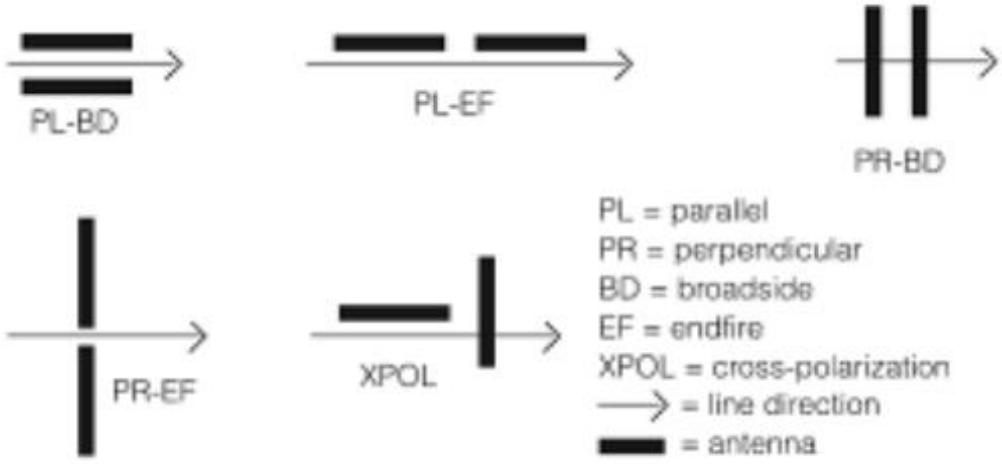

Figure 3.3 Common GPR Antenna Orientation (Annan and Cosway 1992)

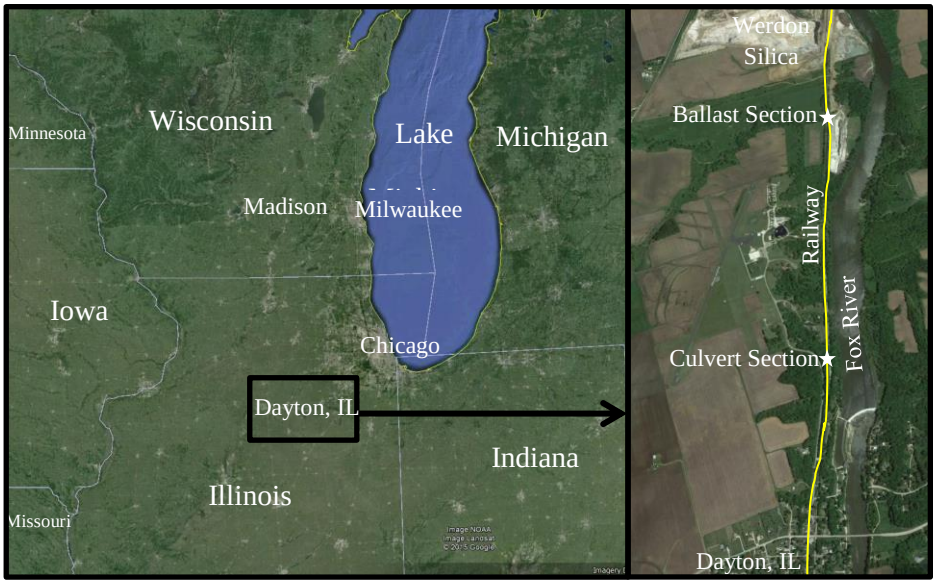

Figure 3.4 Geographic location of the testing site: Dayton, IL (Source: Google Earth)

Figure 3.5 Ballast Site Overview

Figure 3.6 Ballast Site Overview

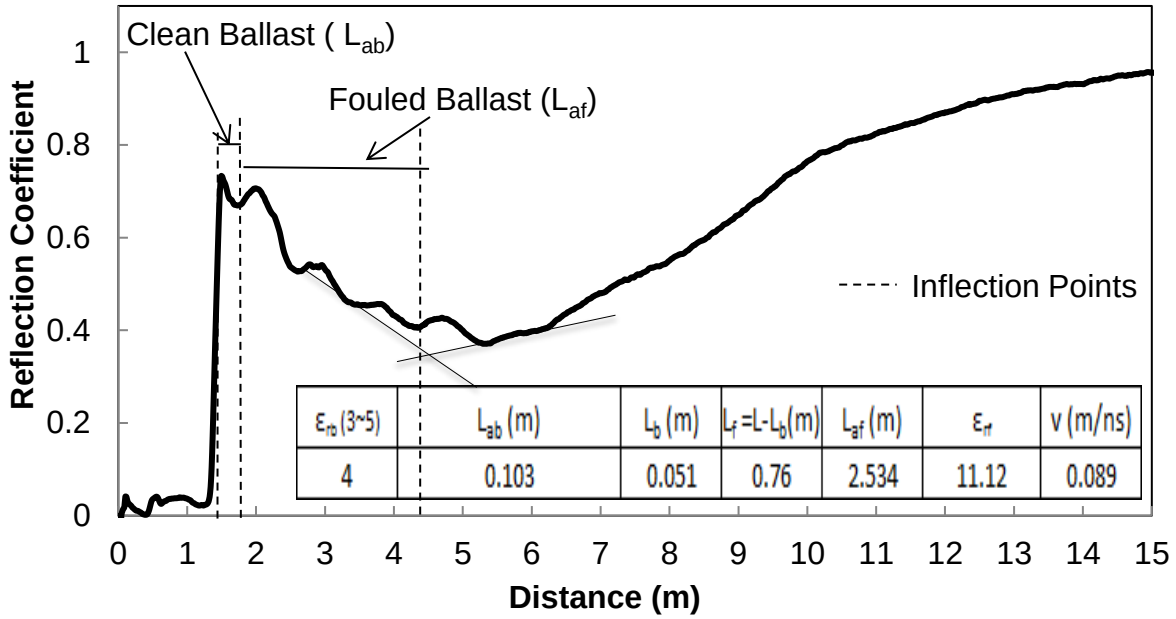

ε_{ro} (3~5)	L_{ab} (m)	L_b (m)	L_f =L-L_b(m)	L_{af} (m)	ε_{rf}	v (m/ns)
4	0.103	0.051	0.76	2.534	11.12	0.089

Figure 3.7 TDR waveform with multiple reflections at the horizontal position 58 m in the Ballast Section

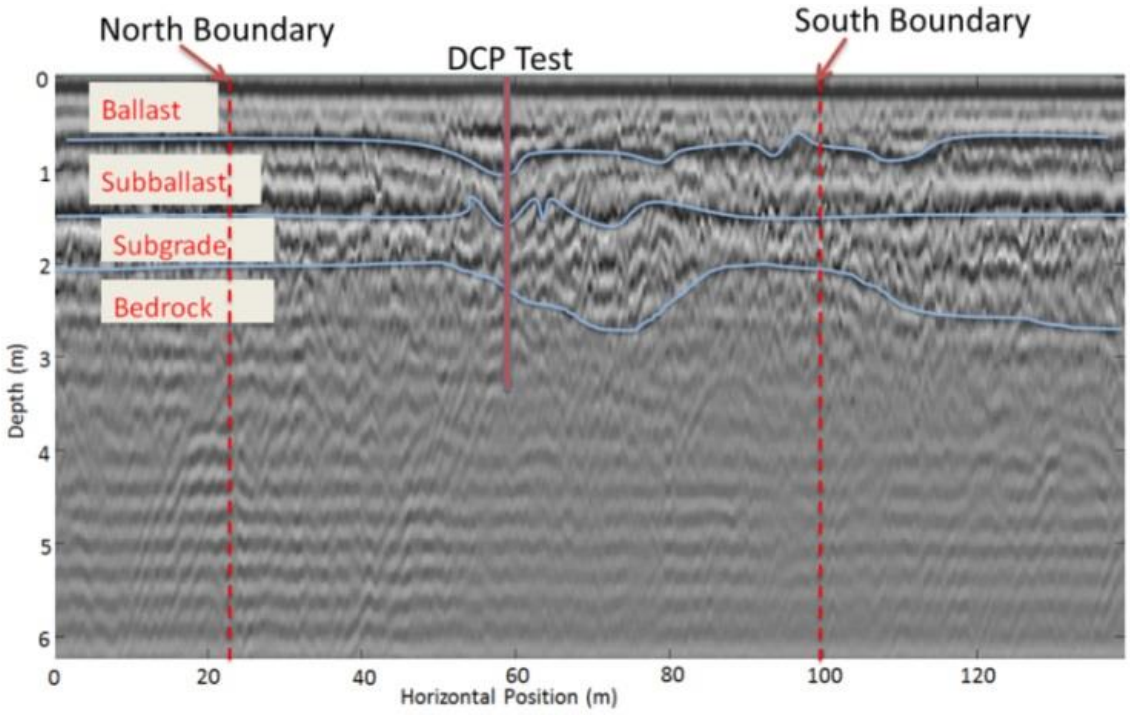

Figure 3.8 GPR profile with DCP overlay at the Ballast Section.

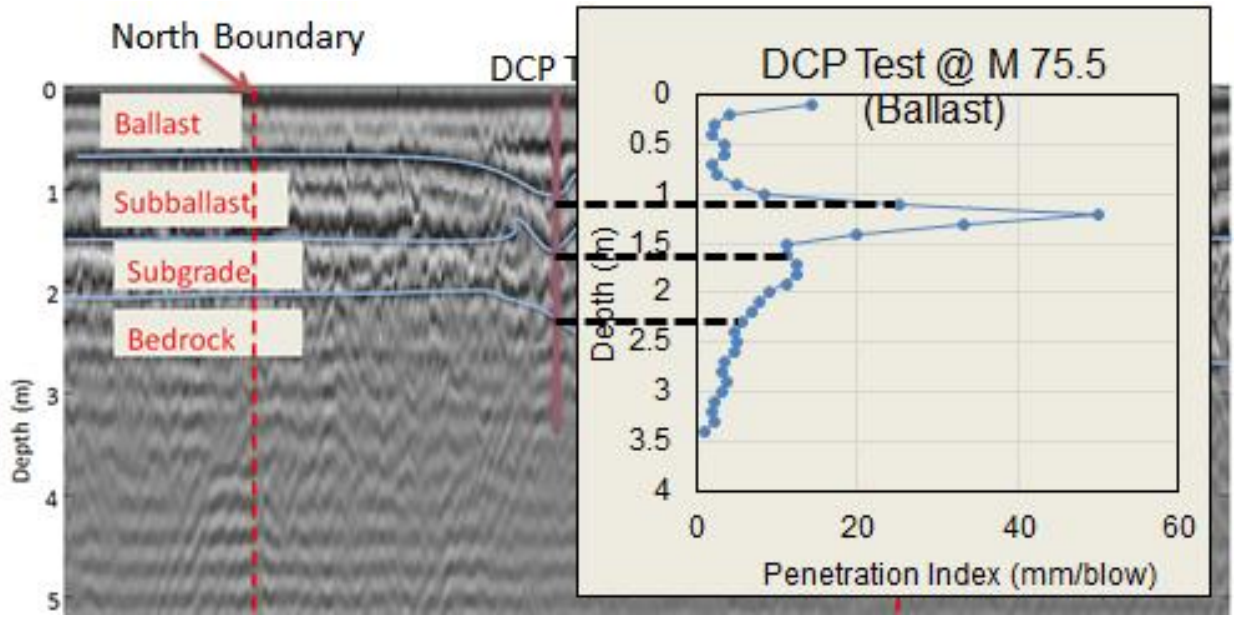

Figure 3.9 Interpretation of the GPR profile with DCP profile at the Ballast Section.

Figure 3.10 Culvert Site. Note Ballast Washout and Culvert.

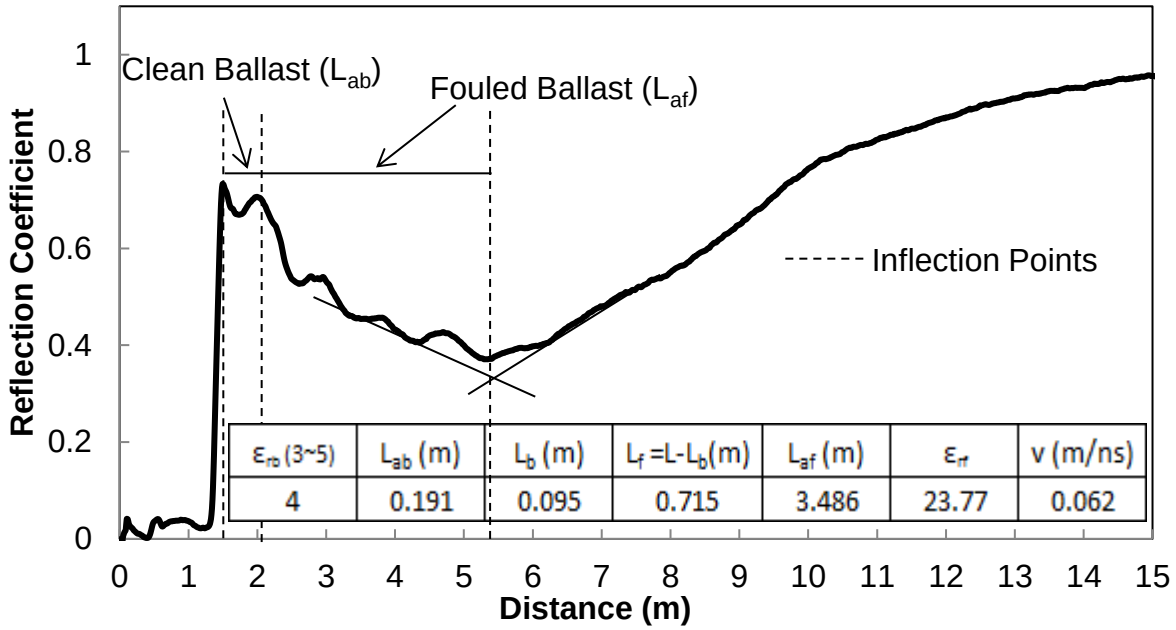

Figure 3.11 TDR waveform with multiple reflections at the horizontal position 59 m in the culvert section

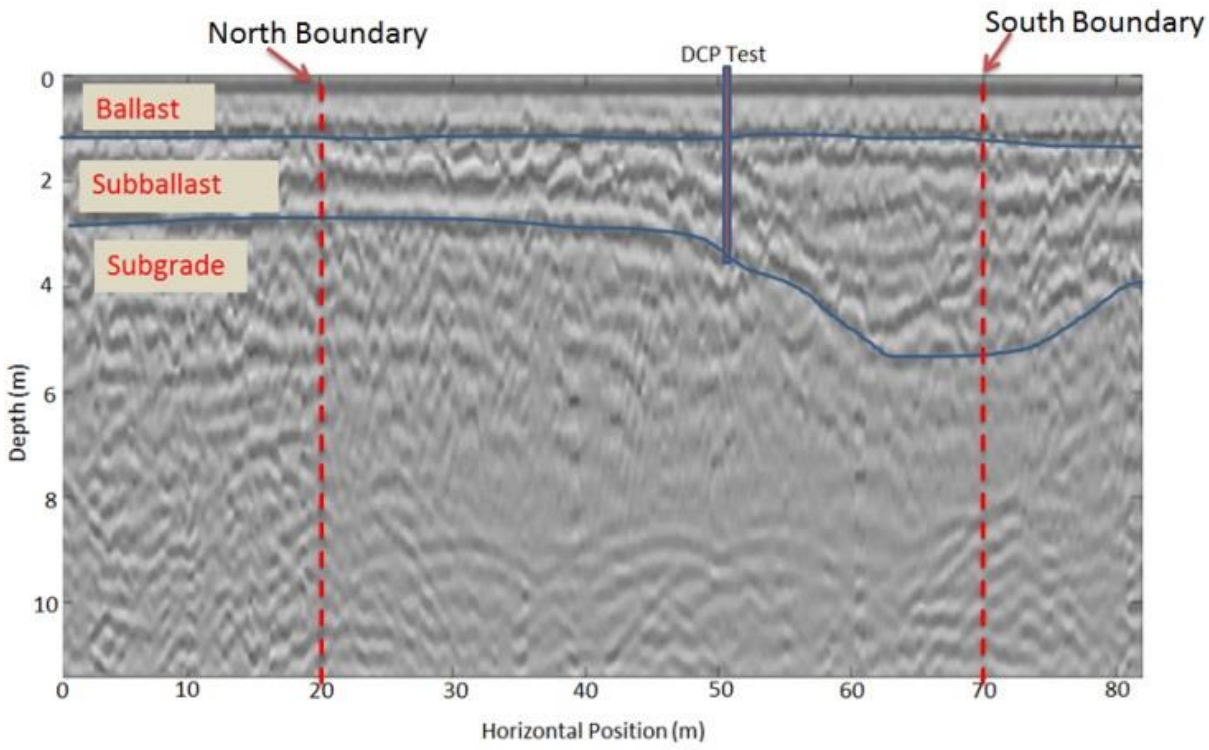

Figure 3.12 GPR profile with DCP overlay at the Culvert Section.

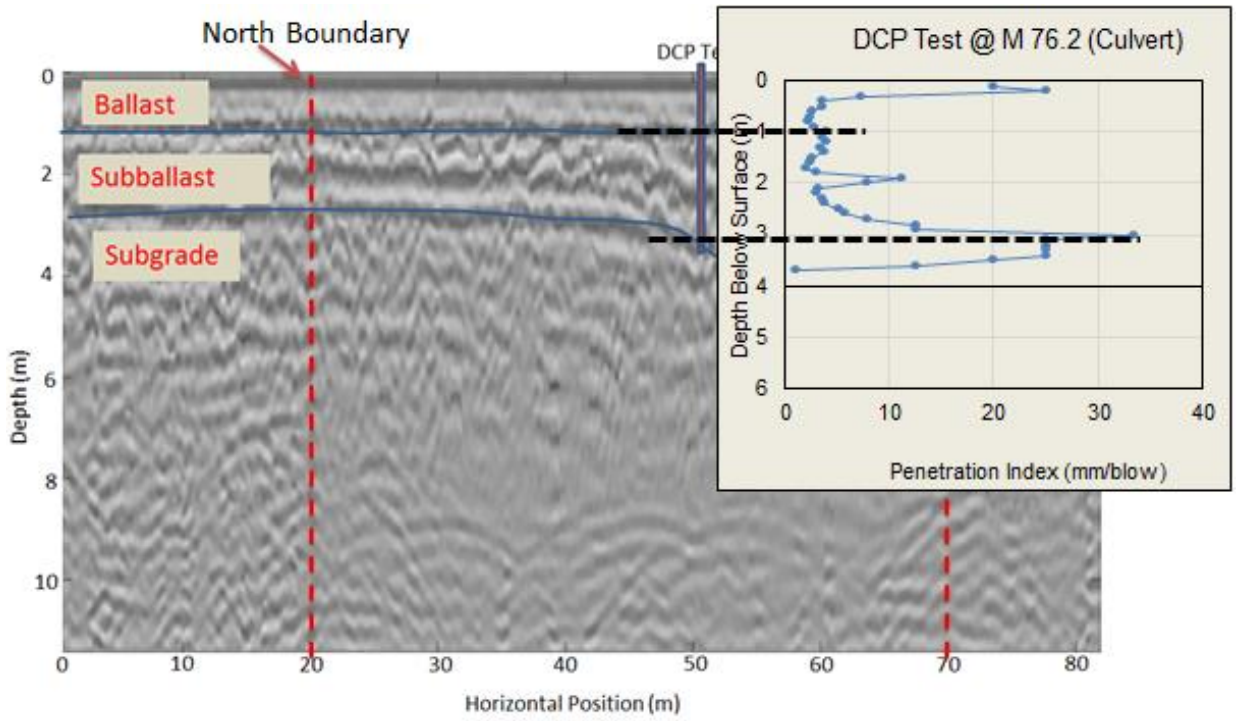

Figure 3.13 Interpretation of GPR profile with DCP profile at the Culvert Section.

This chapter is a reformatted version of the manuscript:

Alsabhan et al., 2016, “Assessment of Fouled Ballast Response using a Full Scale Track Model,” to be submitted to the Journal of Transportation Engineering

CHAPTER 4: Full Scale Track Model (FSTM)

Abstract

Ballast fouling compromises rail track safety, raiders comfort, and railway load capacity. Fouling may lead to excessive track deformation and ultimately train derailment. This problem is quite costly for the railway industry thus, preventing train derailment while optimizing maintenance is very important for reducing the overall cost of freight and passenger transportation. This study presented in this chapter describes a methodology that extends the use of deformation monitoring instruments (e.g., fiber optic sensors (FO) and LVDTs) coupled with Electromagnetic (EM) surveying: Ground penetrating radar (GPR) and a time domain reflectometry (TDR) to monitor both the progression of ballast fouling and its effect on the deformation on the rail track. The methodology aims at creating an early warning system that would allow railway engineers to symptomatically assess the need for maintenance operations. This proposed methodology was tested on a full scale track model (FSTM) which comprises of 2.45 m rail supported by five ties embedded in a ballast layer. This test considered three common types of fouling: mineral fouling, clay fouling, and silica sand fouling. A comparison between rail settlement measurements and rail bending strain measured by FO sensors showed that FO sensors were incapable to provide an indication of track deterioration. In addition, results showed

a good correlation between EM and ballast physical properties (e.g., porosity, volumetric water content, fouling depth, fouling index (FI), clay fouling index (CFI), and non-clay fouling index (NFI). Experimental results also confirmed that EM survey results can be used to determine type of fouling material. Finally, implementing these technologies provide information for strategic and sustainable maintenance activities and it may eventually lead to the development of a reliable, systematic, continuous, and sustainable inspection methodology.

Keywords: Railway, ballast fouling, plastic deformation, GPR, TDR, fouling, dielectric permittivity, electrical conductivity, porosity.

4.1 Introduction and General Description

The need for a reliable, continuous, and remote monitoring routine for maintaining railway infrastructure has become a crucial factor in controlling the safety and the overall cost of the railway operations. Controlling the surface deformation of tracks is the main goal of rail maintenance (Lichtberger 2005; Liu et al. 2012). Track deformation is caused by a reduction in the load bearing capacity of ballast and subgrade layers. Track deformations reduce the load capacity of the rail line, force a reduction in velocity, reduce the comfort of riders, and increase the potential for derailments (Ahlf 2011). Therefore, the proper performance of the ballast in the rail structure is a crucial component in the transportation of freight and passengers by train.

Ballast layers serve several functions: distribute the train loads over a much larger area so that the subgrade soil can support it, provide rapid water drainage, prevent vegetation grows between tracks, and reduce the level of vibration created by the passing

trains (Ahlf 2011). However, ballast layers experience deterioration of its functions in proportion to the volume and weight of traffic, external contamination (car spelling, wind-blown material), ballast mineralogy, and absence of ballast maintenance (Ahlf 2011). Additionally, these mechanisms of deterioration may increase the generation of fine-grained particles leading to the reduction of load capacity, increase in compressibility, and a larger retention of moisture further reducing the shear strength of the ballast during dynamic loading. The combination of these deterioration mechanics is known as 'fouling.' This process compromises the structural integrity of the railway structure leading to large track deformations and ultimately to train derailment (Walter and Selig 1994; Indraratna et al. 2011).

It is reported that North American railroads spent more than $8.9 billion per year on maintenance operations (AAR 2013). Although the cost and effectiveness of track maintenance are associated to the frequency of track inspection (i.e., selective drilling and digging at intervals along the track), it is mainly based on the judgment and experience of rail professionals. There is no quantitative, mechanistic assessment of deterioration yet. Thus, there are risks of functional or mechanical failure between two inspection events or that the inspection may fail to properly evaluate the mechanistic mechanisms of the fouling process. For these reasons, a reliable, systematic, continuous, and sustainable inspection methodology needs to be developed, and demand for new technologies is increasing in the railway industry.

Deformation monitoring instruments (DMI) (e.g., fiber optic (FO) sensors and LVDTs) along with electromagnetic (EM) wave-based surveying techniques are proposed to monitor and manage the ballast fouling process. DMI can create a continuous sensing

array and provide a warning system for inspection and maintenance activities during the rail track service life. However, DMI can only monitor the symptoms but not the causes for ballast fouling. To better interpret the symptoms, it is required to properly evaluate the causes. For these reasons, it is proposed the deployment of (EM) wave-based surveying. Furthermore, combined EM methodology that uses time domain reflectometry (TDR - Ledieu 1986; Roth et al. 1990; Herkelrath 1991; Siddiqui and Drnevich 2000; Fratta et al. 2005) for calibrating the ground penetration radar (GPR) data, particularly in fouled ballast with high moisture content. The local collection of data using TDR will complement the results from GPR for the rapid profiling of the rail substructure. The combination of both local measurements (i.e., TDR) and global measurements (i.e., GPR) is expected to provide not only geometric but also internal material parameters that will generate quantitative data to better maintain the infrastructure. These two techniques are aimed to create the image of the electromagnetic-wave properties of the material within track cross-sections at critical spots identified by DMI. Coupling of these technologies provides information for strategic and sustainable maintenance activities and increases the safety of our national freight rail transportation network. The long term goal of the proposed methodology is to evaluate the rate of track deterioration so the risk of derailment along the track length is decreased by developing a comprehensive warning system.

The Full Scale Track Model (FSTM) is a prototype of railroad section aimed at characterizing both of the measured deformation, and the measured EM properties of the substructure due to the increase in amount of fouling in the ballast layer under laboratory controlled conditions. Figure 4.1 shows the FSTM that was constructed in the Structures and Materials Testing Laboratory at the University of Wisconsin-Madison. It is designed

to contain ballast, ties, and a rail section. It was built as wooden box that has the inside dimensions of 2.5 m in length, 1.7 m in width, and 0.9 m in height. The track consists of 2.45 m rail and 5 ties spaced 0.495 m apart. FSTM was build and tested to assess the hypothesis proposed in this study which is EM properties can be used to characterize ballast physical properties.

4.2 Assessment of Boundary Conditions on the FSTM Results

In order to study the influence of boundary conditions on the FSTM setup, four models with different geometry were created in ABAQUS. Finite element analyses were conducted by including 3 ties, 5 ties, 6 ties, and 7 ties (Figure 4.2). Table 4.1 is showing the material properties that were used in the analysis. Validation of this model is shown in Alsabhan (2013).

Table 4. 1 Materials Properties

Rail Properties		**Ties Properties**	
Spacing (m)	1.51	Spacing (m)	0.495
Cross sectional area (m^2)	$6.4 \cdot 10^{-3}$	Length (m)	2.6
Mass per unit length (kg/m)	50.4	Width (m)	0.229
Young's modulus (MPa)	207,000	Height (m)	0.178
Moment of inertia (m^4)	$2.04 \cdot 10^{-5}$	Young's modulus (MPa)	10,300
Ballast Properties		**Subgrade Properties**	
Resilient modulus (MPa)	290	Resilient modulus(MPa)	50
Poisson's Ratio	0.3	Poisson's Ratio	0.4
Density (kg/m^3)	1610	Density (kg/m^3)	2200

The analyses were conducted using the finite element package ABAQUS using a linear elastic model of materials with hexahedral 8-noded elements (C3D8). By taking the

advantage of symmetry, only half the track was modeled. A wheel load of 135 kN was used in the analysis. The displacements in the bottom of the subgrade were constrained in all direction, while for other ‘infinite and finite boundaries’ only the displacements normal to the plane were constrained to eliminate rigid body motion. Rails and ties were connected using tie constrains. Interaction between ties and ballast was modeled with contact elements having “hard” normal contact and tangential with friction coefficient of 0.35 while the interaction between any two geomaterials in contact was modeled with contact elements having “hard” normal contact (no penetration) and tangential with friction coefficient of 0.5.

The study of the effect of the number of ties on the deformational behavior of ballast. Figure 4.3 presents the calculated strains in the ballast layer beneath the point of load application along tie length for 3 ties, 5 ties, 6 ties, and 7 ties track. The 3-tie track model yields a maximum strain of 0.0011 while this strain decreases to 0.0007 as we increase the number of ties from 3 to 5, and it remains constant as we increase the number of ties increases to 6 and 7. These results show that using just 3 ties in the model influences the tie-ballast contact pressure. On the other hand, using 5 or more ties to simulate the field conditions is adequate.

Figure 4.4 summarizes the results of the effect of the number of ties on deformational behavior of the rail section along the longitudinal axis. The rail exhibits its highest deformation of about 0.00068 m with the 3-tie model, while similar to tie-ballast contact pressure it decreases to 0.00051 m as we increase the number of ties to 5, and the maximum deformation remains constant for the 6 and 7-tie model.

Based on the numerical evaluation conducted in the previous section supported by the literature review presented in Alsabhan (2013), the minimum number of ties to best simulate the real field conditions without getting influenced by the boundary conditions is 5 ties. Thus, this numerical analysis shows that boundary effects on the vertical deformation are insignificant at the center of the rail.

4.3 Materials

Three types of fouling in addition to a clean ballast layer will be investigated in this study. These fouling materials are: silica sand, kaolinite clay, and mineral fouling. AREMA # 25 ballast was used in all tests. Grain size distributions (ASTM D6913) of the studied materials are shown in Figure 4.5, and physical properties are shown in Table 4.2.

Table 4. 2 Index properties of ballast and fouling materials

Sample	D_{50} (mm)	C_u	C_c	G_s	LL (%)	PL (%)	n_B	Sand Content (%)	Fines Content (%)	USCS Symbol
AREMA #25	48	1.4	0.6	2.6	NA	NA	0.4	0	0	-
Silica Sand	0.28	1.6	0.9	2.66	NP	NP	-	100	0.33	SP
Kaolinite	-	-	-	2.63	49	35	-	0	100	CL
Mineral Fouling	1.5	15	0.4	2.67	-	-	-	98	0	SP

Note. NP = not plastic, NA = not applicable, D_{50} = median particle size, C_u = coefficient of uniformity, C_c = coefficient of curvature, G_s = specific gravity, LL = liquid limit, PL = plastic limit, n_B = porosity of ballast. Particle size analysis conducted following ASTM D 422, G_s by ASTM D 854, USCS classification by ASTM D 2487, and Atterberg limits by ASTM D 4318.

4.4 Specimen Preparation

Clean Ballast and Mineral Fouling. During field operations, ballast undergoes a process of densification that is controlled by the magnitude and the frequency of the traffic

load. For this reason, ballast layers were prepared in the FSTM with a targeted density of 15.5 kN/m^3 in an attempt to reproduce field conditions (Indraratna et al. 2005). The clean ballast and mineral fouling layer preparation includes:

1- Ballast is placed in 0.3 m lift.
2- Small vibrator tamper is used to compact ballast. All compaction is uniformly distributed so ballast layer is compacted to achieve 95 percent dry density (15.5 ± 0.3 kN/m^3).
3- Five ties are placed on top of the compacted ballast layer. The ties are spaced 0.495 m center to center.
4- Ballast is placed to fill up the voids between the ties until it reaches 0.5 m height from the bottom of the wooden box.
5- Small vibrator tampers is used to compact ballast until it reaches the desired density.
6- Double shoulder 11 inch tie plates are placed on top of each tie at 0.7 m from he left edge of the tie to the center of the plate.
7- 100 RE Rail with a length of 2.45 m rail is placed on top of the rail pads and secured with standard railway spikes.

Silica Sand. Fouled ballast specimens were prepared in the wooden box to simulate spillage contamination (e.g., spillage of coal dust and silica sand) by spreading the fouling material from the surface according to the following steps:

1- 0.2 m lift of clean ballast were prepared using the *Clean Ballast* procedure.

2- Silica sand was spread over the compacted clean ballast until all the voids were filled.
3- 0.1 m lift of clean ballast were placed on the top of the fouled ballast and prepared using the *Clean Ballast* procedure.
4- Steps 3 to 7 in the clean ballast procedure were performed to prepare the sample.
5- If required, water was evenly added from the top of the track.
6- For a full silica sand fouling depth, at the surface of the track silica sand was spread over the compacted ballast layer until all the voids were filled.

Clay Fouling. Fouled ballast samples were prepared in the wooden box to simulate the real field conditions of clay intrusion from the subgrade layer according to the following steps:

A. For 0.2 m clay fouling depth:
1- Kaolinite clay sample was mixed with water to obtain homogeneous water distribution.
1- Clean ballast was mixed with kaolinite clay and placed in the testing box until it reached 0.2 m depth. This mixing process simulates maintenance activities on railway track where tamping tides rearrange ballast particles mixed with fouling material (Ebrahimi et al. 2012).
2- Small vibrator tampers was used to compact the mixture using the *Clean Ballast* procedure.
3- 0.1 m lift of clean ballast were placed on the top of the fouled ballast and prepared using Clean Ballast procedure.

4- Steps 3 to 7 in the clean ballast procedure were performed to prepare the sample.

5- If required, water was evenly added from the top of the track.

B. For full clay fouling depth:

1- Rail, tie plates, ties, and 0.3 m depth of clean ballast samples were taking out of the testing box after the 0.2 m clay fouling depth experiment was done.

2- New kaolinite clay sample was mixed with water to obtain homogeneous water distribution.

3- 0.1 m lift of clean ballast was mixed with kaolinite clay and placed in the testing box.

4- Small vibrator tampers was used to compact the mixture using the *Clean Ballast* procedure.

5- Five ties are placed on top of the compacted mixture layer. The ties are spaced 0.495 m center to center.

6- A mixture of ballast and kaolinite clay is placed to fill up the voids between the ties until it reaches 0.5 m height from the bottom of the wooden box.

7- Steps 5 to 7 in the clean ballast procedure were performed to prepare the sample.

8- If required, water was evenly added from the top of the track.

4.5 FSTM Instrumentation

MicronOptics os3155 Fiber optic sensors were selected to provide bending strain measurements along the length of the rail. The os3155 is a rugged strain gage with integrated temperature compensation. Both strain and temperature compensation measurements are based on fiber Bragg grating (FBG) technology. The sensors were

installed in the mid span of the 2.45 meters rail using spot welding. Figure 4.6 and Figure 4.7 are showing FBG sensors locations and identification names. One FO was mounted on the bottom flange of the rail, and the other was mounted on the top portion of the rail's web to capture the maximum vertical bending strain in the rail. Data acquisition was conducted using MicronOptic sm130 optical sensing interrogator.

Linear Variable Differential Transformer (LVDT) is used to measure the vertical settlement of the rail. Three LVDTs were placed at three different locations on the rail surface. LVDT1 was placed at the same location as the further tie to the middle tie, LVDT2 was placed at the same location as the adjacent tie to the middle tie, LVDT3 was placed at the same location as the middle tie (Figure 4.8). The LVDTs were used to obtain the global settlement of the track and validate FO sensors measurements. Data acquisition was conducted using LabView data acquisition software.

GPR data were collected using a pulseEKKO PRO system with 450-MHz antennae. Raw GPR data was processed using MATGPR processing software. The data processing technique included time-zero correction, mean spatial filter, median spatial filter, and gain control function to improve the quality of the presentation and help in the interpretation.

Along with GPR data collection, TDR testing was conducted to calibrate the GPR data and to assess the EM properties of the FSTM. A Campbell TDR100 system (Campbell Scientific Inc. 2007) was used in this study with an impedance coaxial cable (Zo) = 50 Ω. PCTDR-V 2.08 software was used to control the TDR100 signal. The record length was 2048 points along with 4-signal stacking. Sacking was used to improve the

signal-to-noise ratio on the reflection waveforms. 0.4-m-long TDR probes, with separation of 0.05 m and diameter of 0.012 m, were driven into the ballast layer.

4.6 Load Transfer Mechanisms

In a rail track system, the wheel load from a train car is distributed through the rail, fastening system, ties, ballast, and sub-ballast to the foundation soil underneath. Thus, the high force applied on the rail is gradually reduced by the different track components before it reaches the foundation soil below the rail track system. Typical wheel loads used in today railway transportation systems vary from 53 kN for light rail passenger service to 174 kN for heavy haul trains in North America, and frequency from 5 up to 20 Hz (Selig et al. 1994). In this study a 5-Hz haversine 132 kN amplitude, bell-shaped loading pulse is used to simulate the traffic loading on ballast. $2 \cdot 10^5$ loading cycle was selected to simulate the traffic loading for a long-term. Loading was exerted on the track by using an MTS hydraulic actuator with a maximum capacity of 245 kN (55 kips).

4.7 Testing Program

The testing program was conducted to simulate the field conditions of a railway track geometric configurations and material conditions. Three types of fouling are being investigated: silica sand, clay, and mineral fouling. In addition, a clean ballast sample was conducted to be used as a reference for comparison. Tests were performed to obtain the effect of fouled materials type and depth on the track deformation and EM properties (e.g. electrical permittivity, and electrical conductivity) under traffic load. EM were measured for each test by means of GPR and TDR. Table 4.3 shows the change in testing parameters that were used in this study.

Table 4.3 FSTM completed testing matrix

Material	Total Depth (m)	Fouling Depth from bottom up (m)	Moisture Content	EM Survey		Deformation		FI (%)= P4+P200
				TDR	GPR	FO	LVDT	
Mineral Fouling	0.5	0.2	Dry	C	C	C	C	Equivalent to 26% FI (fouled)
			10%	C	C	C	C	
Silica Sand Fouling	0.5	0.20	Dry	C	C	C	C	Equivalent to 26% FI (fouled)
			10%	C	C	C	C	
	0.5	0.5	Dry	C	C	C	C	Equivalent to 26% FI (fouled)
			10%	C	C	C	C	
Kaolinite Fouling	0.5	0.20	10%	C	C	C	C	Equivalent to 27 % FI (fouled)
			30%	C	C	C	C	
	0.5	0.5	10%	C	C	C	C	Equivalent to 27 % FI (fouled)
			30%	C	C	C	C	
Clean Ballast	0.5	0	N/A	C	C	C	C	Clean

C: Completed

For each fouling material, four FSTM experiment were performed. Each experiment had $2 \cdot 10^5$ loading repetitions. The targeted total depth of each FSTM substructure is 0.5 m for all tests. Moisture was added to all fouled ballast experiment to investigate the effect of moisture on the track deformation and EM properties. Fouling depth and moisture varies. experiment were given Identification names listed in Table 4.4 to 4.7 based on the variance of moisture content, fouling depth, and loading repetitions that has been experienced by the sample.

Table 4.4 Silica sand fouling testing parameters

Identification name		Depth of Fouled Materials (m)	History of Loading Cycles (N)	Top Layer Moisture Content (%)	Bottom Layer Moisture Content (%)
Test	Sub-test				
S-1	Start	0.2	0	0	0
	End	0.2	200,000	0	0
S-2	Start	0.2	200,000	0	10
	End	0.2	400,000	0	10
S-3	Start	0.5	400,000	0	10
	End	0.5	600,000	0	10
S-4	Start	0.5	600,000	10	10
	End	0.5	800,000	10	10

Table 4.5 Kaolinite clay fouling testing parameters

Identification name		Depth of Fouled Materials (m)	History of Loading Cycles (N)	Top Layer Moisture Content (%)	Bottom Layer Moisture Content (%)
Test	Sub-test				
K-1	Start	0.2	0	0	10
	End	0.2	200,000	0	10
K-2	Start	0.2	200,000	0	30
	End	0.2	400,000	0	30
K'-1	Start	0.5	400,000	10	30
	End	0.5	600,000	10	30
K'-2	Start	0.5	600,000	30	30
	End	0.5	800,000	30	30

Table 4.6 Mineral fouling testing parameters

Identification name		Depth of Fouled Materials (m)	History of Loading Cycles (N)	Top Layer Moisture Content (%)	Bottom Layer Moisture Content (%)
Test					
M-1	Start	0.2	0	0	0
	End	0.2	200,000	0	0
M-2	Start	0.2	200,000	0	0
	End	0.2	400,000	0	0
M-3	Start	0.2	400,000	0	10
	End	0.2	600,000	0	10
M-4	Start	0.2	600,000	0	10
	End	0.2	800,000	0	10

Table 4.7 Clean ballast testing parameters

Identification name / Test		Depth of Fouled Materials (m)	History of Loading Cycles (N)	Moisture Content (%)
B-1	Start	0	0	0
	End	0	200,000	0
B-2	Start	0	200,000	0
	End	0	400,000	0
B-3	Start	0	400,000	0
	End	0	600,000	0
B-4	Start	0	600,000	0
	End	0	800,000	0

4.8 Results and Discussion

4.8.1 Measured Track Deformation

LVDT Analysis. Figure 4.9 shows the raw LVDTs deformation measurements. Plastic deformation, rate of plastic deformation, and the abrupt changes in the amount of plastic deformation during transition were selected to analyze the results. Clean ballast experiment showed the lowest values of deformation whereas, kaolinite clay fouled ballast exhibited the highest amount (δ >14 mm). According to Lichtberger (2005) standard settlement values for maintenance and operation thresholds are 12 mm and 14 mm respectively. As a result, this would give an immediate indication of the effect of fouling and repeated loads on the overall performance of the track.

A rapid increase of plastic deformation is taking place in the first thousands cycles of each experiment (e.g., S-1, K-1, M-1, and B-1). Ebrahimi (2011) defined this phase as the initial compaction phase (ICP) which is due to ballast particles rearrangements and densification. The rate of plastic deformation was calculated from the tangent slope of the tail of each experiment (e.g., at $1.9 \cdot 10^5 \leq N \leq 2 \cdot 10^5$) to eliminate the ICP influence as many of the experiments are continuation of a previous experiment.

Rate of plastic deformation of fouled ballast was normalized to the clean ballast conditions in Figure 4.10 (a). At the first $2 \cdot 10^5$ cycles (e.g., S-1, K-1, and M-1) of each experiment, rate of plastic deformation showed a significant increase relative to the clean ballast condition. However, with the increase of loading cycles the rate of plastic deformation decreases. This observation might be contributed to the effect of shakedown and densification, in which the increase of load cycles and associated deformation decreases the void ratio, and increases the density causing eventually the stiffness to increase (Indraratna et al. 2011). A comparison between different types of fouling materials effect on rate of plastic deformation *versus* number of loading repetitions is shown in Figure 4.10 (b). Generally, ballast fouled with kaolinite clay showed higher values than other fouled materials, which highlights the drastic effect of fines passing sieve #200 on the overall performance of the track.

The abrupt change (jumps) in amount of plastic deformation during transition is associated with the increase of moisture content in experiments S-2, S-4, K-2, K-4, and M-3 or depth of fouling materials in Experiment S-3. Figure 4.11 illustrates the combined analysis of the abrupt change in amount of plastic deformation for fouled ballast normalized to the clean ballast condition. To illustrate the effect of changing moisture content on the overall performance of the track, a comparison was plotted in Figure 4.12 (a). This comparison shows that the increase in moisture content causes a rise in the amount of plastic deformation that ranges from 1.2 to 2.1 relative to the clean ballast condition. Ebrahimi (2011) determined the soil water characteristic curves (SWCC) of fouling materials (Figure 4.13). These curves help in assessing the effect moisture on the deformational behavior of fouled ballast. Ebrahimi (2011) also reported that the

deformational behavior of fouled ballast is function of suction in unsaturated fouling materials. Suction changes the forces acting at the contact points. Suction values as high as 2000 kPa are associated with moisture content of about 3% for mineral and silica sand fouling and with moisture content of about 14 % for clayey fouling materials. These values were found to be the threshold moisture content between for increasing in the rate of plastic deformation (i.e., initial compaction phase - ICP) and for an exponential increase in the rate of plastic deformation (i.e., fouling impact phase - FIP). Furthermore, increasing moisture content of the fouling phase may increase the potential of excess pore water generation during cyclic loading resulting in a sudden reduction of shear strength and an increase in ballast deformation.

Similarly, a comparison that shows the effect of increasing fouling depth is plotted in Figure 4.12 (b). It is noticed that increasing fouling depth reduced the shear strength of the system which resulted in increasing the amount of plastic deformation. However, increasing fouling depth in experiment S-3 stiffened the track and reduced the amount of plastic deformation around 5% relative to experiment S-2. This is because filling up all the voids with silica sand in experiment S-3 increased the confining pressure and density of the specimen that caused stiffness incase and thus a noticeable decrease of plastic deformation is observed. Generally, Figures 4.12 (a) and (b) showed highest jumps of plastic deformation is at the kaolinite clay fouling, then mineral fouling, and the lowest amount of plastic deformation was at the silica sand fouling. In essence, the jumps of plastic deformation is controlled by the shear strength of the ballast layer which is controlled by the shear strength of fouling materials at the ballast particles contact points.

FO Sensors Analysis. FO sensors measurements were expected to provide a continuous real time monitoring. However, FO strain measurements did not provide indication of track deterioration due to cyclic loading, moisture content, and fouling depth. In essence, all FO measurements exhibited a constant pattern throughout the testing program. Figure 4.14 show a sample of FO sensors measurements. This is because FSTM rail is believed to be settling as a rigid body. In Figure 4.15 Note there is no change in rail curvature; hence no change in bending strains. This can be proven by calculating the rail's curvature as follow:

$$\delta = LVDT3 - LVDT1 \quad (4.1)$$

$$\theta = 180 - 2 \cdot \tan^{-1}\left(\frac{L}{2\delta}\right) \quad (4.2)$$

$$\kappa = \frac{1}{\rho} = \frac{1-\cos(\theta)}{\rho} \quad (4.3)$$

where, δ is net deflection due to rail bending, θ is angle of curvature, ρ is radius of curvature, and κ is the curvature. Chapter 6 is focused on discussing this matter in details.

4.8.2 Measured EM Properties

Two EM properties were investigated in this section, relative dielectric permittivity (ε_r) and electromagnetic conductivity (σ). A typical Processed GPR radargram images, TDR and GPR traces are shown in Figure 4.16. ε_r were calculated out of TDR and GPR traces taken at the middle of the FSTM at the horizontal position 1.2 m to ensure measurements consistency. ε_r ranged from 3 to 4 for all FSTM top layer with no previous loading history indicating an open voided clean ballast layer (Alsabhan et al. 2013). Measured values of ε_r versus number of loading repetitions are showing in Figure 4.17. TDR and GPR measurements are showing a similar pattern as the theoretical values

(Topp et al. 1980; Roth et al. 1990; Wensink et al. 1993; Benson and Bosscher 1999). Increase of loading repetitions caused an increase in ε_r. Abrupt change in ε_r during transition is due to the increase of volumetric water content and depth of fouling (Alsabhan et al. 2013). GPR trace calculations showed two distinct reflections corresponding to a top and a bottom layer in the FSTM (Figure 4.16). The bottom layer of the FSTM showed a higher values than the top layer as an indication of a higher fouling content in the bottom layer. Whereas, TDR measured the combined effect of the two layers due to the insignificant differences in the relative dielectric permittivity between the two layers (Alsabhan et al. 2013).

At N= $4 \cdot 10^5$ Kaolinite clay fouled ballast had a lower relative dielectric permittivity corresponding to the synthetic maintenance simulation, ballast layer in K'-1 was disturbed and re-compacted again. The lower value and increased value of relative dielectric permittivity corresponds to the improved ballast stiffness and the loss of stiffness after that, respectively.

Effect of loading repetitions on σ is shown in Figure 4.18. The conductivity of ballast fouled with kaolinite ranges between 0.0075 S/m to 0.0105 S/m depending on the volumetric water content. Whereas the σ of ballast fouled with silica sand and mineral fouling ranges between 0.0032 S/m to 0.0075 S/m for all the tested volumetric water contents. The electrical conductivity of the ballast fouled with kaolinite is an order of magnitude greater than the electrical conductivity of ballast fouled with silica sand. Furthermore, the increase of moisture content caused an abrupt increase in electrical conductivity due to the hydration of excess cations and anions dissolved in the pore fluid. However, interestingly, electrical conductivity increased proportionally with loading

repetitions indicating a similar effect of porosity, as a result of plastic deformation, on electrical conductivity. Santamarina and Klein (2001) described that electrical conductivity is a function of electrolyte, porosity, and degree of saturation, in a low surface medium.

4.8.3 Relationship between EM Measurements and Ballast Physical Parameters

Relative Dielectric Permittivity vs. Porosity. The relationship between relative dielectric permittivity and porosity is illustrated in Figure 4.19. The results show an overall reduction in relative dielectric permittivity with the increase of porosity. Similar responses are observed within each of the materials but with different trend. This difference in response within different material may represent different mineralogy and grain size distributions.

Relative Dielectric Permittivity vs. Volumetric Water Content. A linear relationship between relative dielectric permittivity and volumetric water content was found in Figure 4.20. In essence, the increase of volumetric water content increases the relative dielectric permittivity. This is because relative dielectric permittivity varies between 1 for air, 3 to 8 for most geological materials, and 80 for water. The low relative dielectric permittivity of geological materials compared to water makes relative dielectric permittivity of moist soils and rocks highly dependence on the volumetric water content of soil (Siddiqui and Drnevich 2000). As a result, relative dielectric permittivity can be successfully used to predict volumetric water content in railway substructures.

Relative Dielectric Permittivity vs. Fouling Depth. The variation of relative dielectric permittivity with different fouling depths is shown in Figure 4.21. An increase of the relative dielectric permittivity is associated with the increase of fouling depth at different volumetric contents and loading repetitions. This is because the increase in fouling layer thickness

decreases the porosity in the ballast layer and as a result the relative dielectric permittivity increases.

Relative Dielectric Permittivity vs. FI, NCF, and CFI. Several parameters are used for evaluating the degree of ballast fouling in assessing the physical condition of the railway structure. Fouling index “FI” described by Selig and Walters (1994), the sum of percentage of ballast passing sieve No. 4 and sieve No. 200, is the most common parameters employed for assessing the fouling condition of ballast. Ebrahimi (2011) introduced a non-clay fouling index (NFI) and a clay fouling index (CFI) to account for the factors affecting the plastic deformation to modify FI, e.g., moisture, Atterberg limits (PL and LL), and % of P200. The correlation obtained between FI, NFI, and CFI versus relative dielectric permittivity is shown in Figure 4.22. Generally, the relationships indicates that the increase of fines and moisture content, increases the value of the relative dielectric permittivity. The strongest correlation is with NFI with a correlation coefficient 0.86, then it was with CFI with a correlation coefficient of 0.7, and finally it was with FI with a correlation coefficient of 0.58.

Electrical Conductivity vs. FI, NCF, and CFI. The calculated electrical conductivities presented in Figure 4.18 are plotted against FI, NFI, and CFI in Figure 4.23. Data do not show strong correlation against σ and FI in Figure 4.23 (a). However, using Ebrahimi’s proposed fouling indices, NFI and CFI, a strong correlation was found as shown in Figures 4.23 (b) and (c). Generally, NFI and CFI correlate better with σ because they account for the factors affecting the σ such as the presence of hydrated excess ions dissolved in the pore fluid, and surface conduction (through Atterberg limits and fine content - i.e., P200).

Combining relative dielectric permittivity measurements to predict NFI and electrical conductivity to predict CFI will allow to capture the information needed to assess ballast fouling in a railway track. This new approach may open new options on the development of maintenance techniques.

4.8.4 Ground Truthing

Visual and geotechnical investigation was performed on each FSTM experiment after $8 \cdot 10^5$ loading repetitions. Figure 4.24 shows a vertical profile of the FSTM. Two unique layers were found consistent with GPR results. Ground truthing the FSTM has successfully verified GPR and TDR results. The particle size distributions of clean and fouled ballast are shown in Figure 4.25. Clean ballast had a maximum size distribution of 63mm, whereas fouled ballast was 50.8 mm. Fouling index was found to be equal to 32.4 % with an increase of 6.4 % than the induced percentage due to particle breakage. Table 4.8 contains the thickness, fouling index, and moisture content of each layer.

Table 4.8 Index properties of fouled ballast after N= $8 \cdot 10^5$

Sample	D_{50} (mm)	C_u	C_c	G_s	Top Layer Depth (m)	Top Layer Depth (m)	P# 4 (%)	P# 200 (%)	FI (%)	Moisture Content (%)
Clean Ballast	48	1.3	0.9	2.67	0.5	NA	NA	NA	NA	NA
Silica Sand Fouling	28	213	4.7	2.6	0.3	0.19	30.56	1.86	32.4	11.2
Kaolinite Clay Fouling	32	NA	NA	2.63	0.3	0.2	14.8	13	27.8	28.6
Mineral Fouling	32	175	3.22	2.67	0.3	0.17	27	0.96	28	10.75

Note. D_{50} = median particle size, C_u = coefficient of uniformity, C_c = coefficient of curvature, G_s = specific gravity, P# 4 = passing sieve #4, P# 200 = passing sieve #200, FI= fouling index. Particle size analysis conducted following ASTM D 422, and G_s by ASTM D 854.

4.9 Summary and Conclusions

Full Scale Track Model (FSTM) was developed to assess the methodology of creating an early warning system that would allow railway engineers to develop a symptomatic approach to ballast maintenance procedures. The methodology extends the use of deformation monitoring instruments (e.g., fiber optic (FO) sensors and LVDTs) coupled with Electromagnetic (EM) surveying: Ground penetrating radar (GPR) and a time domain reflectometry (TDR). FSTM aimed at characterizing measured deformation, and EM properties of railway substructure with variance parameters such as: fouling type, fouling depth, moisture content, and number of loading repetitions.

FSTM deformation results indicate that railway track is settling as a rigid body and a special consideration should be taken into account when instrumenting the rail. Furthermore, FO only measured constant strains values and did not provide any indication of plastic strain accumulation in the ballast layer with the increase of loading repetitions. Whereas, LVDTs settlement measurements reflected the amount and rate of plastic deformation accumulated with the increase of loading repetitions. FSTM fouled with kaolinite clay showed the highest deformation among all experiments, whereas FSTM with a clean ballast showed the lowest. Indicating that shear strength of the ballast layer is controlled by the shear strength of fouling materials at the ballast particles contact points. Abrupt increase in track deformation is noticed with the increase of moisture content. It is believed that increasing moisture content in fouling materials between ballast particles may increase the potential of excess pore water generation under cyclic loading may resulting in a sudden reduction of shear strength and an increase in ballast deformation.

EM results shows that an increase in loading repetitions causes an increase in relative dielectric permittivity. The greater the plastic settlement in the ballast layer is, the lower the porosity becomes and as a result the relative dielectric permittivity increases. Abrupt increases in relative dielectric permittivity is due to the increase of volumetric water content and depth of fouling. GPR trace analysis showed two distinct reflections corresponding to a top and a bottom layer in the FSTM. The bottom layer of the FSTM showed a higher values than the top layer as an indication of a higher fouling content in the bottom layer. EM results shows that TDR can be successfully used to calibrate GPR data. In addition, the relative dielectric permittivity ranges from 3 to 4, whereas the electrical conductivity is very low and mainly constant for a clean ballast layer. Electrical conductivity was used successfully differentiate between various types of ballast fouling. Good correlations were found between EM properties and (a) porosity, (b) volumetric water content, (c) fouling depth, (d) fouling index, (e) non-clay fouling index (f) and clay fouling index. Visual and geotechnical investigation was performed on each FSTM experiment after 8·105 loading repetitions. Ground truthing the FSTM has successfully verified GPR and TDR results. The combination of rail track deformation and ballast fouling properties measurements provide an opportunity to assess not only the effect but also the cause of the complex rail track structure deterioration process.

Acknowledgements

Financial support for this study was provided by the Center for Freight Infrastructure Research and Education (C-FIRE) and the King Saud University (KSU – Saudi Arabia). Their support is greatly appreciated. Xiaodong Wang, William Lang, Tolga Dolcek, and Liangquan Wang (David) helped in the development of this work.

References

Ahlf, R. E., 1975. “M/W costs: how are they affected by car weight and the track structure”, Railway Track and Structures, pp. 34-37 and pp. 90-92.

Ahlf, R. E., 2011. “Maintaining, re-habitation, and upgrading conventional railroad track-ballast”, unpublished short course, University of Wisconsin-Madison.

Al-Qadi, I., Xie, W., and Roberts, R., 2008, “Scattering analysis of ground-penetrating radar data to qualify railroad ballast contamination,” NDT&E International, Elsevier, Vol. 41, pp.441–447.

Alsabhan, A. H, 2013. “Development of testing tools for warning system and inspection for maintenance of freight railways”. Master’s thesis, Department of Civil and Environmental Engineering, University of Wisconsin, Madison.

American railway engineering and maintenance of way association (AREMA), 2006. “Economics of railway engineering and operations – construction and maintenance operations” manual for railway engineering, Vol. 4 (16), Part 10.

Association of American railroads (AAR), 2012. “Total annual spending 2011 data,” Available from: https://www.aar.org/Fact%20Sheets/Safety/2013-AAR_spending-graphic-fact-sheet.pdf#search=Total%20annual%20spending

Benson, C. H., and Bosscher, P. J., 1999. “Time-domain reflectometry (TDR) in geotechnics: a review,” Nondestructive and Automated Testing for Soil and Rock Properties, ASTM STP Vol.1350, pp. 113-136

Clark, M. R., Gillespie, R., Kemp, T., McCann, D. M., and Forde, M. C., 2001. “Electromagnetic properties of railway ballast,” NDT & E International, Vol. 34, pp. 305-311.

Ebrahimi, A., 2011. “Deformational behavior of fouled railway ballast.” PhD thesis, Department of Civil and Environmental Engineering, University of Wisconsin, Madison.

Fratta, D., Alshibli, K. A., Tanner, W. M., and Roussel, L., 2005. “Combined TDR and P-wave velocity measurements for the determination of in situ soil density-experimental study,” Geotechnical Testing Journal, Vol. 28, pp. 553.

Herkelrath, W. N., Hamburg, S. P., and Murphy, F., 1991. “Automatic, real - time monitoring of soil moisture in a remote field area with time domain reflectometry,” Water Resources Research, Vol. 27, pp. 857-864.

Indraratna, B., Lackenby, J., and Christie, D., 2005. “Effect of confining pressure on the degradation of ballast under cyclic loading, Geotechnique,” Vol. 55(4), pp.325–328.

Indraratna, B., Salim, W., and Rujikiatkamjorn, C., 2011. Advanced rail geotechnology-ballasted track, CRC Press, Taylor & Francis Group, London, UK.

Indraratna, B., Tennakoon, N. C., Nimbalkar, S. Shrawan. and Rujikiatkamjorn, C., 2013. “Behaviour of clay-fouled ballast underdrained triaxial testing,” Geotechnique: International Journal of Soil Mechanics, Vol. 63 (5), pp. 410-419.

Jeffs, T., and Marich, S., 1978. “Ballast characteristics in the laboratory,” Conference on Railway Engineering, Perth, pp.63–76.

Keene A. K., 2012. “Mitigating ballast fouling impact and enhancing rail freight capacity”. Master’s thesis, Department of Civil and Environmental Engineering, University of Wisconsin, Madison.

Kerr, A. D., 2003. Fundamentals of railway track engineering, Simmons-Boardman Books, Inc., Omaha, Nebraska.

Ledieu, J., De Ridder, P., De Clerck, P. and Dautrebande, S., 1986. “A method of measuring soil measuring soil moisture by time-domain reflectometry,” Journal of Hydrology, Vol. 88, pp. 319-328.

Lichtberger, B., 2005. Track compendium. Hamburg: Eurailpress, Tetzlaff-Hestra GmbH and CO. KG.

Liu, X., Saat, M., and Barkan, C., 2012. “Analysis of causes of major train derailment and their effect on accident rates,” Transportation Research Record: Journal of the Transportation Research Board, vol. 2289, pp. 154-163.

Narayanan R. M., Kumke, C. J., Li, D., 1999. “Railroad track monitoring using ground penetrating radar: simulation study and field measurements,” In SPIE's International Symposium on Optical Science, Engineering and Instrumentation, pp. 243-251.

Roth, K., Schulin, R., Flühler, H., and Attinger, W., 1990. “Calibration of time domain reflectometry for water content measurement using a composite dielectric approach,” Water Resources Research, Vol. 26, pp. 2267-2273.

Santamarina, J. C., Klein, K. A., and Fam, M. A., 2001. Soils and waves: particulate materials behavior, characterization and process monitoring, J. England: John Wiley and Sons Ltd.

Selig, E. T. and Waters, J. M., 1994, Track Geotechnology and Substructure Management. Thomas Telford, New York, NY.

Siddiqui, S. I., Drnevich, V. P., and Deschamps, R. J., 2000. “Time domain reflectometry development for use in geotechnical engineering,” ASTM Geotechnical Testing Journal, Vol. 23, pp. 9-20.

Stewart, H. E. and Selig, E. T., 1982. “Predicted and measured resilient response of track,” Journal of the Geotechnical Engineering Division, ASCE, Vol. 108(GT11), pp. 1423–1442.

Topp, G., Davis, J., and Annan, A., 1980. “Electromagnetic determination of soil water content: measurements in coaxial transmission lines,” Water Resources Research, Vol. 16, pp.574-582.

Wensink, W. A., 1993. “Dielectric properties of wet soils in the frequency range 1-3000 MHz,” geophysical prospecting,” Vol. 41, pp. 671-696.

Figures

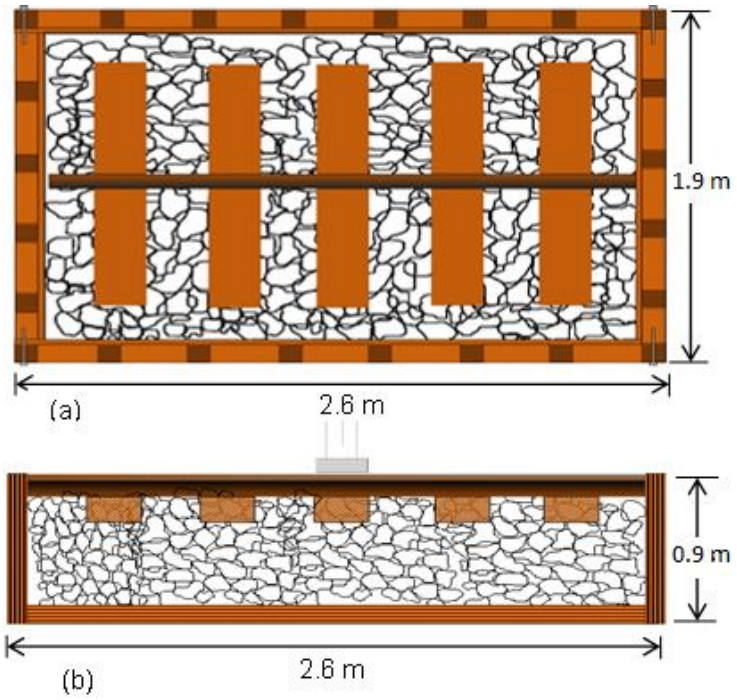

Figure 4. 1 Full Scale Track Model (FSTM), (a) Plane view; (b) Side view

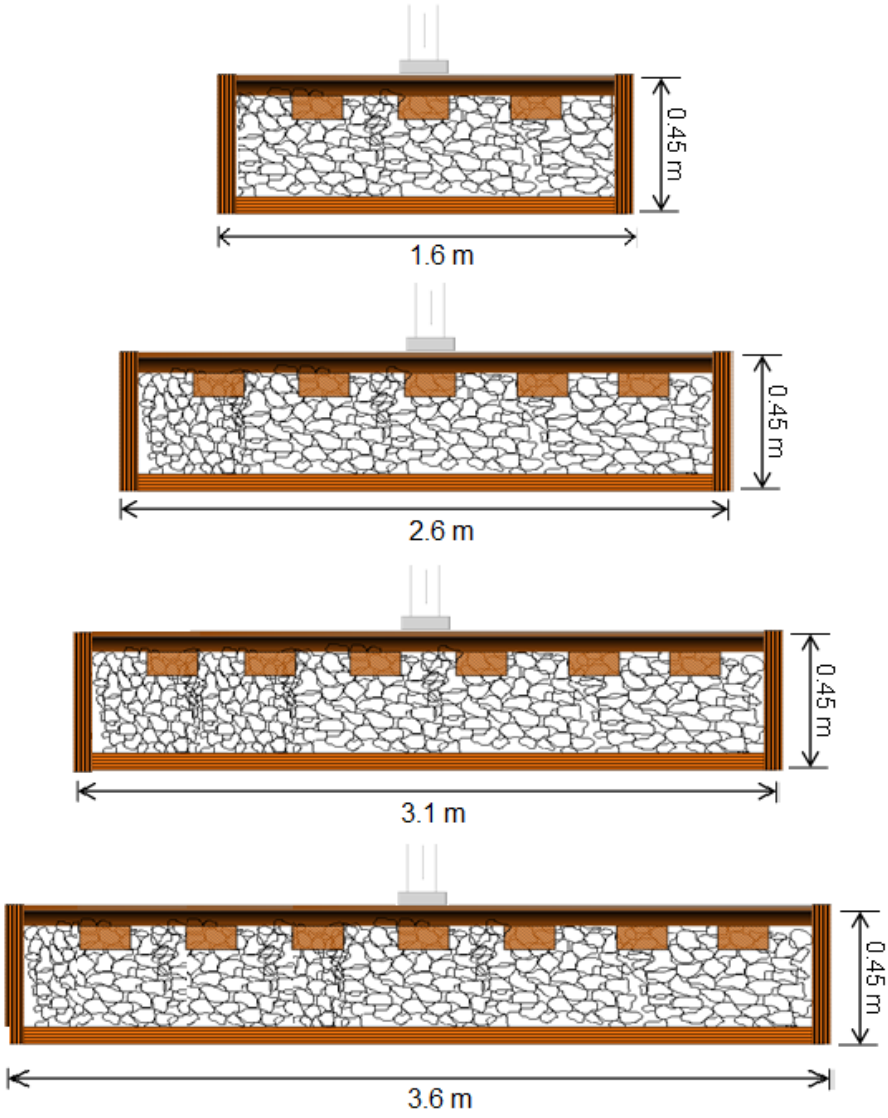

Figure 4. 2 Side View of Modeled FSTM Dimensions with 3 ties, 5 ties, 6 ties, and 7 ties. Tie spacing =0.495 m

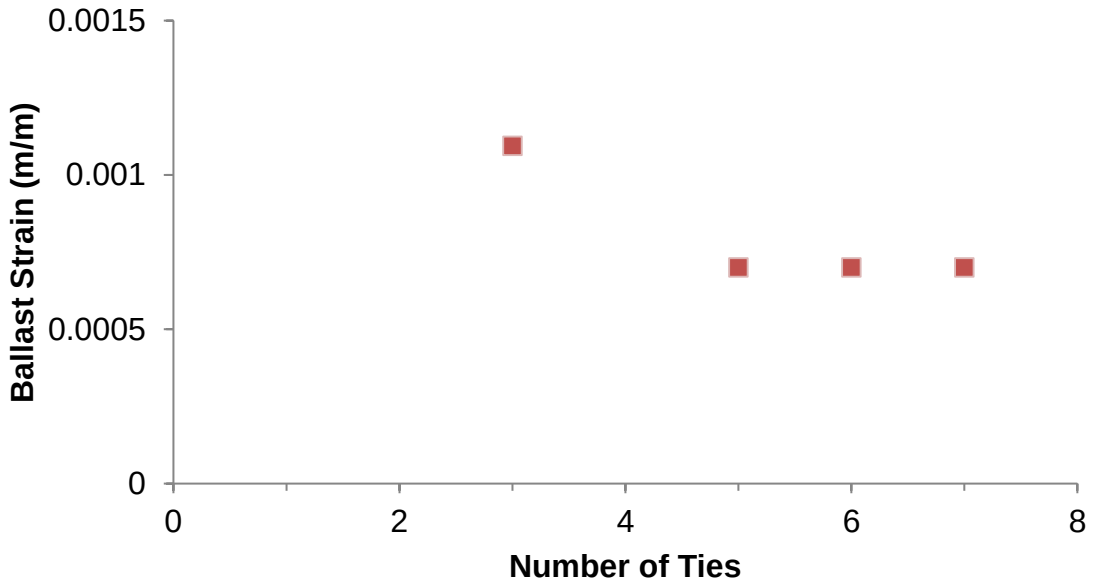

Figure 4.3 Effect of Number of Ties on Deformational Behavior of Ballast

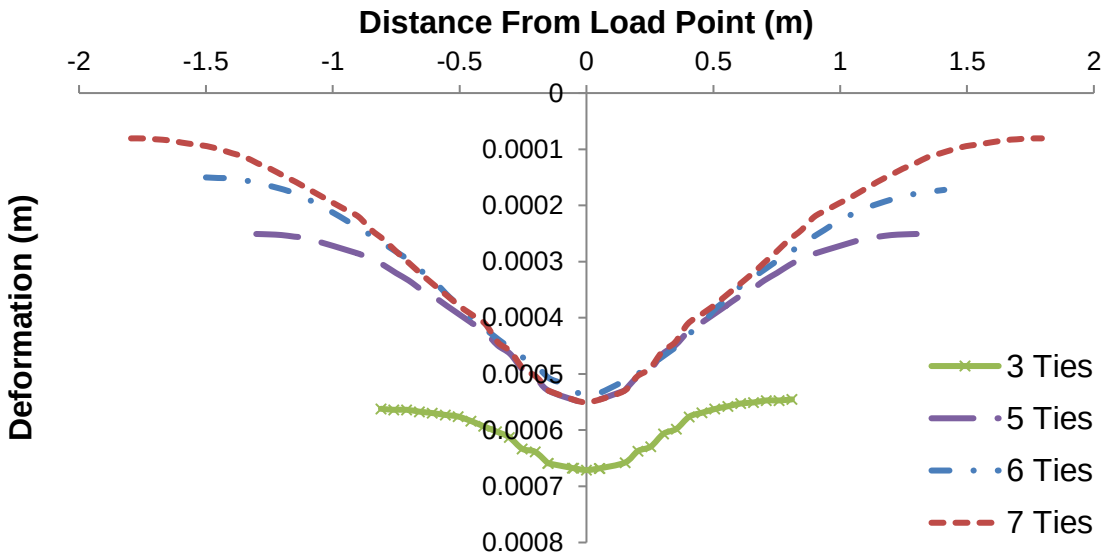

Figure 4. 4 Vertical Rail Deformations

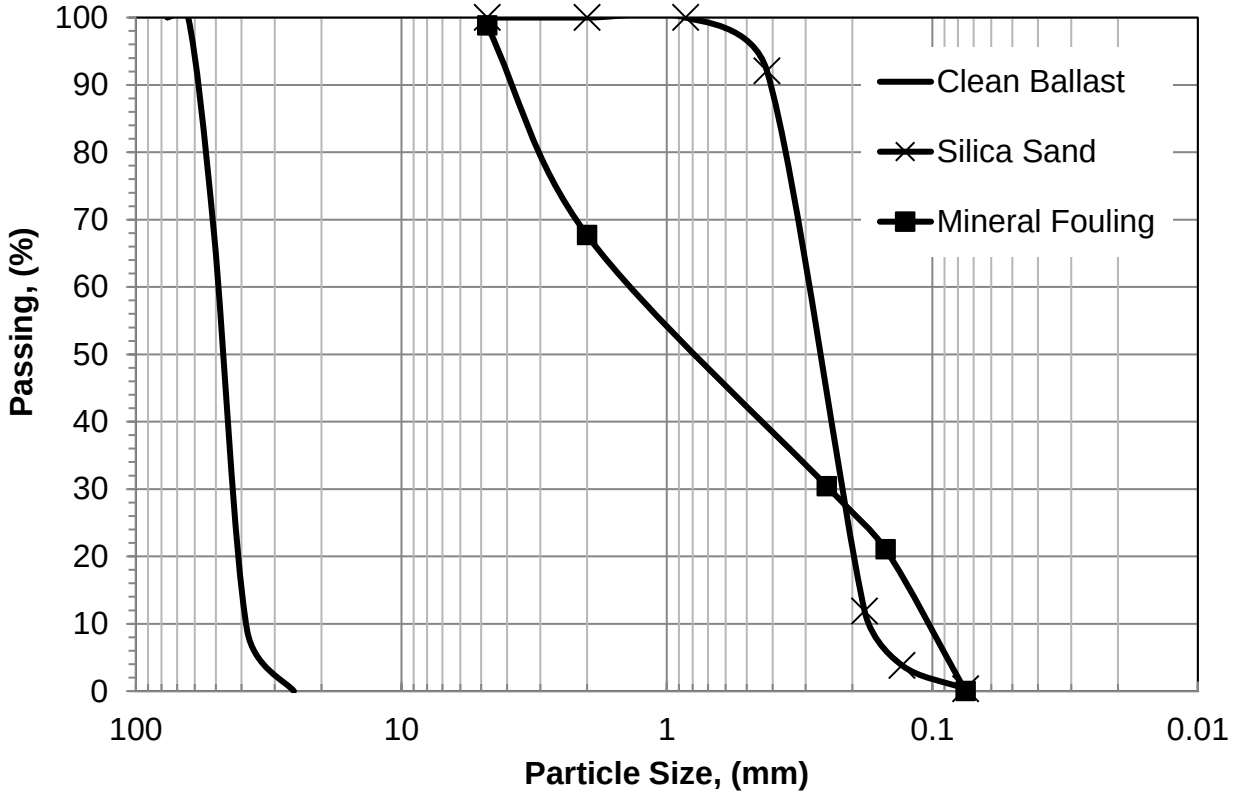

Figure 4. 5 Particle size distributions of ballast (AREMA # 25), silica sand, and mineral fouling

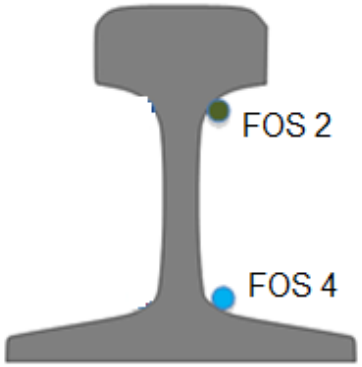

Figure 4. 6 FO sensors identification labels

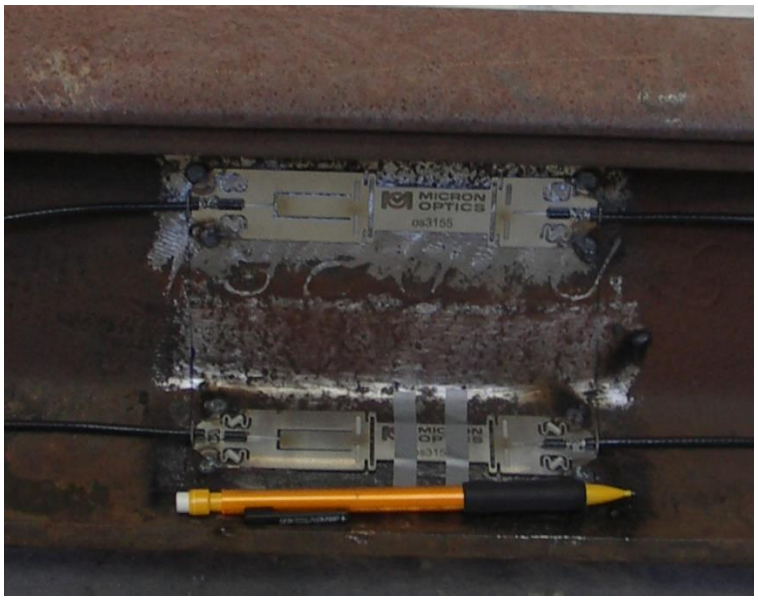

Figure 4.7 FO sensors locations on the rail

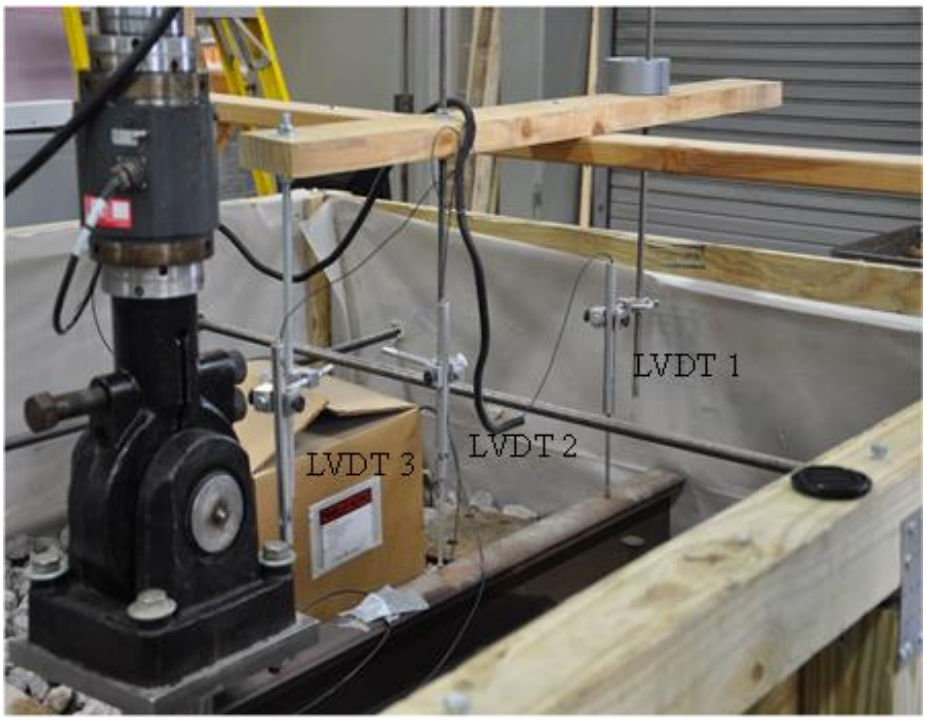

Figure 4. 8 Vertical Rail Deformations Measured with LVDTs

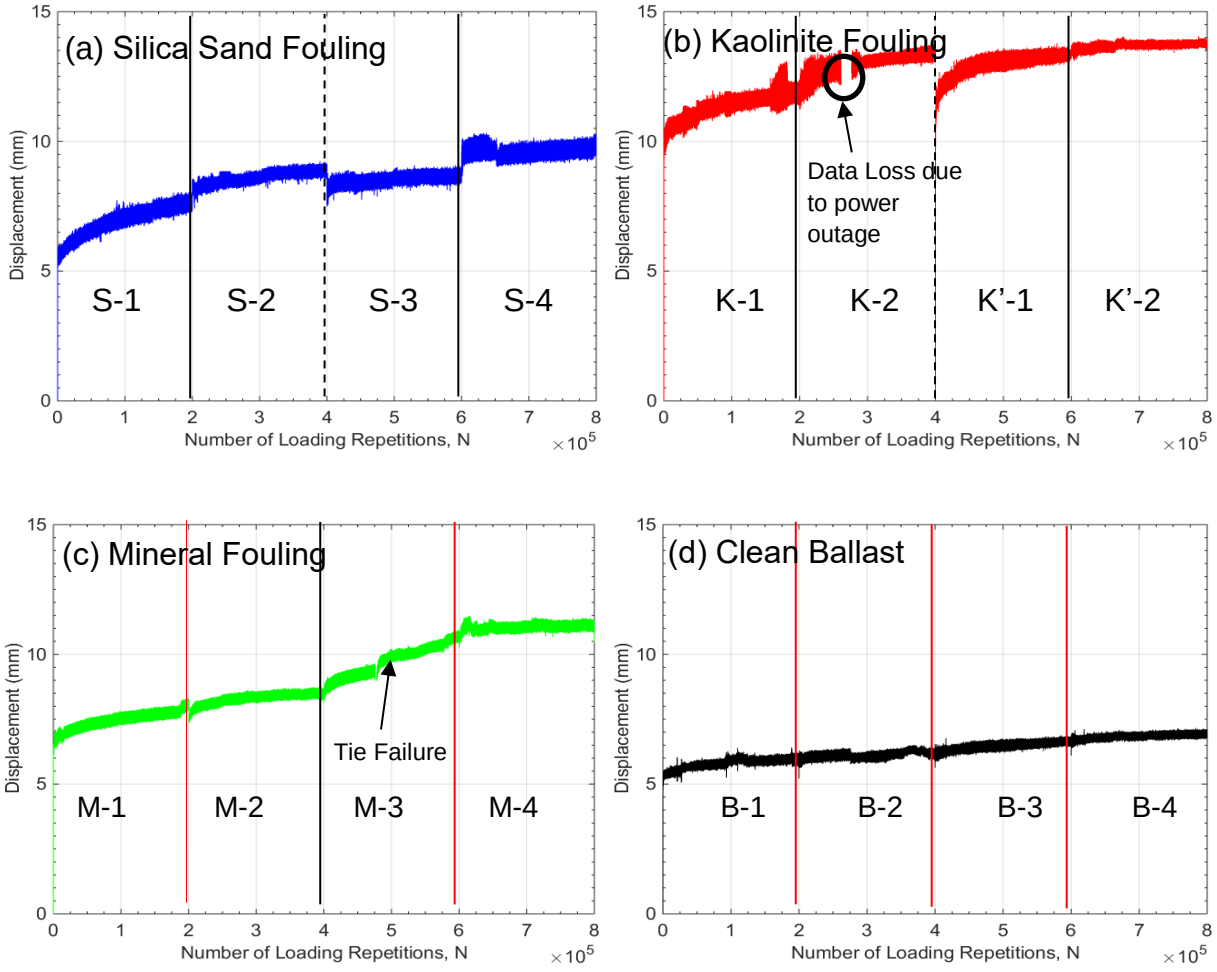

Figure Key

——— Change in Moisture Content

------ Change in Fouling Depth

——— No Change

Figure 4. 9 LVDT raw deformation measurements. (a) Silica sand fouling, (b) Kaolinite clay fouling, (c) Mineral Fouling, (d) Clean ballast.

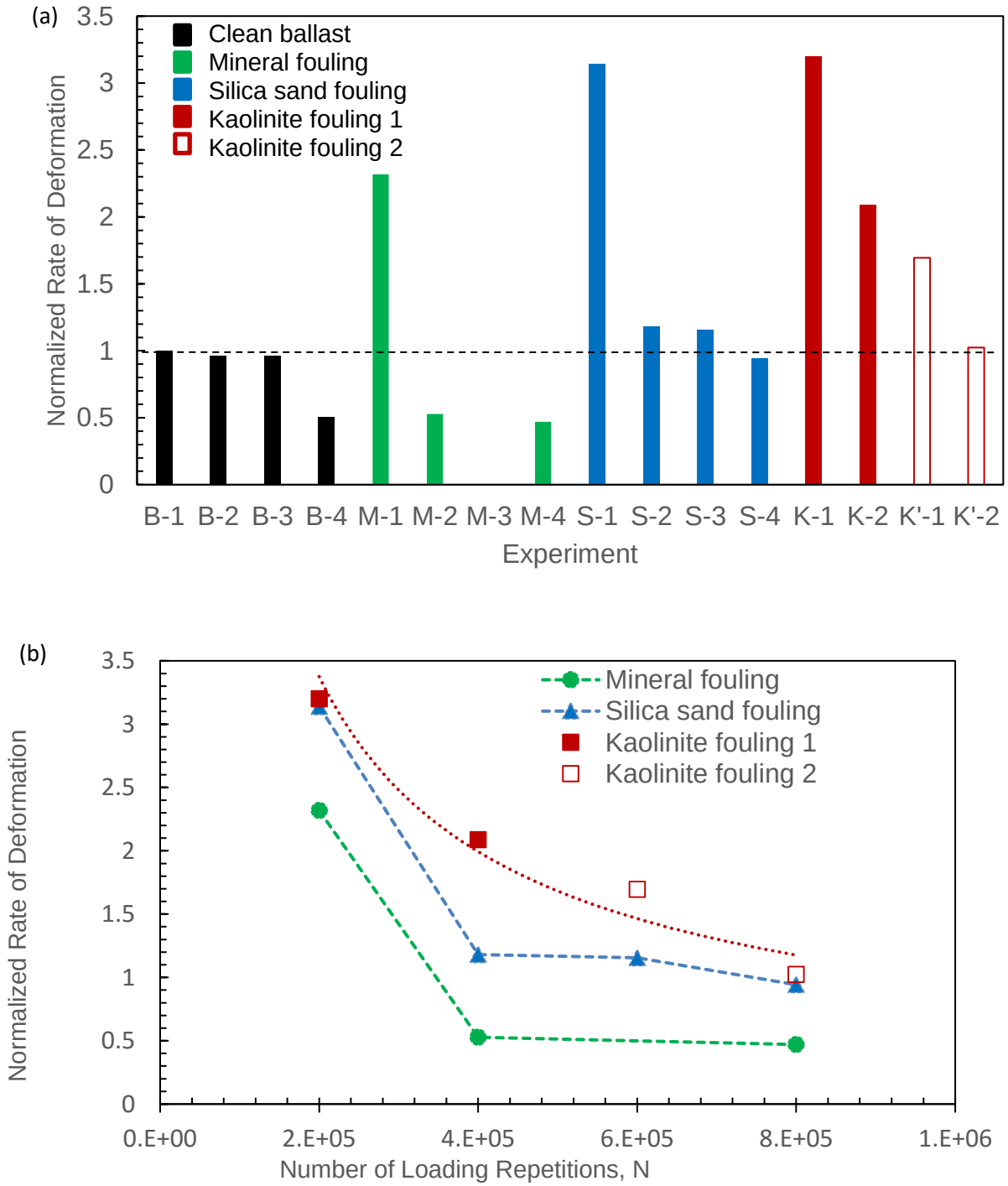

Figure 4.10 Combined analysis of: (a) Normalized rate of plastic deformation, and (b) Relationship between normalized rate of plastic deformation and loading cycles.

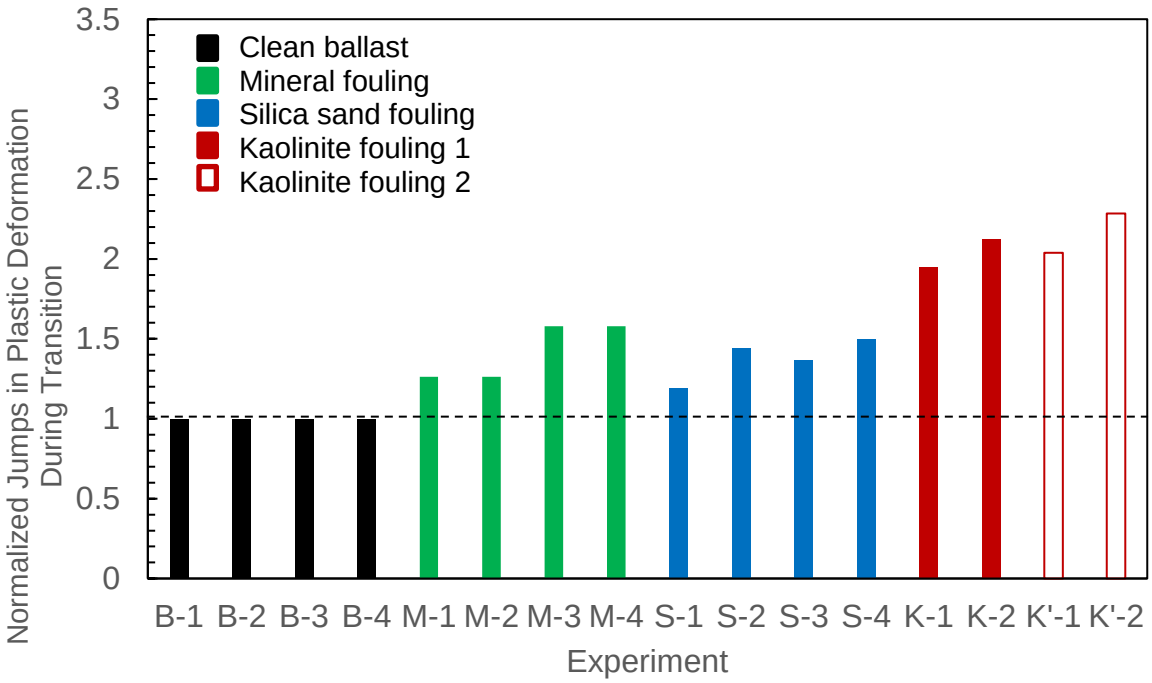

Figure 4.11 Combined analysis of normalized jumps of plastic deformation.

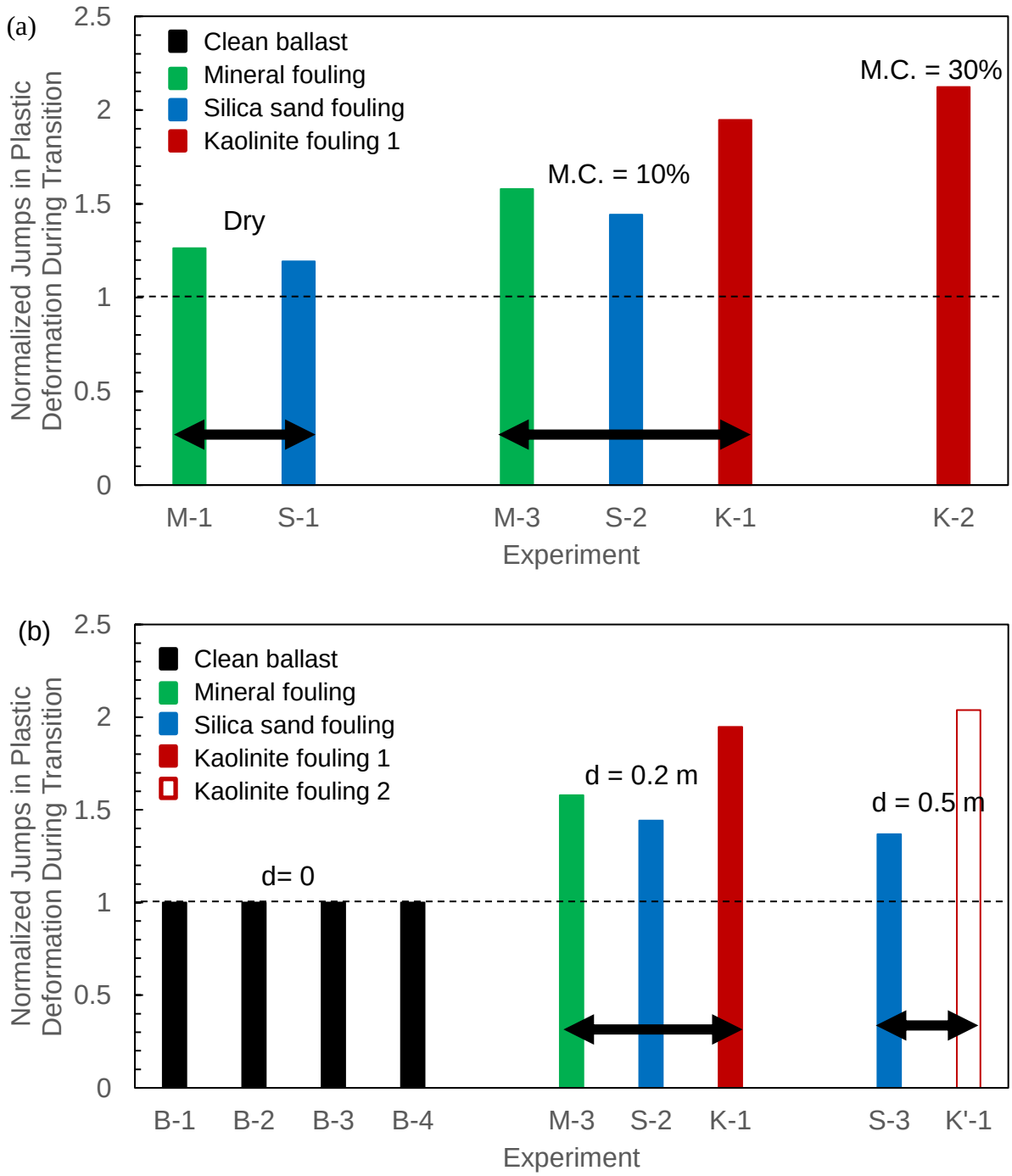

Figure 4.12 Comparison of normalized jumps of plastic deformation due to: (a) Change in moisture content (M.C), (b) Change in depth of fouling (d).

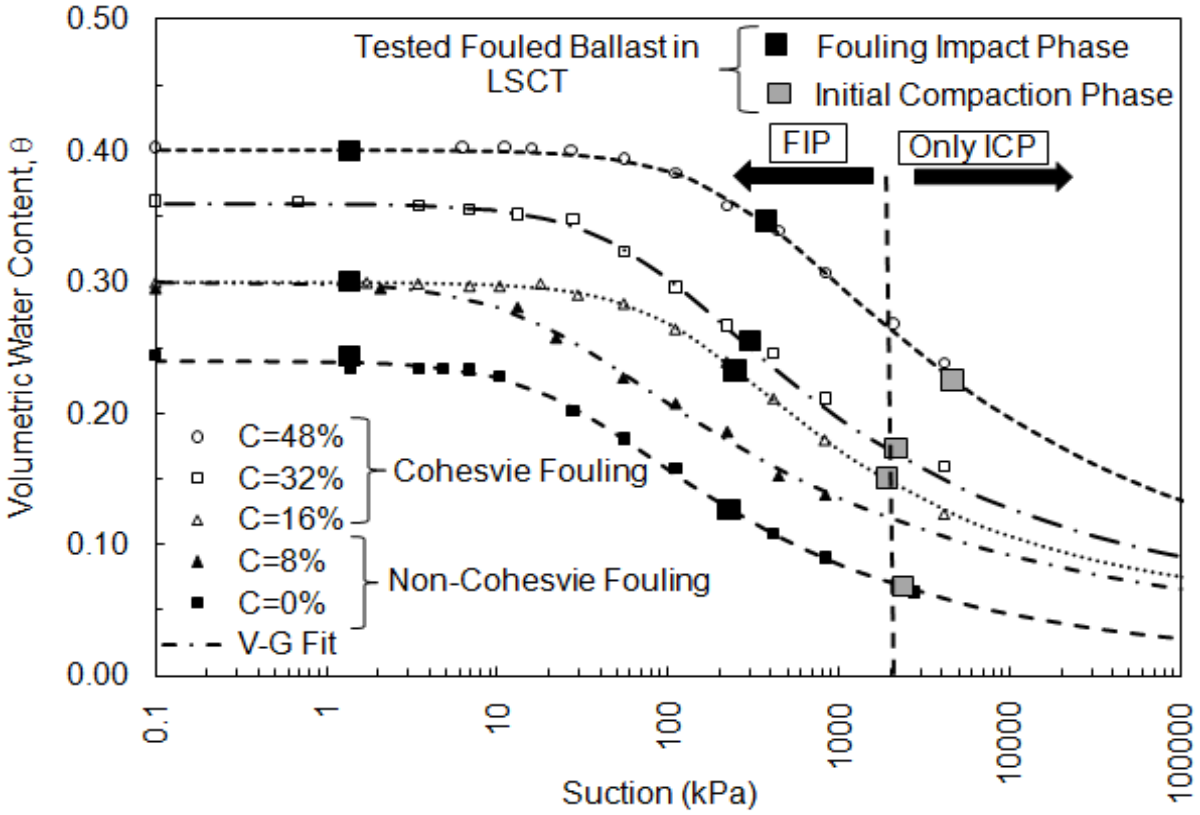

Figure 4.13 Defined Zone for Deformational Behavior of Fouled Ballast in ICP and FIP in the Soil Water Characteristics Curves of Fouling Materials (Note: C=clay fraction) (Ebrahimi 2011).

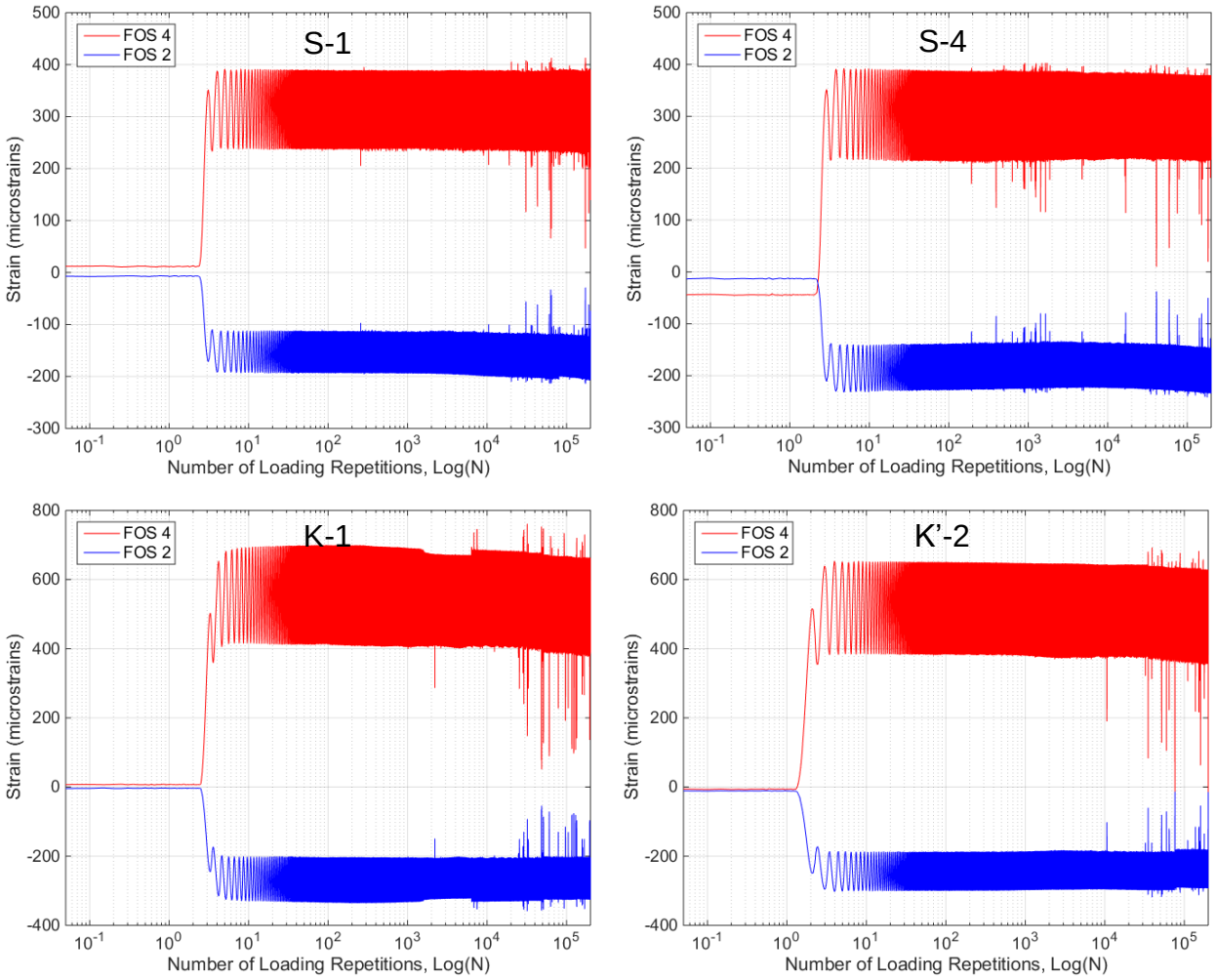

Figure 4.14 FO sensors strain deformation measurements

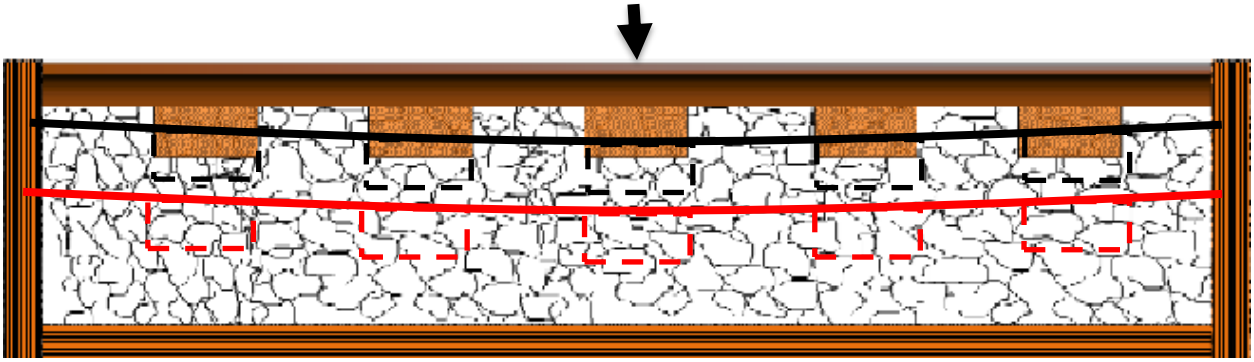

Figure 4.15 Bended rail in FSTM; black line represents the deformed shape immediately after applying load, and red line represents deformed shape after $N= 2 \cdot 10^5$.

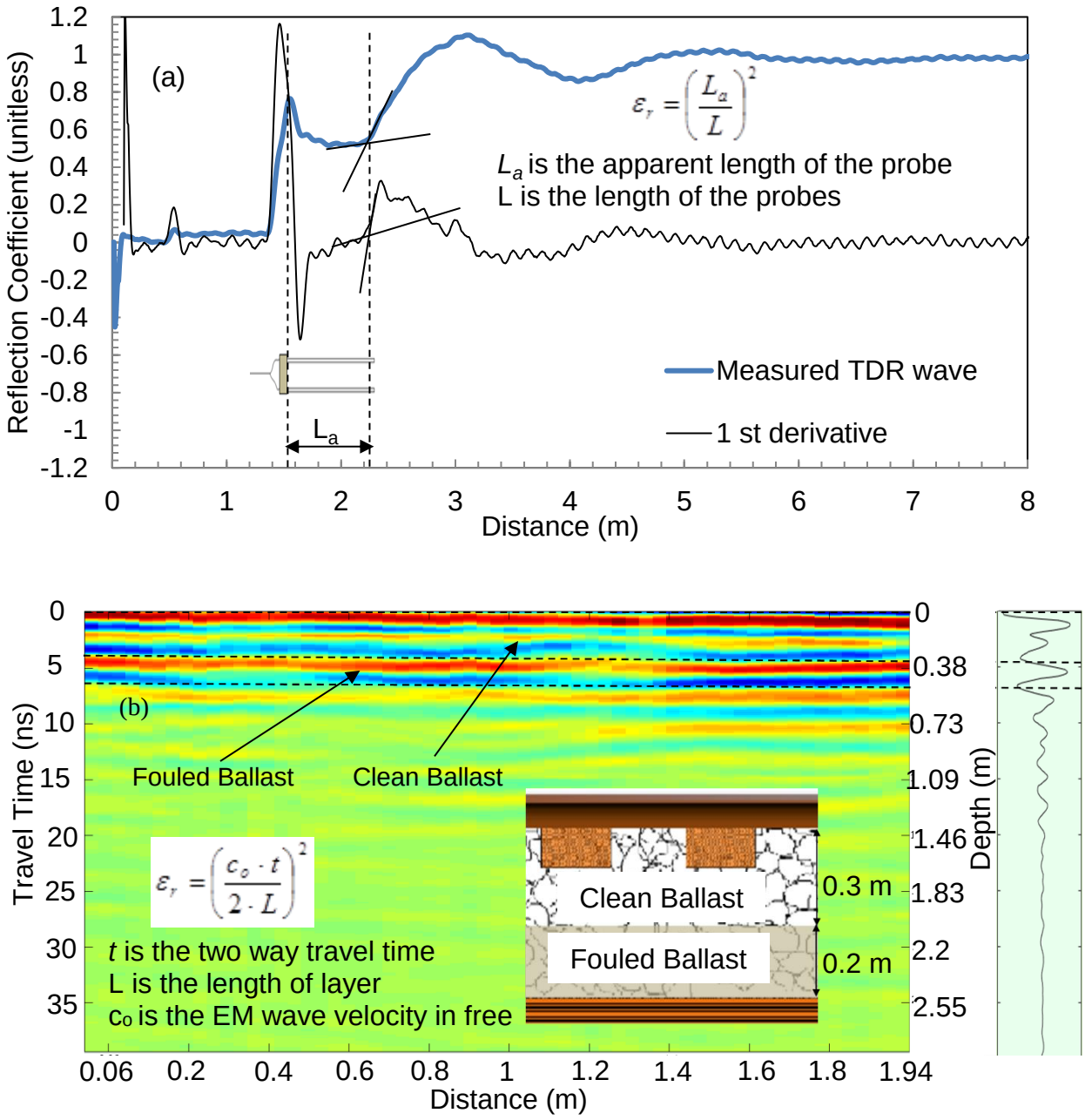

Figure 4.16 An example taking out of experiment S-2-End of (a) TDR waveform reflection and (b) GPR radargram reflection.

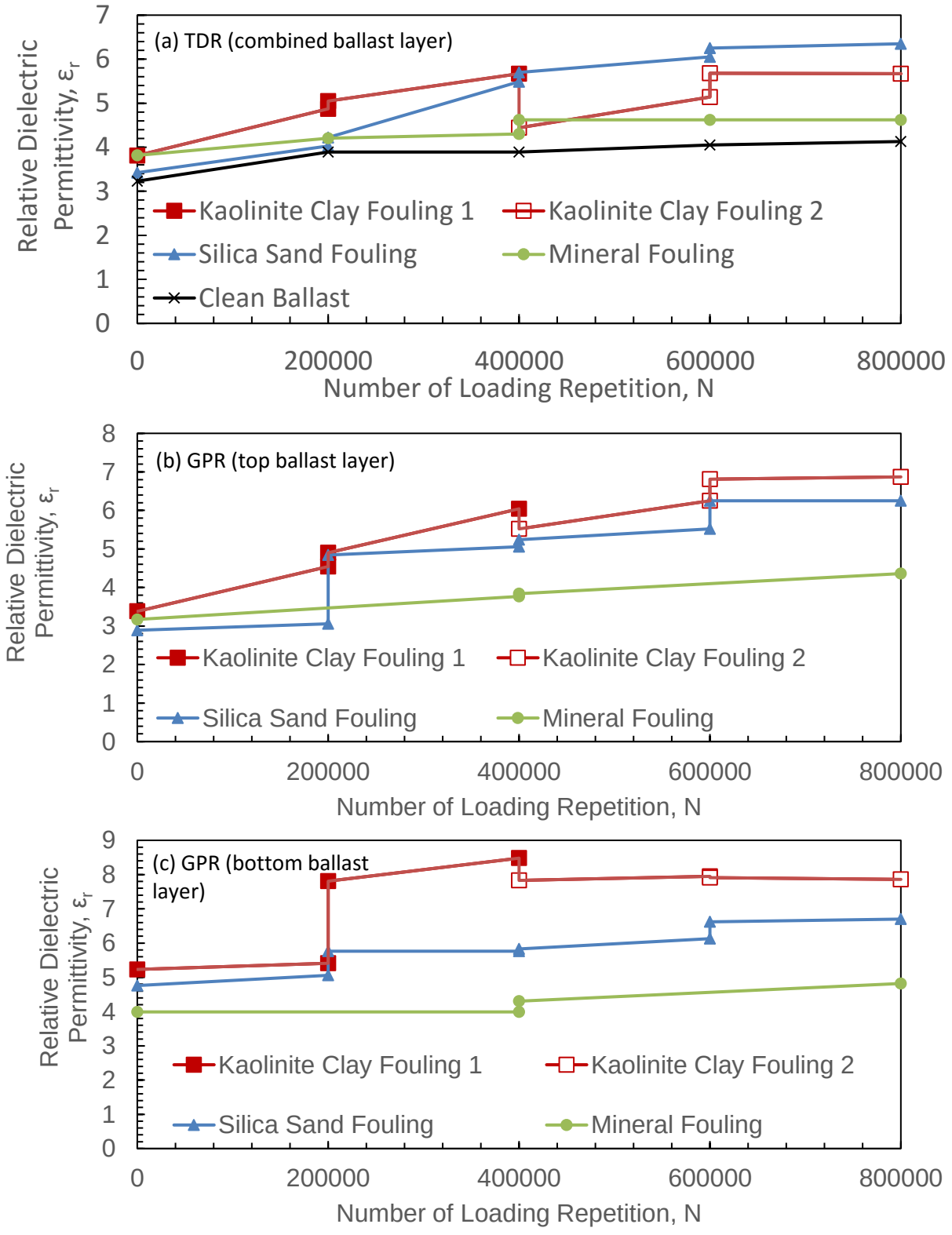

Figure 4.17 Measured relative dielectric permittivity as a function of loading repetitions, volumetric water content, and depth of fouling for: (a) TDR (combined ballast layer), (b) GPR (top ballast layer), and (c) GPR (bottom ballast layer).

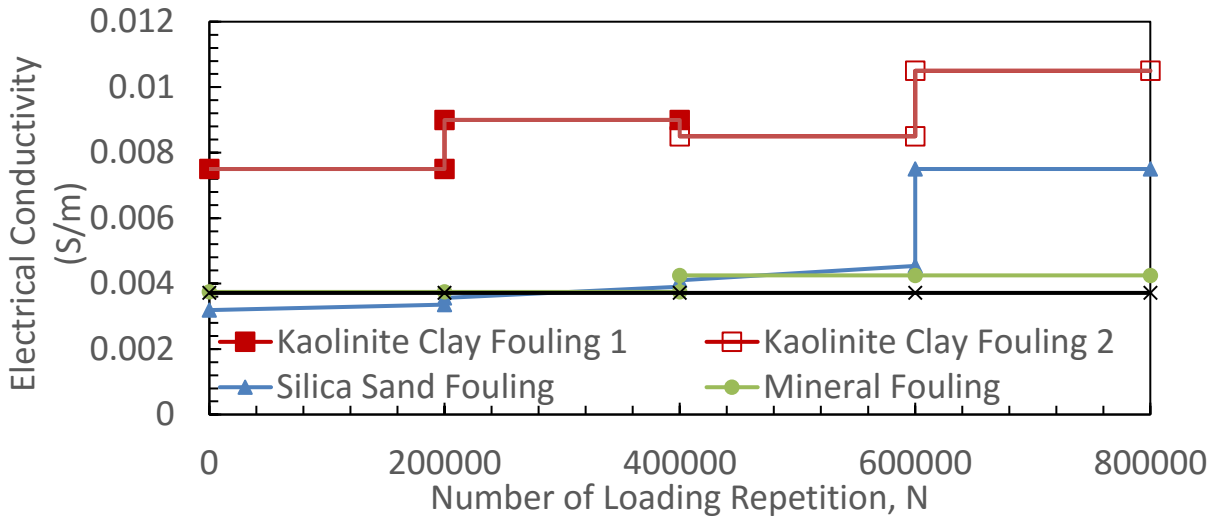

Figure 4.18 FSTM electrical conductivity measurements

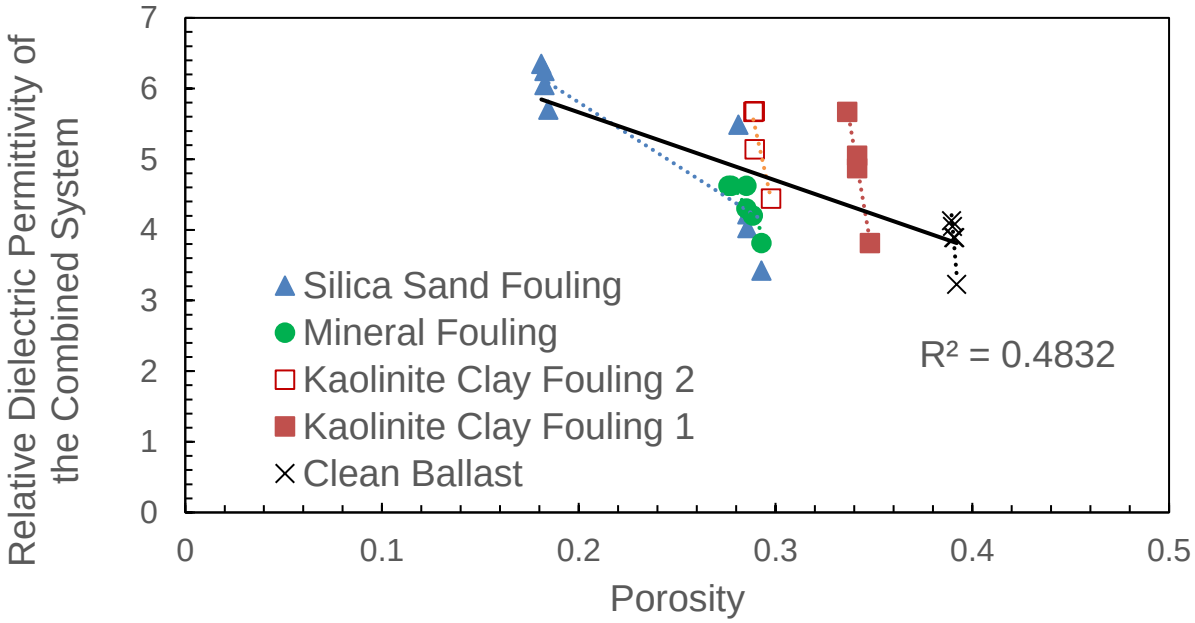

Figure 4.19 Relationship between the combined permittivity of the system and the porosity. The dashed lines are for linear regression, taking for the individual material. Solid line is for linear regression, taking for all the materials.

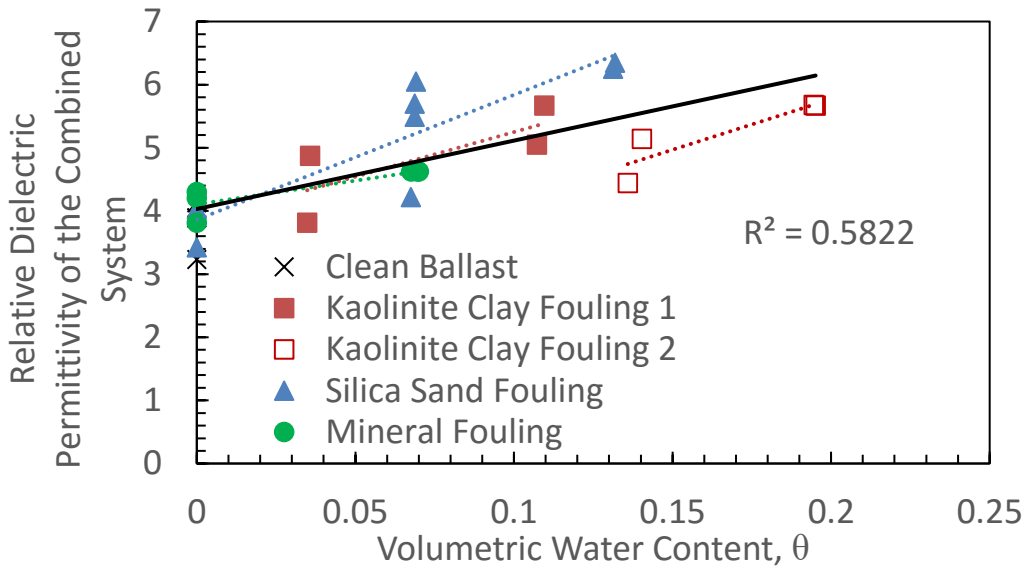

Figure 4.20 Relationship between the relative dielectric permittivity of the combined system and the volumetric water content. The dashed lines are for linear regression, taking for the individual material. Solid line is for linear regression, taking for all the materials.

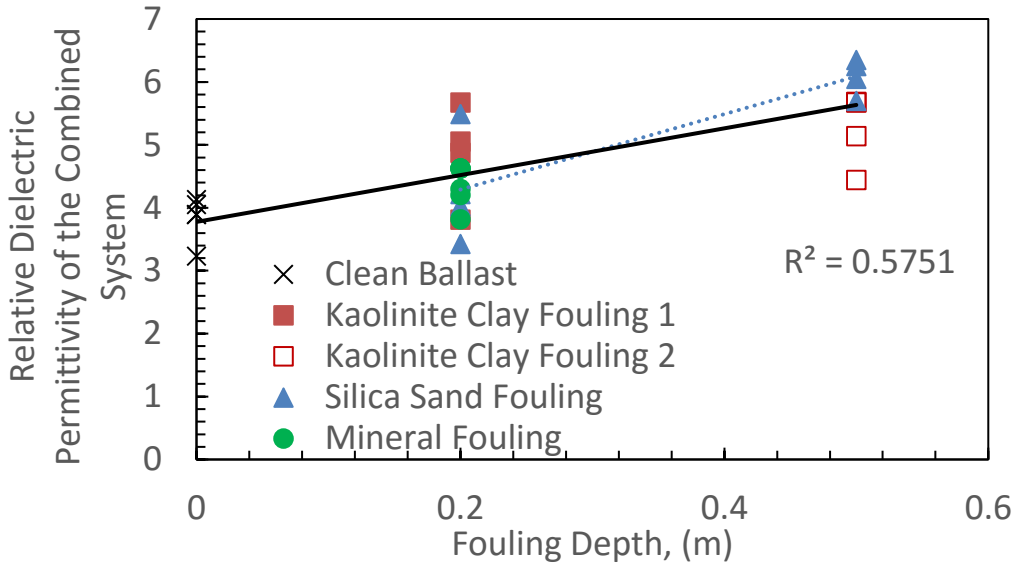

Figure 4.21 Relationship between the relative dielectric permittivity of the combined system and fouling depth. The dashed lines are for linear regression, taking for the individual material. Solid line is for linear regression, taking for all the materials.

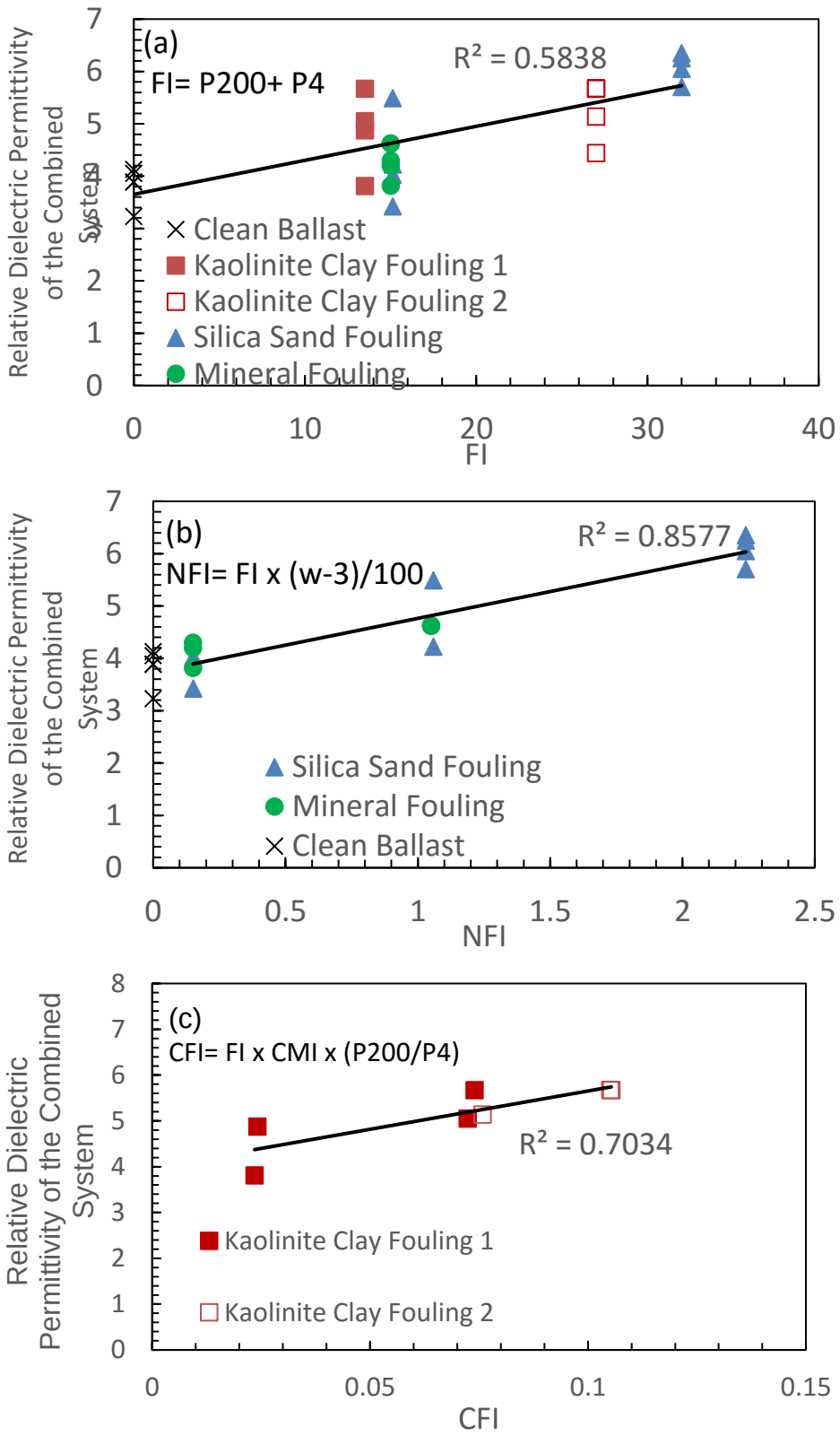

Figure 4.22 Relationship between combined permittivity and (a) fouling index (FI), (b) non-clay fouling index (NFI), and (c) clay fouling index (CFI).

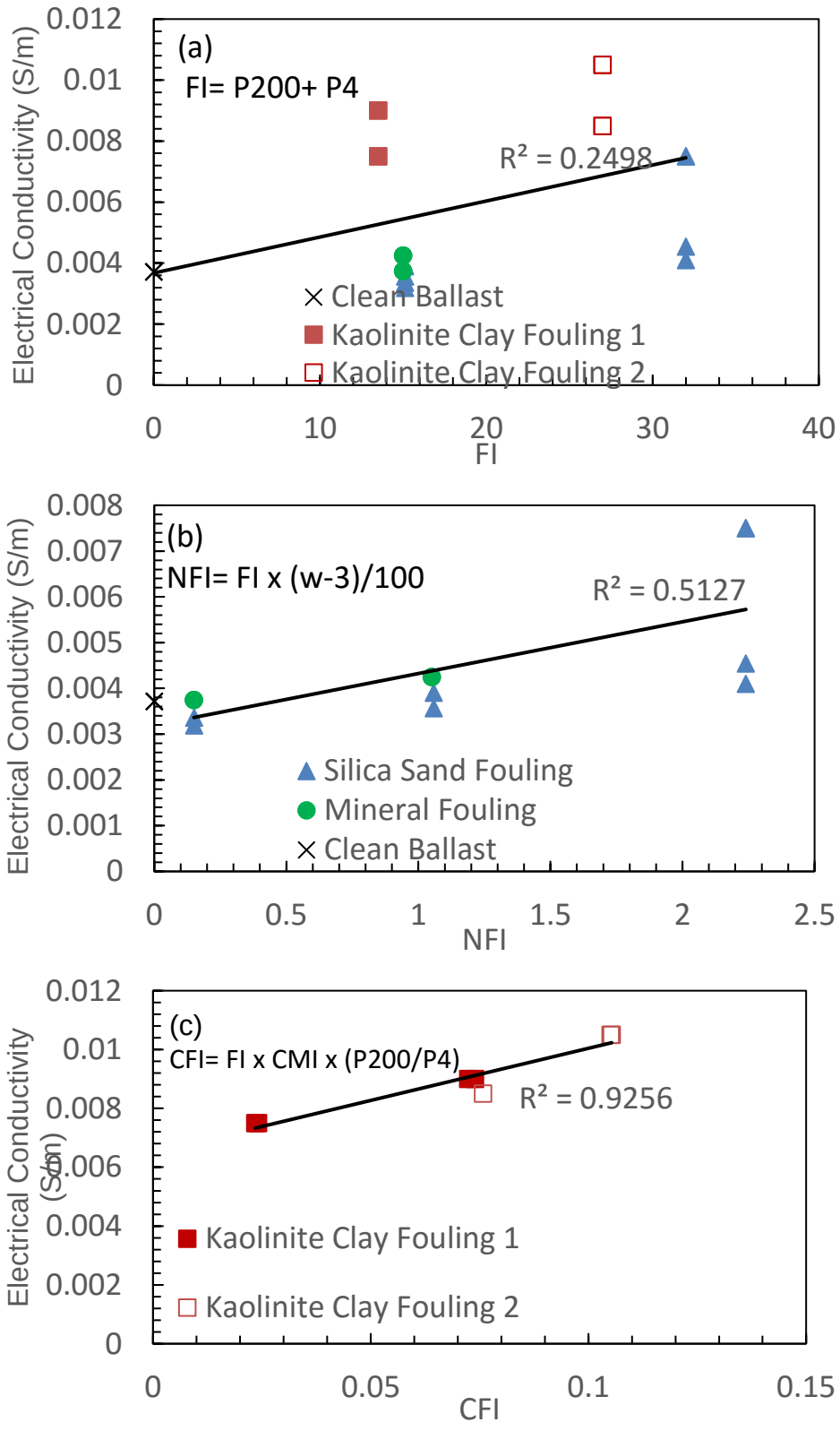

Figure 4.23 Relationship between electrical conductivity and (a) fouling index (FI), (b) non-clay fouling index (NFI), and (c) clay fouling index (CFI).

(a)

(b)

(c)

(d)

Figure 4.24 Vertical profile of FSTM test: (a) Silica sand fouling, (b) Kaolinite clay fouling, (c) Mineral Fouling, (d) Clean ballast.

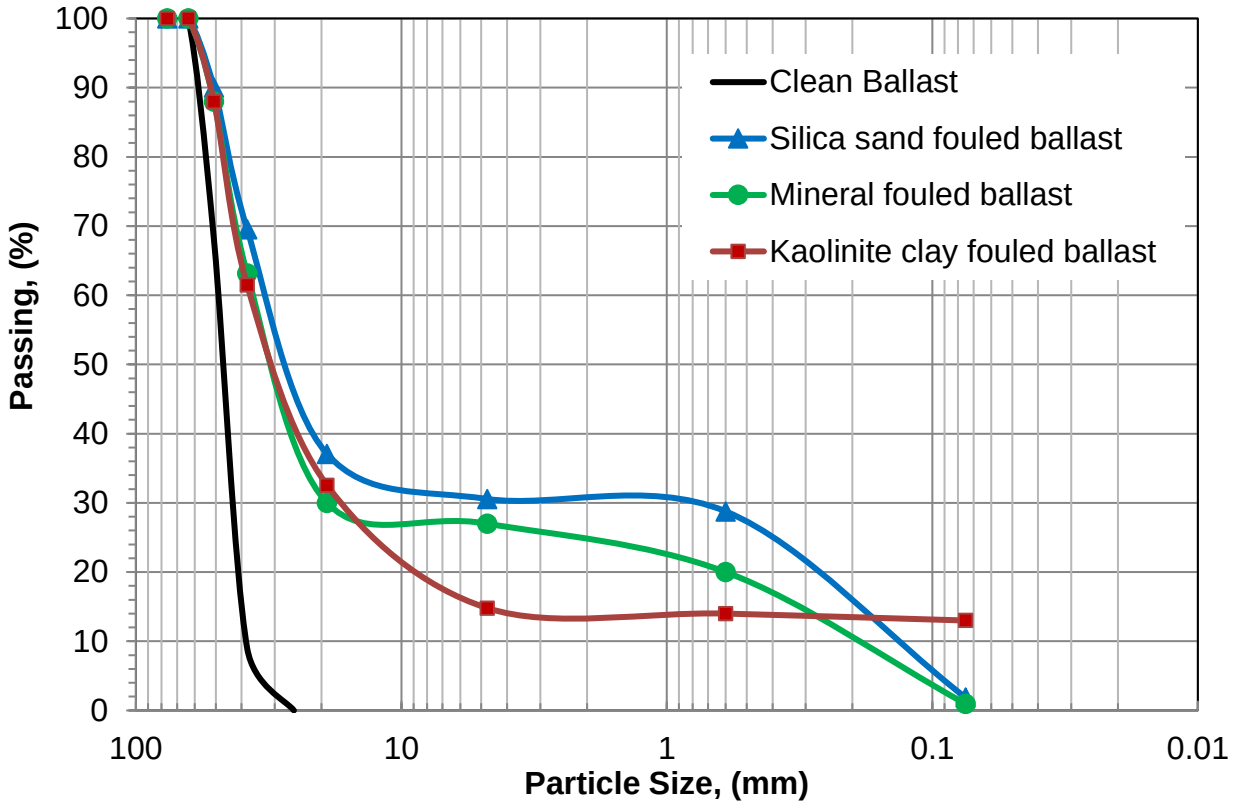

Figure 4.25 Particle size distributions of ballast (AREMA # 25), silica sand fouled ballast, kaolinite clay fouled ballast, and mineral fouled ballast.

This chapter is a reformatted version of the technical note:

Alsabhan et al., 2016, "Limitations of Using Fiber Optic Sensors to Assess the Effect of Ballast Fouling on the Response of Railway Structure," to be submitted to the Journal of Transportation Engineering

CHAPTER 5: Limitations of Using Fiber Optic Sensors to Assess the Effect Ballast Fouling on the Response of Railway Structures

Abstract

Assessing and quantifying the quality of the railway infrastructure components remains a challenging issue in controlling the safety and the overall cost of the railway operations. Many efforts have been made to develop an instrumentation technique to monitor the track quality. One of the most promising technique is the development of fiber optic technology to assess the response of rail tracks along large distances. Fiber optic sensor have the ability of measuring strain either at discrete points or along distributed distances. However, limited studies comprehensively describe using fiber optic sensors to assess the quality of the railway substructure. One of the challenges of fiber optic sensors is that the technique tends to measure localized (e.g., sensing the effect of localized train load) but it is difficult to implement for the evaluation of large scale settlements (e.g., in the evaluation of ballast fouling that tends to create settlements over large distances). This chapter provides an insight about using fiber optic sensors and their measurement capability as a mean to estimate the quality of railway substructure. In addition, the deformation response of railway tracks under various conditions (e.g., multiple axle loads, and effect of joints) is presented in light of potential ballast degradation problems. The results indicate FO sensors were not able to capture the generation of plastic bending strains on the track when the deterioration is not localized. Rather, the FO measurement techniques exhibited a constant pattern of bending strains

under cyclic loading difficulty its implementation to monitor problems such as ballast fouling

Keywords: Fiber optics, Railway Deformation, Track Modulus

5.1 Introduction

The need for a reliable, continuous, and remote monitoring routine for maintaining railway infrastructure has become a crucial in the need for controlling the safety and the cost of the railway operations. Recently, there has been a growing interest in using Fiber Optic (FO) sensors as a reliable railway inspection technique. Glisic and Inaudi (2007) presented the use of a distributed fiber optic sensing as a structural health monitor tool and concluded that distributed sensing in bridges and tunnels can be used as a promising measurement tool to determined deformations in civil structural applications. Several studies have showed that FO sensors can detect and distinguish both lateral and normal strains in infrastructure applications (Ou, 2006; López-Higuera, 2010; Li et al. 2004). However, few studies have examined the use of fiber optic sensors to monitor the response rail track of ballast fouling as part of the overall performance of railway systems (Lee et al. 1999; Filograno et al. 2010; Yoon et al. 2011; Wang et al. 2006).

For many years track modulus was considered as a representative parameter to quantify the structural integrity of railway track (Selig and Li 1994; Kerr 2003; Lichtberger 2005). Selig and Li (1994) described it as the measure of the vertical stiffness of the rail foundation. Furthermore, Selig and Li (1994) used a mathematical model based on the theory of continuous beam on elastic foundations to define track modulus as the supporting force per unit length of the rail, q, per unit vertical deflection of the rail, y.

$$u = -\frac{q}{y} \tag{5.1}$$

By equating the maximum measured rail deflection at one point with the corresponding analytical expression on the differential equation for the bending theory of an elastic beam. Equation (5.1) can be rewritten as:

$$u = \frac{k^{\frac{4}{3}}}{(64EI)^{\frac{1}{3}}} \tag{5.2}$$

where, E is the rail modulus of elasticity, I is the rail moment of inertia, and k is the track stiffness, and it can be calculated as:

$$k = \frac{P}{y_m} \tag{5.3}$$

where P is the wheel load, and y_{m} is the maximum rail settlement. Researchers have adopted these parameters in evaluating railway track conditions (Cai et al. 1994; Read et al. 1994; Norman et al. 2004; Priest and Powire 2009). In order to get a better understanding of the expected railway track response in the field, a railway track section was numerically evaluated using the Winkler's model for a single railway cart, two adjoining railway carts, and effect of poor railway joints.

5.2 Fiber Optic Sensors - Working Concepts

There are several advantages to the use of FO sensors in railway inspection, including lasting durability, high deformation range, high temperature endurance, immunity to electromagnetic noise, electrical isolation, distributed sensing capability,

multiple sensing capabilities, and the potential for relatively low cost when applied to large, distributed structures (Li et al. 2004). Table 5.1 summarizes these advantages. Typical FO cables are made of three components: core, cladding, and jacket (Figure 5.1). The core and the cladding consist of glass with different refraction indexes η_{eff}. These differences in refraction indices maintain light signal within the core (i.e., total reflection effect). The jacket provides strength and protection to the fiber, and may be composed of plastic, ceramic, or metal (Signore et al. 1997). The most important property of FO is photosensitivity. It allows for assessing changes in temperature and strain (Li et al. 2004). Changes in the properties of the transmitted light such as amplitude, wavelength, frequency, and phase are due to the changes that takes place within the length of fiber due to strain and temperature along the fiber or within single FO sensors (Udd, 2002).

Table 5. 1 Advantages of Fiber Optics Sensors

Category	Comments	Researchers
Long durability	They are made from a very durable material (i.e. silica) that is corrosion resistant and withstands high tensile loading (up to 50,000με of elongation).	Li et al. 2004; López-Higuera 2010
High deformation range		
High temperature endurance	They can measure temperatures from - 200 to 800 °C with a silica core and 1500 °C with a sapphire core.	Li et al. 2004; López-Higuera 2010
Immunity to electromagnetic noise interferences	They can operate in electrically noisy environments and can transfer sensing data over a long distance without EM interference.	Li et al. 2004; López-Higuera 2010
Distributed sensing capability	A single FO sensor cable can be deployed at multiple locations and can be easily multiplexed by time or wavelength methods	Li et al. 2004
Multiple sensing capabilities, and	Temperature: FO sensor can be used to measure local and distributed temperature with resolution can be better than 0.1 °C. Strain: can be used to measure displacement, acceleration, pressure, relative fissure, temperature, and inclination, etc. with resolution as low as 1 με. Range: up to 100 km with measurement resolution as small as 1 με.	Li et al. 2004
Relative low cost	In spite of that fiber optics sensing industry is relative new development, FO sensors are already cost-competitive as compared to conventional sensors and prices continue to decrease along with the rapid development of fiber optic communication industry	Li et al. 2004

5.3 Classification of FO Sensors

FO sensors can be classified as local, quasi-distributed, and distributed sensor arrays depending on the sensing methodology and the length of the sensor (Li et al. 2004). Table 5.2 lists the FO sensors available to civil engineering applications and their categories.

Table 5. 2 FO Sensors Categories (Li et al. 2004; Glisic and Inaudi, 2007; Chang 2010)

	Sensors	**Measures**	**Linear response**	**Resolution**	**Range**	**Modulation method**
Local	Fabry-Perot	Strain[a]	Y	0.01%gage length[c]	10,000με	Phase
	Long gage sensor	Displacement	Y	0.2% gage length[d]	50 m	Phase
Quasi-distributed	Fiber Bragg Grating	Strain[b]/Temperature	Y	1 με	100 km	Wavelength
Distributed	Raman/Rayleigh	Strain	N	0.5 m/1C^{o}	2000 m[e]	Intensity
	Brillouin	Strain/Temperature	N	0.5 m/1C^{o}	2000 m	Intensity
	Rayleigh Scattering	Vibration	N	0.5 m	100 km	Intensity phase

[a] Can be configured to measure displacement, pressure, temperature.
[b] Can be configured to measure displacement, acceleration, pressure, relative fissure, temperature, and inclination, etc.
[c] Resolution as low as 0.1 με.
[d] Resolution as low as 0.2 με.
[e] Up to 8 km with spatial resolution as low as 5 m.

5.3.1 Local FO Sensor Measurements

Local fiber optic sensors measure changes at specified local points along a fiber optic cable. They are mostly amplitude-based sensors. The local FO sensor measures

the average strain between two points with optional temperature compensation. The length of the long-gage sensors ranges from 0.2 to 50 m (Li et al. 2004). The most commonly used local sensors are based on Michelson interferometry and Fabry–Perot interferometry.

Michelson Interferometer Sensors. This sensing technique detects the optical phase change generated in the light as it propagates along the optical fiber (Li et al. 2004). The sensor consists of a pair of single-mode fibers in which one of the fibers (sensing fiber) is installed on the host structure while the other fiber (reference fiber) is placed loose, unattached to the host structure (Figure 5.2). The deformation is measured by emitting light from the source through the sensor and measuring the optical phase difference the two fibers, resulting in a ‘‘fringe pattern’’. The shift of the fringe is an indirect indication of the strain. A direct measurement is made by measuring the length difference of a second FO sensor applied at the input/output port of the first fiber-optic (Li et al. 2004). In essence, all deformations of the structure are then result of the change of the length difference between these two fibers.

Fabry–Perot Interferometric (FFPI) Sensors. They consist of a capillary silica tube that contains two cleaved optical fibers facing each other with an air gap of a few micrometers between them (Figure 5.3). Due to different interfaces through the length of the fiber, glass-to-air and air-to-glass, the propagated light will be reflected (Glisic and Inaudi, 2007). The change in the gap width that corresponds to the average strain variation along the fiber results in changes in the physical properties in the reflected light. Furthermore, changes in the properties of the incident light is used to reconstruct the changes in the fiber spacing and, therefore, obtaining the average strain.

5.3.2 Quasi-Distributed Sensors - Fiber Bragg Grating

Fiber Bragg Grating (FBG) is a fiber with local alteration of refractive index in its core that has been produced by exposing the core to intense UV patterns (Figures 5.4 and 5.5). The produced grating has a typical grating spacing length of 10 nm (Glisic and Inaudi, 2007). FBG is considered a quasi-distributed sensor because it can be easily multiplexed to measure strains at several locations along a single fiber. This sensing technique detects the change in the reflected wavelength corresponding to the grating pitch while the other wavelengths will pass through the grating undisturbed (Figure 5.6 - Glisic and Inaudi, 2007). The change in the reflected wavelengths is related to the period/spacing between gratings by:

$$\lambda = 2\, n_{eff}\, \Lambda \tag{5.4}$$

where n_{eff} is the effective index of refraction, Λ is the grating spacing, and λ is the reflected wavelength. The refractive index n_{eff} is related to the index properties of the fiber. Thus, the refractive index changes with changes in temperature and strain at the sensor. As a result, the reflected wavelength λ will shift accordingly (Ou 2009). Equation 4.2 relates the amount of wavelength shift to both strain and temperature:

$$\varepsilon = \left[\frac{\left(\Delta\lambda/\lambda_o\right)_S - \left(\Delta\lambda/\lambda_o\right)_T}{F_G}\right] - \frac{\left(\Delta\lambda/\lambda_o\right)_T}{S_T}\left(CTE_S - CTE_T\right) \tag{5.5}$$

where $\Delta\lambda_S$ is the reflected wavelength shift caused by the strain, λ_S is the Bragg wavelength corresponding to the strain, $\Delta\lambda_T$ is the reflected wavelength caused by temperature changes, and λ_T is the Bragg wavelength corresponding to the temperature sensor. FG is the gage factor at 22 C°, S_T is temperature sensitivity at 22 C°, CTEs is the thermal expansion coefficient for the test specimen, and CTET is the thermal expansion

coefficient for the temperature probe. FBG has very high resolution and accuracy of strain measurements. It can sense strains as low as 1 με and has a range up to 100 km (Li et al. 2004). This type of FO sensors can be installed over the entire railway infrastructure to monitor strains and temperature at various troublesome locations.

5.3.3 Distributed FO Sensors

Distributed FO sensors uses a single FO cable to replace up to thousands of discrete sensors (Glisic and Inaudi 2007). The sensing algorithm is built on the interpretation of scatterers that alter the light amplitude in the fiber due to temperature or strains. Strain and temperature changes along the length of the fiber cause light intensity variations (Li et. al. 2004). Therefore, deformations within various sections of the structure can be detected. Distributed FO sensors have found extensive usage in civil structural applications in monitoring of pile foundations, bridges, dams and geothermal applications (Glisic and Inaudi 2007; Curtis and Kyle 2011; Fisher et al. 2015).

There are different techniques for obtaining strain and temperature information from distributed optical fiber. In essence, when an electromagnetic wave is launched into an optical fiber, the light will be redistributed by various mechanisms in the form of Rayleigh, Brillouin or Raman scattering (Bao and Chen 2012). Bao and Chen reported that the spatial resolution of a distributed fiber optic is:

$$\Delta z = \frac{\tau \cdot c}{2n_{eff}} \tag{5.6}$$

where, τ is the pulse width, c is the speed of light, and n_{eff} the effective refractive index of the fiber.

Rayleigh scattering. Occurs in all directions and is caused by a molecule that is much smaller than the wavelength of light. It occurs as a result of the fluctuation of the refractive index when the light wave travels along the optical fiber. The refractive index is related to the index properties of the fiber and it changes with the change of temperature and strain. The fluctuation of the refractive index along the optical fiber causes the light to scatter in all directions, and therefore, the intensity of the scattered light at different points on the fiber will be altered with changes in temperature and strain along the fiber (Chang, 2010). The measured back scattered light intensity presents an exponential decay with time which is related to the linear attenuation of the fiber. By knowing the speed of light, the time of arrival is converted to distance where temperature and strain changes are measured (Glisic and Inaudi 2007).

Distributed acoustic sensors (DAS) is a relatively recent development in the use of distributed fiber optic sensors to measure ground vibrations (Daley et al. 2013; Parker et al. 2014; Lord et al. 2015). It utilizes Rayleigh scattering to capture changes in the phase of the backscattered light signal. DAS exploits its high sampling capabilities by generating a repeated pulse every 100 μs and continuously processing the backscattered signal every 10 ns leading to a spatial resolution of 1 m and a possibility of monitoring more than 10 km with at higher than 10 kHz sampling rate (Daley et al. 2013).

Raman Scattering. The scattered light has a different frequency than the incident light, caused by the thermal excitation of molecule in the optical fiber. Thus, frequency shifts from the incident light wave will be generated by thermal agitation. The scattered light with a higher frequency is known as anti-Stokes scattering. In the anti-Stokes scattering, the incident light wave gains energy from the molecules it excites yield and it

yields scattered light with a slightly higher frequency than the frequency of the original exciting light. On the other hand, if light wave loses energy when interacts with the molecules, it leads to scattered light with lower frequency than the frequency of the original exciting light. This type of scattering is referred to as Stokes scattering. It has been found that the intensity of the anti-Stokes component is temperature-dependent while the Stokes component is not (Chang, 2010) (Figure 5.7). The phenomenon of Raman scattering is unable to measure strain along the fiber, it can only measure temperature (Glisic and Inaudi 2007). Nevertheless, the magnitude of the spontaneous backscattered light is quite low, thus limiting the distance range of Raman based systems to approximately 8 km and requires long measuring times to improve the resolution of the measured temperature (Glisic and Inaudi 2007).

Brillouin scattering. It results from the interaction between light and thermally agitated acoustic waves in gigahertz range. This interaction that causes fluctuations in the refractive index, giving rise to frequency shifted Stokes and anti-Stokes components (Glisic and Inaudi 2007). It can be seen as diffracted backward light on a moving grating (Glisic and Inaudi 2007). Since the light is traveling at the speed of light, the location of the scattered amplitude can be precisely determined and the location of the temperature and strain measured determined. Information about strain and temperature can be obtained by a process known as simulated Brillouin scattering (SBS) to amplify the amplitude of the scattered light (Figure 5.8).

5.4 FO sensors in Railway Rapid Mentoring

A field study conducted by Lee et al. (1999) in Texas, USA, monitored the dynamic strains of a railroad bridge by instrumenting a steel railroad bridge and a rail at the bridge approach with local fiber-optic Fabry-Perot interferometer (FFPI) sensors, along with resistivity strain gauges to validate FO sensors measurements. The local FO sensors were installed using two configurations: (1) near the top and the bottom of the rail web, and (2) on the rail web with an angle of 45^{o} with respect to the rail natural axis. Lee et al. (1999) show that FO sensors are highly successful in providing a remote measurements for the railway bridge due to its immunity to electromagnetic noise, real time data can be collected via normal communication systems.

Filograno et al. (2010) investigated the application of FBG sensor for real time monitoring of railway traffic on the Spanish High Speed Line (AVE) between Barcelona and Madrid. Two sections of the track were instrumented with 20 FBG sensors. The researchers used different configurations to install FBG sensors. In particular, FBGs were mounted on the rail flange, rail web with an angle of 45^{o} with respect to the rail longitudinal axis, and on the rail natural axis to measure bending strain, shear strain, and change in temperature, respectively. The FBG sensors provide real time measurements of railway elastic strain as the train was passing through. Furthermore, using FBG sensors at different positions relative to the rail cross section allowed different measurements such as train identification, axle counting, speed and acceleration detection, wheel imperfections monitoring, and dynamic load calculation. However, they did not measured plastic strain.

In a study by Yoon et al. (2011), a full-scale railway track model was assembled and tested at a railway track test facility to determine the suitability of using fiber optic distributed sensors for the monitoring of longitudinal strains of the rail. Yoon and colleagues used the Brillouin optical correlation domain analysis (BOCDA) method to enhance the resolution of the detected signal and measure the shift in the local Brillouin frequency. These researchers used a 2.8 m single mode fiber optic mounted on the rail flange. Electric strain gages were also deployed to validate the measurements of the distributed FO sensors. The researchers reported that the distributed FO sensors acquired a spatial resolution of was 3.8 cm and an accuracy of ± 15 με. Which can be a promising technique to monitor the structural integrity of the railway in term of the modification of the stroke at the expansion joint, and proper selection of the track element.

While FO sensors have been used to monitor the structural health of railway tracks during train traffic very limited studies comprehensively described the effect of the long-term deformation of the tract as a response of the degradation of the ballast layer. Furthermore, track deformations are caused by a reduction in the load bearing capacity and stiffness of ballast layer due to a process known as ‘fouling.’ This process compromises the structural integrity of the railway structure leading to large track deformations and ultimately to train derailment. Developing a continuous and remote sensing technology to provide an early warning system for inspection and maintenance activities during the track service life is crucial to improve track safety. The challenge of using local sensing techniques is that for processes such as ballast fouling tend to deteriorate longer section of the railway substructure and strains tend to be distributed

over several section of trail tracks. That is, the strain is not localized and as such the signal captured by the sensors may be compromised.

Quasi-distributed FO sensors, Fiber Bragg Grating (FBG) sensors, with temperature compensation is proposed to be used in this study to evaluate their response under ballast fouling. The sensor was chosen because of its lasting durability, high deformation range, high temperature endurance, immunity to electromagnetic noise, electrical isolation, distributed sensing capability, multiple sensing capabilities, and high range (100 km) and high resolution (1με). The FO sensors arrays will be mounted to the flange of the rail and near the top of the web to measure flexural strains in the vertical and horizontal directions to identify different failure modes. As a result, correlation between FO sensors measurements, deformation of railway track, and ballast fouling will be obtained.

5.5 Railway Deformation Response

The Winkler's model is the generally accepted analytical model for track design purposes (Kerr, 2003). This model is based on the assumption that each rail acts as a continuously supported beam which is governed by the differential equation for the bending theory of an elastic beam:

$$EI\frac{d^4y}{dx^4} + uy\,(x) = 0 \tag{5.7}$$

From equation 5.7 the deformation y(x) at any distance, x, can be calculated for a single point load, P, as:

$$y(x) = \frac{P\beta}{2u} e^{-\beta x}[\cos(\beta x) + \sin(\beta x)] \quad (5.8)$$

where

$$\beta = \sqrt[4]{\frac{u}{4EI}} \quad (5.9)$$

The slope θ (x) at any distance, x, is calculated by deriving Equation 5.8 with respect to x:

$$\theta(x) = -\frac{P\beta^2}{u} e^{-\beta x}[\sin(\beta x)] \quad (5.10)$$

As a result, the moment M(x) at any distance, x, will be found as the first derivative of the slope θ (x) and the shear force V (x) will be the second derivative of the slope θ (x) as follow:

$$M(x) = \frac{P}{4\beta} e^{-\beta x}[\cos(\beta x) - \sin(\beta x)] \quad (5.11)$$

$$V(x) = -\frac{P}{2} e^{-\beta x}[\cos(\beta x)] \quad (5.12)$$

Then, the bending stress σ (x) and the bending strain ε (x) at any distance x is:

$$\sigma(x) = \frac{Mc}{I} \quad (5.13)$$

$$\varepsilon(x) = \frac{\sigma}{E} \quad (5.14)$$

where c is the distance from rail's neutral axis to the measured point on the rail cross section.

5.5.1 Effect Single Railway Cart and Adjoining Railway Cart Loading

Considering Winkler's model is a linear model, superposition of multiple axle loads is commonly used. Four axles loading are modeled in this section to represent the effect

of a single railway cart and adjoining railway carts. Standard four axles railway cart and adjoining railway carts dimensions are taken from American Railcar Industries (2006).

Wheel loads of 132 kN was modeled on 100 RE rail ($I=2.040\cdot10^{-6}$ m^4, $E=2\cdot10^{11}$ Pa), a=0.495 m, and $u=7\cdot10^{6}$ Pa (represents a poor track conditions (Walters and Selig, 1994)). Figure 5.9 (a) and (b) shows a railway track deflection caused by a single cart and adjoining railway carts, respectively. The maximum deflection is located at the halfway between two adjacent wheels. The deflection profile extends for approximately 22 m. The corresponding bending strains are shown in Figure 5.10. The maximum bending strain in the rail is located underneath loading points. Bending strain diagram exhibits positive values underneath loading points. Whereas, bending strains are negative elsewhere. Cumulative bending strain diagram is less than the bending strain diagram of a single axle load. This indicates that using a single axle loading is misleading and do not reflect the real field conditions.

5.5.2 Effect of Railway joints

Railway vertical bending stiffness decreases about 30% where the joints are located (Kerr and Cox, 1999) due to the reduction of section properties (i.e. cross-section area and moment of inertia). In addition, at a case of a loose railway joint, forces will not be adequately transferred from one railway end to another causing a static load increase to the tie supporting the rail at the vicinity of poor joints. Kerr (2003) reported that forces supported by the tie adjacent to a poorly maintained joint are at least three times more than ties far away from the joint. Therefore, due to differential stiffness and static force at the location of railway joints, a local settlement problem will be generated. This disruption

in the rail continuity requires modifications to the boundary conditions of Winkler's model. Kerr solved for Winkler's model using the following boundary conditions:

$$\frac{d^2y}{dx^2} = 0 \qquad \frac{d^3y}{dx^3} = \frac{P}{EI} \qquad \lim_{x\to\infty}\left\{y, \frac{dy}{dx}\right\} \to 0$$

From Equations 5.7 the deformation y(x) at any distance, x, can be calculated for a single point load, P, as:

$$y(x) = \frac{P\beta}{u} e^{-\beta x}\cos(\beta x) \tag{5.15}$$

The bending moment M(x) at any distance, x, will be as follow:

$$M(x) = -EI\ \frac{d^2y}{dx^2}(x) = -\frac{P}{\beta} e^{-\beta x}\sin(\beta x) \tag{5.16}$$

Equations 5.16 and 5.17 were numerically evaluated for the same parameters as the previous sections. Results are showing in Figure 5.11 and 5.12 for deflection and bending strain, respectively. It is clear that the maximum deflection takes place in the location of the joints. However, the maximum bending strains happens between the location of the first and third tie (0.5 m to 1.5 m) away from the joint.

5.6 Experimental Setup

In chapter 4 the author investigated the feasibility of using FO sensors to monitor the condition of the railway infrastructure. In essence, the author developed a Full Scale Track Model (FSTM), a prototype of railroad section aimed at characterizing the measured deformation, due to the increase of loading cycles under laboratory controlled

conditions. It is designed to contain ballast, ties, and rail, and it was built as wooden box that has the inside dimensions of 2.5 m in length, 1.7 m in width, and 0.9 m in height. The track consists of 2.45 m rail and 5 ties spaced 0.495 m apart. Two FO sensors os3155 were selected to provide bending strain measurements along the length of the rail in the laboratory. The sensors were installed in the mid span of the 2.45 m rail using spot welding. One FO sensor was mounted on the bottom flange of the rail and it was given the identification name FOS 4, and the other was mounted on the top portion of the rail's web and it was given the identification name FOS 2. Data acquisition was conducted using sm130 optical sensing interrogator. Linear Variable Differential Transformer (LVDT) is used to measure the vertical settlement of the rail at the same location.

5.7 Results and Discussion

LVDTs deformation measurements show an accumulation of plastic deformation with the increase of cyclic loading in Figure 5.13(a). Track modulus was calculated using Equation 5.2. The results in Figure 5.13 (b) indicates that track condition ranged between average conditions to poor conditions (Ahlf 1975). FO sensors measurements were expected to provide a similar pattern. However, FO sensors strain measurements did not provide any indication of track deterioration due to cyclic loading as it is shown in Figure 5.14. In essence, all FO sensors measurements exhibited a constant pattern throughout the testing program. This is because the rail was settling as a rigid body. As much as FO sensors are highly accurate and suitable for railway applications due to its immunity to electromagnetic noise, they only measure strains. This fact needs to be taken into consideration since track modulus (u) is a function of wheel load and track settlement.

From the deformation response of the railway discussed earlier, bending strains are seen to extend along the railway track profile for a single railway cart, and adjoining railway carts. This indicates that a series of FO sensors should be installed on the rail's flange to capture the maximum bending strain along the railway profile at a critical locations for a minimum distance of 18 m with a separation of one tie (i.e. 0.495 m for wooded ties and 0.6 m for concrete ties) for a total of 36 sensor in order to integrate local strain to displacement. This number of sensors to instrument only 18 m portion of the track is considered economically unfeasible and economical alternatives might be used.

5.8 Alternative Railway Tracks Instrumenting Techniques

Several methods have been adopted to determine the vertical settlement of the track in the field. These methods vary from a static to rolling dynamic measurements of the vertical deformations of track while vehicles are rolling. Cai et al. (1994) and Read et al. (1994) used static measurement of vertical deformations to assess track stiffness and track modulus. While Norman et al. (2004) implemented rolling dynamic measurements to evaluate the real-time, noncontact measurement of track modulus response. Each of the measurements provide different, yet valuable information that can be used by railway engineers to estimate service life of railway structures and model the mechanical behavior of ballast systems (Walters and Selig, 1994). This section describes techniques that are economically feasible alternatives to FO sensors to monitor the railway tracks. These techniques include geophones, MEMS accelerometers, and geodetic survey.

5.8.1 Geophones

Geophones are low cost remote monitoring system suitable for railway applications considering the nature of operations, Maintenance (e.g., ballast tamping). Using this type of instrumentation would allow a non-intrusive and convenient real time monitoring of the rail deformation without direct use of track vehicles. Geophones are based on the detection of the seismic wave induced by any type of vibration in the ground. Ground vibration generates output voltage in the geophone due to motion of coil suspended by spring in a magnetic field inside the geophone, whereas the output voltage of the geophone, expressed as a function of frequency, in response to ground motion for which the velocity is a constant function of frequency (Krohn, 1984). Settlement is found by integrating the velocity obtained from the geophones. Bowness et al. (2006) investigated monitoring the dynamic displacement of railway track. In their study, they showed that 1-Hz geophones measures peak to peak displacements to within 0.07 mm for excitation frequencies higher than 1 Hz. Geophones will be mounted on the tie to be able to capture the deformation of the track due to movement of dynamic loads, wheel loads.

5.8.2 Microelectromechanical System (MEMS) accelerometers

Using this type of instrumentation would allow a non-intrusive and convenient real time monitoring of the rail deformation without direct use of track vehicles. MEMS are based on the detection of the dynamic forces induced by the acceleration of moving objects. Typical accelerometers consist of proof mass supported by a spring and a dashpot. Dynamic forces generates output voltage in the accelerometer due to the motion of the proof mass as a result of a change in acceleration. Settlement is found by double integrating the acceleration obtained from the accelerometers. MEMS will be mounted on

the railway ties to be able to capture the deformation of the track due to movement of dynamic loads, wheel loads.

5.8.3 Geodetic survey

A detailed standard survey will be conducted to monitor long term changes in geometry. Berntsen RSAK130 adapter with smart-angle-retro-reflective survey targets will be installed on the web on the rail with epoxy construction adhesive. Placement will be every 2-m. Upon finalization of the injection lengths, reflectors should be installed the day prior to PUR injections and an initial reading should be conducted.

5.9 Conclusions

Railway infrastructure experience deterioration of its serviceable function in proportion to cyclic loading. This deterioration is exhibited as an accumulation of plastic deformation with the increase of cyclic loading. FO sensors were suggested as continuous real time monitoring aimed at capturing the increase of plastic deformation in form of bending strains on the track due to cyclic loading to be able to quantify the structural integrity of the track. Results showed that FO sensors were not able to capture the generation of plastic bending strains on the track and rather exhibited a constant pattern of bending strains. This response was due to the fact that the track was settling as a rigid body for the five ties located in the vicinity of point of exerted load. Furthermore, a review of the railway mechanical response suggested that FO sensors should be installed on the rail's flange to capture the maximum bending strain along the railway profile at a critical locations for a minimum distance of 18 m with a separation of one tie (i.e. 0.495 m for wooded ties and 0.6 m for concrete ties) for a total of 36 sensor to avoid

this issue. This number of sensors to instrument only 18 m portion of the track is considered economically unfeasible and economical alternatives might be used.

References

Bao, X., and Chen, L., 2012. “Recent progress in distributed fiber optic sensors,” Sensors, vol.12 (7), pp. 8601-8639.

Cai, Z., Raymond, G. P., & Bathurst, R. J., 1994. “Estimate of static track modulus using elastic foundation models,” Transportation Research Record, Vol.1470.

Chang, C., 2010. “Fiber optics smart structure for monitoring and managing the health of transportation infrastructures,” California State University Long Beach, CA.

Curtis, A., and Kyle, P., 2011. “Geothermal point sources identified in a fumarolic ice cave on Erebus volcano, Antarctica using fiber optic distributed temperature sensing,” Geophysical Research Letters, vol. 38(16).

Daley, T. M., Freifeld, B. M., Ajo-Franklin, J., Dou, S., Pevzner, R., Shulakova, V., Kashikar, S., Miller,D. E., Goetz, J., Henninges, J., and Lueth, S., 2013. “Field testing of fiber-optic distributed acoustic sensing (DAS) for subsurface seismic monitoring,” The Leading Edge, vol. 32(6), pp. 699-706.

Donlagic, D., 2000. “Fiber optic sensors: An introduction and overview”. University of Maribor, Faculty of Electrical engineering and Computer Science, Smetanova ulica 17, Maribor.

Fernandez, M. L., Tapenes, E. E, and Zelitskaya, P. V., 1996. “Pipeline hydrocarbon transportation: some operating concerns and R&D trends”. Proceedings of ASME International Pipeline Conferencie, pp. 95–102.

Filograno, M. L., Rodriguez-Barrios, A., Corredera, P., Martin-Lopez, S., Rodriguez-Plaza, M., Andres-Alguacil, A., and Gonzalez-Herraez, M., 2010. “Real-time monitoring of railway traffic using fiber Bragg gratings,” In (EWOFS'10) Fourth European Workshop on Optical Fiber Sensors, international Society for Optics and Photonics, pp. 76533M-76533M.

Fisher, A. T., Mankoff, K. D., Tulaczyk, S. M., Tyler, S. W., and Foley, N., 2015. “High geothermal heat flux measured below the West Antarctic Ice Sheet,” Science advances, vol. 1(6).

Glisic, B., Inaudi, D., 2007. Fiber optic methods for structural health monitoring, John Wiley & Sons, book.

Kerr, A. D., & Cox, J. E., 1999. “Analysis and tests of boned insulted rail joints subjected to vertical wheel loads,” International Journal of Mechanical Sciences, Vol. 41(10), pp. 1253-1272.

Kerr, A.D., 2003. Fundamentals of railway track engineering, Simmons-Boardman Books, Inc., Omaha, Nebraska.

Krohn, C. E., 1984. “Geophone ground coupling,” Geophysics, Vol. 49(6), pp. 722-731.

Kunzler, M., Edgar, R., Udd, E., Laylor, T. H, Schulz, W., and Kunzler, W., 2002. “Fiber grating traffic monitoring system”. Proceedings of SPIE: Smart Structures and Materials and Nondestructive Evaluation for Health Monitoring and Diagnostics, vol. 4696, pp. 238–43.

Lee, W., Lee, J., Henderson, C., Taylor, H. F., James, R., Lee, C. E., and Gemeiner, W. G., 1999. “Railroad bridge instrumentation with fiber-optic sensors,” Applied Optics, Vol. 38(7), pp. 1110-1114.

Li H. N, Li D. S., and Song G. B., 2004. “Recent applications of fiber optic sensors to health monitoring in civil engineering,” Engineering Structures, Vol. 26, pp. 1647–1657.

Lichtberger, B., 2005. Track compendium. Hamburg: Eurailpress, Tetzlaff-Hestra GmbH and CO. KG.

López-Higuera, J. M., 2010. “Fiber optic sensors in structural health monitoring,” presented at the OFC/NFOEC, San Diego, CA.

Lord, N., Herb, W., Fratta, D., 2015. “A Source Synchronous Filter (SSF) for Uncorrelated Receiver Traces from a Swept-Frequency Seismic Source,” Geophysics, (In preparation for publication).

Majumder, M., Gangopadhyaya, T. K, Chakrabortya, A. K, Dasguptaa, K., and Bhattacharya, D. K, 2008. “Fiber Bragg gratings in structural health monitoring—Present status and applications,” Sensors and Actuators A, vol. 147, pp. 150-164.

Mrad, N., 2002. “Optical sensor technology: introduction and evaluation and application”. In: Schwartz M, editor. Encyclopedia of smart materials, New York: John Wiley & Sons, Inc, vol. 2, pp. 715–37.

Norman, C., Farritor, S., Arnold, R., Elias, S. E. G., Fateh, M., and Sibaie, M. E., 2004. “Design of a system to measure track modulus from a moving railcar.” Proc. Int. Conf. of Railway Engineering, Engineering Technics Press, London.

OU, W. W. L., 2009. “Fiber bragg gratin strain sensors for railway applications”. Master’s thesis, department of Electrical and Computer Engineering. University of Illinois at Urbana-Champaign.

Parker, T., Shatalin, S., and Farhadiroushan, M., 2014. “Distributed Acoustic Sensing–a new tool for seismic applications,” first break, vol. 32(2), pp. 61-69.

Priest, J. A., & Powrie, W., 2009. “Determination of dynamic track modulus from measurement of track velocity during train passage,” Journal of Geotechnical and Geoenvironmental Engineering, Vol. 135(11), pp. 1732-1740.

Read, D., Chrismer, S., Ebersohn, W., and Selig, E., 1994. “Track modulus measurements at the Pueblo soft subgrade site,” Transportation Research Record, Vol. 1470.

Selig, E. T. and Walters, J. M., 1994. Track Geotechnology and Substructure Management, Thomas Telford, New York, NY.

Selig, E. T., and Li, D., 1994. “Track modulus: Its meaning and factors influencing it,” Transportation Research Record, Vol.1470.

Signore, Abdel-Maksoud, and Dempsey B. J, 1997. “Fiber-optic sensing technology for rail-buckling detection,” Transportation Research Record, vol.1584, pp. 924-970.

Tapanes, E. E, 1999. “Fiber optic sensing solutions for real time pipeline integrity monitoring”. The Indonesian Pipeliner. pp. 1–10.

Udd E., 2002. “Fiber optics, theory and applications,” In: Schwartz M, editor. Encyclopedia of smart materials, New York: John Wiley & Sons, Inc, vol. 1, pp. 415–422.

Udd, E., Kunzler, M., Laylor, M. H, Schulz, W., Kreger, S., and Corones, J., 2001. “Fiber grating systems for traffic monitoring,” Proceedings of SPIE: Health Monitoring and Management of Civil Infrastructure Systems, vol. 4337, pp. 510.

Vohra, S., Johnson, G., Todd, M., Danver, B., and Althouse, B., 2000. “Distributed strain monitoring with arrays of fiber Bragg grating sensors on an in-construction steel box-girder bridge,” IEICE Transactions on Electron, vol. E83-C (3), pp.454–461.

Wang, C. Y., Wang, H. L., and Chen, M. H., 2006. “Structural health monitoring activities of applying optical fiber sensors in Taiwan,” In Optical Fiber Sensors. Optical Society of America, pp. MD2

Whelan, M. P, Albrecht, D., and Caponi, A., 2002. “Remote structural monitoring of the cathedral of Como using an optical fiber Bragg sensor system,” Proceedings of SPIE: Smart Structures and Materials and Nondestructive Evaluation for Health Monitoring and Diagnostics, vol. 4694, pp. 242–52.

Yasue, N., Naruse, H., Masuda, J. I., Kino, H., Nakamura, T., and Yamaura, T., 2000. “Concrete pipe strain measurement using optical fiber sensor”. IEICE Transactions on Electron vol. E83- C (3), pp.468–474.

Yoon, H. J., Song, K. Y., Kim, J. S., and Kim, D. S., 2011. “Longitudinal strain monitoring of rail using a distributed fiber sensor based on Brillouin optical correlation domain analysis,” NDT & E International, vol. 44(7), pp. 637-644.

Figures

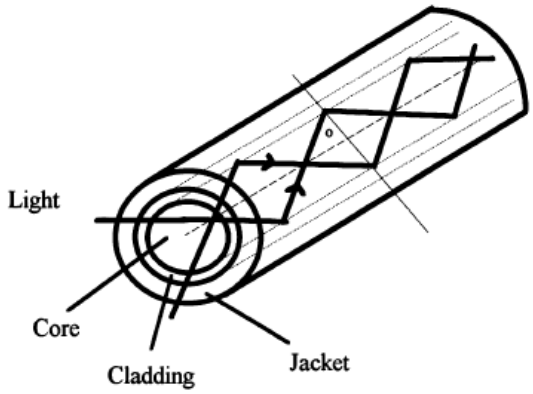

Figure 5.1 FO sensors components (Signore et al. 1997) array.

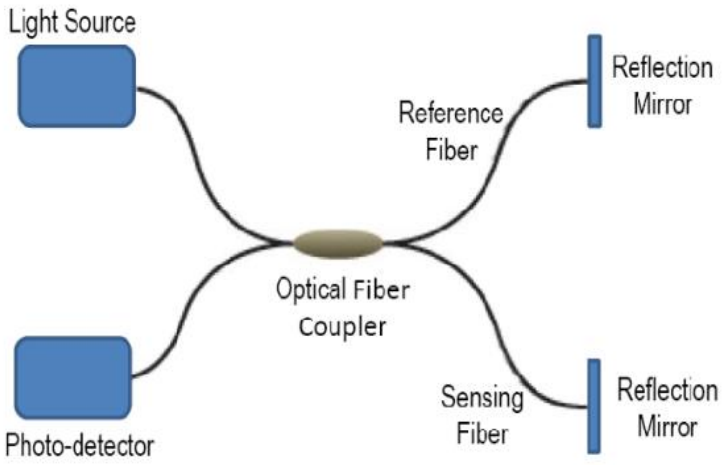

Figure 5.2 Schematic of the Michelson interferometric sensors mechanism (Li et al. 2004)

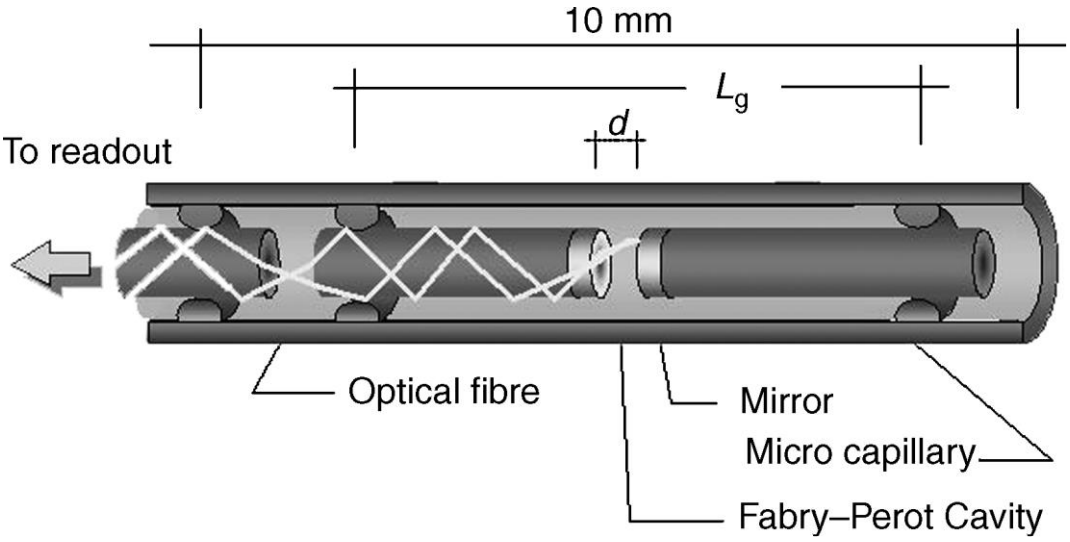

Figure 5.3 Schematic of the Fabry–Perot sensors mechanism (Glisic and Inaudi 2007)

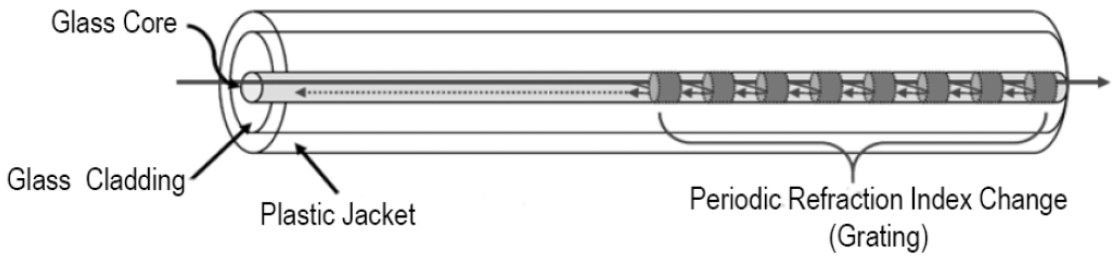

Figure 5.4 Periodic refraction index changes on FBG (Chang 2010)

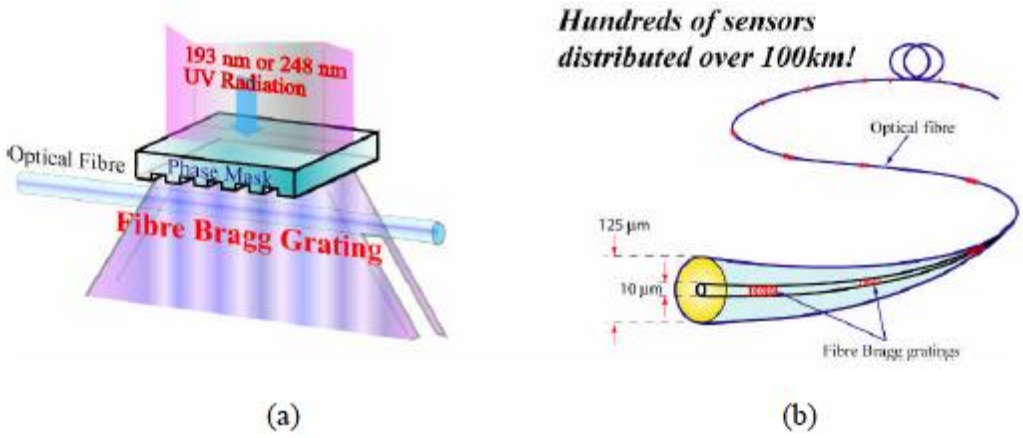

Figure 5.5 (a) FBG fabrication using phase mask; (b) FBG sensor array for distributed sensing (Fernandez et al. 1996)

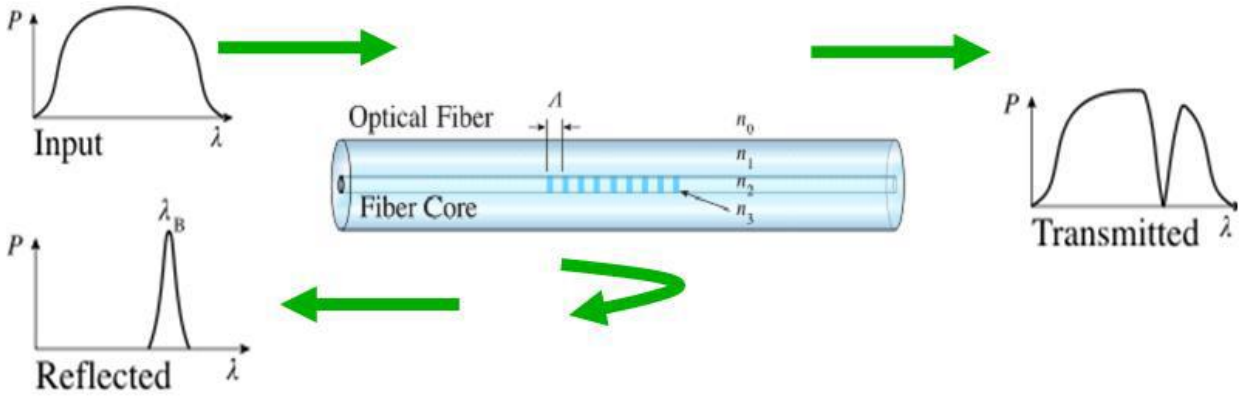

Figure 5.6 Spectral behavior of broadband light through a fiber with Bragg gratings (Fernandez et al. 1996)

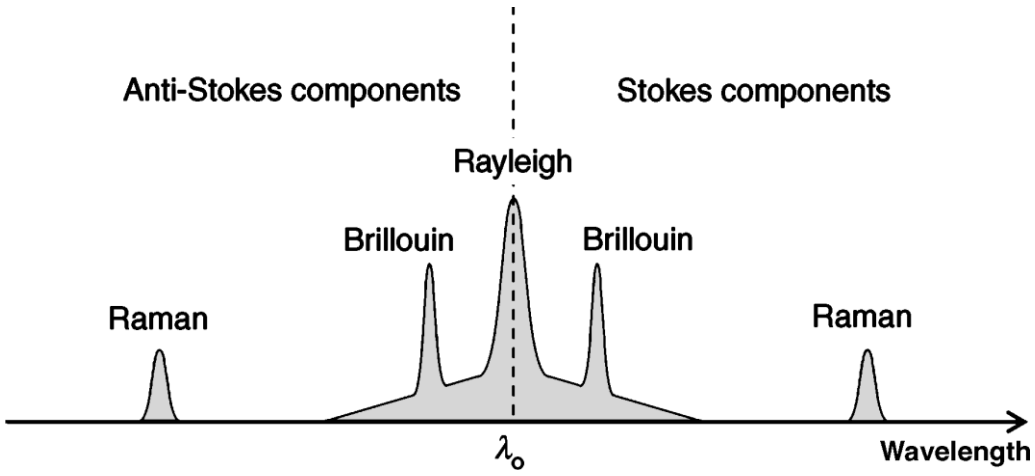

Figure 5.7 Schematic shows simulated Brillouin scattering (SBS) Optical scattering components (Glisic and Inaudi, 2007)

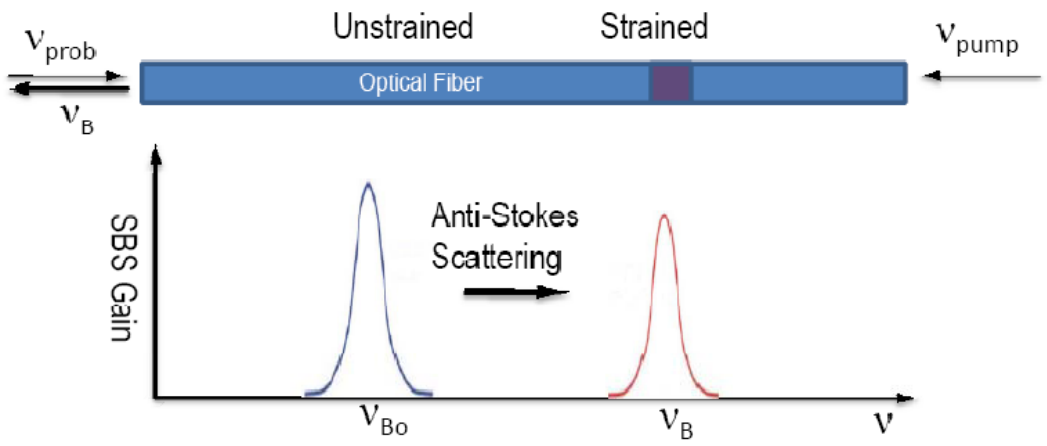

Figure 5.8 Schematic shows simulated Brillouin scattering (SBS) in single mode optical fiber (Chang 2010)

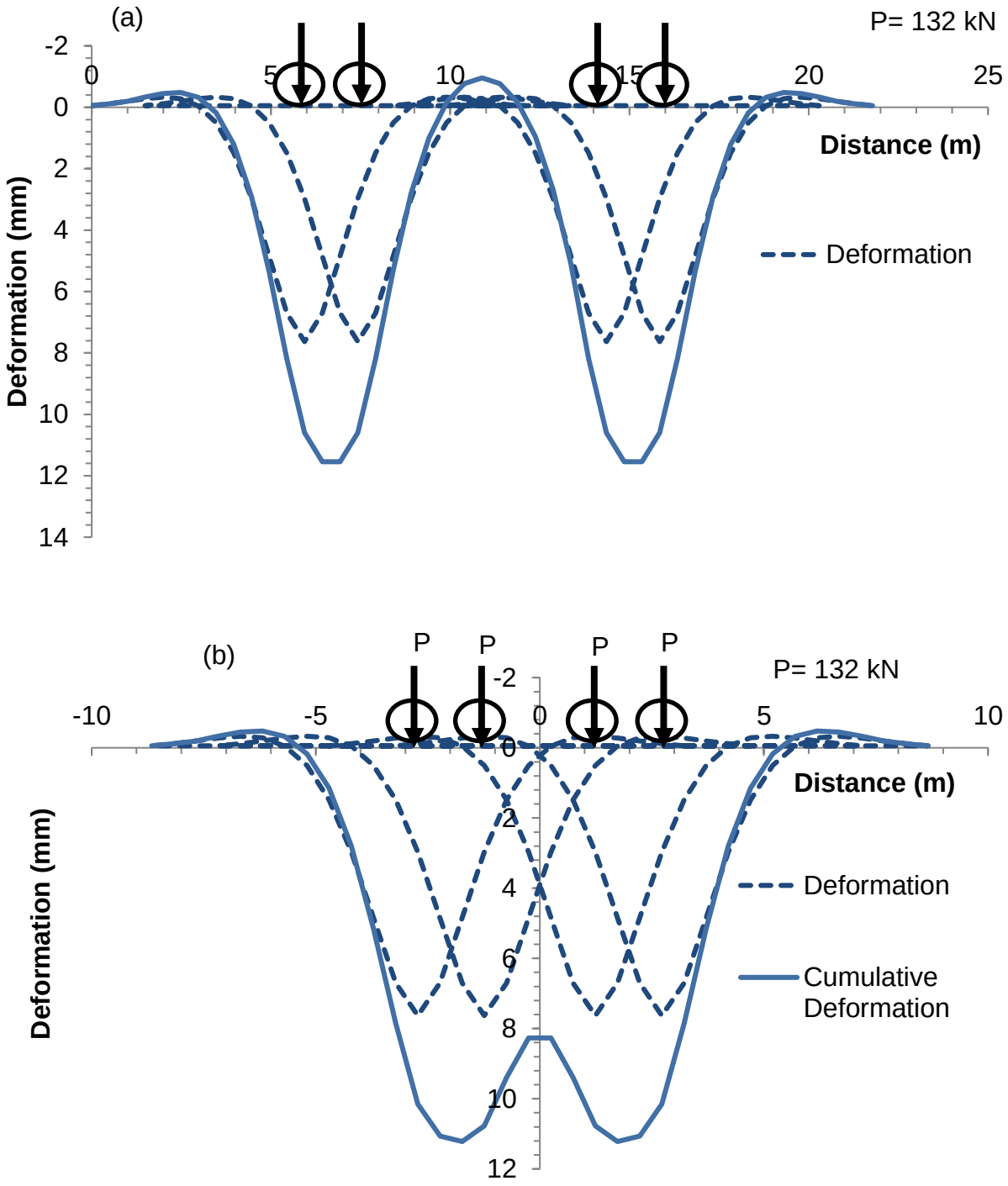

Figure 5.9 (a) Rail deflection for 4- axles single cart loading, and (b) Rail Deformation for 4- axles adjoining carts loading

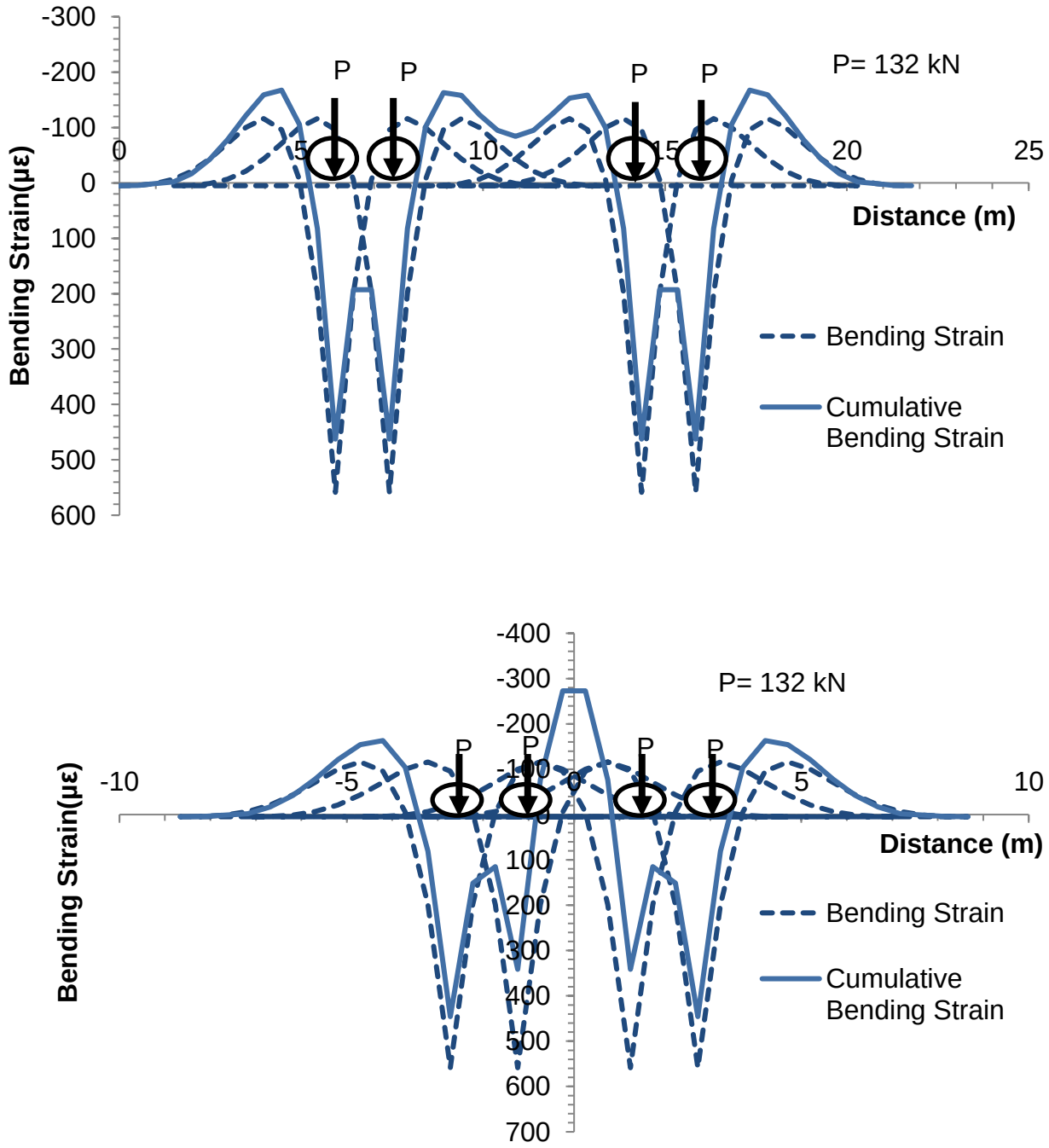

Figure 5.10 (a) Rail bending strain for 4- axles single cart loading, and (b) Rail bending strain for 4- axles adjoining carts

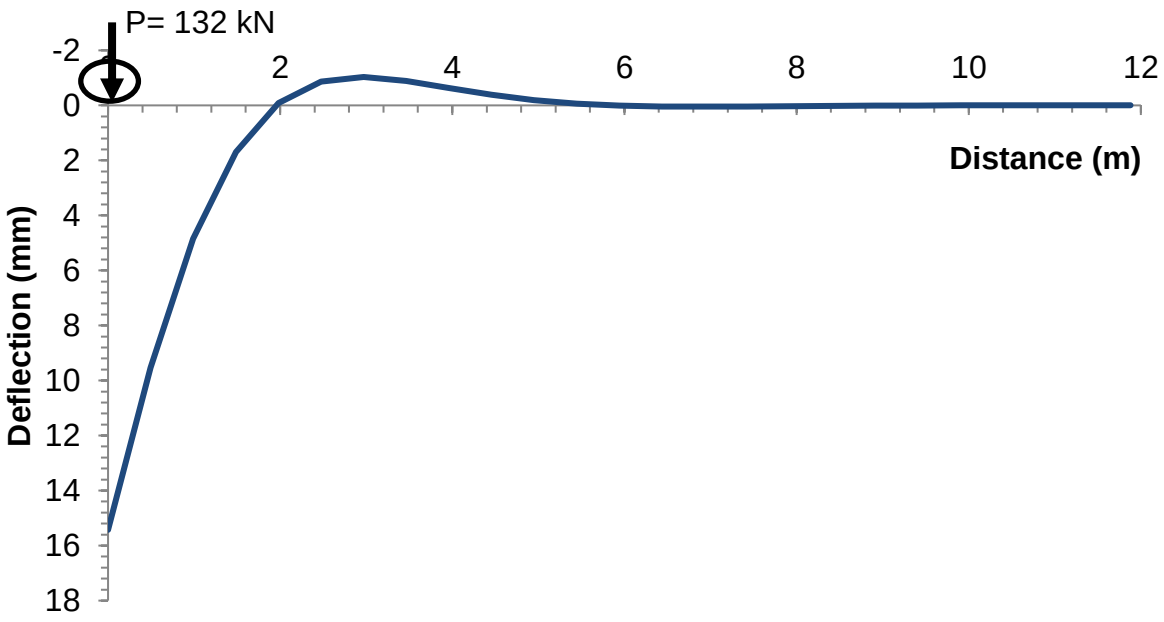

Figure 5.11 Rail deflection for single axle loading near railway joint

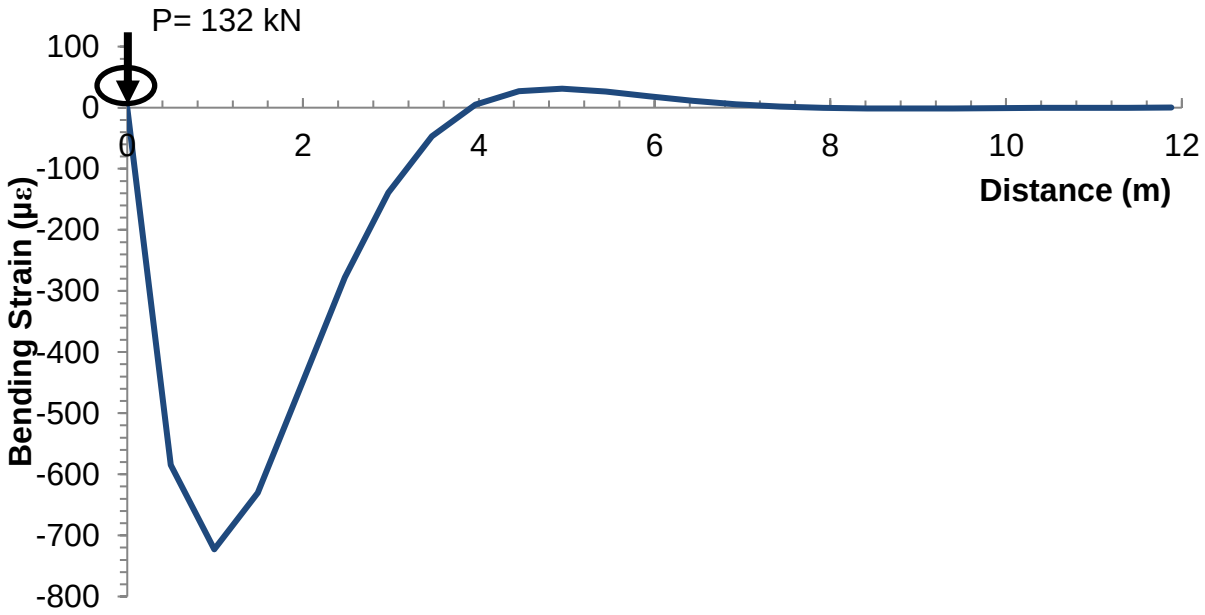

Figure 5.12 Rail bending strain for single axle loading near railway joint

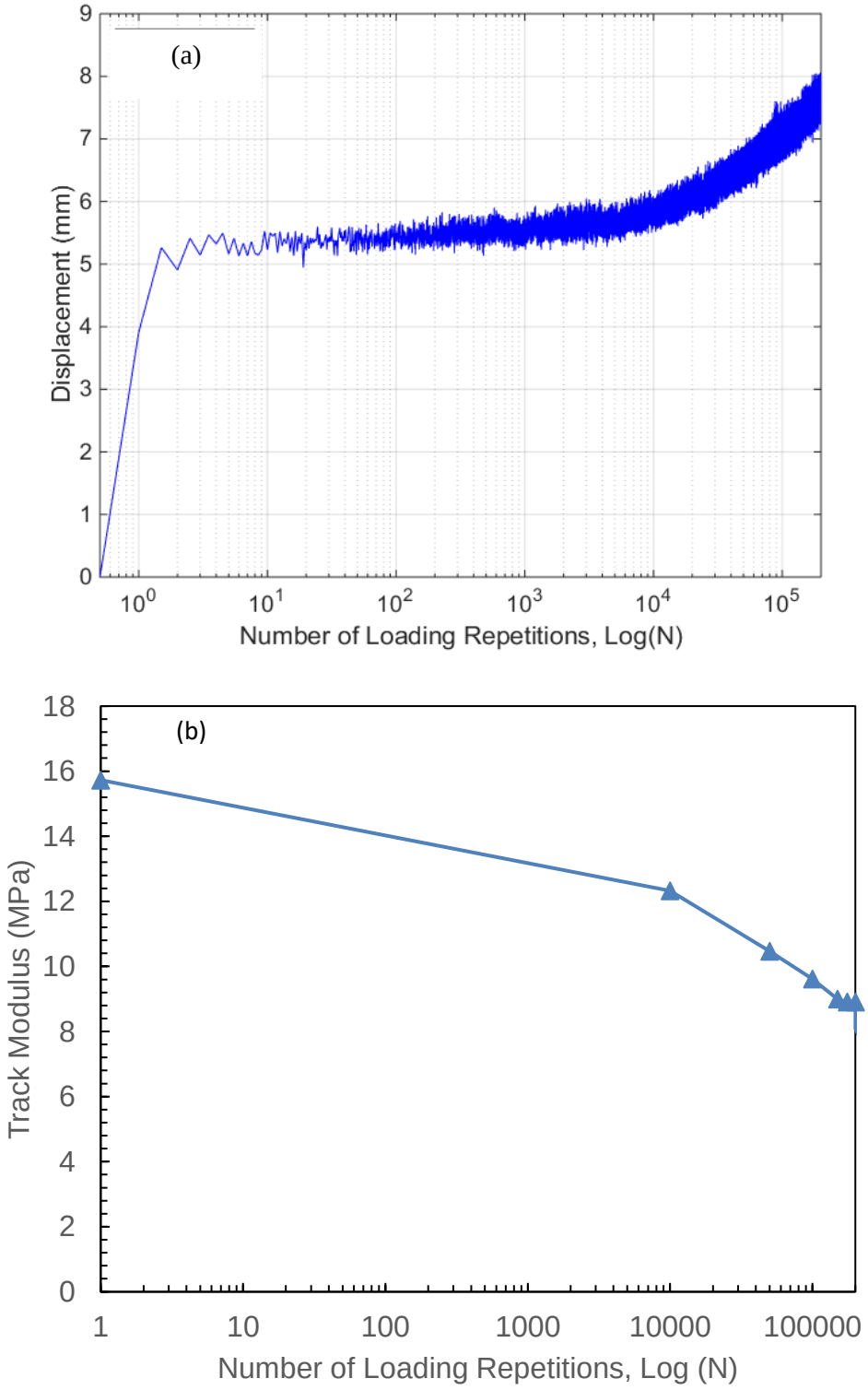

Figure 5.13 (a) LVDT measurements, and (b) calculated track modulus

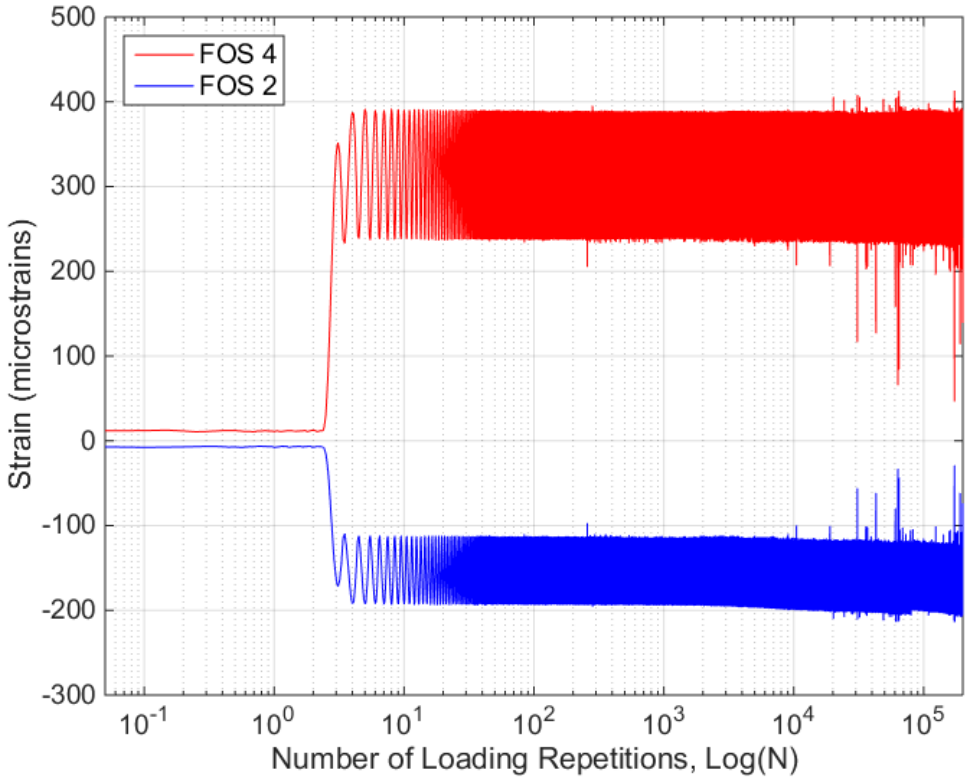

Figure 5.14 FO sensors strain deformation measurements

CHAPTER 6: Summary and Conclusion

6.1 Major Findings

Time Domain Reflectometry (TDR) testing was conducted in chapter 2 to assess the electromagnetic (EM) properties (i.e., real relative permittivity and electrical conductivity) of clean and fouled ballast under different water content conditions, to evaluate the validity of using TDR for calibrating the GPR data, particularly in fouled ballast with high moisture content environments. The spatial sensitivity of TDR probes was assessed to optimize the design of TDR probes in order to obtain accurate dielectric permittivity measurements and estimation of the depth of contrasting layers along the length of the TDR probes. TDR measurements were taken to characterize the effect of ballast gradation and mineralogy on the EM properties of clean ballast. TDR results shows that the relative dielectric permittivity ranges from 3 to 5, whereas the electrical conductivity is very low and mainly constant for different clean ballast types. TDR was successfully able to determine the depth of fouled ballast for specimens that have high volumetric water content. In particular, multiple reflections occur in specimens with high impedance contrast layers. Thus, a relationship between relative dielectric permittivity of clean ballast (ε_{rb}) and the apparent length of the first reflected waveform (L_{ab}) is established to calculate the depth of clean ballast and therefore estimate the depth to the fouled layer. An increase of the relative dielectric permittivity is observed with the increase of fouling depth at different volumetric water contents. The increase in fouling layer thickness decreases the porosity in the ballast layer and as a result the relative dielectric permittivity increases. Electrical conductivity was used successfully differentiate between various types of ballast fouling.

In chapter 3, a field implementation of the technique was conducted on a mainline track section in Dayton, Illinois. TDR and GPR testing was conducted to assess the electromagnetic (EM) properties (i.e., real relative permittivity and electrical conductivity) of railway substructure. TDR successfully distinguished multiple layers in the railway substructure and gave an estimation of the wave velocity of the substructure. Dynamic cone penetrometer (DCP) testing validated the use of TDR to calibrate GPR data and to allow the imaging of the extent of ballast fouling that has contributed to ongoing deformation along two sections of rail track in Dayton, IL.

Full Scale Track Model (FSTM) was developed in chapter 4 to assess the methodology of creating an early warning system that would allow railway engineers to develop a symptomatic approach to ballast maintenance procedures. The methodology extends the use of deformation monitoring instruments (e.g., fiber optic (FO) sensors and LVDTs) coupled with Electromagnetic (EM) surveying: Ground penetrating radar (GPR) and a time domain reflectometry (TDR). FSTM aimed at characterizing measured deformation, and EM properties of railway substructure with variance parameters such as: fouling type, fouling depth, moisture content, and number of loading repetitions. FSTM fouled with kaolinite clay showed the highest deformation among all experiments, whereas FSTM with a clean ballast showed the lowest. Indicating that shear strength of the ballast layer is controlled by the shear strength of fouling materials at the ballast particles contact points. Abrupt increase in track deformation is noticed with the increase of moisture content and fouling depth. The increase in moisture content of fouling materials at the contact points of ballast increases the potential of excess pore water generation at the contact during cyclic loading resulting in a sudden reduction of shear

strength and an increase in deformation. Good correlations were found between EM properties and (a) porosity, (b) volumetric water content, (c) fouling depth, (d) fouling index, (e) non-clay fouling index (f) and clay fouling index. Visual and geotechnical investigation was performed on each FSTM experiment after 8·105 loading repetitions. Ground truthing the FSTM has successfully verified GPR and TDR results. The combination of rail track deformation and ballast fouling properties measurements provide an opportunity to assess not only the effect but also the cause of the complex rail track structure deterioration process.

FSTM deformation results indicate that railway track is settling as a rigid body and a special consideration should be taken into account when instrumenting the rail. Furthermore, FO sensors only measured constant strains values and did not provide any indication of plastic strain accumulation in the ballast layer with the increase of loading repetitions. Whereas, LVDTs settlement measurements reflected the amount and rate of plastic deformation accumulated with the increase of loading repetitions. A review of the railway mechanical response in chapter 5 suggested that FO sensors should be installed on the rail's flange to capture the maximum bending strain along the railway profile at a critical locations for a minimum distance of 18 m with a separation of one tie (i.e. 0.495 m for wooded ties and 0.6 m for concrete ties) for a total of 36 sensor to avoid this issue. This number of sensors to instrument only 18 m portion of the track is considered economically unfeasible and economical alternatives might be used.

APPENDIX A: FSTM GPR Radargram Images

FSTM with Silica Sand Fouling

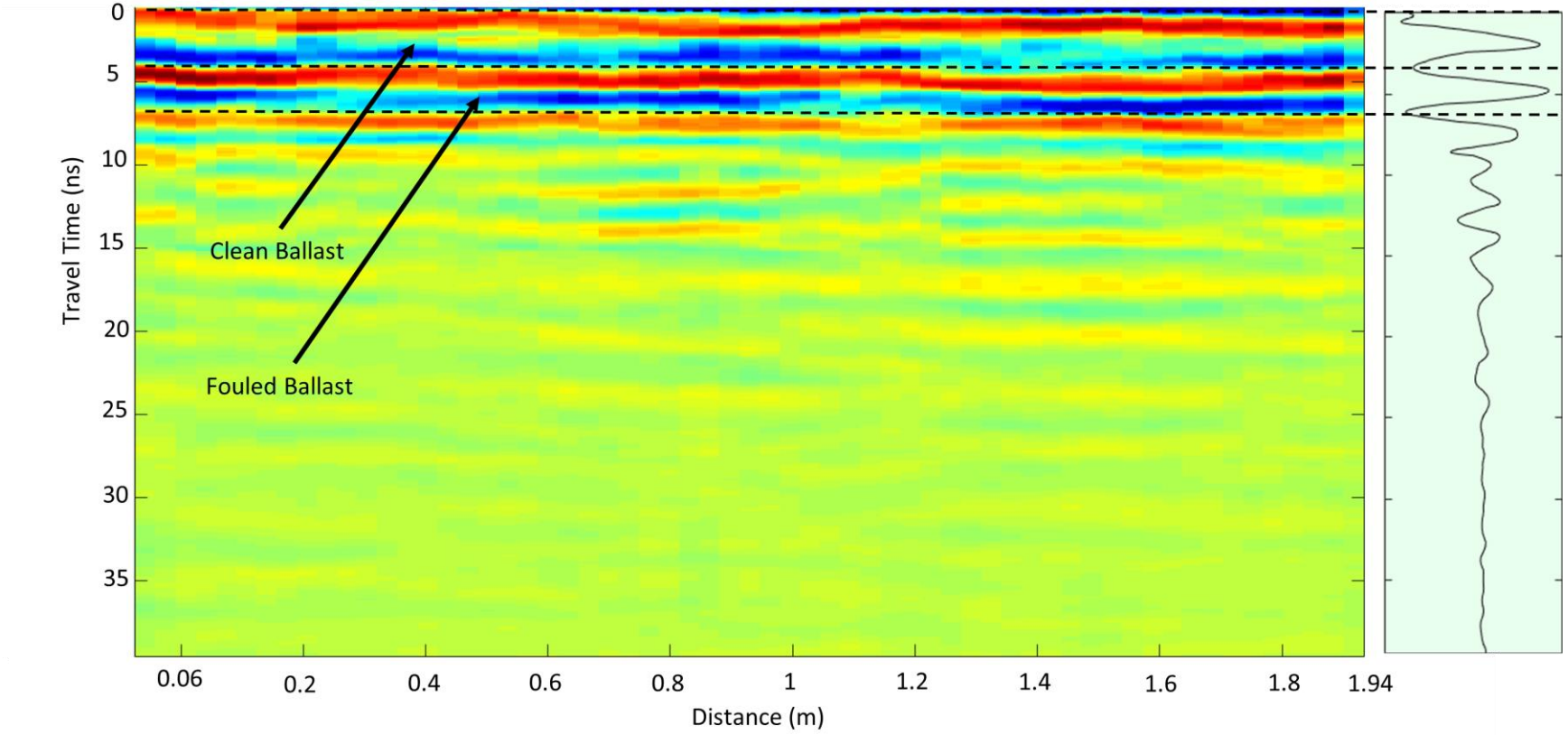

Figure A.1 S-1-Start

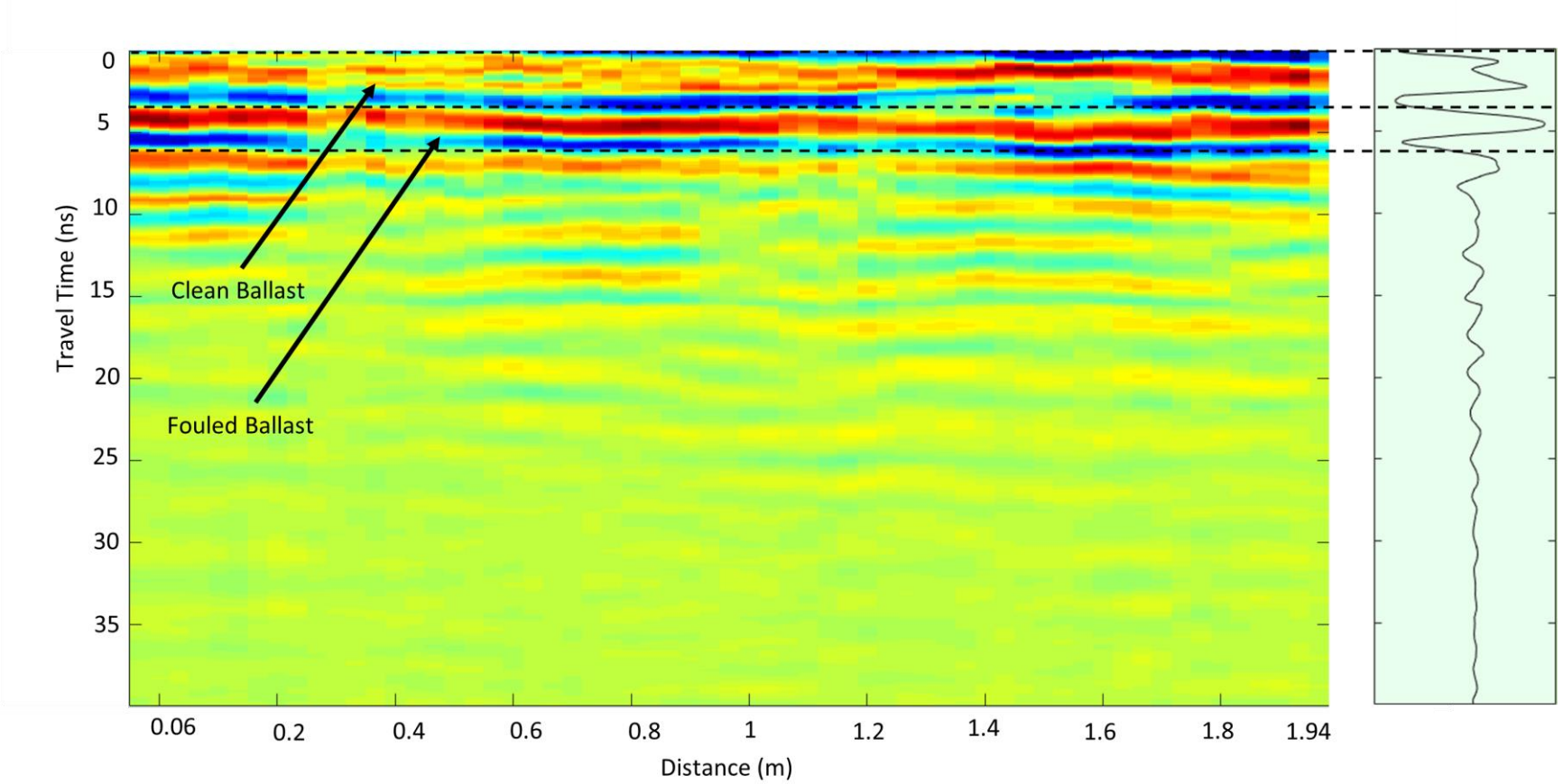

Figure A. 2 S-1-End

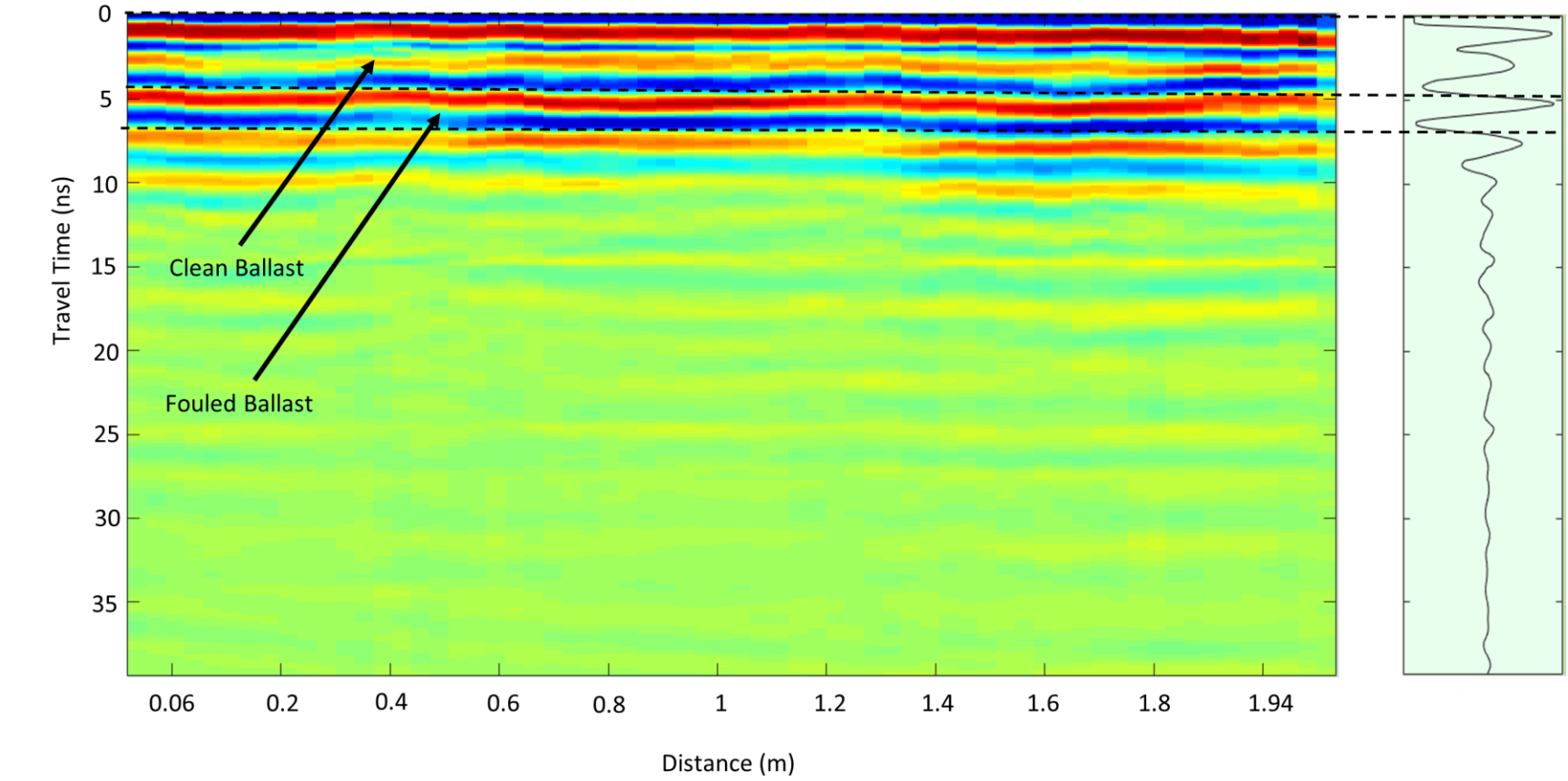

Figure A. 3 S-2-Start

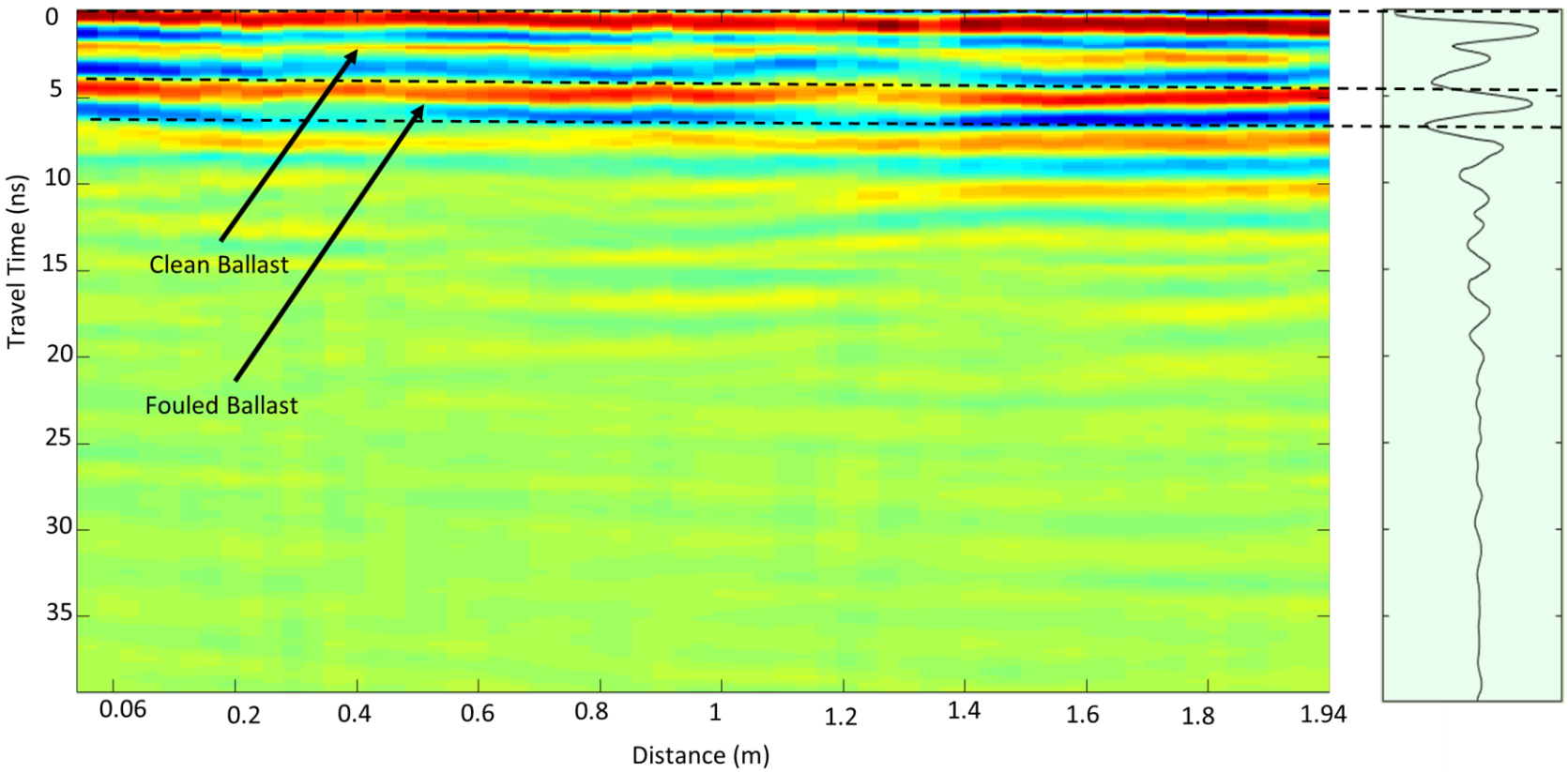

Figure A. 4 S-2-End

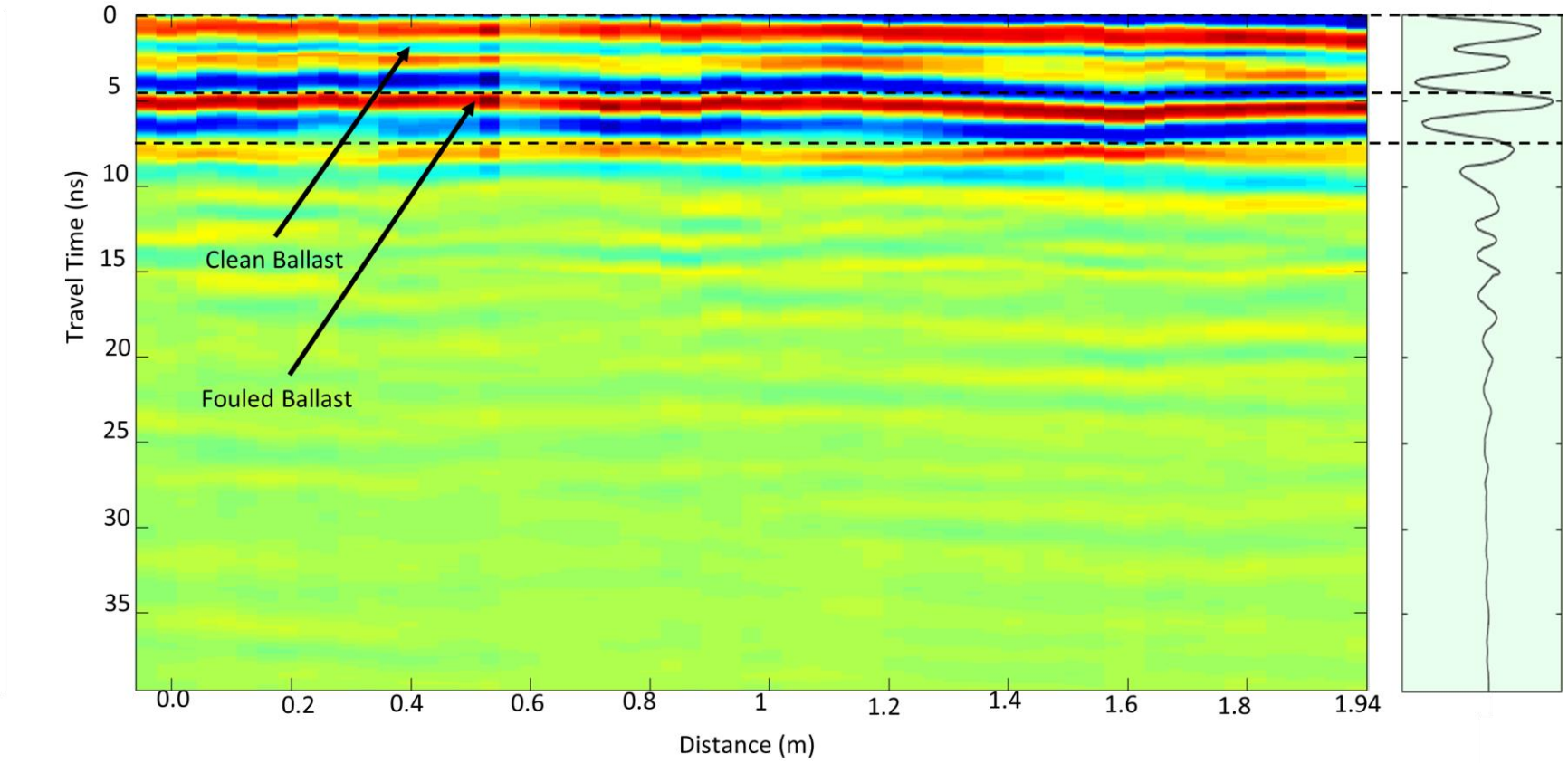

Figure A. 5 S-3-Start

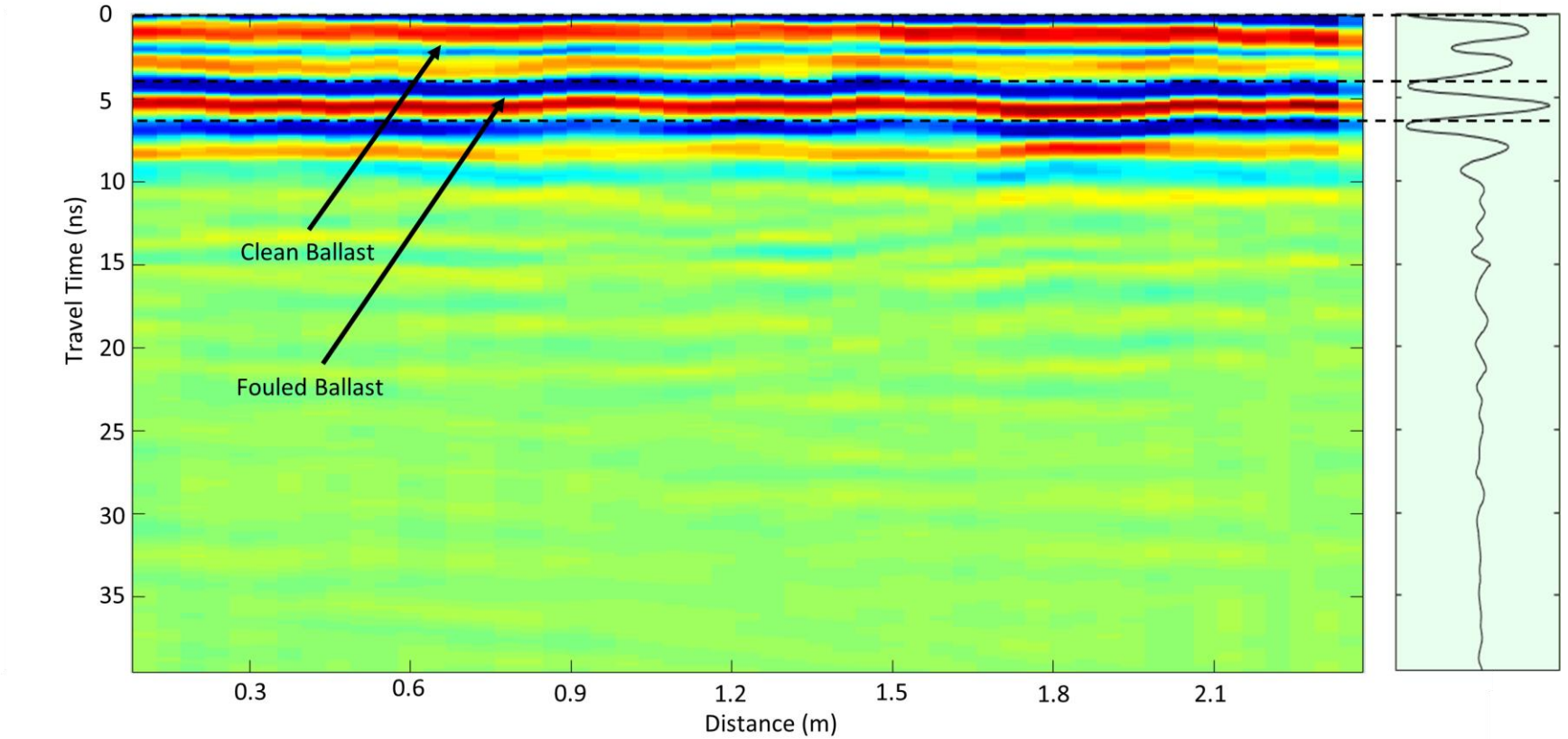

Figure A. 6 S-3-End

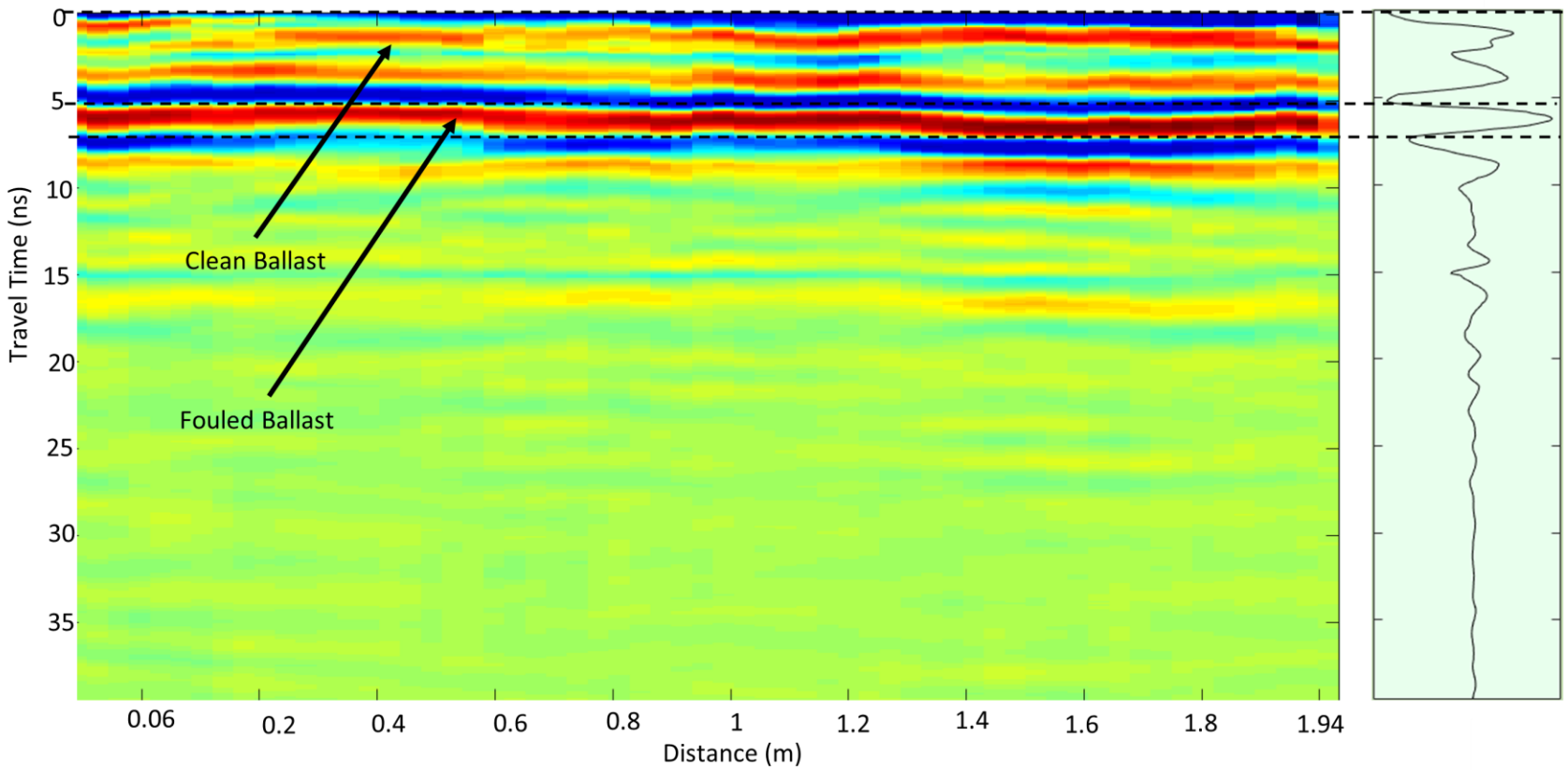

Figure A. 7 S-4-Start

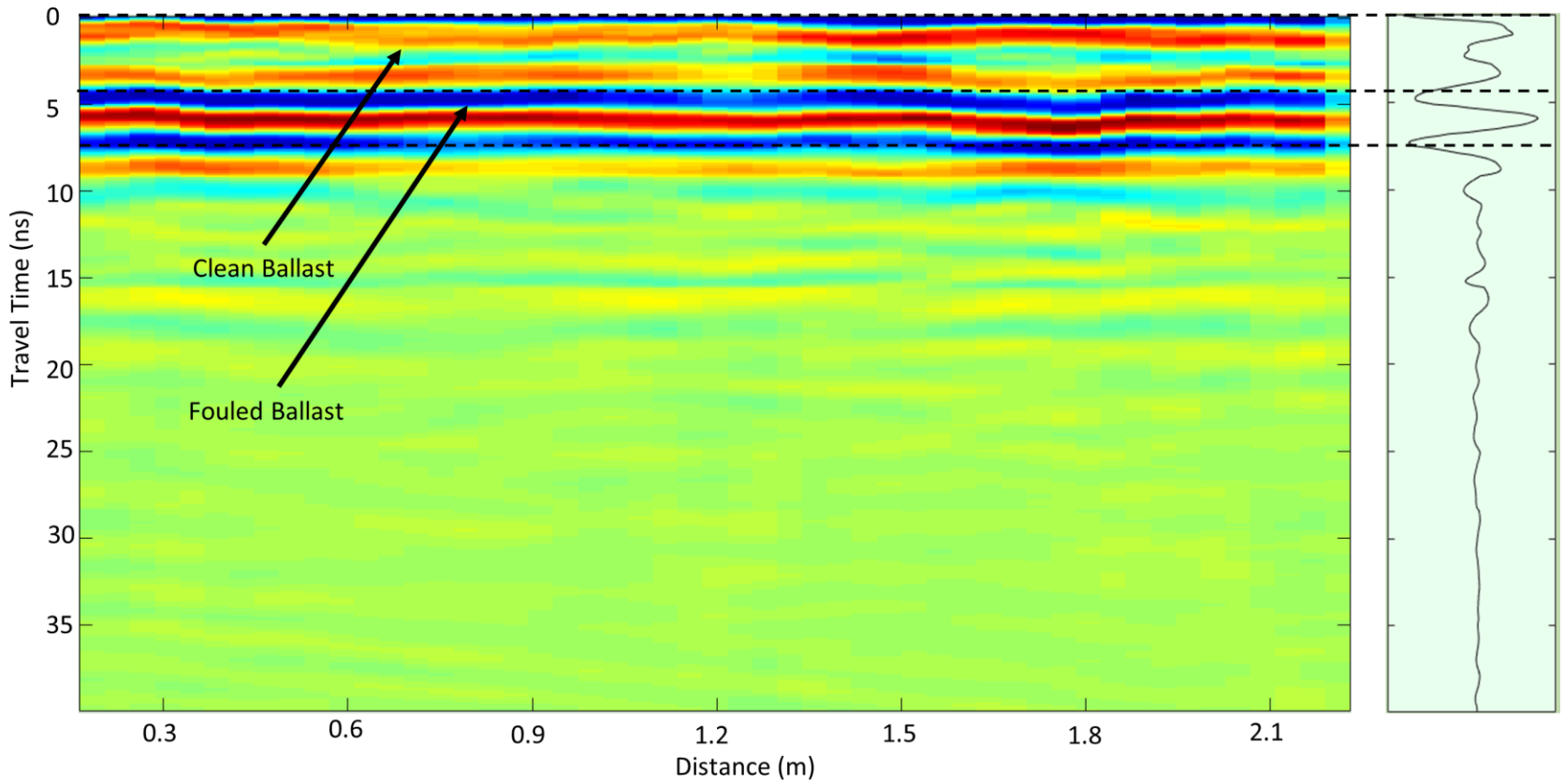

Figure A. 8 S-4-End

FSTM with Mineral Fouling

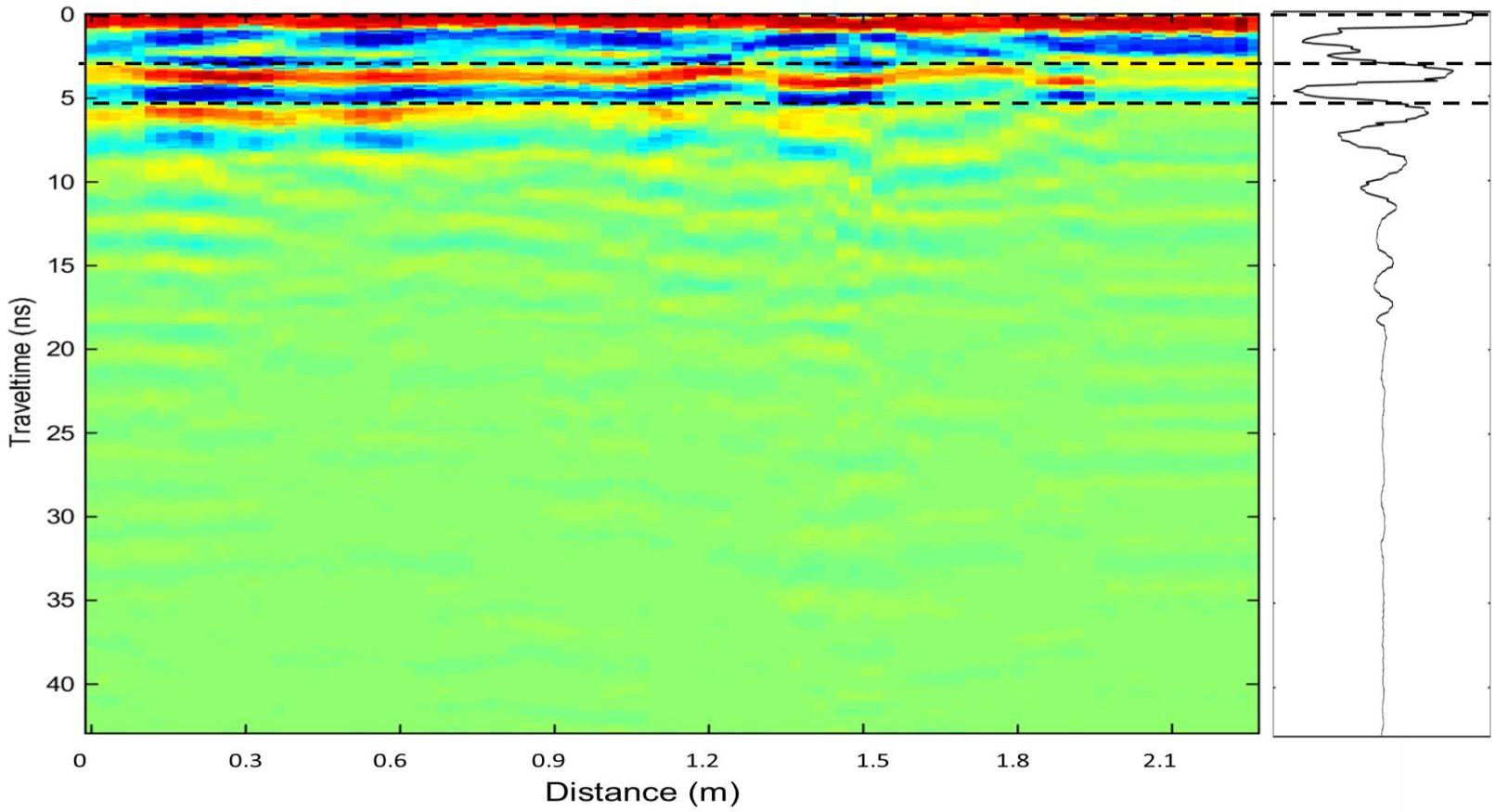

Figure A. 9 K-1-Start

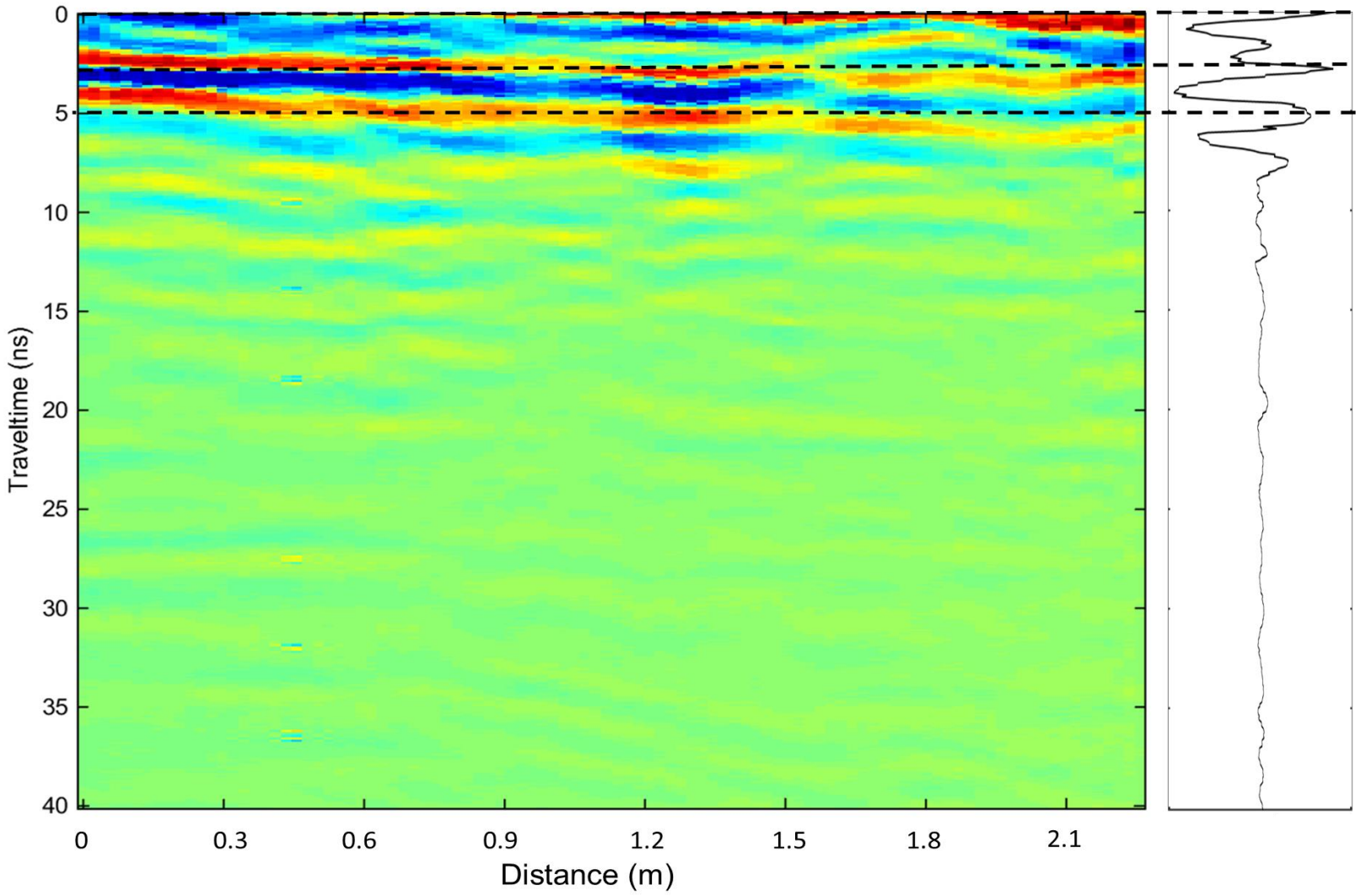

Figure A. 10 M-2-End

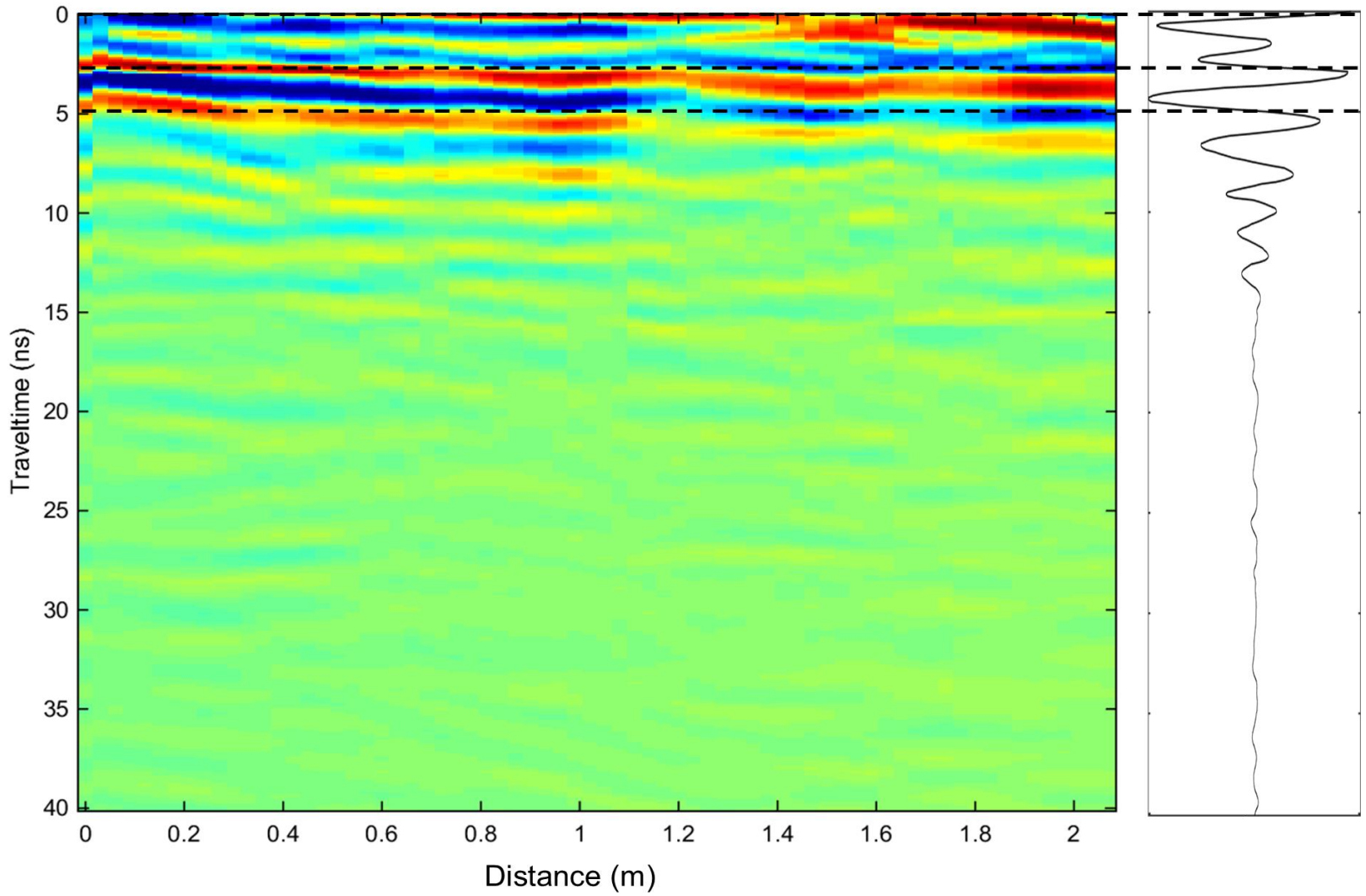

Figure A. 11 M-3-Start

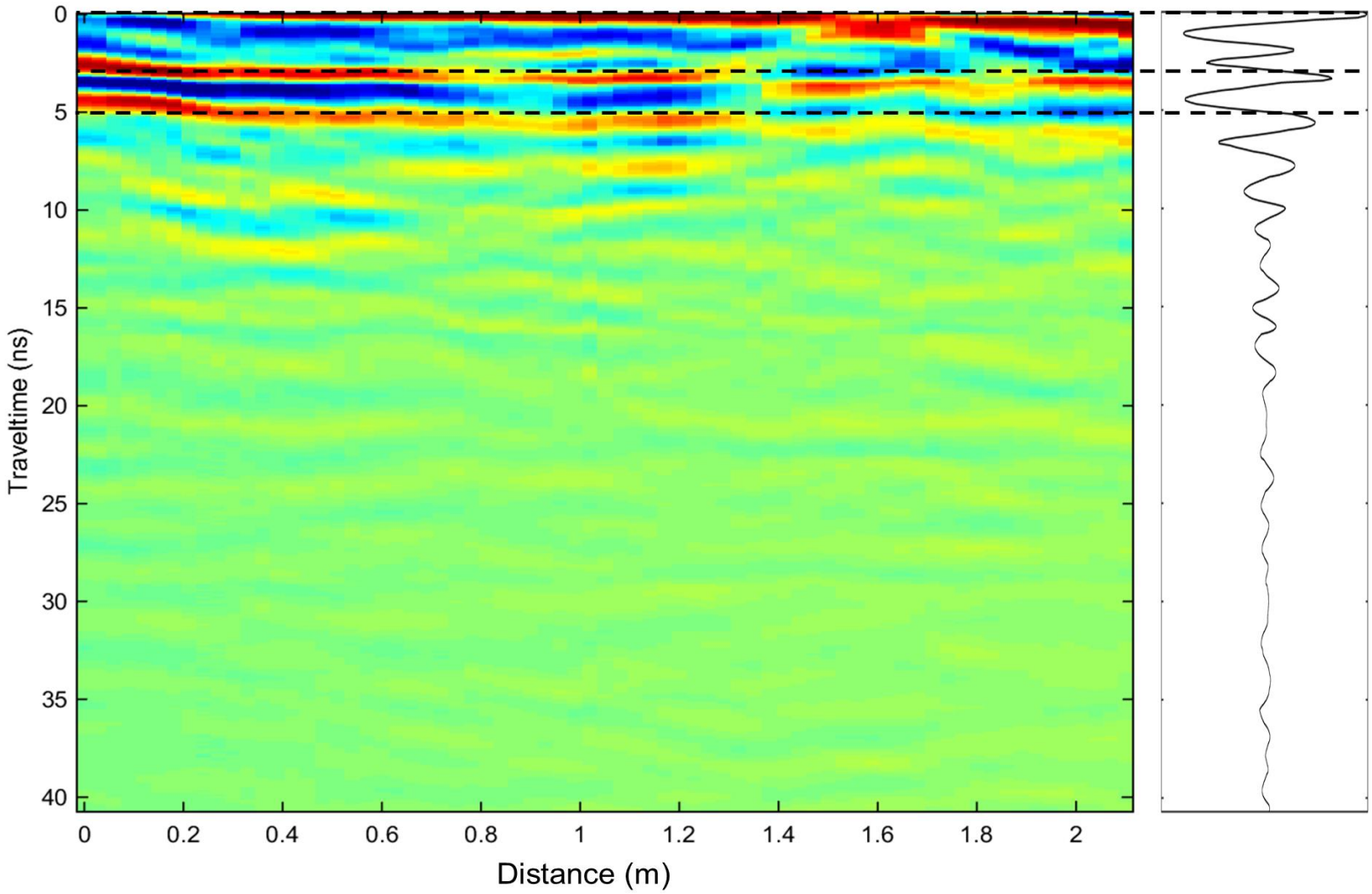

Figure A. 12 M-4-End

FSTM with Kaolinite Clay Fouling

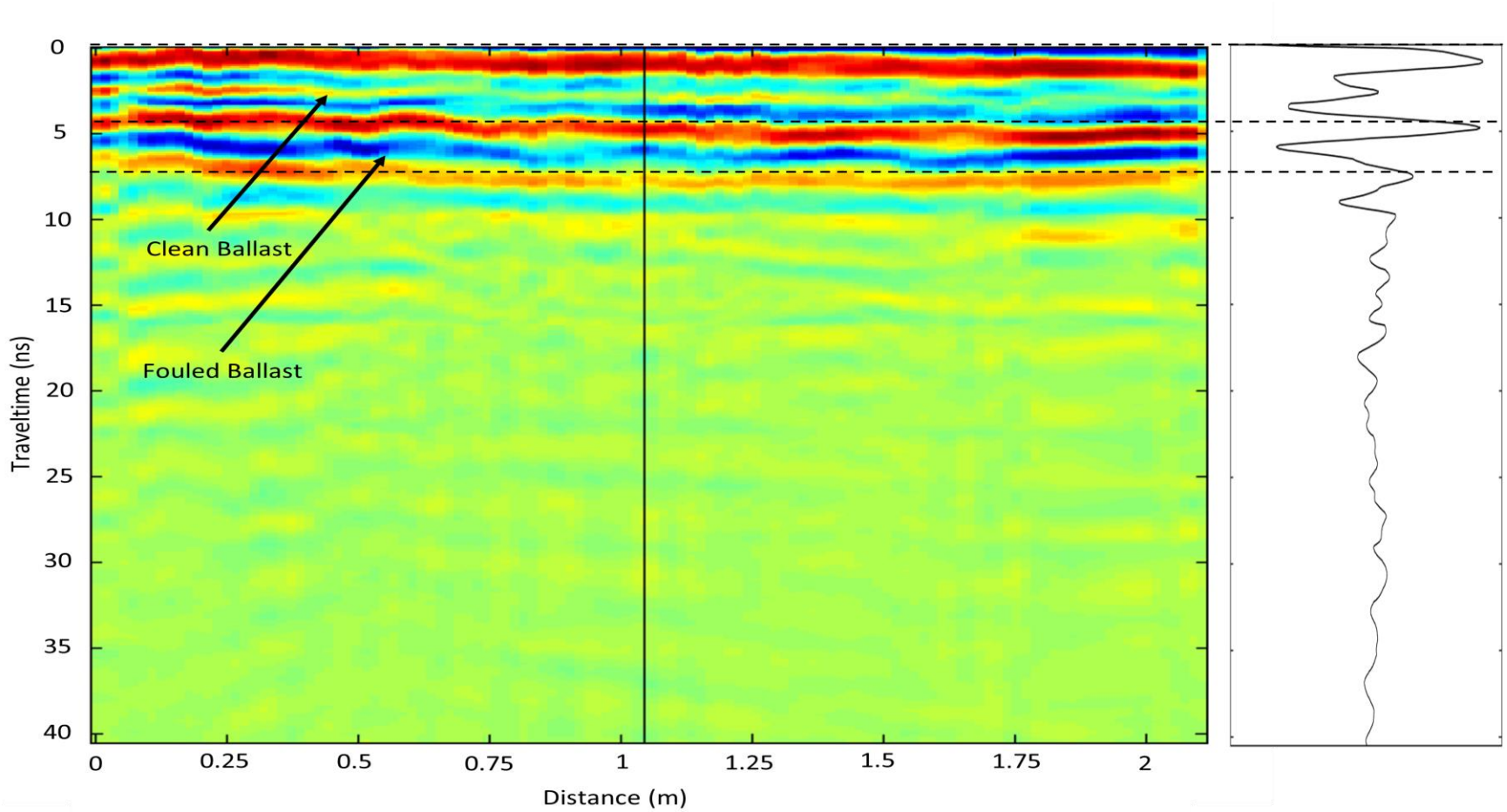

Figure A. 13 K-1-Start

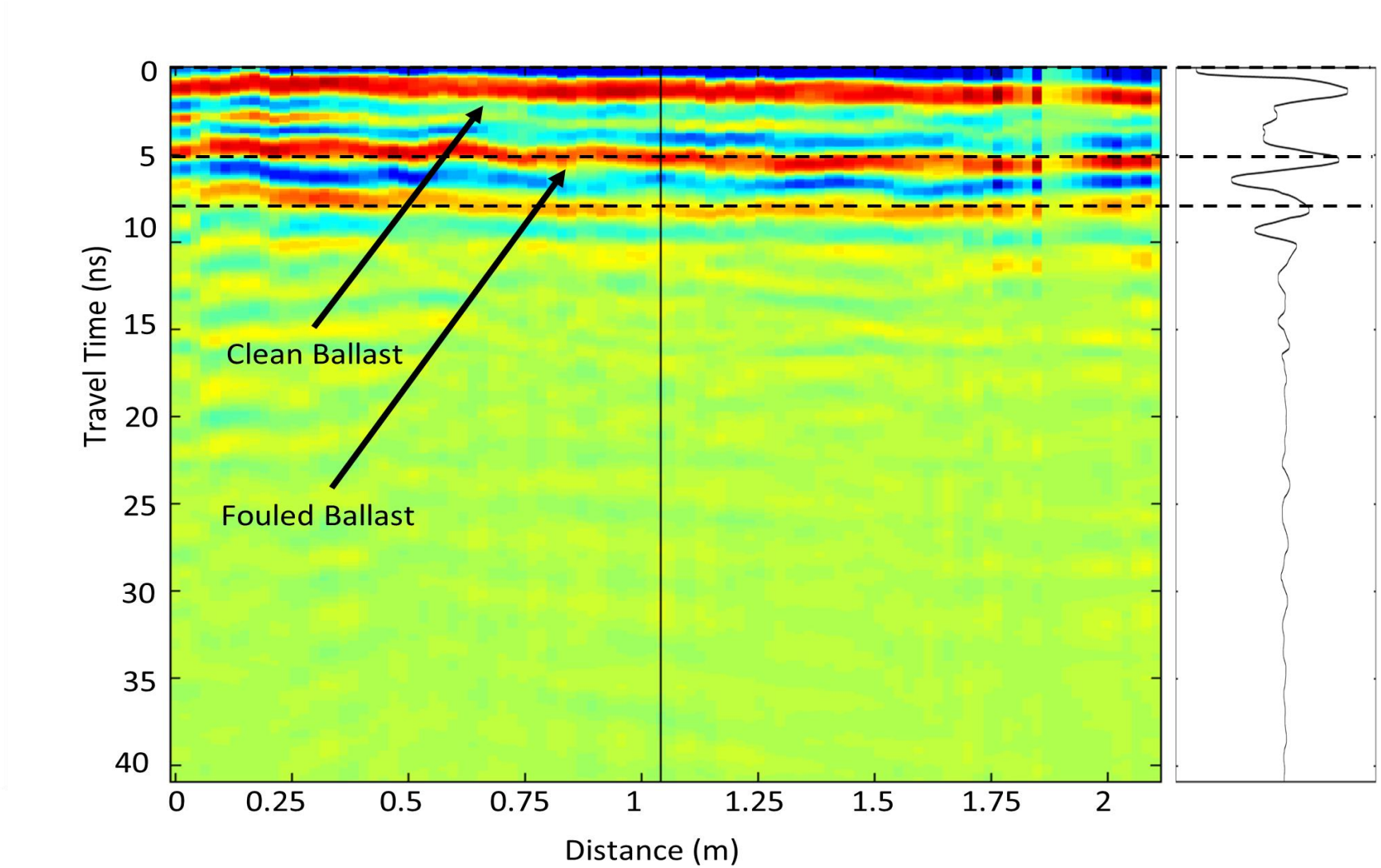

Figure A. 14 K-1-End

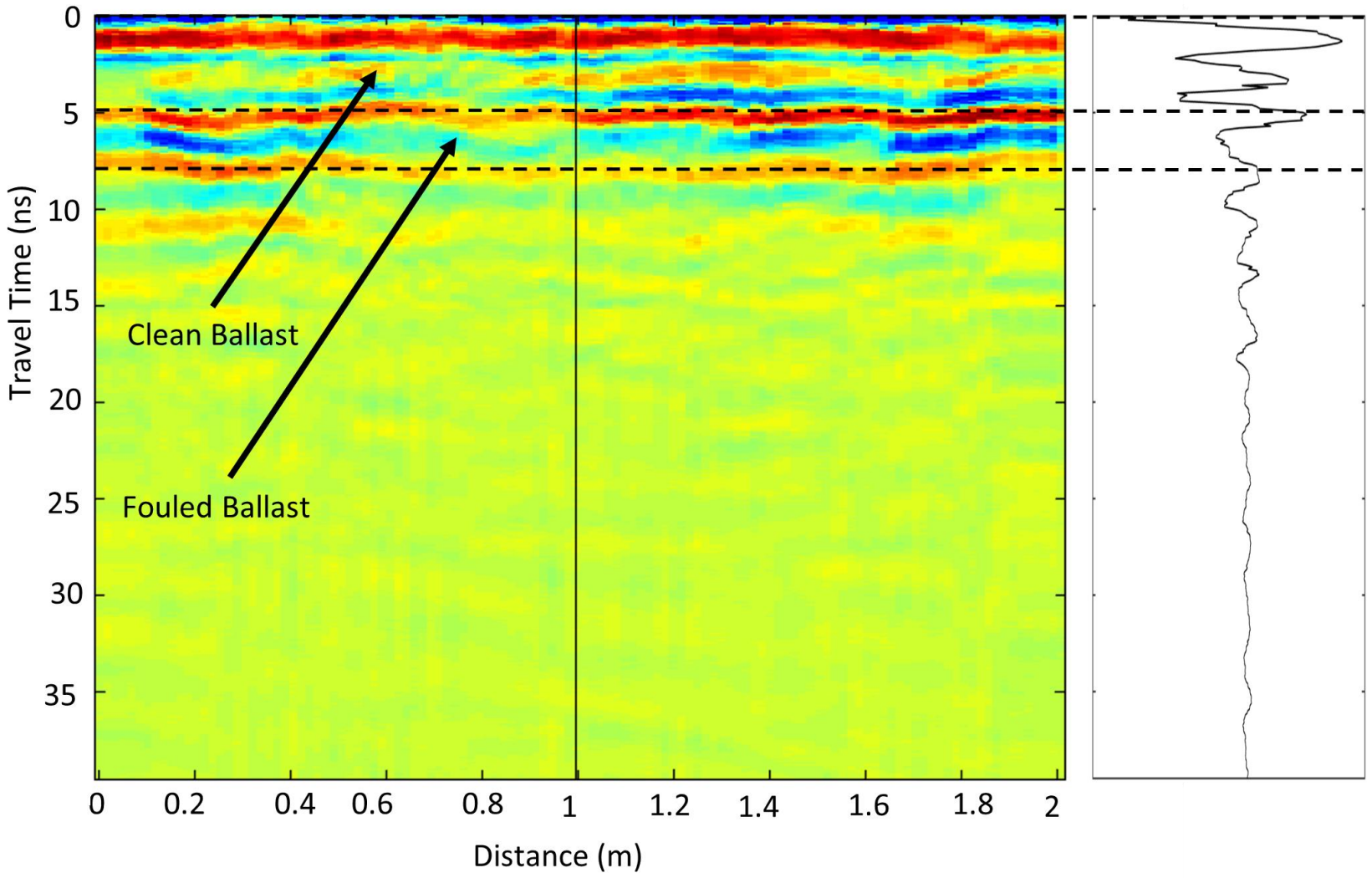

Figure A. 15 K-2-Start

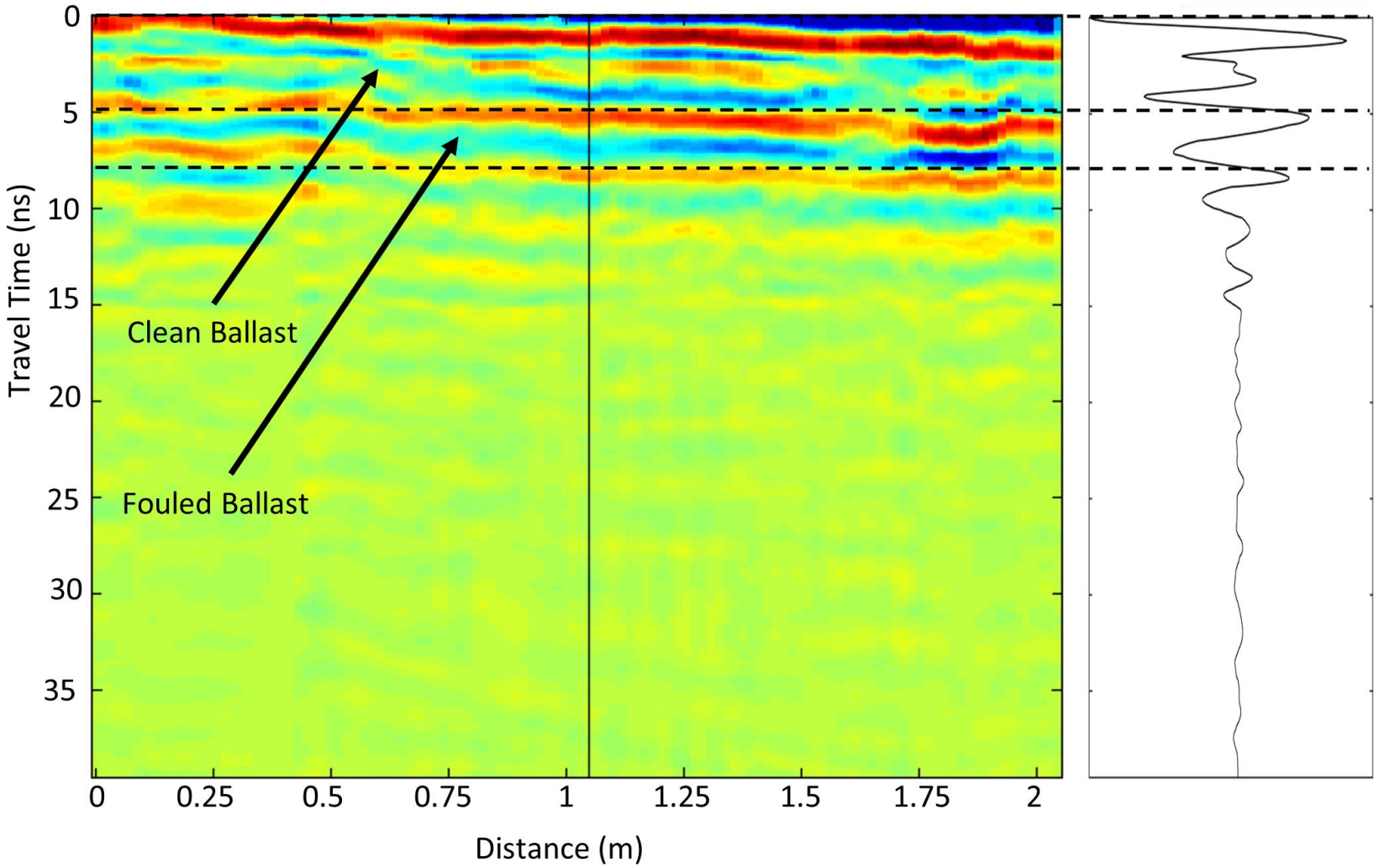

Figure A. 16 K-2-End

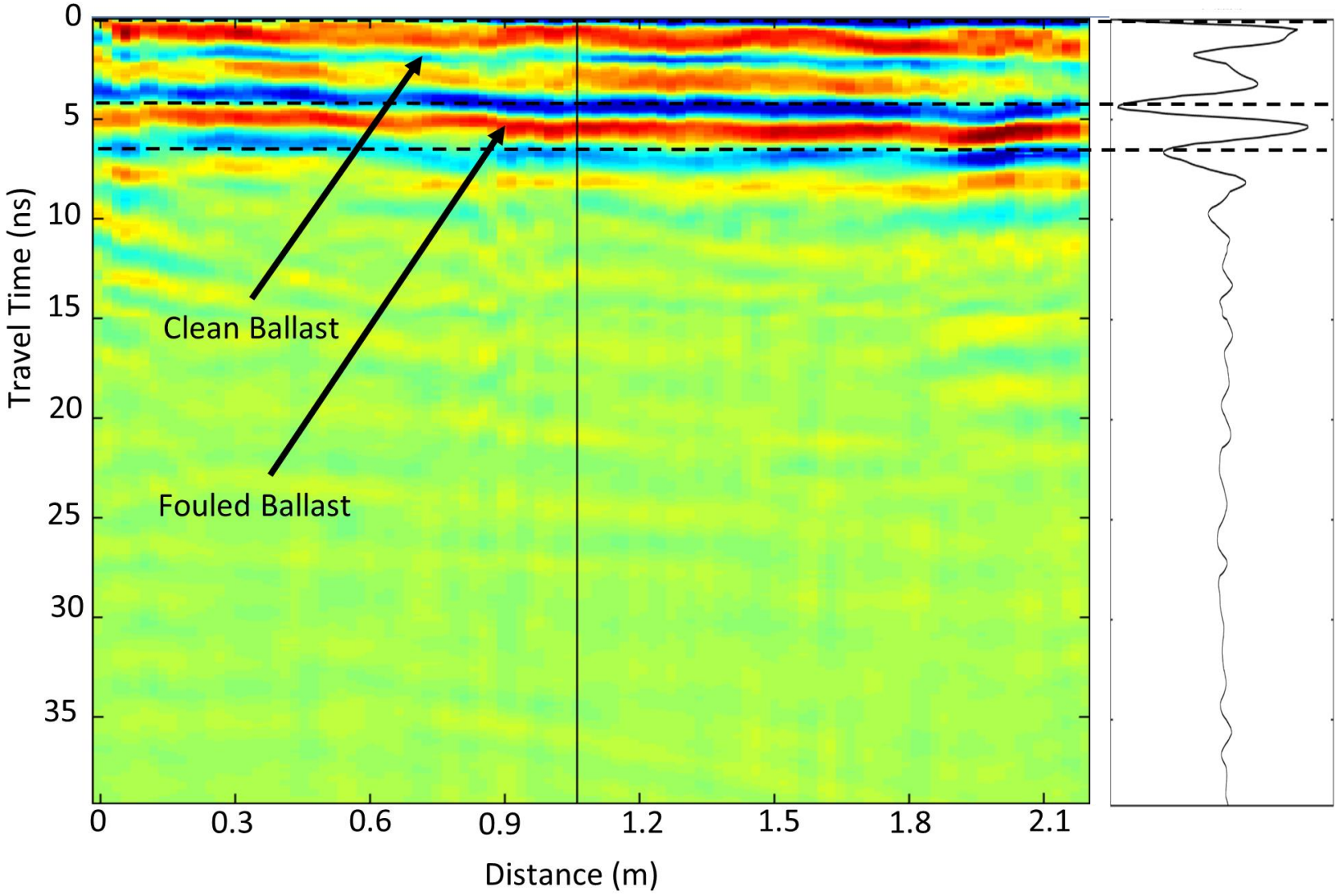

Figure A. 17 K'-1-Start

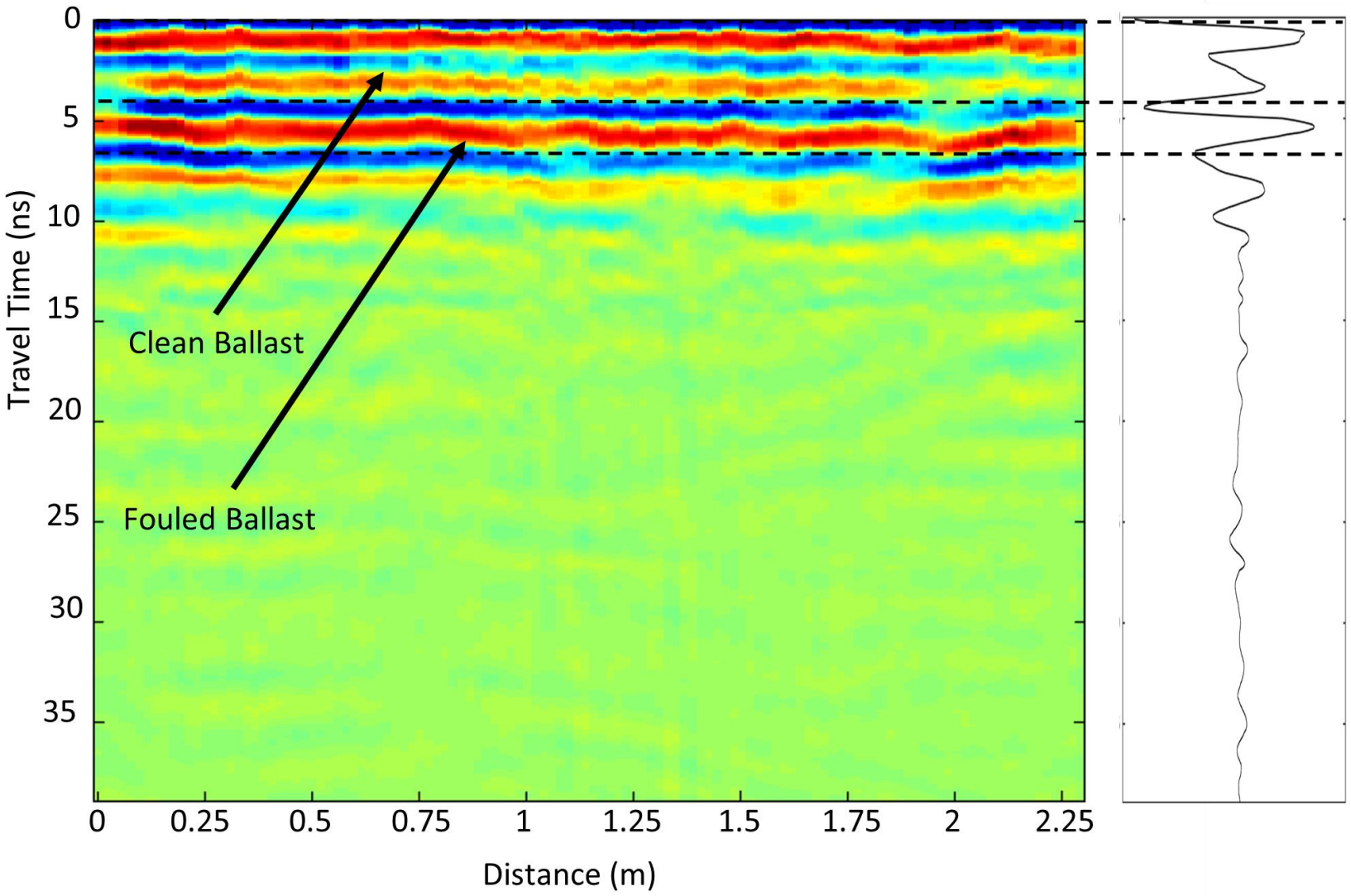

Figure A. 18 K'-1-End

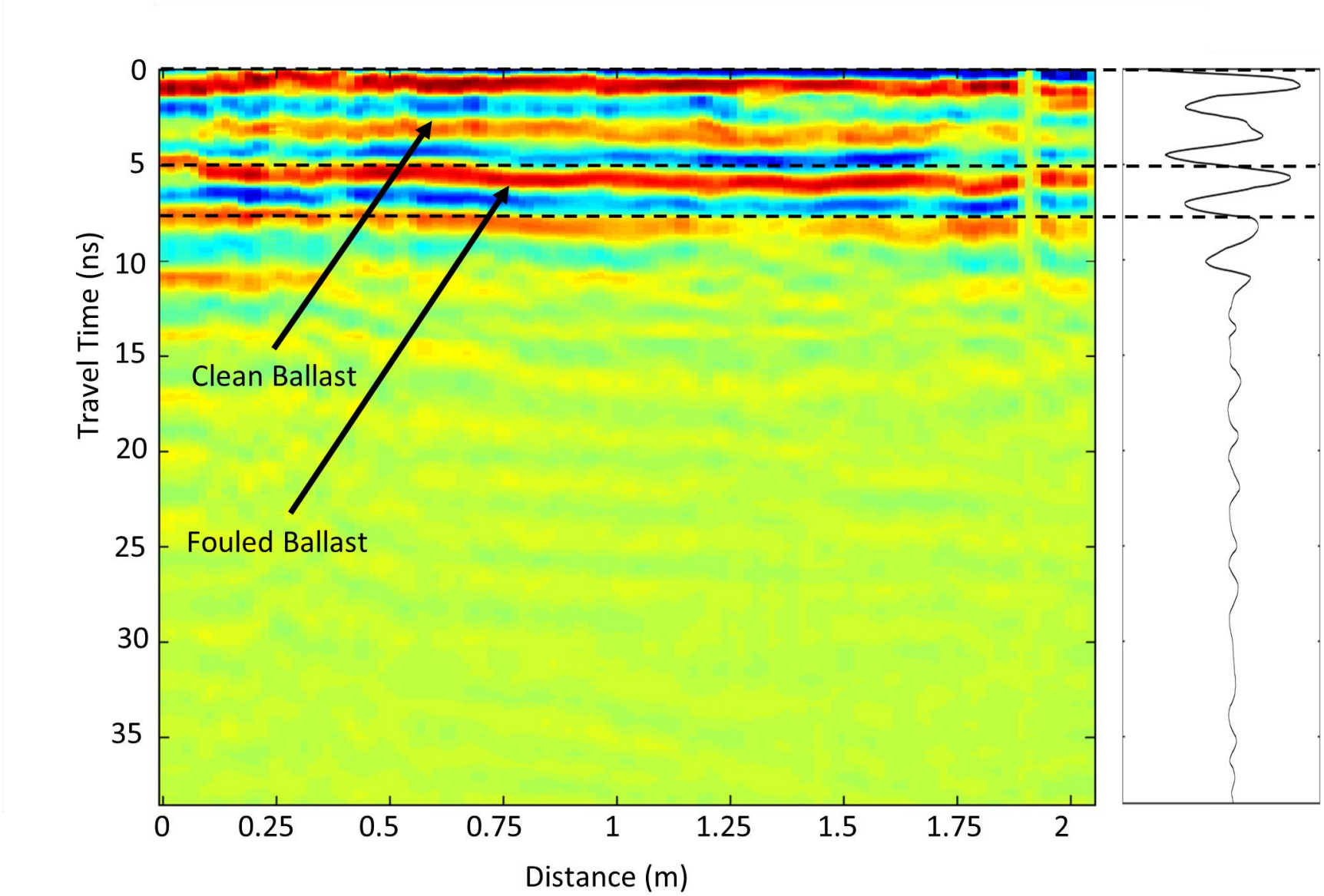

Figure A. 19 K'-2-End

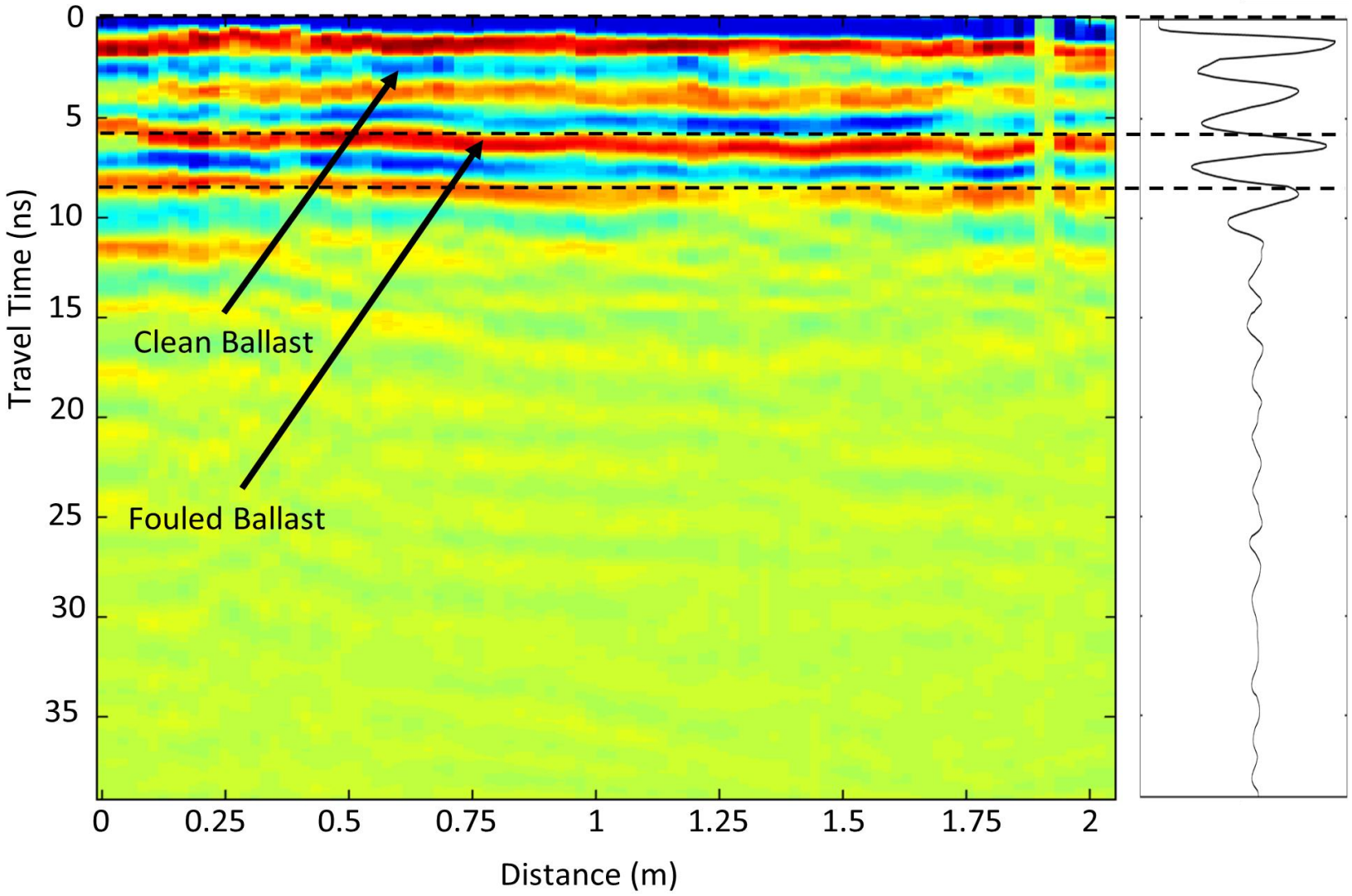

Figure A. 20 K'-2-End

APPENDIX B: TDR TRACES

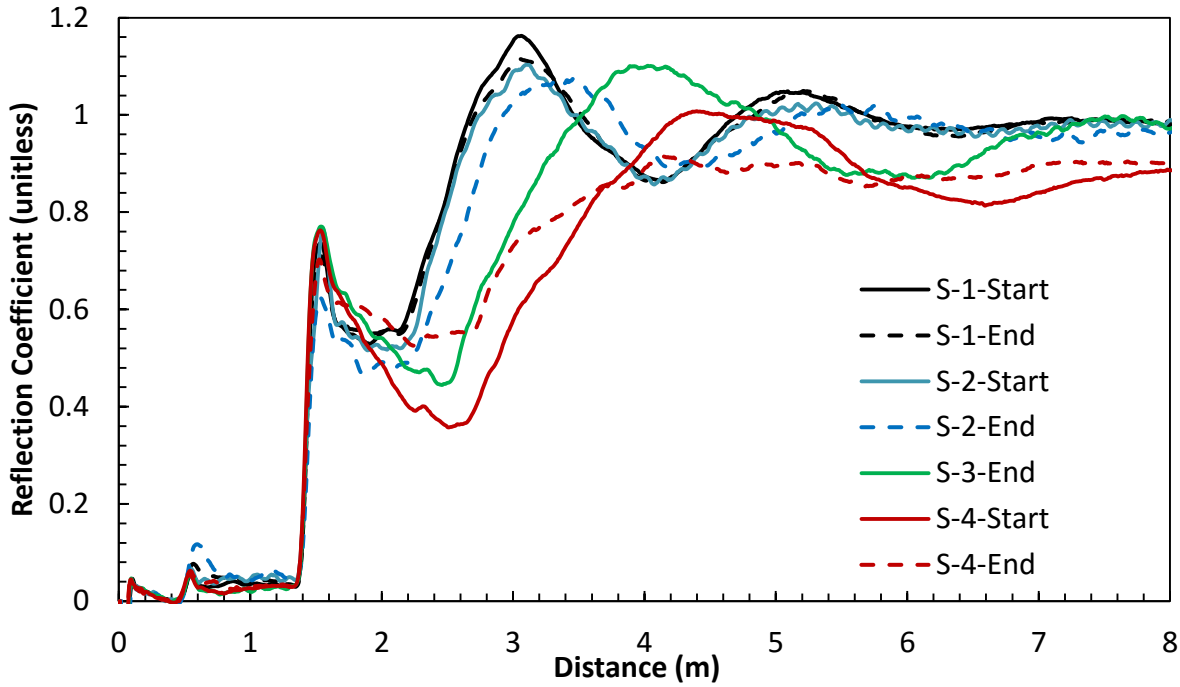

Figure B. 1 TDR waveform for FSTM fouled with Silica sand.

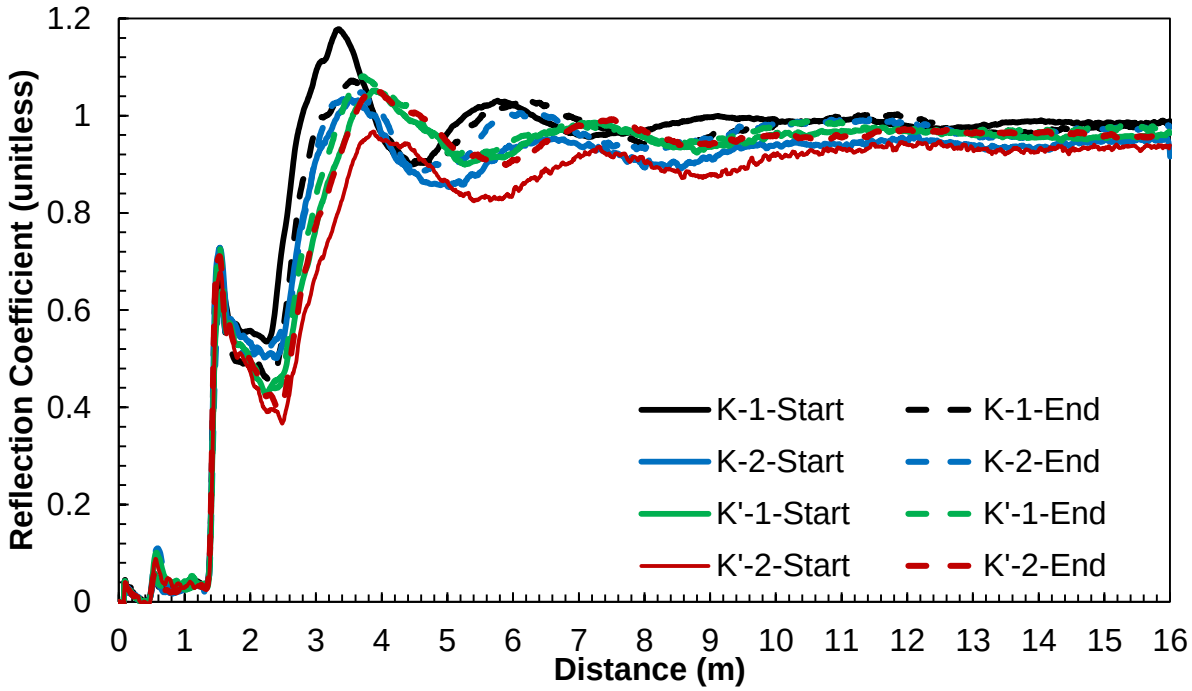

Figure B. 2 TDR waveform for FSTM fouled with kaolinite clay.

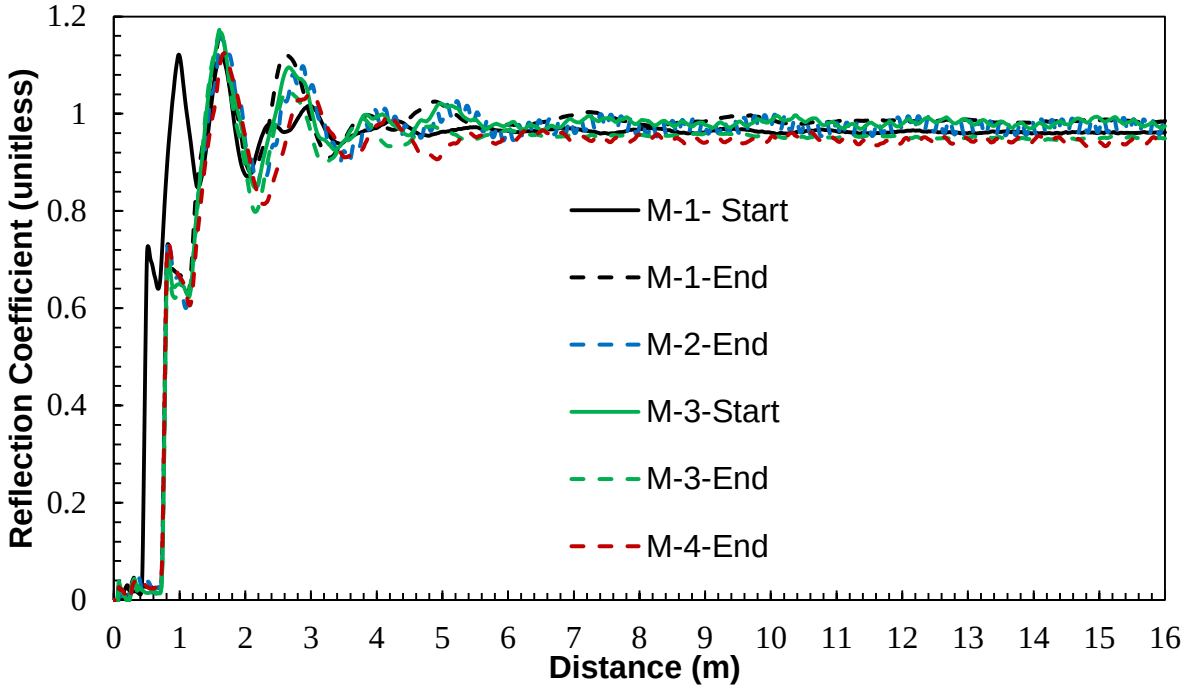

Figure B. 3 TDR waveform for FSTM fouled with minerals.

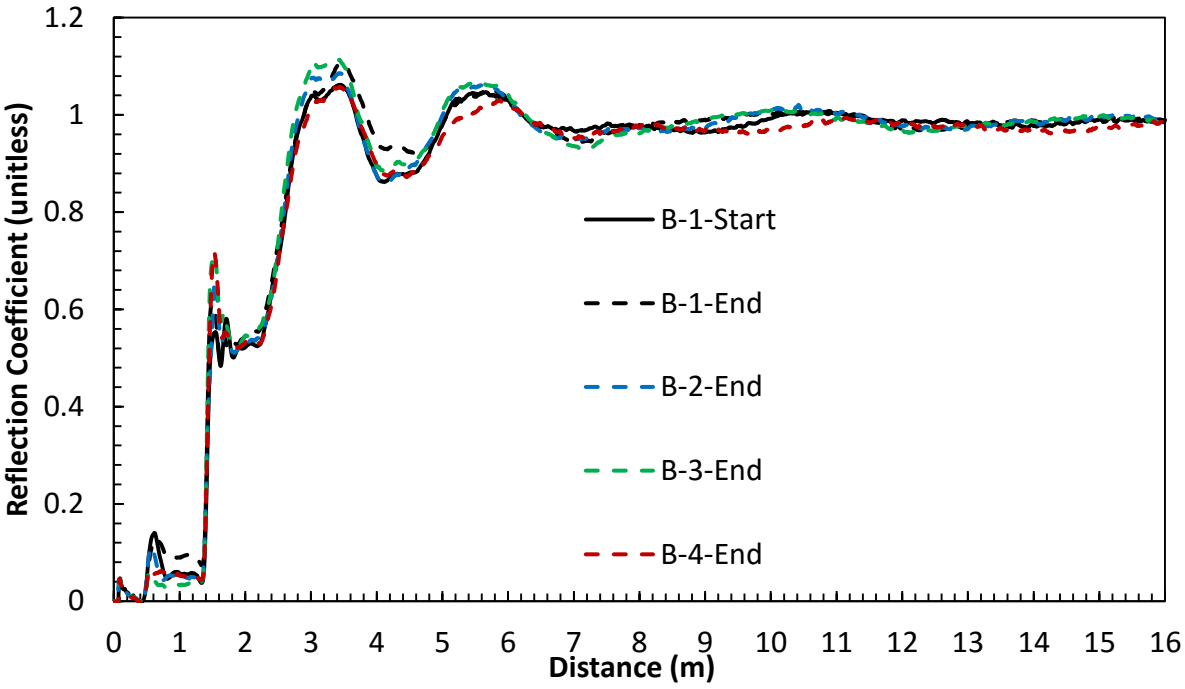

Figure B. 4 TDR waveform for FSTM with clean ballast.

APPENDIX C: FO Sensors Input Data

MICRON OPTICS Sensor Information Sheet

os3155 | Compensated Optical Strain Gage

Part # os3155-1522-1526-1UT-1UT

Serial # C307126

Nominal Wavelength, λ_{0Temp} (nm) @22°C (Temp FBG) 1521.734

Nominal Wavelength, $\lambda_{0Strain}$ (nm) @22°C (Strain FBG) 1526.710

Certified by:

Variable	Description	Value	Units
F_G	Gage Factor @22°C	.620	-
$\Delta\lambda_S$	Wavelength Shift (Strain)	Interrogated	nm
λ_{0S}	Nominal Wavelength (Strain)	Initial Value	nm
S_T	Temp. Sensitivity @22°C	1.833×10^{-5}	-
$\Delta\lambda_T$	Wavelength Shift (Temp)	Interrogated	nm
λ_{0T}	Nominal Wavelength (Temp)	Initial Value	nm
CTE_S	CTE of Test Specimen	User Defined	µm/m-°C
CTE_T	CTE of Temperature Probe	16.6	µm/m-°C

Strain (mechanically induced µm/m):

$$\varepsilon = 10^6 \left[\frac{(\Delta\lambda/\lambda_0)_S - (\Delta\lambda/\lambda_0)_T}{F_G} \right] - \frac{(\Delta\lambda/\lambda_0)_T}{S_T} (CTE_S - CTE_T)$$

Thermal Output and Temperature Compensation

Fiber Bragg grating (FBG) based strain gages respond to both strain and temperature. Temperature induced strain results from a combination of two factors.

1) Thermal expansion of the substrate on which the gage is mounted.
2) Thermally induced index of refraction changes in the FBG.

Both factors affect the FBG's center wavelength.

Several methods are available to decouple strain and temperature components in measurements using this gage. Popular methods involve using FBGs to measure change in temperature or employing dummy FBG strain gages (as with conventional electronic strain gages).

For additional information about temperature compensation techniques and converting wavelength values to strain and temperature, see:

http://www.micronoptics.com/support_downloads/Sensors/

Micron Optics Quality and Performance

TUNED

Products displaying the "Micron Optics Tuned" logo include Micron Optics tunable technologies thus ensuring high quality and performance. Certified sensors have been tested and qualified for use with Micron Optics Sensing Instruments.

Qualification Statement

CERTIFIED ISO 9001:2008

This sensor has been manufactured using procedures and materials documented under Micron Optics, Inc's ISO 9001:2008 qualification process.

Patent Certification

Micron Optics sensors and sensor interrogation instruments are covered under a US and International Patent Licensing Agreement between Micron Optics, Inc. and United Technologies Corporation. This license transfers to the users of Micron Optics sensor products and ensures that Micron Optics products are authorized for use in sensing applications. Certificates are available upon request.

Installation Information

The os3155 Strain Gage is designed to be spot welded to steel using a capacitive-discharge spot welder having 50-150 watt-seconds of energy. The spot welder should be equipped with a spherical tip electrode with a diameter of approximately 0.03 inches (0.76 mm). Practice welds using a blank os3155 gage may be helpful in developing proper technique.

Use firm pressure on the electrode. After making a practice weld, pull the gage off of the surface. A properly formed weld will result in a small piece of the specimen or gage surface to break away. If needed, adjust the weld energy and electrode pressure until a satisfactory weld is obtained.

Detailed installation instructions and welder recommendations are available at:

http://www.micronoptics.com/support_downloads/Sensors/

This Sensor Information Sheet is verification of conformance.

Micron Optics, Inc. 1852 Century Place, NE. Atlanta, GA 30345, Ph 404 325 0005
www.micronoptics.com

MICRON OPTICS Sensor Information Sheet

os3155 | Compensated Optical Strain Gage

Part # os3155- 1532-1536-.5UT-1UT

Serial # C307127

Nominal Wavelength, λ_{0Temp} (nm) @22°C (Temp FBG) 1532.040

Nominal Wavelength, $\lambda_{0Strain}$ (nm) @22°C (Strain FBG) 1536.200

Certified by:

Variable	Description	Value	Units
F_G	Gage Factor @22°C	0.811	-
$\Delta\lambda_S$	Wavelength Shift (Strain)	Interrogated	nm
λ_{0S}	Nominal Wavelength (Strain)	Initial Value	nm
S_T	Temp. Sensitivity @22°C	1.833×10^{-6}	-
$\Delta\lambda_T$	Wavelength Shift (Temp)	Interrogated	nm
λ_{0T}	Nominal Wavelength (Temp)	Initial Value	nm
CTE_S	CTE of Test Specimen	User Defined	µm/m-°C
CTE_T	CTE of Temperature Probe	16.6	µm/m-°C

Strain (mechanically induced µm/m):

$$\varepsilon = 10^6 \left[\frac{(\Delta\lambda/\lambda_0)_S - (\Delta\lambda/\lambda_0)_T}{F_G} \right] - \frac{(\Delta\lambda/\lambda_0)_T}{S_T} (CTE_S - CTE_T)$$

Thermal Output and Temperature Compensation

Fiber Bragg grating (FBG) based strain gages respond to both strain and temperature. Temperature induced strain results from a combination of two factors.

1) Thermal expansion of the substrate on which the gage is mounted.
2) Thermally induced index of refraction changes in the FBG.

Both factors affect the FBG's center wavelength.

Several methods are available to decouple strain and temperature components in measurements using this gage. Popular methods involve using FBGs to measure change in temperature or employing dummy FBG strain gages (as with conventional electronic strain gages).

For additional information about temperature compensation techniques and converting wavelength values to strain and temperature, see:

http://www.micronoptics.com/support_downloads/Sensors/

Micron Optics Quality and Performance

TUNED

Products displaying the "Micron Optics Tuned" logo include Micron Optics tunable technologies thus ensuring high quality and performance. Certified sensors have been tested and qualified for use with Micron Optics Sensing Instruments.

Qualification Statement

CERTIFIED ISO 9001:2008

This sensor has been manufactured using procedures and materials documented under Micron Optics, Inc's ISO 9001:2008 qualification process.

Patent Certification

Micron Optics sensors and sensor interrogation instruments are covered under a US and International Patent Licensing Agreement between Micron Optics, Inc. and United Technologies Corporation. This license transfers to the users of Micron Optics sensor products and ensures that Micron Optics products are authorized for use in sensing applications. Certificates are available upon request.

Installation Information

The os3155 Strain Gage is designed to be spot welded to steel using a capacitive-discharge spot welder having 50-150 watt-seconds of energy. The spot welder should be equipped with a spherical tip electrode with a diameter of approximately 0.03 inches (0.76 mm). Practice welds using a blank os3155 gage may be helpful in developing proper technique.

Use firm pressure on the electrode. After making a practice weld, pull the gage off of the surface. A properly formed weld will result in a small piece of the specimen or gage surface to break away. If needed, adjust the weld energy and electrode pressure until a satisfactory weld is obtained.

Detailed installation instructions and welder recommendations are available at:

http://www.micronoptics.com/support_downloads/Sensors/

This Sensor Information Sheet is verification of conformance.

Micron Optics, Inc. 1852 Century Place, NE. Atlanta, GA 30345, Ph 404 325 0005
www.micronoptics.com

MICRON OPTICS Sensor Information Sheet

os3155 | Compensated Optical Strain Gage

Part # os3155-1542-1546-1UT-.5UT

Serial # C307121

Nominal Wavelength, λ_{0Temp} (nm) @22°C (Temp FBG) 1542.066

Nominal Wavelength, $\lambda_{0Strain}$ (nm) @22°C (Strain FBG) 1546.282

Certified by:

Variable	Description	Value	Units
F_G	Gage Factor @22°C	0.820	-
$\Delta\lambda_S$	Wavelength Shift (Strain)	Interrogated	nm
λ_{0S}	Nominal Wavelength (Strain)	Initial Value	nm
S_T	Temp. Sensitivity @22°C	1.833×10^{-5}	-
$\Delta\lambda_T$	Wavelength Shift (Temp)	Interrogated	nm
λ_{0T}	Nominal Wavelength (Temp)	Initial Value	nm
CTE_S	CTE of Test Specimen	User Defined	µm/m-°C
CTE_T	CTE of Temperature Probe	16.6	µm/m-°C

Strain (mechanically induced µm/m):

$$\varepsilon = 10^6\left[\frac{(\Delta\lambda/\lambda_0)_S-(\Delta\lambda/\lambda_0)_T}{F_G}\right]-\frac{(\Delta\lambda/\lambda_0)_T}{S_T}(CTE_S-CTE_T)$$

Thermal Output and Temperature Compensation

Fiber Bragg grating (FBG) based strain gages respond to both strain and temperature. Temperature induced strain results from a combination of two factors.

1) Thermal expansion of the substrate on which the gage is mounted.
2) Thermally induced index of refraction changes in the FBG.

Both factors affect the FBG's center wavelength.

Several methods are available to decouple strain and temperature components in measurements using this gage. Popular methods involve using FBGs to measure change in temperature or employing dummy FBG strain gages (as with conventional electronic strain gages).

For additional information about temperature compensation techniques and converting wavelength values to strain and temperature, see:

http://www.micronoptics.com/support_downloads/Sensors/

Micron Optics Quality and Performance

TUNED

Products displaying the "Micron Optics Tuned" logo include Micron Optics tunable technologies thus ensuring high quality and performance. Certified sensors have been tested and qualified for use with Micron Optics Sensing Instruments.

Qualification Statement

CERTIFIED ISO 9001:2008

This sensor has been manufactured using procedures and materials documented under Micron Optics, Inc's ISO 9001:2008 qualification process.

Patent Certification

Micron Optics sensors and sensor interrogation instruments are covered under a US and International Patent Licensing Agreement between Micron Optics, Inc. and United Technologies Corporation. This license transfers to the users of Micron Optics sensor products and ensures that Micron Optics products are authorized for use in sensing applications. Certificates are available upon request.

Installation Information

The os3155 Strain Gage is designed to be spot welded to steel using a capacitive-discharge spot welder having 50-150 watt-seconds of energy. The spot welder should be equipped with a spherical tip electrode with a diameter of approximately 0.03 inches (0.76 mm). Practice welds using a blank os3155 gage may be helpful in developing proper technique.

Use firm pressure on the electrode. After making a practice weld, pull the gage off of the surface. A properly formed weld will result in a small piece of the specimen or gage surface to break away. If needed, adjust the weld energy and electrode pressure until a satisfactory weld is obtained.

Detailed installation instructions and welder recommendations are available at:

http://www.micronoptics.com/support_downloads/Sensors/

This Sensor Information Sheet is verification of conformance.

MICRON OPTICS Sensor Information Sheet

os3155 | Compensated Optical Strain Gage

Part # os3155- 1552-1556-1UT-1UT

Serial # C307130

Nominal Wavelength, λ_{oTemp} (nm) @22°C (Temp FBG) 1551.990

Nominal Wavelength, $\lambda_{oStrain}$ (nm) @22°C (Strain FBG) 1556.366

Certified by:

Variable	Description	Value	Units
F_G	Gage Factor @22°C	0.825	-
$\Delta\lambda_S$	Wavelength Shift (Strain)	Interrogated	nm
λ_{oS}	Nominal Wavelength (Strain)	Initial Value	nm
S_T	Temp. Sensitivity @22°C	1.833×10^{-5}	-
$\Delta\lambda_T$	Wavelength Shift (Temp)	Interrogated	nm
λ_{oT}	Nominal Wavelength (Temp)	Initial Value	nm
CTE_S	CTE of Test Specimen	User Defined	µm/m-°C
CTE_T	CTE of Temperature Probe	16.6	µm/m-°C

Strain (mechanically induced µm/m):

$$\varepsilon = 10^6 \left[\frac{(\Delta\lambda/\lambda_0)_S - (\Delta\lambda/\lambda_0)_T}{F_G} \right] - \frac{(\Delta\lambda/\lambda_0)_T}{S_T} (CTE_S - CTE_T)$$

Thermal Output and Temperature Compensation

Fiber Bragg grating (FBG) based strain gages respond to both strain and temperature. Temperature induced strain results from a combination of two factors.

1) Thermal expansion of the substrate on which the gage is mounted.
2) Thermally induced index of refraction changes in the FBG.

Both factors affect the FBG's center wavelength.

Several methods are available to decouple strain and temperature components in measurements using this gage. Popular methods involve using FBGs to measure change in temperature or employing dummy FBG strain gages (as with conventional electronic strain gages).

For additional information about temperature compensation techniques and converting wavelength values to strain and temperature, see:

http://www.micronoptics.com/support_downloads/Sensors/

Micron Optics Quality and Performance

TUNED

Products displaying the "Micron Optics Tuned" logo include Micron Optics tunable technologies thus ensuring high quality and performance. Certified sensors have been tested and qualified for use with Micron Optics Sensing Instruments.

Qualification Statement

CERTIFIED ISO 9001:2008

This sensor has been manufactured using procedures and materials documented under Micron Optics, Inc's ISO 9001:2008 qualification process.

Patent Certification

Micron Optics sensors and sensor interrogation instruments are covered under a US and International Patent Licensing Agreement between Micron Optics, Inc. and United Technologies Corporation. This license transfers to the users of Micron Optics sensor products and ensures that Micron Optics products are authorized for use in sensing applications. Certificates are available upon request.

Installation Information

The os3155 Strain Gage is designed to be spot welded to steel using a capacitive-discharge spot welder having 50-150 watt-seconds of energy. The spot welder should be equipped with a spherical tip electrode with a diameter of approximately 0.03 inches (0.76 mm). Practice welds using a blank os3155 gage may be helpful in developing proper technique.

Use firm pressure on the electrode. After making a practice weld, pull the gage off of the surface. A properly formed weld will result in a small piece of the specimen or gage surface to break away. If needed, adjust the weld energy and electrode pressure until a satisfactory weld is obtained.

Detailed installation instructions and welder recommendations are available at:

http://www.micronoptics.com/support_downloads/Sensors/

This Sensor Information Sheet is verification of conformance.

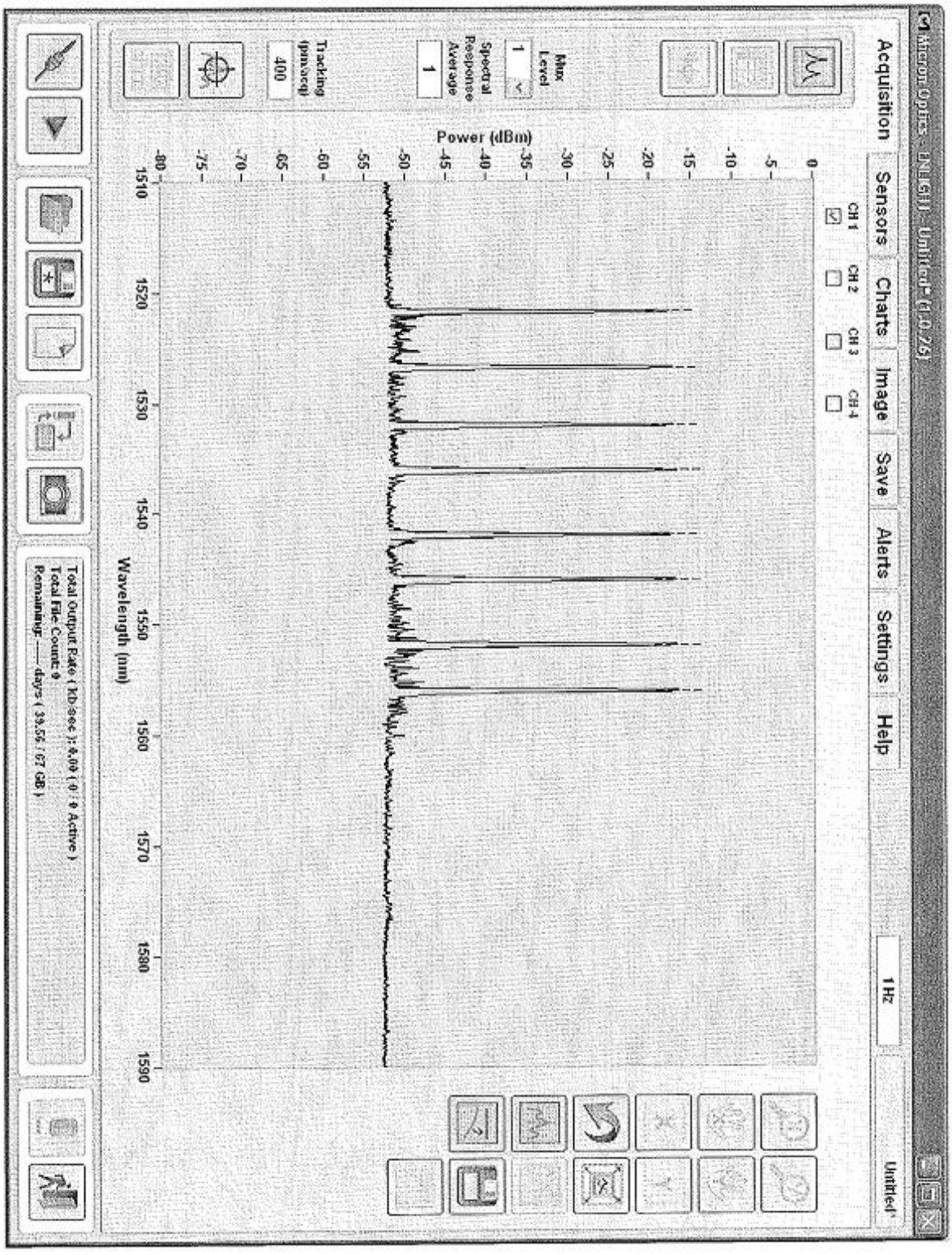
Micron Optics - ENLIGHT - Untitled* (1.0.26)
Acquisition
Sensors
Charts
Image
Save
Alerts
Settings
Help
1 Hz
Untitled*
CH 1
CH 2
CH 3
CH 4
Max Level
Spectral Response Average
Tracking (pan,acq)
400
Power (dBm)
Wavelength (nm)
Total Output Rate (kb/sec): 8.00 (0 : 0 Active)
Total File Count: 0
Remaining: ____ days (39.56 / 67 GB)